PhD-FSTM-2023-128
The Faculty of Science, Technology and Medicine

DISSERTATION

Defence held on 29/11/2023 in Esch-sur-Alzette
to obtain the degree of

DOCTEUR DE L'UNIVERSITÉ DU LUXEMBOURG

EN *PHYSIQUE*

by

Marta Inês Pires FERREIRA

Born on 6 February 1994 in Leiria, Portugal

DEPOSITION OF NANOCOMPOSITE COATINGS BASED ON Al_2O_3 AND GOLD NANOPARTICLES EXHIBITING SURFACE PLASMON RESONANCE.

Dissertation defence committee

Dr Patrick Choquet, dissertation supervisor
Doctor, Luxembourg Institute of Science and Technology

Dr Phillip Dale, Chairman
Professor, Université du Luxembourg

Dr Albano Cavaleiro, Vice Chairman
Professor, Universidade de Coimbra

Dr David Horwat
Professor, Institut Jean Lamour

Dr Naoufal Bahlawane
Doctor, Luxembourg Institute of Science and Technology

Acknowledgment

Embarking on my PhD journey was an exhilarating adventure filled with countless challenges. Like a brave explorer, I faced numerous challenges—intellectual puzzles, scholarly expeditions, and relentless perseverance. Navigating through uncharted territories of knowledge, I delved into ancient archives, battled with theories, and conquered self-doubt. I emerged from this adventure with newfound wisdom, resilience, and a treasure trove of academic achievements.

I would like to express my sincere gratitude to all those who have supported and contributed to the completion of this Ph.D. thesis. Their guidance, encouragement, and assistance have been invaluable throughout this research journey.

I want to extend my deepest appreciation to my PhD supervisor, Dr. Patrick Choquet, for providing me with the opportunity to work at the Luxembourg Institute of Science and Technology (LIST) and for engaging in informative scientific discussions. I am also grateful to the CET committee: Phillip Dale from University of Luxembourg and Naoufal Bahlawane from LIST for following the progress of my Thesis over these four years. Their insightful comments and challenging questions have helped me broaden my research from various perspectives.

A special acknowledgment goes to Diego Martínez, with whom I had numerous brainstorming sessions using the whiteboard and his famous "*Holy book*." Many research roadblocks were overcome during our lengthy scientific discussions. I want to express my sincere gratitude for his sense of humour, captivating stories, and, of course, the unforgettable reference to the spaghetti monster. Thank you for making my scientific journey both enlightening and enjoyable.

The completion of my dissertation would not have been possible without the support of Jérôme Guillot, Nathalie Valle, Brahime El Adib, Yves Fleming, João Fernandes, Simon Bulou and Cristina Rojas. Furthermore, I would like to express my gratitude to Jean-Baptiste Chemin for his invaluable help and

guidance regarding the PVD machine. His expertise and support were crucial in navigating the challenges I encountered during my research.

Along my journey, I was lucky to share my lab and office with different people such as Vasu, Kishor, Benjamin, Alex, Greg, Ali, Ingrid, Thiago (Viva à Fátima), João, Zahra, Jordi, Marko, Marek, Marco, Shiv and Poorani.

Additionally, I owe a tremendous debt of gratitude to my family, whose unwavering support made this work possible. Thank you all for being a constant source of encouragement and love throughout this journey.

Finally, a special thanks goes to the legendary Eliseu.

Abstract

Nanoparticles exhibit unique properties due to their small size, which are absent in bulk materials. These properties can be employed for innovative applications, making them highly promising. Nanocomposite coatings containing metal nanoparticles, particularly their ability to support Localized Surface Plasmon Resonances (LSPRs), have garnered significant attention from both researchers and industries. The precise control over the morphology and distribution of nanoparticles in the matrix material becomes crucial for tailoring the LSPR signal, making it imperative for successful applications. In this Thesis, alumina and gold were chosen as a dielectric and metal nanoparticle.

The growth of Al_2O_3 films in an oxidizing atmosphere was investigated using reactive magnetron sputtering. Challenges such as process instability and the formation of insulating layers on the target leading to arcing events were addressed by implementing an active feedback reactive sputtering control for the deposition of Al_2O_3 thin films. These films were deposited using two sputtering sources: high-power impulse magnetron sputtering (HiPIMS), mid-frequency (MF) and a combination of both (MF + HiPIMS) at varying powers and deposition temperatures. X-ray diffraction (XRD) analysis indicated the formation of polycrystalline γ-Al_2O_3 films, except for those deposited at low temperature, which were amorphous. Additionally, energetic depositions (higher power, HiPIMS) yielded films with higher grain density and refractive index. However, HiPIMS deposition resulted in higher compressive stress due to increased ion energy and lower deposition rate.

Prior to Au deposition, an optimization process was conducted for alumina films. It was observed that alumina films produced at room temperature exhibited decreased roughness, lower likelihood of delamination and ensured no thermal impact on the subsequent Au deposition.

The alumina surface underwent a plasma pre-treatment involving argon and hydrogen to evaluate its impact on the following growth of Au nanoparticles. The findings revealed that such treatment had advantageous effects on

depositing Au nanoparticles; thus, this treatment led to a decrease in the formation of a continuous film (percolation) over time and higher levels of absorbance compared to untreated surfaces. This effect was analysed using AFM and XPS techniques. Both techniques revealed that treated surfaces exhibited greater height/roughness and lower coverages/correlation length, which retarded the percolation effect and enhanced the growth of nanoparticles when comparing with untreated surfaces. The effect of Ar/H_2 plasma treatment was studied using continuous and pulsed DC sources for deposition of Au. It was observed that the use of both sources yielded the same optical behaviour for plasmonic properties, indicating that the effect is independent of the source but dependent on the surface treatment.

Finally, it is worth mentioning that samples prepared with Ar/H_2 plasma proved effective for Surface-Enhanced Raman Scattering (SERS) applications for detecting low concentrations of Rhodamine-6G, in contrast to the much lower effect observed for the Au grown on untreated alumina surfaces.

Keywords: Localized surface plasmon resonance (LSPR), Au nanoparticles, Al_2O_3, HiPIMS, MF, MF+HiPIMS, physical vapour deposition, sputtering, SERS.

Glossary

Abbreviations

NPs	Nanoparticles
SPs	Surface Plasmons
SPR	Surface Plasmon Resonance
LSPR	Localized surface plasmon resonance
SERS	Surface-enhanced Raman scattering
SC	Solar cells
MEF	Metal-enhanced fluorescence
QDs	Quantum dots
PVD	Physical Vapour Deposition
CVD	Chemical Vapour Deposition
ALD	Atomic layer deposition
DC	Direct current
NIR	Near-infrared
RF	Radio-frequency
MF	Mid-frequency
MG	Mie Gustav
RIS	Refractive index sensitivity
S	Sensitivity
XPS	X-ray photoelectron spectroscopy
XRD	X-ray diffraction
XRR	X-ray reflectivity
SEM	Scanning electron microscopy
AFM	Atomic force microscopy
ToF-SIMS	Time-of-Flight Secondary Ion Mass Spectrometry
GIXRD	Grazing incidence X-ray diffraction
OR	Ostwald ripening
HHCF	Height-height correlation function
2D	Two dimensions
3D	Three dimensions
AR	Aspect ratio
BE	Binding energy
LIST	Luxembourg Institute of Science and Technology
MFP	Mean free path
UV	Ultraviolet
Vis	Visible
HiPIMS	High-Power Impulse Magnetron Sputtering
HRTEM	High-resolution transmission electron microscopy
EELS	Electron energy loss spectroscopy
FFT	Fast Fourier transform
TEM	Transmission electron microscopy
AOS	Amount of substance
ML	Multilayer
STEM	Scanning transmission electron microscopy
FWHM	Full width at maximum
IMFP	Inelastic electron mean free path
TPP-2 M	Tanuma, Powell, Penn 2 Method
Sccm	Standard cubic centimeters per minute
AOS	Amount of substance
EF	Enhancement factor
AR	Aspect ratio

Chemicals

R6G	Rhodamine 6G, 9-[2-(Ethoxycarbonyl)phenyl]-*N*-ethyl-6-(ethylamino)-2,7-dimethyl-3*H*-xanthen-3-iminium chloride.
Au	Gold
Al_2O_3	Aluminium oxide
H_2	Hydrogen
Ag	Silver
Cu	Copper
CuO	Copper oxide
SiO_2	Silicon oxide
TiO_2	Titanium oxide
WO_3	Tungsten trioxide
Si	Silicon
NiO	Nickel oxide
DMSO	Dimethyl sulfoxide
CO	Carbon oxide
OH	Hydroxyl
Me-O	metal-oxide
CdSe	Cadmium selenide

Symbols

w	Roughness
ξ	Correlation length
α	Hurst parameter
r	Radius
D	Fractal dimension
z	Dynamic exponent
m	Local slope
A	Absorbance
h	Island height
c	Surface Coverage
t_{off}	Time-on
t_{on}	Time-off
S	Stiffness
n	Refractive index
λ	Wavelength
d	Interplanar spacing
θ	Angle of incidence
β	Full width at half maximum or growth exponent
β_{inst}	Instrumental broadening
β_D	Size of crystallite broadening
β_s	Strain broadening
$\tilde{N}$	Complex refractive index
Ψ	Psi
Δ	Delta
k	Extinction coefficient
i	Imaginary number
ϕ_1	Angles of incidence
ϕ_2	Angles of refraction
σ	Residual stress
t_s	Wafer thickness
t_f	Film thickness

R_F	Curvature of the film
R_S	Curvature of the substrate
R	Radius
h	Planck's constant
E_k	Kinetic energy
ν	Frequency of X-rays
σ_{th}	Thermal stress
σ_{int}	Intrinsic stress
σ_{ext}	Extrinsic stress
T	Texture parameter or Transmittance
M	Molecular weight
Eg	Energy gap
K(T)	Inelastic scattering cross section
Ω	Solid angle of emission
c(z)	Number of atomes per unit volume at depth z
J(E)	Experimental spectrum of the foil
F(E)	Spectrum of a single atom
ε_0	Permittivity of the vacuum
ε_1	Dielectric constant of the nanoparticle
ε_m	Dielectric constant of an embedding medium
E_i	Internal field
E_o	Incident electrical field
p	Dipole moment
α	Polarizability
σ_{abs}	Absorption cross-section
σ_{scat}	Scattering cross-section
σ_{ext}	Extinction cross-section
k_o	Wavenumber of light in vacuum
I_m	Imaginary part
V_O	Volume of a particle
L_i	Geometrical depolarization factor
γ_s	Surface tension
γ_F	Surface tension of the film surface
$\gamma_{S/F}$	Surface tension of the film/substrate interface
E_f	Elastic modulus
ν_f	Poisson's ratio
α_f	Linear thermal expansion coefficient of the film
α_s	Linear thermal expansion coefficient of the substrate
T_1	Initial temperature
T_2	Final temperature
ρ	Density
N_A	Avogadro's constant
I_{SERS}	Intensity of the specific peak
I_{RAMAN}	Intensity of the analyte
N_{SERS}	Concentration in SERS
I_{RAMAN}	Concentration in Raman

Table of Contents

1. Introduction ____ 1

1.1. Motivation ____ 2

1.2. Selection of Materials ____ 10

1.2.1. Metal Nanoparticles ____ 10

1.2.2. Dielectric matrixes ____ 10

1.3. Objectives and structure of the Ph.D. ____ 19

2. Deposition and characterization methods: description and theory ____ 24

2.1 Physical vapour deposition and magnetron sputtering ____ 25

2.1.1 Direct-current magnetron sputtering ____ 28

2.1.2 Mid-frequency ____ 29

2.1.3 High power impulse magnetron sputtering ____ 30

2.1.4 Reactive magnetron sputtering ____ 31

2.2 Thin films growth modes ____ 34

2.2.1. Structure Zone Models ____ 39

2.3 Experimental conditions of magnetron sputtering deposition ____ 42

2.3.1. Deposition chamber ____ 42

2.3.2. Deposition of alumina coatings ____ 43

2.3.3. Deposition of Gold nanoparticles ____ 46

2.3.4. H_2 + Ar plasma treatment ____ 47

2.4 Characterization techniques ____ 48

2.4.1 X-Ray Diffraction ____ 48

2.4.2 Specular X-ray Reflectivity ____ 56

2.4.3 Ellipsometry ____ 58

2.4.4 Stylus profilometry ____ 60

2.4.5 Atomic force microscopy ____ 62

2.4.6 Scanning electron microscopy ____ 68

2.4.7 Transmission electron microscopy ____ 69

2.4.8 Electron energy loss spectroscopy ____ 72

2.4.9 X-ray photoelectron spectroscopy and method of Tougaard ____ 74

2.4.10 Time-of-Flight Secondary Ion Mass Spectrometry ____ 80

2.4.11 Raman spectroscopy ____ 81

2.4.12 UV-Vis spectroscopy ____ 82

2.5 Localized surface plasmon resonance ____ 83

2.5.1 Effect of Nanoparticle Size ____ 85

2.5.2 Effect of Nanoparticle Shape ____ 88

2.5.3 Material dependence ____ 91

2.5.4 Effect of surrounding media ____ 92

3. Alumina coatings ____ 95

3.1. Deposition conditions ____ 96

3.2. XRD analysis 99
3.3. TEM analysis 102
3.4. EELS analysis 104
3.5. SEM analysis 105
3.6. Additional structural properties of the coatings 106
3.7. Conclusion 113
4. Selection and optimization of Au/Al_2O_3 deposition conditions 116
4.1 Optimization of the alumina surface properties for Au NPs deposition 117
4.2 Conditions of deposition of Au nanoparticles deposition parameters 124
4.3 Conclusion 129
5. Deposition of Au/Al_2O_3 films 131
5.1 XPS results and analysis based on Tougaard method 132
5.2 SEM results 136
5.3 AFM results and HHCF 137
5.3.1 Analysis of the stiffness images 139
5.3.2 Analysis of the topographical images using the height-height correlation function 143
5.4 Geometrical models of Au growth 147
5.5 Optical properties 150
5.6 Origin of the influence of the Ar/H_2 plasma pre-treatment on the film growth 154
5.7 Growth mechanisms of Au NPs 161
5.8 Application of samples for SERS 163
5.9 Conclusions 166
6. Advanced synthesis of Au/Al_2O_3 films 169
6.1. Au/Al_2O_3 monolayers using pulsed DC sputtering for Au 170
6.1.1. Tougaard analysis of XPS results 171
6.1.2. AFM measurements 172
6.1.3. Optical properties 174
6.2. $Au@Al_2O_3$ multilayers using continuous DC sputtering for Au 176
6.2.1 Microstructure of the multilayers evaluated by TEM 177
6.2.2 Optical properties 180
6.3. Conclusion 182
7. Conclusions and perspectives 183
8. References 188
9. Scientific Outputs 217

List of Figures

Figure 1-1 - The Lycurgus cup (left): illuminated from outside. (right): illuminated from inside. Image from [11]. 3

Figure 1-2 - Schematics of plasmon oscillation for a metallic sphere, exhibiting the movement of the conduction electron charge of the cloud relative to the nuclei. Adapted from [17]. 4

Figure 1-3 – (Top-image) Illustration of a colloidal gold samples (I-V) after reduction with sodium citrate. Stability is attained through electrostatic stabilisation (Bottom image) with citrate ions ($C_3H_5OCOO_3^{3-}$), and the coloration indicates the various sizes of gold nanoparticles with distinctive LSPR. Adapted from [22]. 5

Figure 1-4 – Different coloration depending on the core size of the quantum dots. Adapted from: [44] 6

Figure 1-5 – Top image: spectrum of the visible light. The numbers represent the wavelength in nm. Middle image: colloidal suspensions of CdSe quantum dots of decreasing size from ~4.0 nm to 1.8 nm from left to right. Bottom image: QDs exposed to UV light. Bottom image: exposed to ambient illumination. Adapted from: [44] 7

Figure 1-6 - Diagram of some of the most important methods for synthesis of NP's. 8

Figure 1-7 – Colour pictures of Au coatings on TiO_2 and Al_2O_3 deposited on glass substrates. Adapted from [28]. 11

Figure 1-8 – Images of a) snooker ball (spherical shape, where $r_1=r_2=r_3$), b) submarine (prolate shape with $r_1=r_2<r_3$, i.e. 'uniaxially elongated') and c) a frisbee (oblate shape with $r_1=r_2>r_3$, i.e. 'uniaxially smashed'). 16

Figure 1-9 – Depolarization factor in function of aspect ratio for a sphere, prolate and oblate. a) against r_3/r_1 in a logarithmic axis, where the yellow and green shaded areas indicate oblate and prolate geometries, respectively. b) against nanoparticle asymmetry (using r_{minor}/r_{major} $minor\ axes\ major\ axes$ in linear scale. From Figueiredo et al. [161] 17

Figure 1-10 - Schematic of the PhD structure, including the main aspects studied. A. Al_2O_3 deposition (Ch. 3); B. Au growth and surface treatments (Ch. 4 and 5); C. Au deposition mode (Ch. 6). D. Multilayer (Ch. 6). 20

Figure 2-1 – Regimes of operation of DCMS, MPP (modulated pulse power) and HiPIMS (or HPPMS) based on peak power density and duty cycle. Adapted from [179]. 27

Figure 2-2 - Schematic of the power density during the discharge (HiPIMS, MPPMS and DCMS) operated at same average power P = 300 W. Adapted from [177] 28

Figure 2-3 - Asymmetrical bi-polar pulsed dc sputtering of dielectrics. t_{on} represents the "on-time", t_{off} "off-time" or "reverse time", and t_{cycle} represents a full cycle. Adapted from [182]. The duty cycle is defined as t_{on}/t_{cycle}. 29

Figure 2-4 - Deposition rates of various metallic target materials measured for both DCMS and HiPIMS under the same conditions ($P_{average}$ = 125 W, p = 0.67 Pa, $d_{substrate\ holder}$ = 6.5 cm). The HiPIMS to DCMS deposition rate ratio is plotted as scattered points. Reproduced from [191]. 31

Figure 2-5 - a) Illustration of the evolution of N_2 partial pressure and target poisoning during reactive sputtering under nitrogen. b) Hysteresis curve in reactive sputtering: i) deposition rate ii) chamber pressure iii) discharge voltage as a function of flow of reactive gas. Adapted from:[203,204] 32

Figure 2-6 - Schematic of the common atomistic processes occurring during nucleation and growth on surfaces. 35

Figure 2-7 - Schematic of ripening mechanisms a) Ostwald ripening (OR) or atom migration, and (b) Smoluchowski ripening (SR) or particle migration and coalescence. 36

Figure 2-8 - Schematic representation of the three basic growth modes in thin films a) Volmer-Weber b) Stranski-Krastanov and c) Frank-van der Merwe. Θ denotes the overlayer coverage in monolayers (ML). 36

Figure 2-9 - Schematic of the surface tensions present in a film island on a substrate. 38

Figure 2-10 – SZM of Movchan and Demchishin. T represents the substrate temperature and T_m the melting point temperature of the coating-material, both in Kelvin. Adapted from [221]. 40
Figure 2-11 – Schematic of the SZM developed by Anders et al. showing a cross-sectional view of the types of the possible polycrystalline film microstructure, with t indicating the net thickness, E* representing the normalized energy flux and T* the generalized substrate temperature. It should be noted that the boundaries between the different zones and numerical values provided are for illustrative purposes only. Adapted from [228].* 41
Figure 2-12 – a) Image of PVD system used in this Ph.D. b) Interior of the PVD chamber composed of Al and Au targets and 3 microwave antennas for Ar/H_2 treatment. 42
Figure 2-13 - Schematic (to scale) of the movement of the substrates in front of the aluminium target during the deposition. 44
Figure 2-14 - Schematic (to scale) of the movement of the substrates in front of the gold target during deposition. 46
Figure 2-15 - Schematic representing Bragg's Law. 48
Figure 2-16 – Characteristics of a XRD peak. 49
Figure 2-17 – Schematic of the influence of macro stress (left) and micro stress (right) in a XRD peak. Adapted from [206]. 50
Figure 2-18 - Williamson-Hall plot, where the intersection of the fitting line with the y-axis represents the crystallite size, and the slope represents the microstrain. 52
Figure 2-19 – a) Schematic of GIXRD. b) XRD pattern of a film with (dark purple line) and without (blue line) the Si (311) contribution. 53
Figure 2-20 – XRR pattern and respective information that can be obtained from it. Adapted from [244]. 56
Figure 2-21 – a) Ellipsometry measurement demonstrates the use of linearly polarized light directed at the sample with both p- and s-components of polarization. As the light interacts with the sample, the reflected p- and s-polarizations exhibit varying amplitudes (Ψ, degrees) and phases (Δ, degrees), resulting in the generation of elliptically polarized light.[246] b) An incident light beam interacting with the interface separating air and a material characterized by a complex refractive index $\tilde{N}_2$. Adapted from [247] 58
Figure 2-22–- Schematic of the residual stress present in thin films and how it affects the curvature of the substrate. When a film has a propensity to expand, it leads to the development of compressive stress (shown as (a)), while a film that has a tendency to shrink generates tensile stress (shown as (b)). Adapted from [250]. 61
Figure 2-23 – Schematic of control in AM-FM Mode. Adapted from Hurley et al. [256]. 63
Figure 2-24 – Experimental fitting of the HHCF using Eq. 2-27, and physical meaning of the of the fitting parameters. 66
Figure 2-25 – Interpretation of the parameters obtained from the fitting of the HHCF. a) Comparison between the local surface morphology for surface with similar w but different α. b) Schematic of a rough surface with the mean heigh (h), correlation length (ξ) and roughness (w). Adapted from [262]. 66
Figure 2-26 - log-log plot of HHCF, H(r,t) as a function of distance r for Cu thin films on glass substrate at different deposition times (0-45 minutes). Adapted from [260]. 67
Figure 2-27 – Schematic of the interaction of the electrons with a sample. 69
Figure 2-28 - Schematic diagram of electron energy loss spectrum showing typical regions of different energy losses. Adapted from [267]. 72
Figure 2-29 - Relationship between the DOS and the ELNES intensity in the ionization edge fine structure (Adapted from William and Carter et al. [267]). 73
Figure 2-30 - Cu2p spectra from Cu atoms with different concentration distributions in an Au matrix. Adapted from [274]. 76
Figure 2-31 - Process for the determination of the height and coverage of the islands from XPS spectra using Tougaard method. The important equations are included. 79
Figure 2-32 - Extinction efficiencies (σ_{ext}) and scattering cross section (σ_{scat}) of Au spherical NPs in a medium with a refractive index of 2.0 with an increasing in the NP size. Adapted from [115]. 85

Figure 2-33 - Absorption spectra of 9 nm, 22 nm, 48 nm and 99 nm of Au nanoparticles. Adapted from [286]. 86
Figure 2-34 - Au dielectric permittivity for bulk gold as a function of wavelength. Adapted from [288]. 89
Figure 2-35 - Absorption spectra for a sphere, oblate and prolate. The relevant shape factors are shown. Adapted from [285]. 89
Figure 2-36 – (top) TEM images of Au nanoparticles with different shape and sizes a) Nanospheres b) nanocubes c) nanorods (AR = 2.4) d) nanorods (AR = 3.4) and e) nanorods (AR = 4.6), and (bottom) normalized extinction spectra from the above structures. Adapted from [287]. 90
Figure 2-37 - Dielectric permittivity for silver bulk as a function of wavelength. Adapted from [291] 91
Figure 2-38 - Half-width of the dipolar resonances of different sizes of Au nanoparticles versus the respective peak position for a refractive index of 1.5, 2.0 and 2.5. Adapted from [115]. 92
Figure 2-39 - The DDA findings involving a sinking sphere model that examines the displacement caused by a substrate. Specifically, a metal core is gradually submerged into a semi-spherical piece of mica, positioned at intervals of 0, 5, 10, and 15 nm from the edge, along the diameter of the core. Adapted from [292]. 93
Figure 3-1 - Hysteresis plots (PEM signal vs O_2 flow) obtained for a HiPIMS process at 2000 W in an Ar/O_2 atmosphere at 450°C. 96
Figure 3-2 - The waveforms of the target and current were recorded for different operations. a) HiPIMS. b) MF with the current multiplied by a factor of 10. c) shows MF+HiPIMS with 5 MF pulses. d) shows MF+HiPIMS with 10 MF pulses. The average power for each source was set at 2500 W. 97
Figure 3-3 – XRD patterns of Al_2O_3 films deposited by MF, HIPIMS and MF+HiPIMS at various temperatures (450ºC, except indicated otherwise) and powers (indicated in W next to each pattern). The position of a reference of γ-Al_2O_3 is indicated by dotted lines. In the case of MF+HiPIMS an average power of 2500 W was set for each source for both 5 and 10 pulses. a) without rotation b) with rotation of 45°. 99
Figure 3-4 – Integrated intensity of peaks of Al_2O_3 located at a) 37°, b) 46° and c) 67°, and d) for the silicon peak from Figure 3-3. 100
Figure 3-5 – Schematics of two films with identical texture, thickness, and grain size, but different grain density. An increase in the density of γ-Al_2O_3 grains, from left to right, is observed in films deposited by HIPIMS rather than MF or at higher deposition powers. The red arrows represent the incoming and outgoing X-ray beams. It is illustrated how increased grain density contributes to a reduction in the amount of radiation that reaches and/or leaves the Si substrate. 101
Figure 3-6 – A close-up view of the (400) peak of alumina for films deposited under various power conditions by HIPIMS and MF. 102
Figure 3-7 – High resolution TEM images of selected films deposited under varying conditions. a) MF at 3500W and 200ºC. b) MF at 2500W and 450ºC. c) MF at 3500W and 450ºC. d) HiPIMS-2500W-450ºC. Insets are shown in the images, displaying FFTs from the HRTEM images and the red dashed semi-circumferences highlight the position of the first 8 planes of γ-Al_2O_3 reference [JCPDS Card No. 00-050-0741]. The Miller Indexes of these planes are labelled in (a). The scale bars in all images represent 5 nm. 103
Figure 3-8 – EELS measurement of the Al-L edge of selected films at various temperatures (450ºC, except indicated otherwise) and powers (indicated in W next to each pattern) with a reference of γ-Al_2O_3 included at the top. 104
Figure 3-9 – SEM images of cross-sections of Al_2O_3 films produced by (a) HiPIMS at 2000 W, (b) HiPIMS at 2500 W, (c) MF at 2000 W and (d) MF at 3500 W at 450°C. The scale bars for all images correspond to 200 nm. 105
Figure 3-10 – Characteristics of the deposited alumina films by MF, HiPIMS and MF+HiPIMS at various temperatures and powers. a) Deposition rate. b) compressive residual stress. c) density. d) refractive index. The reference value for the density of γ-Al_2O_3 [JCPDS Card No. 00-050-0741] is indicated by a horizontal line in (c). 106

Figure 3-11 – Refractive index (n) of the films measured at a wavelength of 632.8 nm in function of the density. The back line represents a linear fitting of all the samples, excluding the amorphous film deposited at 200ºC. The orange lines correspond to the Lorentz-Lorenz equation (Eq. 3.2), using polarizabilities of Al_2O_3 of 5.0×10^{-40} $C{\cdot}m^{-2}{\cdot}V^{-1}$ (solid line) and 5.14×10^{-40} $C{\cdot}m^{-2}{\cdot}V^{-1}$ (dashed line). 111
Figure 3-12 – Map of samples influenced by the power source, power and deposition temperature. The direction of the arrow indicates the general trend of the increase in grain size, residual stress, film density, and refractive index. The colour code using in this Figure is coherent with the colours employed for each sample in previous figures. 112
Figure 4-1 – Top-view SEM images of a) HiPIMS film and b) MF film, both deposited at 450°C with 200 nm of thickness. Both scales represent 100 μm. 117
Figure 4-2 – Closer look to the surface of Alumina deposited by HiPIMS a) Top-view SEM image with two types of features: first, irregular particles from the discharge (indicated by the pink arrow); secondly, circles that are related to punctual adhesion issues and large stress, resulting from a large ion bombardemnet during HiPIMS (indicated by the blue arrow). b) TEM image highlights this local delamination. 118
Figure 4-3 – a) Profilometer scan on an Al_2O_3 surface produced using HiPIMS 2500W and MF 2500W and 3500W at 450°C. b) scan after subtraction of a polynomial function c) scan after subtraction of an average line (black line in b)). 119
Figure 4-4 – Histograms of the height profiles for different depositions. a) HiPIMS b) MF c) MF+HiPIMS with 5 pulses and d) MF+HiPIMS with 10 pulses. Black solid lines represent Gaussian fittings. The histograms were displaced horizontally to set the position of the Gaussian curves to zero. Each histogram has different bin size. 119
Figure 4-5 – Schematic representing the "natural roughness" given by the Gaussian curve, as well as the effect of particles and droplets, which are represented by the tail of the same curve. 120
Figure 4-6 – a) Histograms of Figure 4-4 re-calculated using the same bin size and represented in a logarithmic scale. b) Detailed view of the around the origin. 121
Figure 4-7 – Top-view SEM images of a 10 nm thin film deposited by HiPIMS at room temperature. 122
Figure 4-8 – Top-view SEM images with different zones I) Alumina without Au II) Alumina with Au NPs and III) Au NPs in a droplet. Both scales represent 200 nm. 123
Figure 4-9 – AFM images of Au NPs deposited on alumina. a) Topography. b) Stiffness. The units of the x and y axes are nm. A particle or droplet can be observed in the bottom-right corner. 123
Figure 4-10 –The absorption spectra of gold clusters deposited on Al_2O_3 coatings with two distinct powers a) 67 W and b) 32W for different deposition times indicated in the figure. The squares indicate the SPR position of the maximum. 126
Figure 4-11 – The absorption spectra of gold clusters on a) amorphous Al_2O_3 at room temperature and b) γ- Al_2O_3 at 450°C with/without Ar and H_2 treatment. 126
Figure 4-12 – Absorption spectra of alumina films deposited for 30 s and treated with argon and different fluxes of hydrogen a) 1.5 sccm and b) 3 sccm during 10, 20 and 30 minutes. 128
Figure 5-1 – Experimental Au 4d spectrum of gold deposited on a) untreated and b) treated alumina coatings for different deposition times, which are indicated in the figure. The black spectra represent the Au foil (reference) with the respective units on the right axis. 132
Figure 5-2 – Fitting of the experimental Au 4d spectrum with the modelled background and the subtracted spectrum for a) Au reference foil and b) Treated Al_2O_3 sample with Au deposited for 80 s. J(E) represents the experimental data and F(E) the subtracted background, i.e. the single atom spectrum. 133
Figure 5-3 – Experimental spectrum for a) untreated and b) treated surfaces with their respective associated background. The black line represents the Au foil (reference) with the respective units on the right axis. 134
Figure 5-4 – Data obtained after XPS peak-shape analysis of spectra in Figure 5-3 for treated and untreated alumina surfaces. a) amount of substance (AOS) as a function of time, where the dashed lines represent linear fittings going through origin. b) island height vs. surface coverage. The dashed lines represent AOS isolines. 135
Figure 5-5 – Top view SEM images of Au nanoparticles deposited on Al_2O_3 films with depositions times from 30 s to 60 s. All the scale bars represent 50 nm. 136

Figure 5-6 – Selected AFM stiffness and topography maps of 200x200 nm^2 scan area of the Au clusters deposited on untreated and treated alumina from 10 s to 80 s. The values of S_{max} and S_{min} (in GPa) and Z_{max} (in nm) are included below each image. 138
Figure 5-7 – Histograms of the stiffness images from Figure 5-6 for a) untreated and b) treated samples. 139
Figure 5-8 – Integrals of histograms of Figure 5-7 for a) untreated and b) treated samples. 140
Figure 5-9 – Detailed view of the integrated curves of the stiffness histograms of the treated samples (Figure 5-8). The horizontal dotted line represents the threshold of 1% counts, which is used to characterize each sample. The values of $S_{1\%}$ for each sample are illustrated with vertical dashed lines. 140
Figure 5-10 – Stiffness at 1% for untreated and treated surfaces at different deposition times. a) Measurement of all the images. b) average of each condition, considering all the datapoints in (a). c) average of each condition, excluding the hollow points in (a). 141
Figure 5-11 – Stiffness and topography for untreated and treated alumina surfaces with Au deposited for 60 s and 70 s, respectively. 142
Figure 5-12 – log-log plot of the HHCF for gold clusters deposited on a) untreated and b) treated alumina surfaces with deposition times from 0 s to 80 s. The solid lines represent the fittings to Eq. 2-27. 143
Figure 5-13 – The variation of a) roughness (w), b) correlation length (ξ), c) Hurst parameter (α) and d) local slope with deposition time. Straight lines in (a) and (b) represent linear fittings, and dashed lines in (c) and (d) are guides to the eye. 144
Figure 5-14 – Plots of 'vertical' vs. 'horizontal' parameters by AFM and XPS. a) w vs. ξ from AFM. b) island height vs. surface coverage from XPS. A scheme illustrating the growth of Au on treated and untreated Al_2O_3 coatings is also included. 146
Figure 5-15 – Profile of a) untreated and b) treated surfaces with time depositions from 10 s to 80 s. 147
Figure 5-16 – 3D geometrical model illustrating the growth of untreated and treated surfaces for different Au deposition times. 149
Figure 5-17 - Colours of Au-Al_2O_3 for untreated and treated surfaces deposited with different deposition times of gold on glass substrates. 150
Figure 5-18 – Absorption spectra of Au clusters deposited on a) untreated and b) treated Al_2O_3 surfaces for different deposition times indicated in the figure. The squares indicate the position of the SPR maxima. 151
Figure 5-19 – a) Values of absorbance of the SPR peak in function SPR peak position. b) Island height as a function of surface coverage, divided into two zones: Particle-like behaviour (blue zone) and Continuous-like behaviour (orange zone). c) Absorbance of the SPR peak in function of the roughness of the coatings (w). d) Wavelength of the SPR peak in function of roughness (w) for untreated and treated samples. Dashed lines are guides to the eye. 152
Figure 5-20 – Topographic 3D images for alumina surfaces with different plasma treatments: untreated (Z = 1.3 nm), treated with Ar (Z = 1.1 nm), and Ar/H_2 (Z = 1.4 nm) reference. 155
Figure 5-21 - Left: SIMS profiles of the 5 samples under study, in log scale. Right: comparison of the SIMS profiles per element, in linear scale. The reference depth is illustrated with a vertical black line situated in zero. 159
Figure 5-22 - Detail of the SIMS profiles of sample S5. 160
Figure 5-23 – Schematic of the growth mechanisms of Au on an untreated and treated alumina surface at different stages of the Au deposition. 161
Figure 5-24 – Optical microscope image of Au-Al_2O_3 coatings with two distinct zone: presence and absence of Au nanoparticles. 163
Figure 5-25 - Raman spectra of a) R6G analyte (10^{-5} M) for untreated (60 s) and treated (80 s) surfaces. b) R6G analyte (10^{-3} M) in treated surfaces at different deposition times (30 s, 50 s and 70 s). A reference of an area without Au NP is also plotted for comparison. 164
Figure 5-26 – Reproducibility of SERS using a concentration of 10^{-3} M of R6G 2 different areas of treated surfaces with Au deposition time of 70 s. 165

Figure 6-1 – Data obtained after XPS peak-shape Tougaard analysis for treated and untreated alumina surfaces using Pulsed DC. a) amount of substance (AOS) as a function of Au deposition time, where the dashed lines represent linear fittings b) island height vs. surface coverage. 171
Figure 6-2 – The variation of a) roughness (w), b) correlation length (ξ), c) Hurst parameter (α) and d) local slope with deposition time for Au deposits prepared by Pulsed and continuous DC (hollow and filled symbols, respectively) on plasma treated and untreated alumina surfaces (triangles and squares, respectively). 172
Figure 6-3 – Roughness (w) as function of correlation length (ξ) for samples prepared by Pulsed and continuous DC (hollow and solid symbols, respectively). 173
Figure 6-4 – UV-Vis absorption spectra of Au clusters deposited by Pulsed DC on a) untreated and b) treated Al_2O_3 coatings using different deposition conditions (duty cycles indicated in the plot). The squares indicate the position of the maximum of the SPR peak. 174
Figure 6-5 – Maximum absorbance vs. wavelength of the SPR peak for different samples. 175
Figure 6-6 – Correlation of the characteristics of the SPR peak with the roughness of samples. a) Absorbance. b) Wavelength. 175
Figure 6-7 – Schematic of a multilayer composed of alumina (4),Au NPs (3) layers and 3 pre-treatments of Ar/H_2. 176
Figure 6-8 – TEM micrographs of the Au/Al_2O_3 multilayer with 30 s of Au deposition a) STEM b) HRTEM. 177
Figure 6-9 – FFT analysis of the micrograph in Figure 6-8b. Top: overall FFT of the image. Bottom: FFT of a region where Al_2O_3 planes were observed. Left and right: FFT images of the regions where planes can be observed in alumina (blue square, left) and Au (red square, right). The distances of the different points in the FFTs are indicated. Inverse FFT images highlighting the planes (by selecting the diffraction points in the FFTs) are also shown. Finally, colour profiles of these images are also depicted, where the wavelength (interplanar distance) is indicated. 178
Figure 6-10 – Diffractogram obtained from the radial integration of the FFT of the whole image of Figure 6-9 top. Vertical lines represent the positions of Au and γ-Al_2O_3 references. 179
Figure 6-11 – Chemical mapping of the multilayer deposited at 30 s for Au. The top-left image depicts a STEM image of the analysed area. 179
Figure 6-12 –Absorption spectra of $Au@Al_2O_3$ multilayers with deposition times of 10, 30 and 60 s of Au. The squares indicate the position of the maximum of the SPR peak. 180
Figure 6-13 – Absorbance of the Multilayer coatings for deposition times of 10, 30 and 60 s compared with untreated and treated samples for DC and Pulsed DC from Figure 6-5. Dashed lines are guides to the eye. 181

List of Tables

Table 1-1 – Deposition methods used for preparation of different combinations of dielectrics and metal nanoparticles in literature. ________ *9*
Table 2-1 - Typical discharge parameters and plasma characteristics of HiPIMS, MFMS, and DCMS [177,178] ________ *27*
Table 2-2 – Parameters employed for the deposition of Al_2O_3 and Au. ________ *43*
Table 2-3 – Operation parameters of the MF and HiPIMS power sources. ________ *45*
Table 2-4 – Information about the peak position (2θ), plane spacing (d_{hkl}) and Miller indices (hkl) for Silicon (JCPDS Card No 00-005-0565). The angles with the (100) plane, and the difference with the Bragg's angle are calculated. ________ *55*
Table 3-1 – Information on the synthesis conditions and characteristics of Al_2O_3 films, including the grain size calculation from the broadening of the 400 and 440 diffraction peaks of Al_2O_3. ________ *98*
Table 4-1 – Deposition parameters of Au explored in this Ph.D. Sputtering conditions (source type, power and duty cycle), and characteristics of the Ar+H_2 plasma treatment of the Al_2O_3 surface (flow of H_2 and duration). The values of the cells represent the deposition time of Au in seconds (all between 10 to 80 s), and the dash (-) indicates that such condition was not explored. Au was grown on alumina deposited at room temperature in all cases, except 2 samples where the deposition temperature was 450ºC. The term 'ML' indicates 'multilayer'. Colours indicate that samples are included in Chapter 4 (Figure 4-10, Figure 4-11, and Figure 4-12), Chapter 5 and Chapter 6. ________ *125*
Table 5-1 - Samples prepared for SIMS analysis. The samples were prepared in the sequence S1-S5. _ *156*
Table 6-1 - Characteristics of Pulse DC operation for a deposition time of 30 s of Au on treated and untreated alumina. ________ *170*

Chapter 1

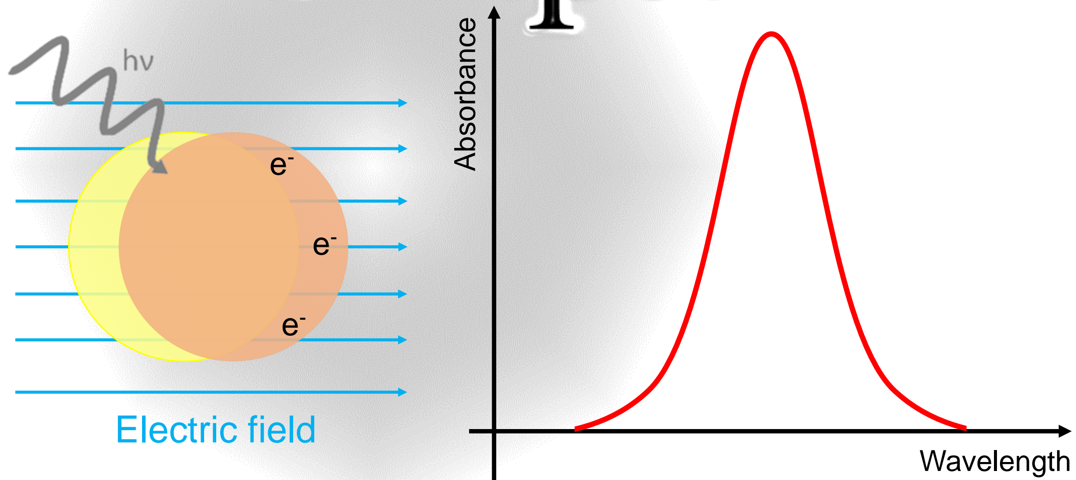

1. Introduction

This chapter provides a concise introduction and literature review of the field of Plasmonics. It describes the research aim, objective, and the structure of the PhD, including an overview of each chapter's content.

1.1. Motivation

In 1959, the Nobel Prize-winning physicist Dr. Richard Feynman introduced the concept of Nanotechnology in a lecture called "*There's Plenty Room at the Bottom*" at a meeting of the American Physical Society at the California Institute of Technology. Nanotechnology is a multidisciplinary science that contributes to a vast variety of distinct fields, such as chemistry, biology, physics, computer science, materials science and engineering. The word "nano" comes from Greek and means "dwarf" or something small, referring to one thousand millionth of a meter (10^{-9} m).[1] This field has witnessed exponential growth in the last couple of decades leading due to quicker, smaller and more efficient devices. Research in this field can be divided into two categories: nanostructure synthesis and characterization.[2] Materials that possess at least one dimension in the nanometre scale (1-100 nm) are typically referred to as nanostructured materials. These materials are composed by an assemble of atoms, molecules, or macromolecules.[3] For instance, a 3D particle with a diameter of 2 nm corresponds to 147 gold atoms. The reduction of the dimensions of bulk materials influences the optical, electronic and chemical properties, the density of states, and the spatial length scale for electronic motion is diminished.[4] Additionally, a wide range of effects may be produced by just manipulating the size and shape distribution of the material, which can be used for new applications. These effects can alter the properties such as resistivity[5], mechanical properties (such as hardness or elastic modulus)[6,7], thermal conductivity[8], and magnetic properties[9], among others. Among the different possibilities, materials whose three dimensions are in the sub-wavelength, particularly metal nanoparticles (NPs), have increased in popularity due to their unique physical and optical properties.

Metal nanoparticles already have a long history, dating back to the 4th century with the apparition of coloured glass.[10] Church windows had this type of glass, which is composed of silver, copper and gold nanoparticles embedded in it. Another outstanding example is the *Lycurgus Cup* (Figure 1-1).

Figure 1-1 - The Lycurgus cup (left): illuminated from outside. (right): illuminated from inside. Image from [11].

This cup shows a mythological scene, which is the triumph of Dionysus over Lycurgus, with different colourations when exposed to light depending on the location of the light source (inside and outside). The green jade and ruby red colours are due to a composition of silver and gold nanoparticles with 50-100 nm diameter and a ratio of 70:30, respectively.[11] The ruby red colour results from the absorption of green light (~520 nm) by gold nanoparticles and the complimentary colour appears as red. In other words, when light containing green wavelengths interacts with the gold nanoparticles, it causes the collective oscillation of electrons within the nanoparticles, generating a resonance effect. This resonance effect leads to the absorption of green light by the Au nanoparticles. As a consequence, the green light is effectively "removed" from the incident light spectrum, resulting in the complementary colour of red becoming predominant. So, what we perceive as red is actually the remaining light that is not absorbed by the gold nanoparticles but rather transmitted or scattered. The green jade colour is attributed to the light scattering by colloidal dispersions of silver particles.[12] However, it took until 1857 to unfold the phenomenon behind the coloured glass with Michael Faraday with the production of colloidal gold solutions with different optical properties. [13] It was only in 1908 that Gustav Mie provided a theoretical explanation by solving Maxwell’s equations for the case of an incoming wave interacting with a spherical colloidal particle.[14] In fact, the origin of the optical properties of metallic nanoparticles was understood with the pioneering work of Gustav Mie and others, creating the field of plasmonics.

Plasmonics (or nanoplasmonics) is based on the investigation of electrons oscillations in metallic nanostructures and nanoparticles.[15] This electron oscillation is caused by the excitation through an external electromagnetic wave, also known as *surface plasmons* (SPs). The term *plasmon* was not used until the 1950s and referred to the collective oscillation of conduction band electrons in metals. For materials with sizes smaller than the wavelength of light, especially metal nanoparticles, the plasmon oscillates locally around the particle at specific wavelengths. This phenomenon is referred to as *localized surface plasmon resonance* (LSPR). When the electromagnetic field of the light reaches the metal nanoparticle, a part of the incident light is absorbed by moving the conduction electrons towards the NP surface. This leads to a displacement of the conduction electrons with respect to the positively charged metal lattice, thereby creating a dipole.[16] The dipole produces an electric field inside the NP, which in turn, gives rise to a restoring force provided by the coulombic attraction between the negatively charged electron cloud and the positively charged metal lattice, see Figure 1-2. [16]

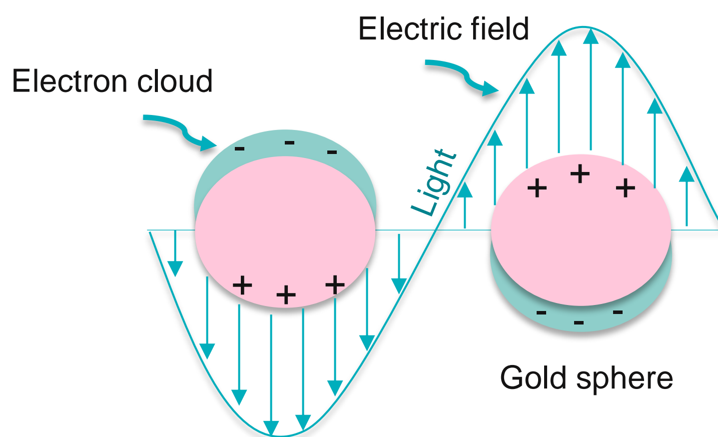

Figure 1-2 - Schematics of plasmon oscillation for a metallic sphere, exhibiting the movement of the conduction electron charge of the cloud relative to the nuclei. Adapted from [17].

The oscillations happen at a specific resonance frequency and usually appear in the visible to near-infrared section of the spectrum for nanostructures of noble metals (Au, Ag, Cu).[18,19]

If the shape, size, or permittivity (dielectric constant) of the metal nanoparticle itself or the surrounding medium changes, an alteration in the electric field on the

surface is induced.[20] Thus, the oscillating frequency of the electrons will be changed.[21] For this reason, it is possible to tune the properties of the metal nanoparticle by changing these parameters. An example of this is seen in Figure 1-3, where different colourations are obtained when a colloidal composed of Au is reduced with sodium citrate. The colours indicate various sizes of gold nanoparticles with unique LSPR.

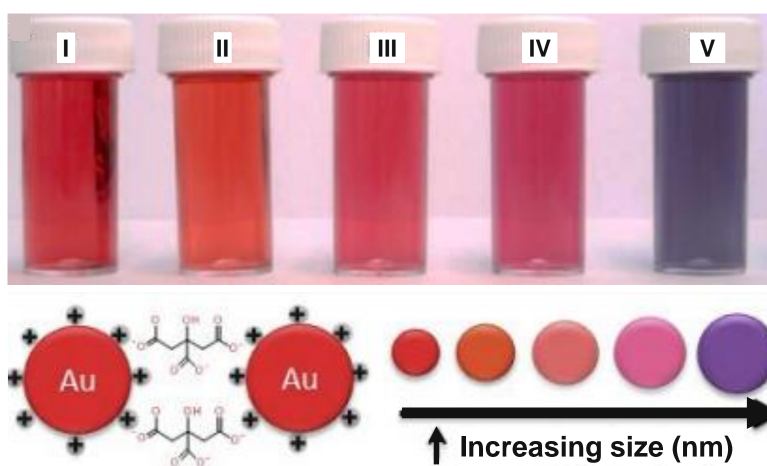

Figure 1-3 – (Top-image) Illustration of a colloidal gold samples (I-V) after reduction with sodium citrate. Stability is attained through electrostatic stabilisation (Bottom image) with citrate ions ($C_3H_5OCOO_3^{3-}$), and the coloration indicates the various sizes of gold nanoparticles with distinctive LSPR. Adapted from [22].

While colloidal solutions with gold nanoparticles are suspensions of tiny metal particles in a liquid, with sizes ranging from some units or tens of nanometres to hundreds of nanometres. This versatility offers a great potential for applications including surface-enhanced Raman scattering (SERS) [23–25], destruction of solid tumours using hyperthermia [26], decorative coatings [27,28], organic solar cells (SC) [29], refractive index sensing [30], plasmonic antennas [31], metal-enhanced fluorescence (MEF)[32], plasmonic-mediated nanosurgery of cells [33], multichromatic switchable pixels [34], plasmonic nanolithography [35], photocatalysis [36], photochromic displays [37], plasmonic metamaterials [38,39], photodetectors [40,41], among others.

Nanoparticles that exhibit LSPR share similarities with quantum dots, also known as "artificial atoms." These are colloidal fluorescent semiconductor nanocrystals with diameters below 10 nm. The optical properties (such as coloration) of quantum dots are highly dependent on their size (see Figure 1-4), as the band gap decreases with increasing size, resulting in a size-dependent emission spectrum. [42,43]

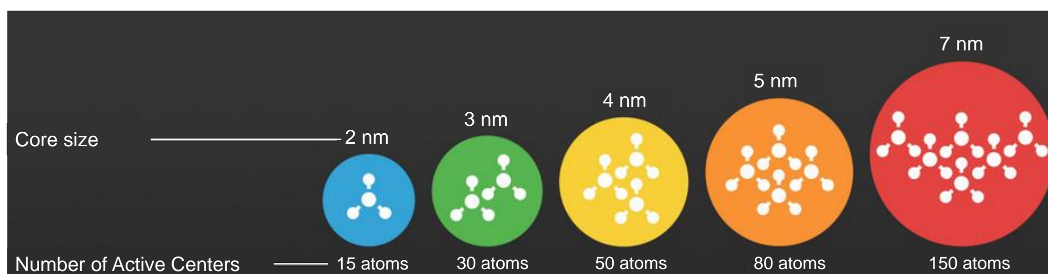

Figure 1-4 – Different coloration depending on the core size of the quantum dots. Adapted from: [44]

This phenomenon happens when a quantum dot is illuminated by UV light (Figure 1-5, middle) and absorbs photons equal to or larger than their band gap, causing the electrons in the QDs to become excited and transition to the conduction band. This excited state is not stable and can relax back to its ground state by emitting a photon (radiative decay) or by losing energy through heat losses (non-radiative decay). This process of emission is known as fluorescence. It is interesting to note that a QD sample shows different colours when exposed to UV or visible light (although the band gap remains constant), as illustrated in Figure 1-5.

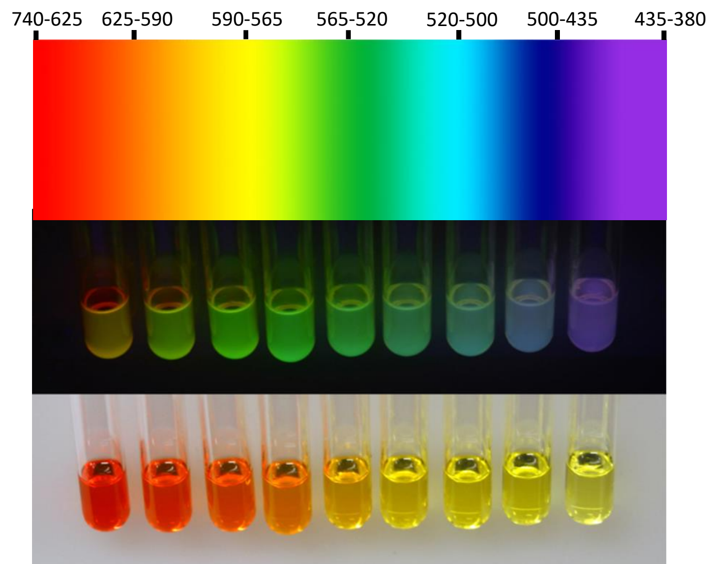

Figure 1-5 – Top image: spectrum of the visible light. The numbers represent the wavelength in nm. Middle image: colloidal suspensions of CdSe quantum dots of decreasing size from ~4.0 nm to 1.8 nm from left to right. Bottom image: QDs exposed to UV light. Bottom image: exposed to ambient illumination. Adapted from: [44]

For instance, when exposed to UV, a CdSe suspension emits light with the same or slightly lower energy than the band gap energy, resulting in e.g. an orange coloration (large particle size in Figure 1-5, center, left sample). However, when exposed to ambient illumination, it reflects or transmits the wavelengths that were not absorbed, giving a red coloration in this case (Figure 1-5, bottom left); In other words, the absorption threshold of the QD is determined by the colour emitted in fluorescence (orange in this case), and the colour observed in visible light corresponds to the light whose energy is lower than that band gap and it is not absorbed by the QD (cf. that the red colour is the only one with lower wavelength than the orange in Figure 1-5, top). In conclusion, QD's show different colours due to the change in the band gap, while metal nanoparticles have different colorations due to the LSPR effect, which is connected to size, shape of the NPs, among others.

Nanoparticles of a wide range of materials can be prepared by a variety of chemical and physical methods [45,46], and some of the most popular are summarized in the scheme Figure 1-6.

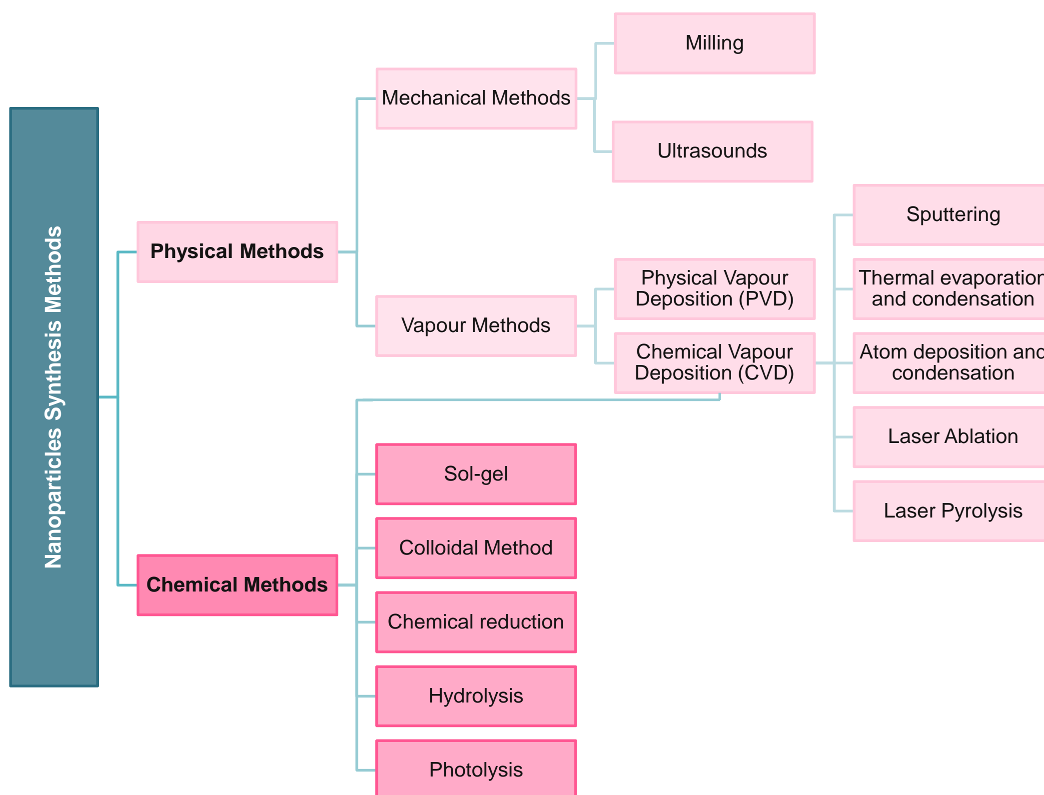

Figure 1-6 - Diagram of some of the most important methods for synthesis of NP's.

Usually, chemical methods are based on chemical reactions [47], e.g. sol-gel processes, chemical vapor deposition (CVD), colloidal method, or chemical reduction (where the growth of NPs is bottom-up, i.e., the nanostructures are created by adding atom-to-atom, molecule-to-molecule, or cluster-to-cluster).[46] In contrast, physical methods normally do not necessarily involve a chemical reaction, and the absence of solvent contamination may be an advantage compared with the chemical methods.[48] In general, the synthesis of NP by physical methods requires 'breaking' the precursor bulk materials into smaller particles. As such, mechanical methods are top-bottom, and present a major drawback to produce regular shapes and to avoid nanoparticle agglomeration.[49,50] In the other hand, vapor methods involve the evaporation from a bulk material followed by a re-ensemble process. Among these techniques, sputtering is a process where a target is bombarded by energetic ions of a plasma, and ejects species which are deposited in a substate, leading to nanoparticles or thin films. One of the advantages of this approach is the low level of impurities of the sputtered material. The major purpose in this area is to

tune the size/shape of metallic nanoparticles that can be i) deposited onto a dielectric surface [45], ii) incorporated within a host matrix [25], or iii) both [46], and control their growth. Table 1-1 summarizes the deposition methods used to prepare different combinations of dielectrics and metal nanoparticles.

Table 1-1 – Deposition methods used for preparation of different combinations of dielectrics and metal nanoparticles in literature.

Metal Nanoparticles	Dielectric materials: Al_2O_3	TiO_2	SiO_2	WO_3	CuO
Au	Sputtering [28,51–54] Sol-gel[55] Ion implantation[56] Electrodeposition [57] ALD [58]	Sputtering[59–63] Spin-coating[64]	Sputtering [65–67] Ion implantation [56] Sol-gel [68] Spin-coating [64]	Sputtering [69,70]	Sputtering [71–73]
Ag	Sputtering [74] Electrodeposition [57], ALD [75]	Sputtering [76]	Ion implantation [77]		Sputtering [78]
Cu	Ion implantation [79] Pulsed laser deposition [80] Sputtering [81]	Sputtering [82–84] ALD [85]			Lithography [86]

Sputtering has been widely used due to the reduced complexity of synthesis and large flexibility for combination of materials.[87] Additionally, this technique also facilitates control over size, shape, and aggregation of nanoparticles.[88] In addition, magnetron sputtering can be scaled-up from lab to industrial environments, where it is used in many different fields. For these reasons, magnetron sputtering has been selected as the approach to prepare plasmonic films in this Ph.D.

1.2. Selection of Materials

1.2.1. Metal Nanoparticles

Generally, materials with a negative real and small positive imaginary dielectric constant are able of support surface plasmon resonance.[89] In practice, the materials must have free conduction band electrons that can resonate with the incoming light at an appropriate wavelength.[28] This is the case for metals such as Ag, Cu and Au, which are great candidates for plasmonic applications.[90] Out of the materials mentioned, Copper has good conductivity and is second-best only to Silver. Silver also has desirable properties, such as the lowest optical loss in the visible and NIR spectra ranges. Aluminum has a higher plasma frequency than both gold and silver, enabling significant surface plasmon response in the ultraviolet.[91] However, all three materials face chemical instability due to oxidation in atmospheric conditions. [90,92] In contrast, gold is a popular plasmonic material with good performance in the visible and NIR spectral ranges, and it has the benefit of being chemically stable.[92] Such characteristics allows an easier preparation and better stability in the presence of air. In fact, in academic literature gold is the most used material for NPs in the field of plasmonics, with a publication rate of 44% in 2020 (in comparison, Ag was the next choice, with a rate of 29%).[93] When prepared by magnetron sputtering, different approaches and power sources are reported, such as direct current (DC)[94–99], radio-frequency [100–103] and pulsed DC[104–106]. In this work, gold nanoparticles will be produced by magnetron sputtering using DC and Pulsed DC power sources.

1.2.2. Dielectric matrixes

In this work, transparent oxides in the visible range are preferable to avoid interferences with the coloration given by the nanoparticles due to the LSPR effect. In plasmonics, aluminum oxide (Al_2O_3), silicon oxide (SiO_2), titanium oxide (TiO_2), tungsten trioxide (WO_3) and copper oxide (CuO) have been widely used as matrix due to their specific optical properties. WO_3 has a narrow band gap (Eg = 2.4-2.8 eV)[107], good corrosion resistance, high refractive index (2.5)[108] and

a hardness between 13 to 15 GPa. [108,109] However, pure WO_3 does not exhibit coloration up to 400°C, but presents light-bluish tones at 500°C.[110] CuO is a semiconductor with a lower energy band gap (Eg = 1.2-2.1 eV).[111] However, the optical transmittance spectrum reveals to be semi-transparent in the visible range at around 700°C.[78]

TiO_2 shows hardness between 11.6 and 18.5 GPa [112] and it is well known for its photocatalytic properties. The combination of TiO_2 with gold nanoparticles leads to the injection of hot electrons from Au NPs to TiO_2 (by LSPR), which can overcome the Schottky barrier and flow back into TiO_2 under mixed UV and visible radiation. These electrons can balance those transferred from titanium oxide to gold nanoparticles and facilitate the recombination of electron-hole pairs.[113] The large refractive index (2.2) of TiO_2 causes the LSPR to shift to higher wavelengths, leading to darker colors. For instance, Au deposited on TiO_2 shows tones of blue-green colors when increasing the Au content, while on Al_2O_3 smaller shifts are seen leading to different tones of blue due to a lower refractive index around 1.6, as seen in Figure 1-7. [114,115]

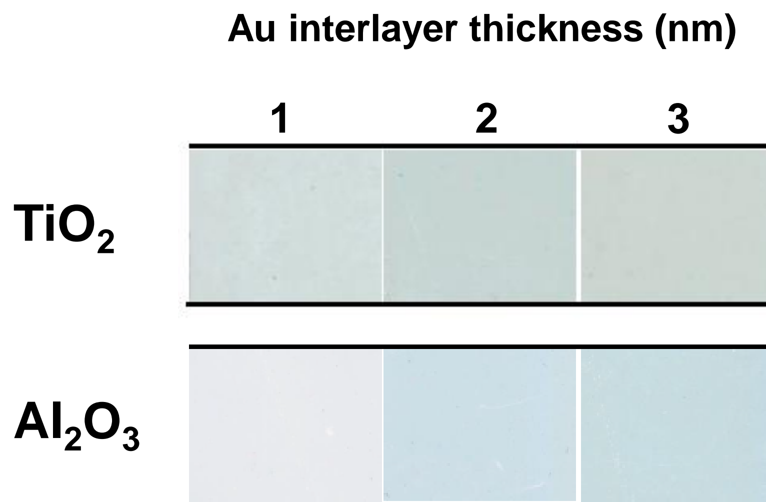

Figure 1-7 – Colour pictures of Au coatings on TiO_2 and Al_2O_3 deposited on glass substrates. Adapted from [28].

SiO_2 has an excellent transmittance (98% between 190-1100 nm), a hardness between 5 – 9 GPa and a lower refractive index (1.45).[114,116] However, SiO_2 is present in the substrates that will be employed normally in this

work (glass, and as native oxide in Si wafers), which would complicate the differentiation between the deposited coating and the substrates.

Al_2O_3 is commonly known as alumina. It is one of the most interesting ceramic materials given its appealing properties, making it a good candidate for a wide range of applications, e.g., tooling, electronics, optical devices, and machining.[117–119] It is known for its good mechanical properties, such as relatively high hardness (27 GPa) [120] even at high temperatures, or good corrosion and wear resistance (~10^{-7} $mm^3N^{-1}m^{-1}$).[121] Also, it is thermally and chemically stable.[122,123] Given its transparency (extinction coefficient of $4x10^{-4}$ at 550 nm)[124] and insulating properties, it is widely used in the semiconductor industry.[125] Therefore, alumina was selected as the dielectric explored in this work.

Depending on the substrate temperature, alumina exists in several crystalline (polymorphs) and amorphous states. Compared with the crystalline phases, the amorphous phase has lower hardness and chemical and thermal resistance.[126,127] Different crystalline structures of Al_2O_3 have been reported, labeled as α, κ, θ, γ, among others. α-Al_2O_3 is the only thermodynamically stable oxide of aluminium. Its structure is called *corundum* and crystallizes in the hexagonal-rhombohedral system, space group $R\bar{3}C$.[128] It is a crystal and can be found in gemstones like ruby and sapphire. γ-Al_2O_3 has high thermal stability and it is transparent in the visible region. [129] The ease with which this material can attain higher porosity enables it to acquire a high surface area (50-300 m^2g^{-1}), making it a good choice for applications in heterogeneous catalysis. [129] The structure of γ-alumina can be described as defect cubic spinel with space group $Fd\bar{3}m$.[130] θ-Al_2O_3 is the intermediate structural form into which the transition alumina's could evolve before converting into a corundum phase. θ-Al_2O_3 has a monoclinic structure belonging to space group C2/m and is well defined, unlike some other metastable phases.[131] The metastable κ-Al_2O_3 is used for wear-resistant applications. However, at temperatures above 1000 K the κ phase transforms into the stable α phase.[132] The crystal structure of the κ-Al_2O_3 unit cell belongs to the orthorhombic class with point group *mm*2 and space group

Pna2_1.[133] Commonly, metastable phases like γ or θ are desired for catalysis applications,[134] while for wear-resistant or diffusion barrier applications, the α phase is preferred.[135,136] This is because of the better chemical inertness, mechanical properties, and thermal stability of the α phase.[137,138]

In literature, Al_2O_3 films have been deposited by magnetron sputtering using a various different power supplies such as direct current (DC)[51,139], radio-frequency [140–143], pulsed DC [120,144–147], mid-frequency (MF)[148–150], and by the more recent approach known as *high-power impulse magnetron sputtering* (HiPIMS)[151–157]. In this work, HiPIMS is selected to explore the deposition of alumina films because of the interesting possibilities of this recent technology. These films are compared with other films prepared on the same deposition chamber using the more conventional MF power source. Therefore, the combination of Au-Al_2O_3 was selected in this research, since it is a good system to study new sputtering-based approaches as well as surface treatments. Furthermore, the literature lacks a comprehensive exploration of Al_2O_3 using HiPIMS, making it an interesting subject for further study on its own. Since Au nanoparticles are associated with a plasmonic effect, a literature review was made combining Au NPs in an Al_2O_3 matrix. In this Thesis, we will refer to Au@Al_2O_3 when nanoparticles are embedded in alumina and Au-Al_2O_3 only for the deposition of Au on the surface of Al_2O_3.

Over the last decade, size-dependent SPR has been extensively studied for different research groups, where red-shifts and blue-shifts are reported with increasing particle size.[140,158–161] For instance, Hosoya et al.[159], observed a blue-shift as the size of Au particles, in Au@Al_2O_3 nanocomposites prepared using sol-gel method, increased between 4.6-12.7 nm. Belahmar et al. [162] also reported a blue-shift of the absorption band when increasing the size of the Au NPs from 1.2 to 7.3 nm when producing Au@Al_2O_3 films by co-sputtering. Additionally, Jaiswal et al.[140] reported a blue-shift with increasing average Au crystallite size (5-9.2 nm) for Au@Al_2O_3 using RF magnetron co-sputtering. A shift in the same direction was observed when increasing the filling factor (i.e. volume fraction) of Au. However, Figueiredo et al. [115] obtained an opposite trend on the filling factor for simulations on similar nanocomposite films using the

Maxwell-Garnett (MG) theory. The direction of the shift (whether blue or red) can be explained by considering two factors: the spill-out of free electrons through the surface of the particles, and to the inner surface-shell of vanishing ionic core polarizability due to d-electrons.[163–166] These quantum effects result from electronic confinement and are not considered in Mie Theory. The red shift is caused by the first effect, while the second effect leads to a blue shift. When it comes to Au, the blue shift is more prominent, and the resonance is damped and broadened as the cluster size decreases. This is due to the presence of interband transitions in the same spectral region as the SPR.[115,167]

The content and diameter of gold nanoparticles can be easily controlled by varying the deposition time. For instance, Tanahashi et al.[168] tuned the diameter of gold nanoparticles embedded in alumina between 2.0 and 6.0 nm by changing the deposition time and the RF input power (25 W to 250 W), leading to LSPR of Au located at 543-587 nm. The use of SiO_2 instead Al_2O_3 causes a larger shift to shorter wavelengths (from 568 nm to 530 nm) due to the lower refractive index of SiO_2. This phenomenon is also studied by Figueiredo et al. [115], who found that for the same Au interlayer thickness (1 nm) a peak shift from 662 nm to 600 nm is observed when changing the dielectric from TiO_2 to Al_2O_3, respectively.

Another important factor that affects the behavior of the LSPR peak is the content of Au of the NPs. Figueiredo et al. [52,161] observed that as the gold content increased from 5 to 11 at. % (being the rest Al and O, i.e., the constituents of the alumina substrate), there was a red-shift (from yellow to dark-orange) in the absorption band with higher intensity and increased SPR widths (changing from 600 nm to 740 nm). The change in gold content causes variations in the metal clusters sizes and the morphology of the absorption band, leading to a shift in the coloration of the coatings. [52,161] Nevertheless, Zhao et al. [169] reported both red and blue-shifts with increasing the Au content (from 8.4 to 45.2 wt%) in Au@NiO nanocomposite films prepared by chemical solution method. On the other hand, Rahman et al. [170] found that altering the film thickness of Au@Al_2O_3 coatings (50 nm, 65 nm, 130 nm and 150 nm) and composition (Au composition increases from 22 vol% to 30 vol%) resulted in a variety of colours on coloured

stainless-steel surfaces, including light orange, blue, magenta, yellow-green, orange, and dark yellow-green. However, after annealing, the Au nanocomposite films became crystallized (peaks corresponding to Au were detected, but no peak for Al_2O_3 was observed) and both magenta and blue turned into dark yellow-green while yellow-green and orange coloured turned into light orange, resulting in a red-shift.[170]

Changes on the thickness of the films and the amount of Au can also influence the surface energy of the nanocomposite. Jaiswal et al.[140], also observed when increasing the thickness of the nanocomposite while increasing the atomic percentage of Au lead to lower surface energies. For a thickness of 10 nm with 9.6 at. % percentage of Au lead to a surface energy of 20.8 mN/m while, 40 nm of thickness with 14.1 at. % of Au decreased the surface energy to 13.1 mN/m. In addition, the surface roughness of Au-Al_2O_3 nanocomposite and the contact angle followed Wenzel's rule [171], justifying the influence of roughness (root mean square roughness between 1.2 and 7.0 nm) on the contact angle (85.7°- 99.4°).

The surface can also be altered using plasma treatments as an alternative. Meira et al. [51] evaluated how a surface modification using argon plasma treatment might affect the micro- and nanostructure of Au@Al_2O_3 films. For the same deposition temperature (400°C), it was identified an increase in the NPs density (from 40 μm^{-2} to 315 μm^{-2}) as well as a decrease in the average nearest neighbour distance (from 65 nm to 23 nm) after the plasma treatment. It is also worth to mention that most optical changes happened within the first 60 min of plasma treatment. A good stability was also demonstrated for the Au NPs embedded on alumina films when using DC magnetron where no considerable film thickness variation was seen after 60 minutes of argon plasma treatment for samples annealed at 400°C and 700°C. The same author, [52] tested the Au-Al_2O_3 nanocomposite as sensors for the RIS (refractive index sensitivity) using two dielectric (liquid) environments, deionized water and DMSO since they exhibit different refractive indexes. [51] However, it resulted in low values for RIS of -5.39 nm/RIU and -2.601 nm/RIU before and after argon plasma (as mentioned previously), respectively.[51] This work was extended by Figueiredo et al. [161] and co-authors in a theoretical study, which was conducted to determine the

optimal coating parameters for sensing experiments based on the refractive index sensitivity. The major parameter affecting sensitivity is the depolarization factor (L), which varies depending on the particle shape (see Figure 1-8).

Figure 1-8 – Images of a) snooker ball (spherical shape, where $r_1=r_2=r_3$), b) submarine (prolate shape with $r_1=r_2<r_3$, i.e. 'uniaxially elongated') and c) a frisbee (oblate shape with $r_1=r_2>r_3$, i.e. 'uniaxially smashed').

To increase RIS, L should be reduced. Three values of depolarization factors L_i, (i = 1, 2, 3) are identified for a particle depending on the three spatial axes, with $\sum_i L_i = 1$. Figure 1-9a shows the variation of L_i depending on the aspect ratio of an ellipsoid (r_3/r_1). In this case, two of the dimensions are equal (i.e. $r_1=r_2$), and the third dimension (r_3) varies. As a consequence, the value of two of the depolarization factors is the same ($L_1=L_2$). Three cases can be identified; if $r_1=r_2=r_3$, the particle has a spherical shape, and. $L_1=L_2=L_3=1/3$. If r_3 is reduced, we obtain an oblate shape, and L_3 grows to reach 1 when the asymmetry of the ellipsoid increases (i.e. the shapes separates from a sphere). In contrast, if r_3 increases, the shape of the particle becomes prolate, and, when the asymmetry increases, L_3 goes to zero while $L_1=L_2=1/2$. To compare between the prolate and oblate cases, the aspect ratio of the nanoparticle can be represented through its asymmetry, i.e. the ratio between the minor and the major axis (r_{minor}/r_{major}). This representation is included in Figure 1-9b, and the sphere case is now located at r_{minor}/r_{major}= 1. It is observed that, for the same degree of asymmetry, the lowest values of L are obtained for prolate particles.

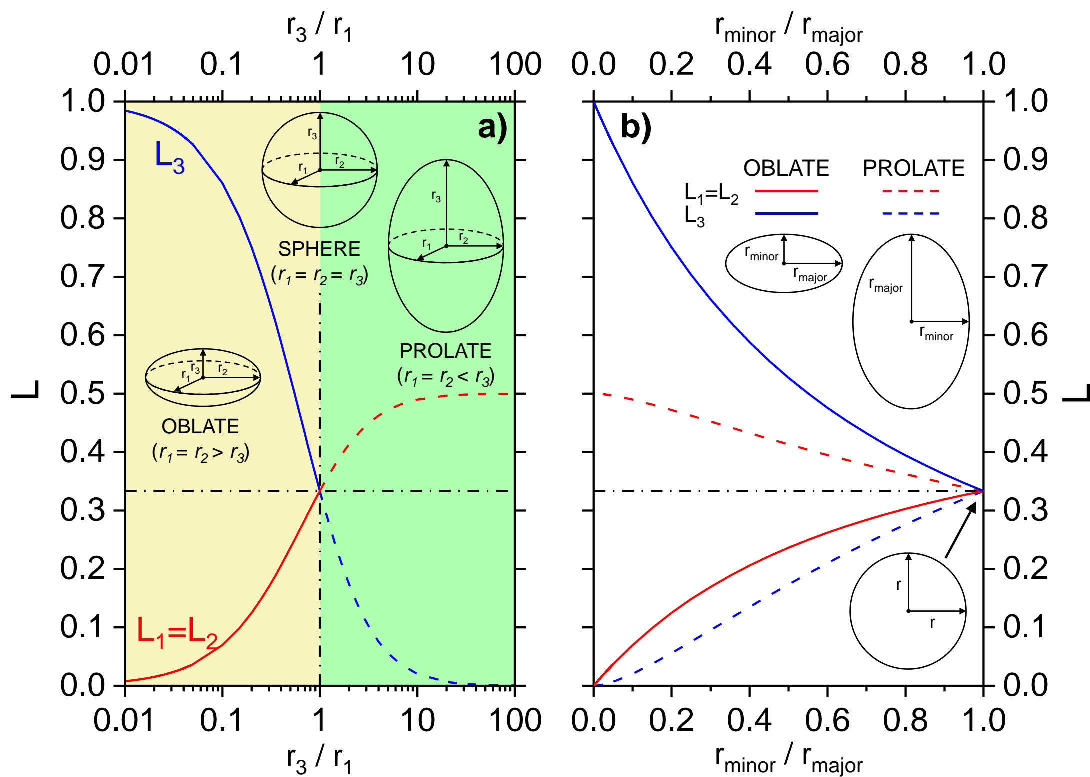

Figure 1-9 – Depolarization factor in function of aspect ratio for a sphere, prolate and oblate. a) against r_3/r_1 in a logarithmic axis, where the yellow and green shaded areas indicate oblate and prolate geometries, respectively. b) against nanoparticle asymmetry (using $r_{minor}/r_{major} = \frac{minor\ axes}{major\ axes}$ in linear scale. From Figueiredo et al. [161]

As a consequence, the sensitivity values for prolate forms were nearly double that of oblate forms, reaching a maximum of 650 nanometres per refractive index unit (nm/RIU). An aspect ratio of 0.42 is considered optimal for balancing sensitivity and peak width.[161] On the other hand, Gao et al. [172] enhanced the biotin-streptavidin (SA) sensitivity by tuning the surface coverage and the interparticle distance of Au-Al_2O_3 nanocomposite. NPs with 5.4 nm of size, 52% of coverage, and 3.7 nm of interparticle distance obtained the best sensing properties. All these results indicate the versatility for tunability the characteristics of Au-Al_2O_3 films that can be used for sensing applications (e.g. humidity, refractive index, gases (CO)).[173]

Another application of these films with LSPR is surface enhanced Raman spectroscopy (SERS). SERS is a powerful analytical technique that is used to detect and identify molecules at low concentrations. It is based on the Raman effect, which is a phenomenon where light interacts with a molecule, causing it to

vibrate, and the scattered light provides information about the molecular vibrations. SERS enhances the Raman signal by many orders of magnitude, making it possible to detect very small concentrations of molecules. The enhancement is achieved by using a substrate that has a rough or nanostructured surface, such as silver or gold nanoparticles, that can amplify the electromagnetic field at the surface. When a molecule is placed on the surface of the substrate, the electromagnetic field generated by the surface enhances the Raman signal of the molecule.

Costa et al.[174] produced nanocomposites of Au-Al_2O_3 followed by a thermal treatment at different temperatures (300°C, 500°C and 700°C) to promote the growth of the NPs. At a temperature of 300°C, the material exhibited plasmonic behaviour, with a peak in SPR at 560 nm. As the annealing temperature was raised to 500°C and 700°C, the crystallinity and grain size of the gold increased. However, this led to changes in the morphology of the material that reduced its overall transmittance and caused the LSPR band to become broader with increasing temperature. Rhodamine 6G (R6G) was used to assess SERS measurements. However, the Raman spectra intensity of R6G did not exhibit any enhancement in the Al_2O_3 matrix due to inadequate crystallization of Au NPs across the alumina matrix. In contrast, an enhancement factor of 10^{10} and 10^{11} was estimated for Au-TiO_2 and Ag-TiO_2, respectively, using a combination of experimental and theoretical data.

To date, there has been a lack of literature on the SERS application of Au-Al_2O_3 films prepared by sputtering. Therefore, after a complete study of the growth mechanism of Au NP on Al_2O_3 thin film, we will study the SERS effect on samples of specific interest to evaluate its potential applicability.

1.3. Objectives and structure of the Ph.D.

This research deals with the deposition of Au/Al_2O_3 films by magnetron sputtering, with the goal of achieving and tuning the LSPR effect. Most of the results involve Au particles deposited on top of alumina, but some multilayers where Au is embedded in Al_2O_3 are also reported. The films will be extensively characterized (morphologically, optically, and chemically) to investigate the individual and combined properties of the materials. The influence of various deposition parameters on the characteristics and properties of the films are studied to establish a large degree of control over the deposited materials. Finally, the potential applications of these films as SERS are also evaluated.

The strategy followed in this work is to study each part of the system in a progressive approach. This strategy is summarized in Figure 1-10, and it can be described according to the following points:

A. Study of the deposition of Al_2O_3 films: these results are summarized in Chapter 3.
B. Deposition of Au on Al_2O_3 films, and influence of the plasma treatment of Al_2O_3 surface on the growth of Au nanoparticles: these results are summarized in Chapters 4 and 5.
C. Influence of the power source employed to deposit Au: Chapter 6.
D. Deposition of films where Au is embedded in Al_2O_3. This is explored in Chapter 6 by the deposition of multilayers formed by alternating Al_2O_3 and Au sections.

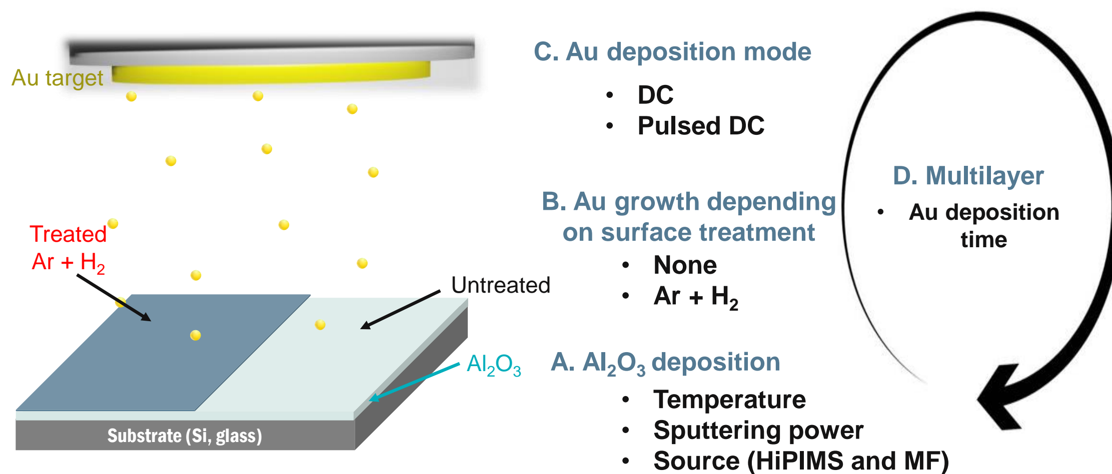

Figure 1-10 - Schematic of the PhD structure, including the main aspects studied. A. Al_2O_3 deposition (Ch. 3); B. Au growth and surface treatments (Ch. 4 and 5); C. Au deposition mode (Ch. 6). D. Multilayer (Ch. 6).

Therefore, this Thesis is organized in 6 Chapters:

Chapter 1, an introduction and literature review of the field of plasmonics are presented, along with a summary of the objectives and structure of this Ph.D.

Chapter 2 summarizes the equipment, techniques, and experimental parameters used in the Ph.D. research. It is divided into two sections. The first one covers the principles of physical vapor deposition (PVD), film growth, and PVD implementation with different power sources. The second section describes the experimental techniques and parameters employed in the Thesis for film characterization. The chapter also includes a discussion on the influence of nanoparticle characteristics on the plasmonic effect, considering size, shape, environment, and material properties.

Chapter 3 investigates the deposition of alumina films on silicon. These alumina films will serve as a substrate for the deposition of Au NPs in the subsequent chapters. The objective of this chapter is to obtain an in-depth knowledge about the growth of Al_2O_3 by magnetron sputtering, and the control of the characteristics and phases formed. The objective is to understand the influence of the following parameters:

- Sputtering source: MF, HiPIMS and MF-HiPIMS.
- Sputtering power: between 2000 and 3500 W.

- Deposition temperature: 200 and 450ºC.

Chapter 4 introduces the deposition of Au on Al_2O_3 films. The objective of this chapter is to select optimal conditions for Al_2O_3 and Au deposition. The objective is to find a set of interesting deposition conditions to perform detailed analyses in the next chapters. To do so, a quick screening comprising different parameters is performed:

- Topographical characteristics of alumina depending on power source and thickness.
- Characteristics of the LSPR peak depending on i) phase of alumina, ii) conditions of Al_2O_3 surface plasma pre-treatment (flow of H_2 and duration), and iii) DC deposition power.
- Deposition power of Au in DC mode.

Chapter 5 studies in detail the influence of the plasma treatment on the alumina film on the growth characteristics of Au nanoparticles. Therefore, gold is sputtered on alumina films that underwent a previous surface plasma treatment of argon and hydrogen and compared with alumina films not subjected to such pre-treatment. The growth of Au on both surfaces was evaluated for different deposition times using the method of Tougaard (XPS) and the height-height correlation function (HHCF) from AFM results. The objectives of this chapter are:

- Monitor the Au growth with XPS and AFM.
- Understand the influence of the surface treatment on the growth of the nanoparticles.
- Understand the influence of the Au characteristics on the LSPR.
- Evaluate its potential application for SERS.

Chapter 6 focuses on the influence of the sputtering source of Au deposition (DC vs. pulsed DC) and the deposition of a multilayer composed of alumina and gold nanoparticles by controlling the time deposition of Au. The objectives are:

- Understand the impact of the Au growth by changing deposition source (DC and pulsed DC).
- Growth of Au embedded in Al_2O_3 and evaluate its influence on the LSPR.

To summarize, it can be reported that the main novel point of this research is focused on the influence of Ar/H_2 plasma pre-treatment of the Al_2O_3 coatings on the growth of Au nanoparticles and their LSPR characteristics. The potential application of these films for surface-enhanced Raman spectroscopy (SERS) applications is also explored. To do so, the characteristics of Al_2O_3 coatings prepared with different parameters have been examined in detail first. In addition, the growth of Au nanoparticles has been exhaustively analysed using XPS (method of Tougaard) and AFM (HHCF). The optical characteristics of the deposits are finally explained in terms of the characteristics of the films.

Chapter 2

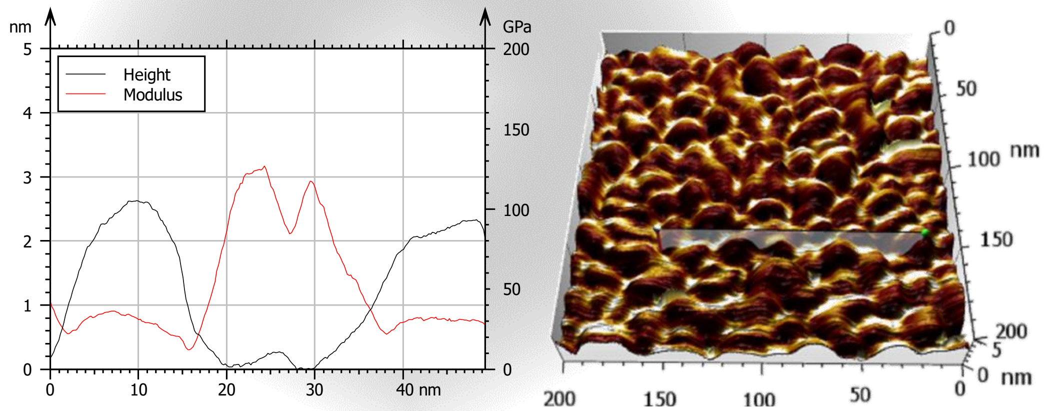

2. Deposition and characterization methods: description and theory

This chapter summarizes the equipment and techniques used in this Ph.D., and it is divided into two parts. The first part focuses on the general principles of physical vapor deposition (PVD) utilizing various power sources and on the concepts regarding the film growth. The second part describes the experimental techniques employed throughout the Thesis work, including the respective experimental parameters utilized. A discussion on the impact of nanoparticle size, shape, environment, and material dependence on the plasmonics effect is also included.

2.1 Physical vapour deposition and magnetron sputtering

Physical vapor deposition (PVD) is a technique used to coat surfaces by vaporizing material and transferring it onto the substrate at an atomic level under vacuum conditions. This process can be sub-divided into several steps. Firstly, the material to be deposited is vaporized by either a high-temperature vacuum or gaseous plasma. Secondly, the vapor is transported to the substrate. During this stage, the evaporated species may react with appropriate reactive gases, such as oxygen or nitrogen. Finally, the coating is deposited onto the surface of the substrate, where additional processes may take place.[175]

Sputtering has proven to be effective in depositing many materials, but it is not without limitations. These include low deposition rates, reduced ionisation efficiency within the plasma, and elevated substrate heating effects.[176] The introduction of magnetron sputtering has resolved to a large extent, the restrictions previously encountered.

A plasma discharge occurs attracting positively ionized gas atoms towards the cathode where the target is located, resulting in the atomic erosion of the target material taking place beneath this region. In magnetron sputtering, magnets are located at the back side of the target material to strengthen the sputtering process. These magnets create a magnetic field that confines the electrons near the target (cathode), leading to a localized rise of the electronic density and consequently, a higher number of collisions with the discharge gas, (typically Ar) to promote the ion density. This one is highest in the zone close to the target surface and due to their high mass by comparison with electrons, the ions are only sensitive to the electric field.

There are two types of magnetrons equipment's: balanced magnetic field (BM) and unbalanced magnetic field (UBM). The main factor that distinguishes them is their effect on plasma confinement. In BM magnetrons, the magnetic field lines form closed loops above the target surface, which effectively confines the plasma and prevents it from expanding far from the cathode surface. On the other hand, in UBM magnetrons, the magnetic field lines extend into the chamber due to the unequal strengths of the outer and inner magnets, which causes the

plasma to spread further away from the target. This causes ion fluxes towards the substrates and enhance the properties of the coatings.

Generally, the use of high sputtering powers is desired to increase the sputtering and deposition rates of the process. However, when high-energy ions from the plasma impinge on the target material, they transfer their kinetic energy to the atoms or molecules on the target surface. This energy transfer causes localized heating of the target material, which requires cooling, typically achieved through water flowing in the back of the target. Such cooling effect can be limited for certain case, as it is related to the power applied on the target material in regard to the thermal properties of the material. As a consequence, to increase plasma density, the applied power density should be raised while considering the cooling capacity. In addition, it is worth noting that increasing the sputtering power will reach a maximum point where the sputtering rate gests saturated, and further increase of power becomes useless. Pulsed sputtering sources offer a favourable solution because the intermittent nature of the pulses allows to operate with the same average power, but applying stronger powers peaks for reduced times, leaving *off times* between pulses. Such approach allows reaching peak powers that would not be sustainable in continuous mode. If pulsing is operated in bi-polar mode (i.e. the target voltage changes from positive to negative, as in radio-frequency sources), isolating materials can be sputtered, since the positive charge accumulated in the target surface when applying negative voltage (Ar^+ bombardment) is neutralized by electrons from plasma when positive voltage is applied. In addition, pulses allow concentrating power in short periods of time, leading to modification of plasma characteristics if very high peak powers are reached, such in HiPIMS (e.g. highly concentration of ionized species, double ionized particles, etc).

Table 2-1 summarizes the main characteristics of the magnetron sputtering discharges that will be discussed: Direct Current (DCMS), Medium Frequency (MFMS) and High-Power Impulse (HIPIMS)

Table 2-1 - Typical discharge parameters and plasma characteristics of HiPIMS, MFMS, and DCMS [177,178]

	Cathode voltage (V)	Peak current density (A/cm²)	Peak power density (kW/cm²)	Electron density (m^{-3})
DCMS	300 – 700	4 – 60 mA/cm²	< 0.05	10^{15} - 10^{17}
MFMS	300 – 800	0.1 - 1	0.05-0.5	10^{17} - 10^{18}
HiPIMS	500 – 2000	3 – 5	> 0.5 – 10	10^{18} – 10^{19}

The use of pulsed sources allows increasing the current and power densities of the peaks, leading to higher electron densities. This is illustrated in Figure 2-1, which represents the typical regimes of operation of power sources, by plotting the duty cycle vs. the peak power density at the target.

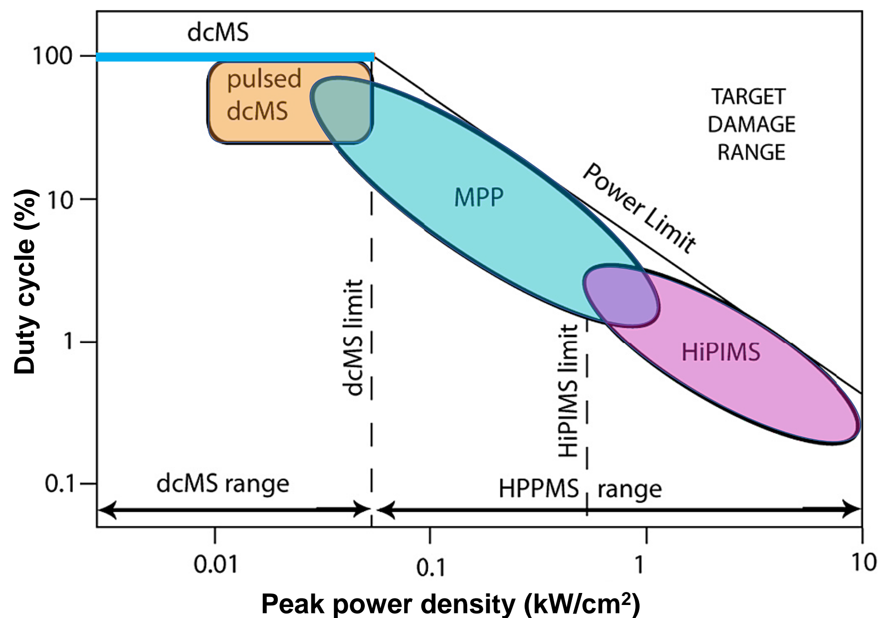

Figure 2-1 – Regimes of operation of DCMS, MPP (modulated pulse power) and HiPIMS (or HPPMS) based on peak power density and duty cycle. Adapted from [179].

Finally, Figure 2-2 illustrates the correlation between power density and pulse time. When the pulse time is reduced (typically, due to a reduction of duty cycle), higher peak powers can be applied, while keeping the average power more or less constant.

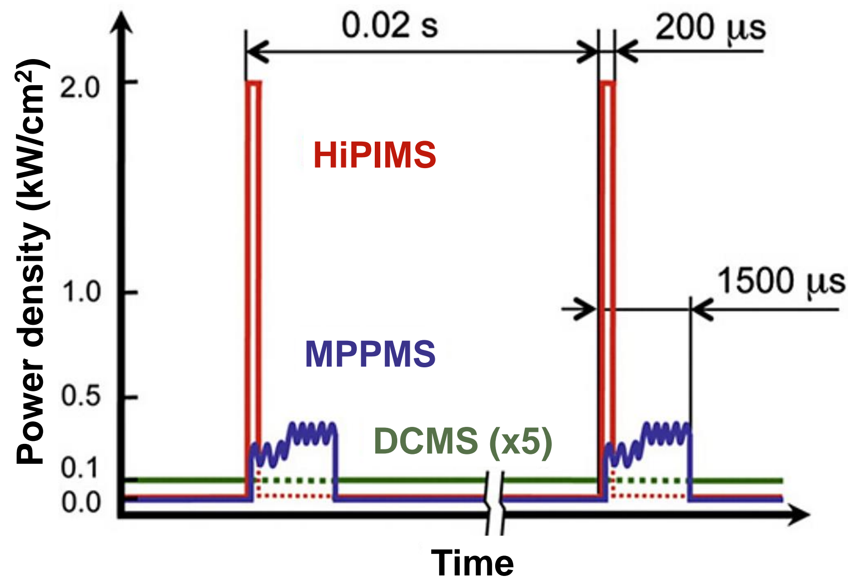

Figure 2-2 - Schematic of the power density during the discharge (HiPIMS, MPPMS and DCMS) operated at same average power P = 300 W. Adapted from [177]

2.1.1 Direct-current magnetron sputtering

DC magnetron sputtering (DCMS) is a significant technology utilized for thin film deposition in various industrial applications. The process involves the creation of a glow discharge between a conductive target and the cathode, typically using argon as the working gas in a pressure range of 0.1 to 5 Pa. [178,180] A DC acceleration voltage of around 300-700 V is used, while a confining magnetic field with a strength of 20-60 mTesla (mT) is applied at the target surface. These conditions result in current densities ranging from 4-60 mA/cm^2 and power densities of several tens of W/cm^2.[178] Typically, a static deposition rate is between 20 and 200 nm/s. However, the degree of ionization of the sputtered material is usually low, often at around 0.1% or even less.[178,181] A commonly accepted maximum threshold for power density in a DCMS discharge is 0.05 kW/cm^2 before the target material is at risk

of damage. When pulsed magnetron sputtering discharges are operated under this threshold, they are known as pulsed DCMS and include the bipolar asymmetrically pulsed discharges (i.e. the target voltages changes from positive to negative sign, with different values of maximum and minimum voltage).[178] In cases where discharges operate beyond the DCMS limit, a lower duty cycle (ratio of the on time (active pulse duration) to the total pulse duration, cf. Figure 2-3) must be implemented to balance out the higher peak power.[178]

In some applications, the magnetron discharge is operated in the pulsed DCMS mode. Deposition is commonly performed by utilizing pulse frequencies ranging from 10-350 kHz, and duty cycles between 50-90%.[182] In reactive sputtering, the use of bipolar pulses can be advantageous, especially when dealing with non-conductive compounds that may form on the target surface. The positive bias in the pulse attracts plasma electrons, which helps to neutralize any charge build-up that may occur during the negative part of the cycle, see Figure 2-3.[183]

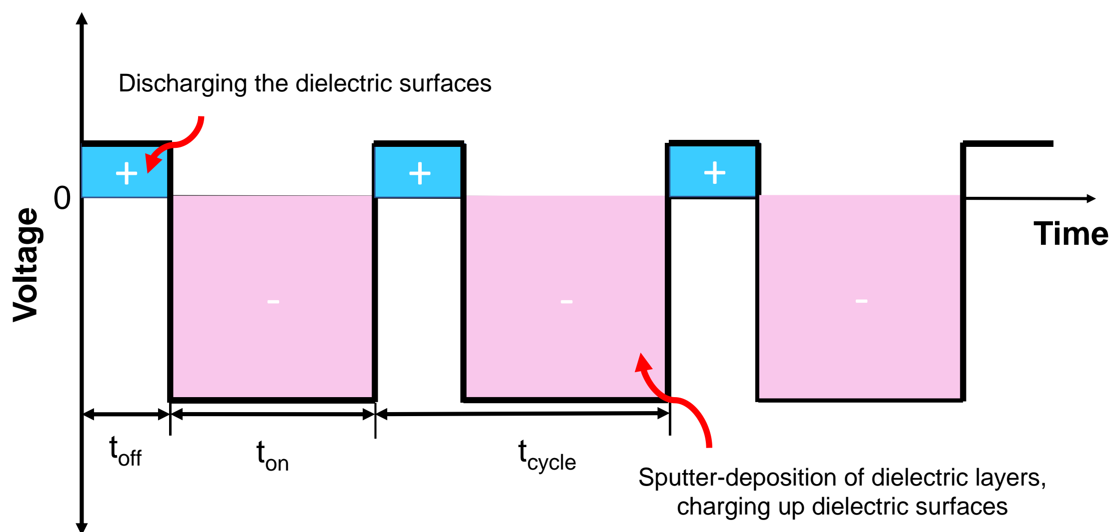

Figure 2-3 - Asymmetrical bi-polar pulsed dc sputtering of dielectrics. t_{on} represents the "on-time", t_{off} "off-time" or "reverse time", and t_{cycle} represents a full cycle. Adapted from [182]. The duty cycle is defined as t_{on}/t_{cycle}.

2.1.2 Mid-frequency

When depositing insulating films, applying pulsed magnetron sputtering discharge in the medium frequency range (MFMS) of 10 to 250 kHz can effectively minimize arc formation and subsequently decrease the occurrence of defects in the film produced. [184] Normally, the duty cycle ranges between 50 to 90 percent. MFMS pulses usually start at a low power level, frequently within the

DCMS range, and then proceed to a more robust pulse with an intermediate power density of 0.05 to 0.5 kW/cm^2.[178]

2.1.3 High power impulse magnetron sputtering

HiPIMS is an emerging technology that bridges the gap between academic research and industrial applications, since it involves the merging of magnetron sputtering and pulsed power technology of high current.[185–187] One of the benefits of this technique is that it can generate high peak powers at low duty cycles (ranging from 0.5% to 5%). As a result, the cathode experiences high peak power (0.5 - 10 kW/cm^2) or current densities, which lead to a rise in the charge carrier density at the target's surface. The increased ionization of the target material enables the substantial alteration or enhancement of the growing films' properties, such as density, hardness, roughness, and refractive index. Furthermore, the discharge voltage pulses, which typically range from 500 to 2000 V, create peak current densities of 3 to 5 A/cm^2.[185,188] Typically, pulse lengths for depositing thin films range from 20 to 500 μs, although they are usually around 30-100 μs with a repetition frequency of 50 - 5000 Hz.[179] A definition concerning this technique could be: "*HiPIMS is pulsed sputtering where the peak power exceeds the time-averaged power by typically two orders of magnitude.*"[189] Despite its benefits, HiPIMS is not without challenges, such as the occurrence of arcing phenomena. The arcing phenomenon is followed by a quick increase in the current and a decrease of target voltage (from the typical few 100 V to less than 40 V).[190] This creates an arc, which leads to the ejection of microdroplets into the deposited film. Another challenge is the low deposition rate in non-reactive HiPIMS process in comparison to DCMS, see Figure 2-4.

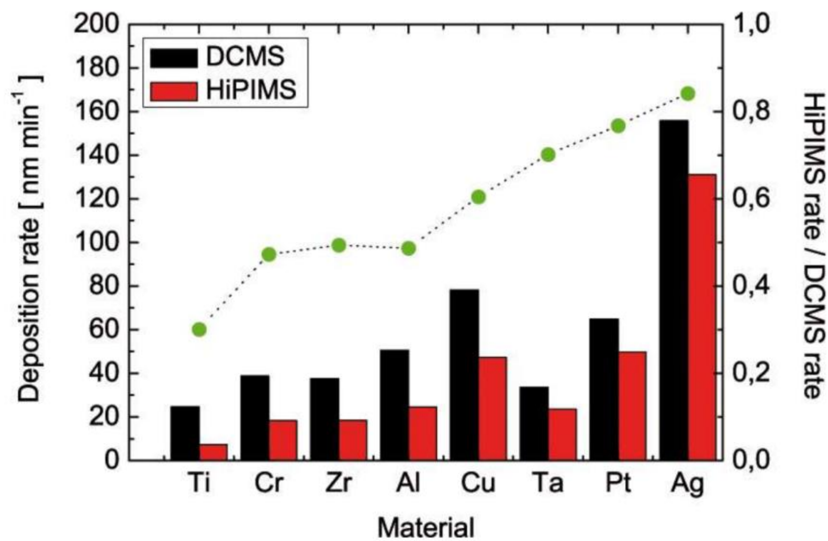

Figure 2-4 - Deposition rates of various metallic target materials measured for both DCMS and HiPIMS under the same conditions ($P_{average}$ = 125 W, p = 0.67 Pa, $d_{substrate\ holder}$ = 6.5 cm). The HiPIMS to DCMS deposition rate ratio is plotted as scattered points. Reproduced from [191].

The observed decrease in deposition rate can be attributed to several physical factors, including (i) less-than-linear dependence of the sputtering yield on the energy of bombarding ions [192,193] (ii) loss of the sputtered material via ionization and subsequent back-attraction towards the target,[192,194] and (iii) modified target-substrate transport geometry by changing the magnetic field configuration.[177,194,195]

In contrast, when operated in reactive gas mixtures, HiPIMS may demonstrate higher deposition rates than conventional DCMS at the same current [196,197] or power.[198] This phenomenon is thought to be due to additional factors that influence the deposition process, such as reduced or eliminated hysteresis and increased erosion rates.[177]

2.1.4 Reactive magnetron sputtering

Unlike metal films, compound films provide us with the opportunity to exhibit a diverse range of characteristics, including electrical, optical, mechanical, chemical, and more. Commonly employed compounds for such films include oxides, nitrides, carbides, and similar substances, which are produced by reactive sputtering. In reactive sputtering, the reaction between the metal target and a chemically reactive gas leads to the formation of a compound.

Consequently, when depositing a new compound using reactive sputtering (such as in the case of the deposited Al_2O_3), it is crucial to control the partial pressure of the reactive gas, chamber pressure, target voltage or deposition rate, as depicted in simplified generic schematics in Figure 2-5.

Initially, the reactive gas (O_2 in our case, although N_2 is used in Figure 2-5) reacts with the metal of the target, known as the metallic mode (**A**), Figure 2-5. Increasing the partial pressure of the reactive gas leads to the formation of a chemisorbed monolayer on both the target and all the surfaces of the deposition including the substrate, modifying the sputtering yield and sometimes the secondary electron yield, and consequently changing the plasma composition and its electrical properties as its impedance.[199] The pressure remains constant (**B**) until the chemisorbed oxygen monolayer covers the entire surface of the target, resulting in a sudden increase in oxygen partial pressure and total pressure and a decrease in deposition rate, known as target poisoning (**D**).[190,200–202]

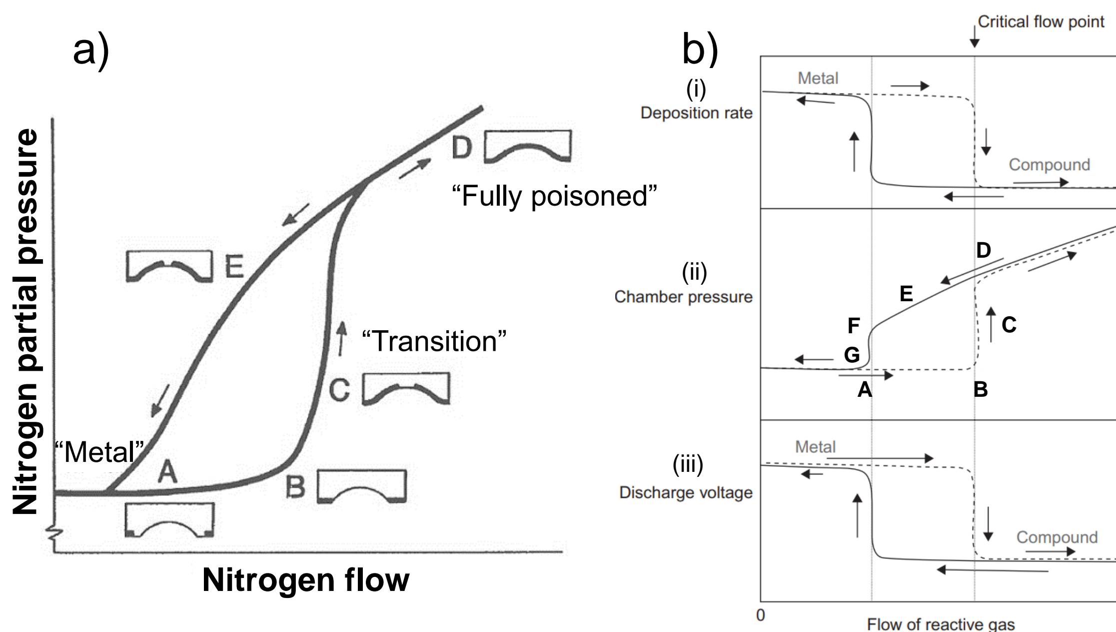

Figure 2-5 - *a)* Illustration of the evolution of N_2 partial pressure and target poisoning during reactive sputtering under nitrogen. *b*) Hysteresis curve in reactive sputtering: i) deposition rate ii) chamber pressure iii) discharge voltage as a function of flow of reactive gas. Adapted from:[203,204]

Normally, the chemical bonds of metals are weaker than the bonds of their corresponding compounds, leading to a lower sputtering yield when the target is poisoned, which leads to a lower deposition rate of alumina.[190] Also, the ion-induced secondary electron emission coefficient of aluminium increases when reacting with oxygen to form an oxide.[202] As a consequence, the electron availability will increase, leading to a reduction of the absolute discharge voltage (when operating in constant current or constant power mode) when the target shifts from metallic to oxidized mode. This is accompanied by a clear decrease of deposition rate due to the low sputtering yield of the oxide, dashed lines in Figure 2-5b (i and iii). As the O_2 pressure increases, the discharge voltage remains constant and low. When the O_2 pressure firstly decreases (**E**) the voltage remains relatively stable until it starts to increase again, solid line in Figure 2-5b (iii). In addition, the O_2 pressure and the total partial pressure decreases until it reaches again the metal mode (**A**).

It is important to note that there are two pathways (metal to oxide and vice versa) depending on the state of the target, creating the well-known *hysteresis* shapes in these plots. Initially, a relatively high O_2 flow is required to poison the target. However, once the target is fully poisoned, it exhibits ceramic-like behaviour. In this scenario, there is sufficient O_2 in the chamber to continuously supply oxygen to the racetrack, maintaining the target in a "ceramic" state. The only way to reverse this situation is by significantly reducing the O_2 flow, which eventually removes the oxide layer since it cannot be replenished with O_2. These modifications indicate that the target undergoes a shift from being metal$\rightarrow$poisoned to poisoned$\rightarrow$metal along a distinct trajectory, creating a hysteresis curve. For this reason, the O_2 partial pressure needs to be maintained relatively low to obtain an oxide film with a high sputtering rate. Therefore, the optimal range lays between metallic and poison states.

2.2 Thin films growth modes

The type of film formed, whether amorphous (lacking a defined crystal structure, i.e. order at long range), single crystal, or polycrystalline (consisting of crystallites with varying crystallographic orientations), depends on the crystallographic properties of both the substrate and the target material, as well as the growth conditions. In this section, we will focus specifically on the mechanisms that govern the growth and microstructure of polycrystalline films.[205] The initial step in the growth of polycrystalline thin films involves the arrival of vapor species (atoms, molecules, ions, radicals, etc.) onto the surface of the substrate with a certain kinetic energy, E_{kin}. Upon colliding with the substrate, these particles lose their velocity component normal to it and lower their potential energy through adsorption on the surface ($E_{kin} – E_{ads}$). Through the process of adsorption, these species become accommodated on the substrate, and they are collectively known as adatoms. The adatoms then undergo a thermally activated random walk on the substrate surface (adatom surface mobility/diffusion), which depends on the deposition conditions and the substrate surface properties. It is interesting to note that, when the E_{kin} is high, adatoms can cover greater distances across the substrate's surface, thereby increasing the chances to find favourable positions, leading to the formation of more crystalline and dense materials. On the contrary, lower kinetic energy typically produces more amorphous and porous materials, since adatoms tend to remain stationary in close proximity to their arrival point. When surfaces are rough, or the substrate temperature is low, shading processes known as *shadowing* can also occur. In this case, the deposited material blocks the new arriving material from accessing the substrate, leading to porosity.[206] Additionally, the surface of the substrate is usually not a perfect terrace, but rather consists of a range of features such as ledges, kinks, vacancies, impurities, and point defects. These features serve as preferred sites for the nucleation of adsorbed species. In fact, these surface imperfections impact the adhesion of adatoms to the substrate, and thus have an effect on the processes of adsorption, diffusion, and nucleation.[207] During their movement, the adatoms can come into contact with other adatoms, forming stable atomic islands that are spatially separated (nucleation). As these

islands grow in size, they incorporate material from either the vapor phase or the adatoms present on the substrate (island growth) and merge with each other to form new, larger islands (coalescence), see Figure 2-6.

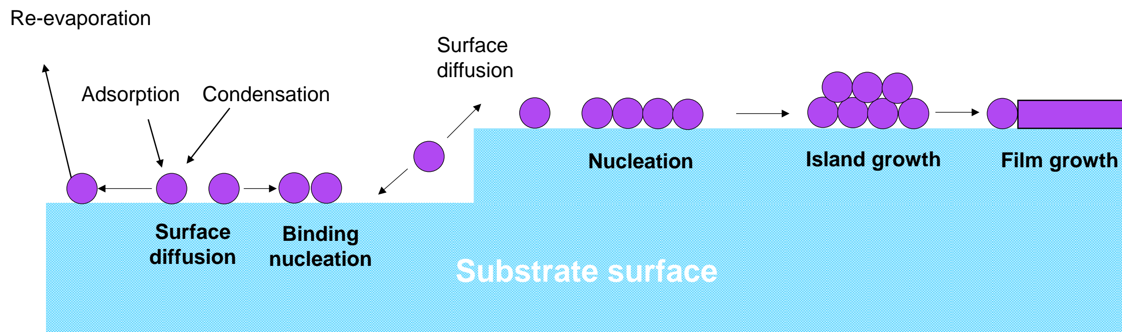

Figure 2-6 - Schematic of the common atomistic processes occurring during nucleation and growth on surfaces.

There are two distinct mechanisms that explain the process of particle growth, namely Ostwald ripening (OR) and Smoluchowski ripening (SR), also referred to as particle migration and coalescence, see Figure 2-7. OR leads to the growth of larger particles at the expense of smaller ones, which can occur either through surface diffusion or vapor phase diffusion due to the difference in chemical potentials between smaller and larger particles.[208–210] This occurs because the larger particles have a lower surface energy than the smaller particles, making them more energetically favourable for the small particles to attach to. On the other hand, SR involves smaller particles migrating onto the substrate surface and subsequently coalescing with larger particles, with the smaller particles typically diffusing faster.[208,211]

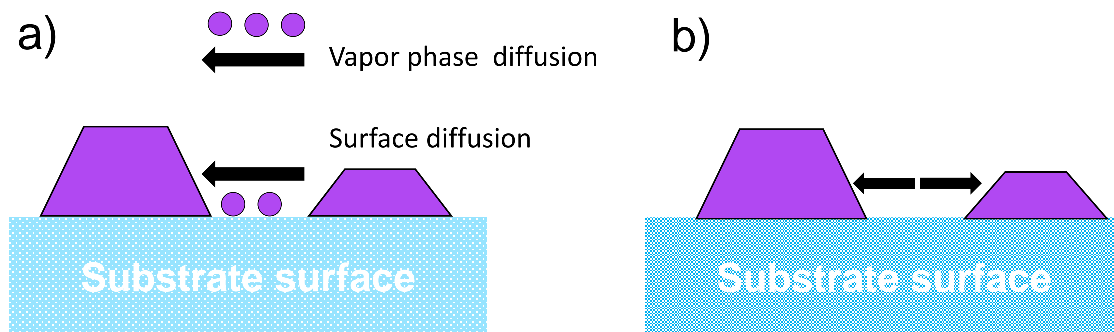

Figure 2-7 - Schematic of ripening mechanisms a) Ostwald ripening (OR) or atom migration, and (b) Smoluchowski ripening (SR) or particle migration and coalescence.

This coalescence process continues until the boundaries between single-crystalline islands (referred to as grains) become immobile and coalescence is no longer possible, resulting in the formation of polycrystalline islands and ultimately a continuous film.[205,212]

During thermal equilibrium, the early stage of film deposition is governed by one of the three growth mechanisms illustrated Figure 2-8, each leading to distinct morphologies of thin films.[213,214]

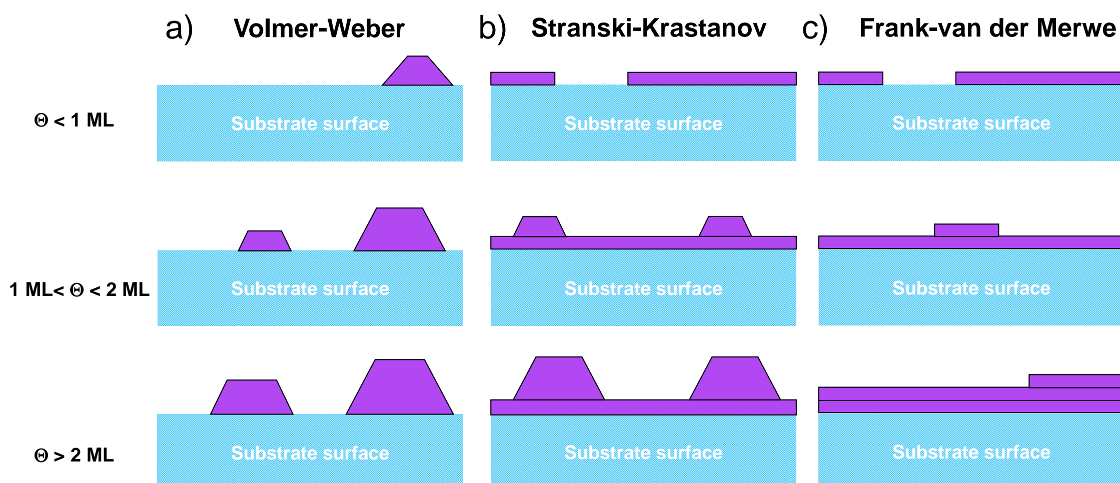

Figure 2-8 - Schematic representation of the three basic growth modes in thin films a) Volmer-Weber b) Stranski-Krastanov and c) Frank-van der Merwe. Θ denotes the overlayer coverage in monolayers (ML).

The *Volmer-Weber* growth mode, as depicted in Figure 2-8a, refers to a three-dimension growth that starts with the formation of small islands, which then enlarge and merge to form relatively large structures. This growth mode occurs when the adatoms of the deposited material have a stronger affinity to each other

than to the substrate. Frequently, this phenomenon is seen in metal systems placed over insulators substrates. In contrast, when the adatoms of the deposited material have a stronger attraction to the substrate than to each other, it leads to the formation of a complete monolayer (ML) before another starts to grow.[215] This growth mode is referred to as *Frank-van der Merwe* (Figure 2-8c) or *layer-by-layer* growth. This is mostly the case in metal/semiconductor (e.g. Fe/GaAs) systems. The latter case, *Stranski-Krastanov* or *layer-plus-island* (Figure 2-8b), is an intermediate situation between the models of Volmer-Weber and Frank-van der Merwe. After few 2D monolayers have formed, further growth becomes energetically unfavourable due to increase in the total film elastic strain energy, and 3D islands form.[207] The growth mode is frequently with metal-on-semiconductor or semiconductor-semiconductor systems.

One can gain a qualitative understanding of the various growth modes by considering the surface energy (or surface tension), γ. The nature of the bond between the film and substrate determines the structure and the morphology of the film, which can be explained by the Young's equation (Eq. 2-1). This equation shows that the contact angle (θ) between the film island and the substrate (Figure 2-9), relies solely on the surface properties of the materials in question:[216]

$$\gamma_S = \gamma_{S/F} + \gamma_F \cos\theta \quad \text{(Eq. 2-1)}$$

Where γ_S denotes the surface tension of the substrate surface, γ_F the surface tension of the film surface, and $\gamma_{S/F}$ the surface tension of the film/substrate interface. For island growth (*Volmer-Weber* growth), $\theta > 0$ and corresponding condition is

$$\gamma_S < \gamma_{S/F} + \gamma_F \quad \text{(Eq. 2-2)}$$

For the case of layer-by-layer (*Frank-van der Merwe)* growth, the situation is contrary to the previous one, and therefore we could write:[216]

$$\gamma_S \geq \gamma_{S/F} + \gamma_F \quad \text{(Eq. 2-3)}$$

For layer-plus-island (*Stranski-Krastanov)* growth, the condition on Eq. 2-3 for layer growth is initially fulfilled. However, the formation of the intermediate layer changes the values o f$\gamma_{S/F}$ and γ_S, thereby resulting in the condition equation Eq. 2-2 for the subsequent island growth.[216]

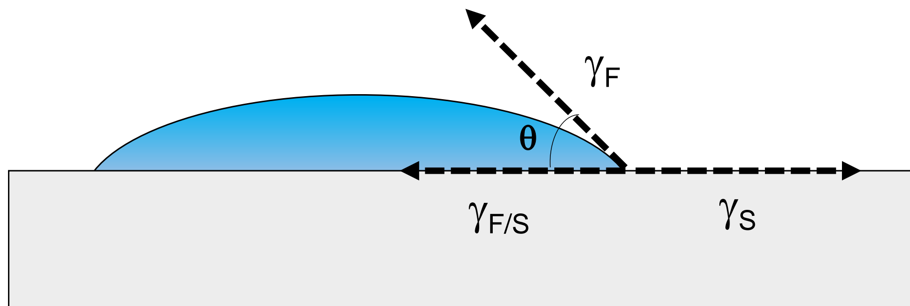

Figure 2-9 - Schematic of the surface tensions present in a film island on a substrate.

The island-like growth of an Au on Al_2O_3 (γ_S(a-Al_2O_3) = 0.97 J/m^2 and γ_S(γ-Al_2O_3) = 1.5-1.7 J/m^2)[217] is largely due to the poor wettability of the Au, (γ_F(Au)= 1.51 J/m^2)[218][219]. In fact, in general, the surface free energy of metals is usually larger than on oxides.[220] The values of surface energy correspond to the condition of island growth (Eq. 2.2), particularly for the case of amorphous alumina, which has a surface tension clearly lower than Au. For this reason, when Au nucleates on an oxide surface (amorphous alumina), Au nanoclusters initially form to minimize their surface area to lower their surface energy. This is why the growth of metal on an oxide substrate often results in an island growth mode.

2.2.1. Structure Zone Models

Over the past decades, there has been a systematic characterization of the self-organized structural evolution of polycrystalline films that were deposited using PVD techniques under various growth conditions. In the characteristic types of film, their microstructural evolution was correlated with their growth conditions, which was categorized in the so-called structure zone models (SZM). The concept of SZM can be viewed as a guide that enables the prediction of the morphology and structure of manufactured films based solely on the deposition parameters. In 1969, Movchan and Demchishin proposed the initial model,[221] which is based on the observation of the microstructure characteristics of Ni, Al_2O_3, W, Fe, Ti and ZrO_2 films by electron beam evaporation. Their SZM describes the influence of the substrate temperature (represented by the ratio of substrate temperature T, and the melting point of the coating-material, T_m) on the coating morphology. This model has 3 different structural zones, as seen in Figure 2-10:

- **Zone 1 ($T/T_m < 0.3$):** this zone is characterized by a low T/T_m ratio, at which the adatom energies are insufficient to overcome substrate irregularities, and shadowing effects, leading to inadequate surface diffusion. In Zone 1, the resulting fined-grained structure of textured and fibrous grains, pointing in the path of the arriving vapor flux and ending with domes.[221,222]
- **Zone 2 ($0.3 < T/T_m < 0.5$):** This zone has high substrate temperatures (T) at which both surface and grain boundary diffusion take place in a significant level. This Zone 2 has columnar grains separated by distinct, dense, intercrystalline boundaries. The surface appears to be more uniform and smoother as the substrate temperature increases homogenously.[221]
- **Zone 3 ($0.5 < T/T_m < 1$):** Zone 3, which leads to the final structure of the film, involves the formation of equiaxed grains and recrystallization, resulting in increased grain growth and a more pronounced crystalline structure.[221,223]

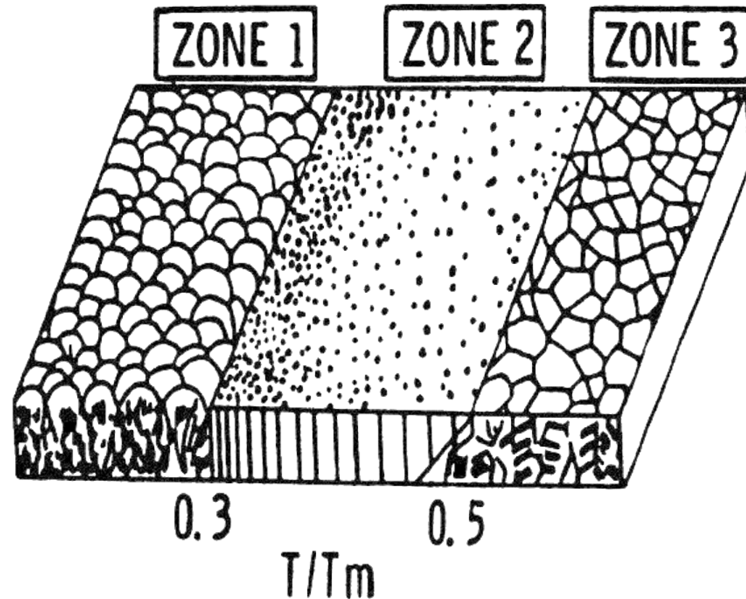

Figure 2-10 – SZM of Movchan and Demchishin. T represents the substrate temperature and T_m the melting point temperature of the coating-material, both in Kelvin. Adapted from [221].

To provide a more comprehensive description of the microstructure of sputter-deposited films, this SZM model has been sequentially expanded by Thornton,[224] Messier et al.,[225] and Kelly and Arnell.[226] Barna and Adamik established new boundaries and added an area referred to as zone T, positioned between zones 1 and 2. This region exhibits an inhomogeneous structure across the thickness of the film. It features a finely crystalline composition near the substrate, followed by V-shaped grain formations in the subsequent thickness range. Towards the upper portion of thicker films, the structure may become columnar.[227] Typically, surface diffusion is "remarkable", but grain boundary diffusion is strongly limited.[228] The latest modification to SZM, recently introduced by Anders et al.[228] extended the concept to energetic deposition where the flux of ions is large, including filtered cathodic arc and HiPIMS (see Figure 2-11). The average energy per incoming particle is one of the most critical parameters, with higher values resulting in increased surface mobility. [229,230] Increasing the deposited energy per particle leads to a higher transient mobility of the atoms that hit the surface, thus elevating the apparent surface temperature.[231] When deposition rates are identical, the higher mobility will increase diffusivity, allowing for further transport from the original arrival site and

earlier coalescence.[232] Therefore, higher energies result in changes in surface morphology and texture, with larger grains and fewer defects in the resulting films, while the momentum of incoming particles can lead to the alignment or orientation of growing crystallites.[233–235] As a consequence, it is possible to escape from Zone 1 without need to apply heating during the growing of the film. In Figure 2-11, the microstructure of the film is depicted in three-dimensional space for the SZM of Anders. The vertical axis represents the net thickness, and the horizontal axes represent two thermodynamical variables: generalized substrate temperature (T*), and the normalized energy flux by the arriving species (E*). A new zone is added called *ion etching;* as E* increases (e.g., by biasing), the deposited film thickness decreases due to higher sputtering yield. At a material-dependent energy threshold (400-1400 eV), sputtering rate equals film formation rate. Beyond that, substrates are etched, as seen in Figure 2-11.[228] Once the average yield approaches unity, which typically occurs between 400 eV and 1400 eV for most elements, film growth stops, and the surface starts to etch with further energy increases.[233–235]

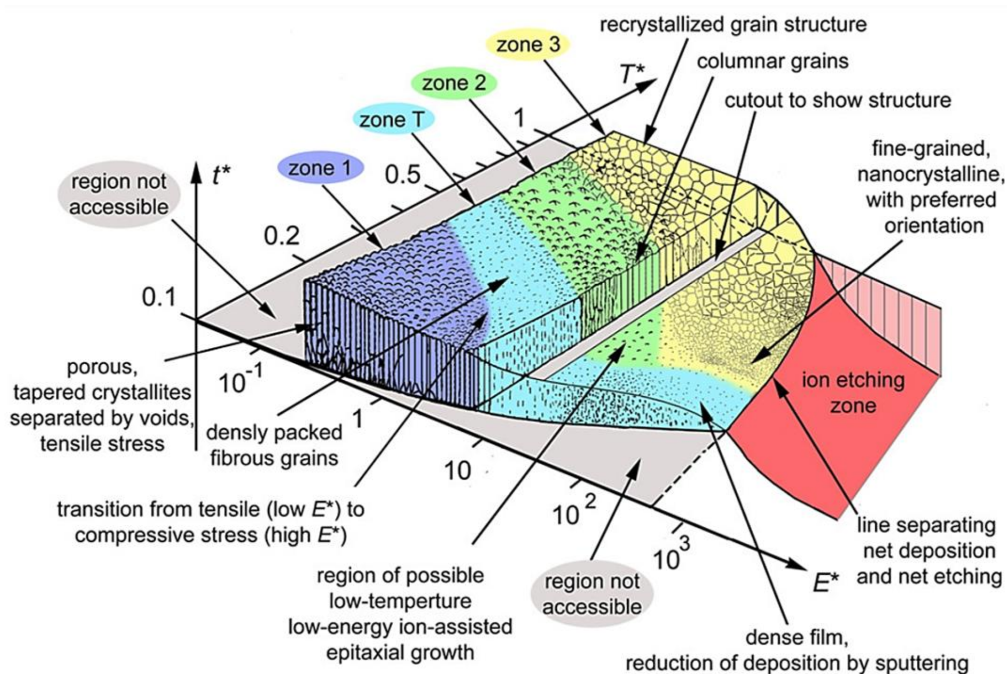

Figure 2-11 – Schematic of the SZM developed by Anders et al. showing a cross-sectional view of the types of the possible polycrystalline film microstructure, with t* indicating the net thickness, E* representing the normalized energy flux and T* the generalized substrate temperature. It should be noted that the boundaries between the different zones and numerical values provided are for illustrative purposes only. Adapted from [228].

2.3 Experimental conditions of magnetron sputtering deposition

2.3.1. Deposition chamber

A PVD coater machine (850 L), Figure 2-12, was used to deposit coatings through reactive magnetron sputtering. The process took place in an Ar or Ar/O_2 mixture (purity 99.998%) under a working pressure of approximately 2.2×10^{-3} mbar.

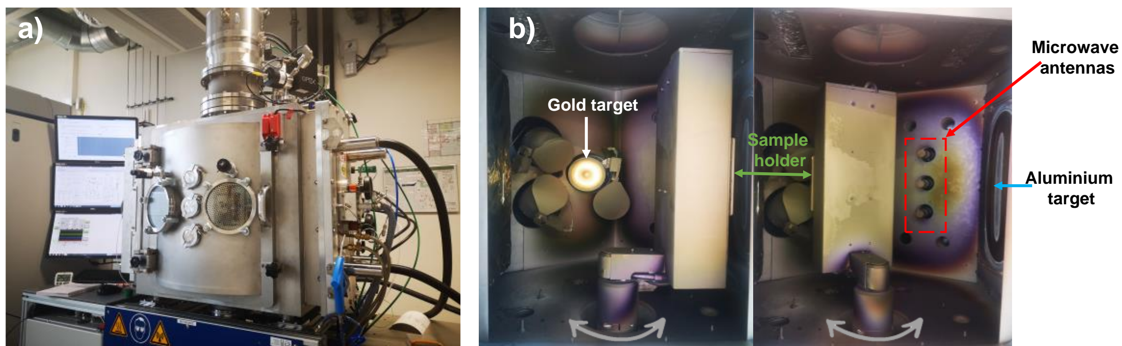

Figure 2-12 – a) Image of PVD system used in this Ph.D. b) Interior of the PVD chamber composed of Al and Au targets and 3 microwave antennas for Ar/H_2 treatment.

The following Table 2-2 summarizes the characteristics used in the deposition of Al_2O_3 coating and Au nanoparticles.

Table 2-2 – Parameters employed for the deposition of Al_2O_3 and Au.

	Al_2O_3	Au
Target characteristics	Al, rectangular (40 x 12.5 cm)	Au, circular (∅ 10.14 cm)
Power sources (W)	HiPIMS (2000, 2500) MF (2000, 2500, 3500), MF+HiPIMS (2000)	DC (31) Pulsed-DC (42-54)
Gases (sccm)	Ar/O_2 (50/9)	Ar (50)
Substrate temperature (ºC)	R.T., 200, 450	R.T.
Amplitude of the dynamic mode (º)	15, 70	70

The films studied in this Ph.D. can be divided into 2 sections: deposition of alumina coatings (described in detail in Chapter 3) and deposition of gold nanoparticles on top of Al_2O_3 coatings (described in Chapters 4, 5 and 6).

2.3.2. Deposition of alumina coatings

As reported in the section 2.1.4, the sputtering mode of a magnetron target can shift rapidly from a metallic state to a fully poisoned state when a reactive gas as oxygen is introduced into the sputtering discharge. This sudden transformation renders the process unstable and less efficient, and results in substantial fluctuations in the sputtering rate. One potential solution is to operate the target in a fully poisoned mode, where the entire target surface is covered by the reaction product. However, compounds on the target sputter at a significantly slower rate compared to pure metals, making this approach generally unfavourable. A more effective strategy involves utilizing a feedback control system able to manage the reactive gas flow in response to the plasma conditions. This allows operating in a non-stable situation where the target surface is *quasi-poisoned*, but the sputtering rate is still high. Therefore, it becomes possible to obtain enhanced deposition rates and increased process reliability, which are unattainable with a constant flow of the reactive gas.[236]

In this Thesis, a system with an active feedback control was used for the deposition of alumina films. This system has an algorithm (Speedflo's PDF) that

dynamically modifies gas input flow in real-time based on sensor data, ensuring the stability of the process at a predetermined setpoint with adjustments made every millisecond.[236] Additionally, a remote plasma spectroscopy (Optix, Gencoa Ltd.) was used. Optix involves the generation of a small plasma within the sensor head with a spectrometer integrated within the device analyses the plasma's light spectrum. The resulting data allows for gas detection and quantitative measurement of its concentration within the vacuum.[236] In our specific case, we monitored the intensity of the atomic O emission line at 777.6 nm (from O($3p^5$ P) to O($3s^5$ S)).[237] It is important to note that sensor calibrations were performed prior to each deposition to define the setpoint where target poisoning was almost achieved, but the deposition rate was still high.

All the coatings were deposited in dynamic mode, which consists of an oscillating motion of the substrates in front of the target, with a rotation speed of 5 rpm and an amplitude of 15° (70° for the Al_2O_3 film deposited at 200ºC), as shown in Figure 2-13).

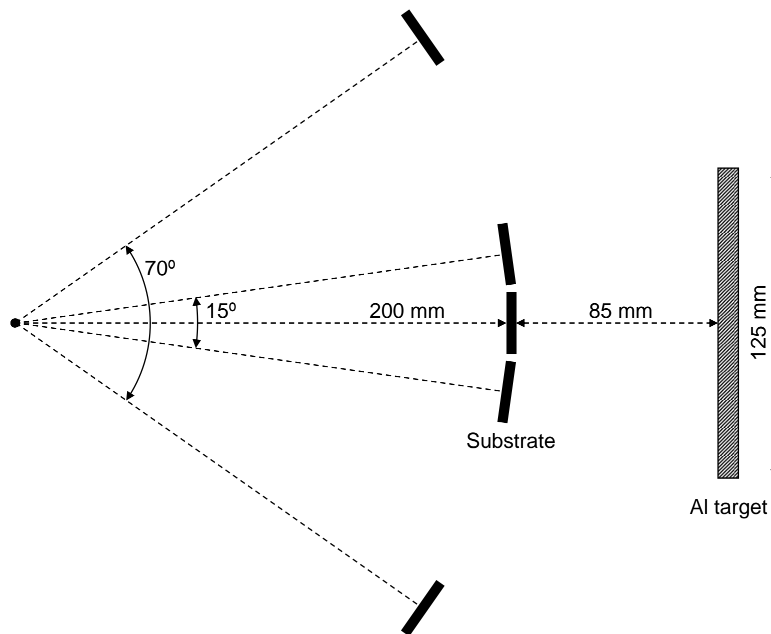

Figure 2-13 - Schematic (to scale) of the movement of the substrates in front of the aluminium target during the deposition.

The alumina coatings were sputtered in an atmosphere composed of Ar (50 sccm) and O_2 (7-9 sccm). The distance between the substrate holder and the

targets was ca. 85 mm. The deposition times were adjusted to achieve a Al_2O_3 thickness of 200 nm for all films, except for the film deposited at 200°C, which had a thickness of 386 nm.

For the deposition of Al_2O_3 (see Chapter 3) two different power sources and temperatures were used, namely HiPIMS at 450°C, and MF at 200°C and 450°C. Three average values of power were used, 2000 and 2500 W for HiPIMS and MF, and 3500 W for MF. A combination of HiPIMS and MF operating at 2500 W was also explored, using 5 or 10 MF pulses between 2 consecutive HiPIMS pulses (instead the 40 pulses which are produced in conventional MF operation). Table 2-3 shows the operation parameters applied for MF and HiPIMS sources on an aluminium target (purity: 99.999%, surface: 500 cm^2) during deposition.

Table 2-3 – Operation parameters of the MF and HiPIMS power sources.

Source	Frequency (kHz)	Duty cycle (%)	T_{on} (μs)	T_{off} (μs)
MF	**40**	**80**	**20**	**5**
HiPIMS	**1**	**3**	**30**	**970**

The power was supplied to the target by MELEC SIPP 2000 generator. The current and voltage were monitored during the experimental process as a function of time with a Teledyne Lecroy HDO4054 oscilloscope.

2.3.3. Deposition of Gold nanoparticles

Gold nanoparticles were deposited on a Al_2O_3 layer of 7 nm, which was deposited at room temperature in dynamic mode of 70°. The gold target was sputtered in an atmosphere composed by Ar gas (50 sccm) during 10 s to 80 s in dynamic mode (70°, see Figure 2-14).

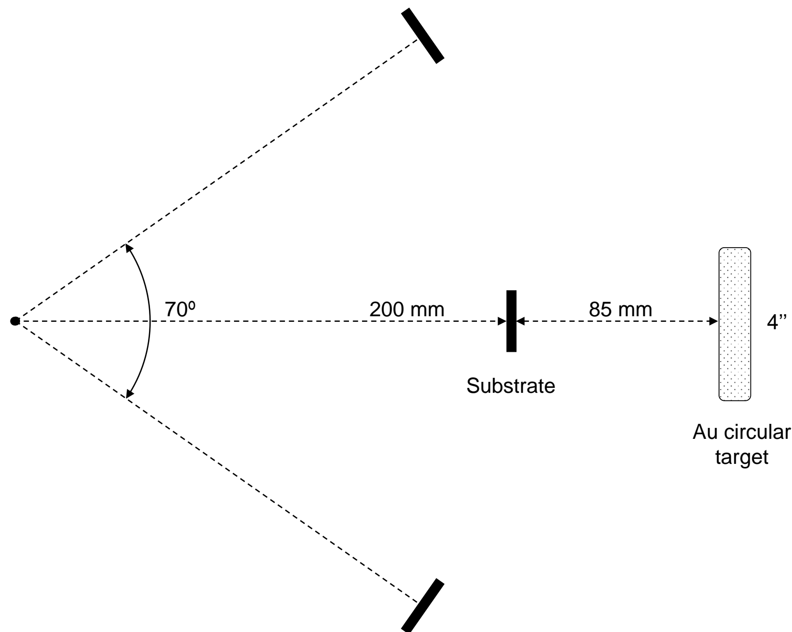

Figure 2-14 - Schematic (to scale) of the movement of the substrates in front of the gold target during deposition.

The Au sputtering was carried out in DC and Pulsed-DC modes (see Chapters 5 and 6, respectively). For the investigation of the Pulsed-DC, four duty cycles of 40%, 20%, 4.1% and 1.5 % were selected (t_{on} of 95, 50, 15, and 15 µs and t_{off} 145, 200, 350 and 50 µs, respectively). The average power was around 31 W and 42-54 W for DC and Pulsed DC, respectively. The power was supplied to the target by MELEC SIPP 2000 generator.

2.3.4. H_2 + Ar plasma treatment

In some samples, an Ar/H_2 plasma pre-treatment was carried out on the Al_2O_3 films prior the deposition of Au nanoparticles, to evaluate modifications of the surface mobility of Au adatoms and their effects on the cluster formation. The base pressure of the chamber was 0.005 Pa, and the pressure of the Ar/H_2 mixture during exposure treatment was about 0.08 Pa. The plasma treatment took place for 10-30 minutes, by applying a microwave power of 150 W. The influence of different Ar/H_2 ratios (33.3, 16.6) and treatment times (0-30 minutes) are explored in Chapter 4.

2.4 Characterization techniques

2.4.1 X-Ray Diffraction

X-ray diffraction (XRD) is a non-destructive characterization technique used to determine the crystalline structure, stress, grain size and preferred growth directions of thin film materials, without requiring preparation prior to the analysis. This technique consists of directing an incident beam of monochromatic X-rays onto a specimen, leading to scattering and diffraction by the atoms of the sample. The interference occurring due to scattering of X-rays can be interpreted using the Bragg's law: [95]

$$n\lambda = 2d\sin\theta \quad \text{(Eq. 2-4)}$$

Where n is the diffraction order, λ the wavelength of the X-rays, d is the interplanar spacing of the diffracting atomic planes, and θ is the angle of incidence, as shown in Figure 2-15.

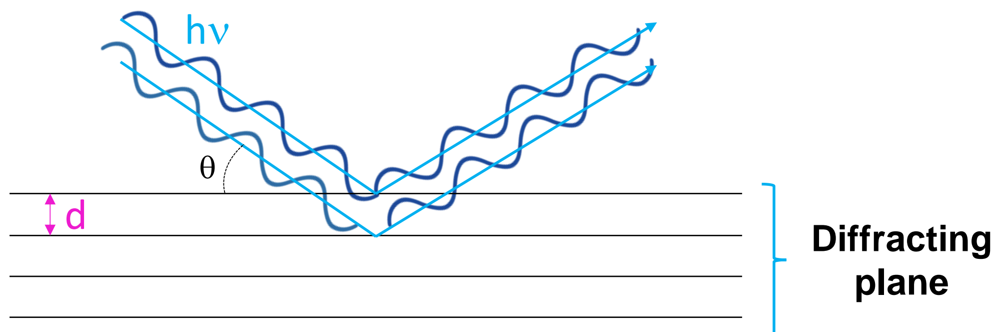

Figure 2-15 - Schematic representing Bragg's Law.

The intensity of the diffracted radiation is dependent on the interaction of the beam with the sample (which depends on the type, arrangement, and density of atoms that constitute the plane), while the angle is a function of the interatomic distances. The appearance of diffraction peaks is a sign of the presence of ordered crystalline structures in the system (crystal planes).

The grain size "*d*" of a material can be estimated by the Scherrer equation for the broadening of the peak.

$$d = \frac{k\lambda}{\beta \cos\theta}$$ (Eq. 2-5)

Where β is the full width at half maximum FWHM of the diffraction peak (in radians), θ the diffraction angle, and k is a constant (k~0.9 for spherical crystallites).

The characteristics of a peak include its intensity (which is connected with sample texture), position (associated with the lattice parameter), and width (dependent on the crystallite size and microstrain), as seen in the following Figure 2-16.

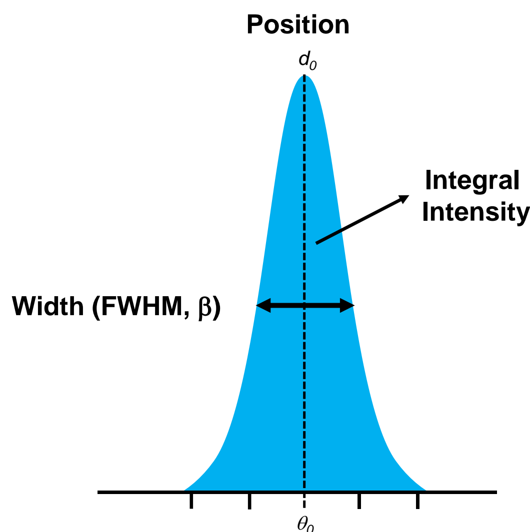

Figure 2-16 – Characteristics of a XRD peak.

Typically, each grain within a polycrystalline aggregate possesses a distinct crystallographic orientation compared to its neighbouring grains. The orientations of all the grains can exhibit two possibilities: they can be randomly distributed in relation to a chosen frame of reference, or they can exhibit a tendency to cluster, to varying degrees, around specific orientations. An aggregate that demonstrates the latter condition is described as having a preferred orientation or texture. In simple terms, this means that the distribution of crystal orientations is non-random. The presence of a preferred orientation can significantly impact the intensities of diffracted rays measured through diffractometry.[238] The texture of the film can be characterized by the textural parameters (T_{hkl}):

$$T_{hkl} = \frac{I_{hkl}/I_{hkl}^{0}}{\frac{1}{m}\sum_{i=1}^{m} I_{h_i,k_i,l_i}/I_{h_i,k_i,l_i}^{0}} \quad \text{(Eq. 2-6)}$$

Where *h,k,l* represent the Miller indexes corresponding to the diffraction reflection under study. The parameter m denotes the number of peaks being considered. I_{hkl} and I_{hkl}^{0} denote the peak intensities of the reflection of the (*hkl*) plane observed on the sample and a misoriented reference, respectively. A value greater than 1 for the textural parameter, T_{hkl}, indicates a preferential growth of the (*hkl*) plane parallel to the sample surface. In the case of a total misoriented sample, the T_{hkl} would equal to 1 for each (*hkl*) plane, while a value less than 1 indicates restricted growth of the (*hkl*) plane.[239]

Additionally, the diffraction angle of a crystalline structure is influenced by its interplanar distance. If the material experiences any form of tension or stress, the interplanar distance can be altered, leading to an impact on the peaks observed in the diffractogram. The two possible effects of stresses in a the XRD peak are shown in the following Figure 2-17.

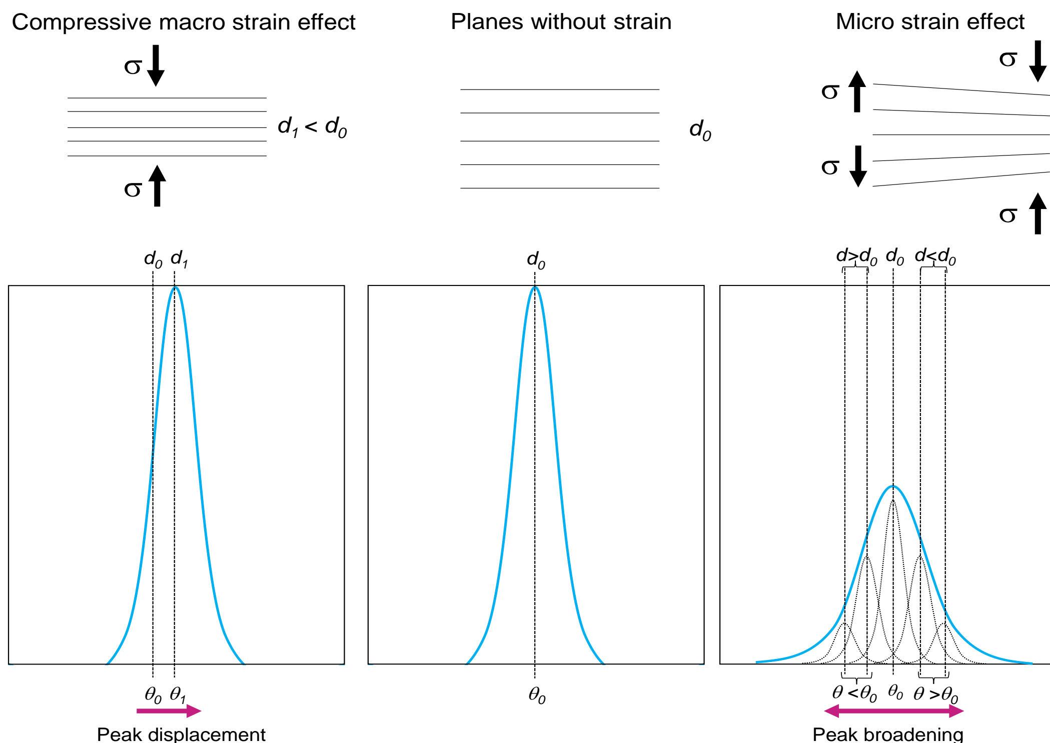

Figure 2-17 – Schematic of the influence of macro stress (left) and micro stress (right) in a XRD peak. Adapted from [206].

Macrostresses arise when the interplanar distances of planes are higher or lower than the equilibrium values, but relaxation is avoided due to the restriction of a thicker underlying substrate. Consequently, this causes a shift in the positions of the peaks in the diffractogram compared to the reference (unstressed) state. If a film is subjected to compressive stress, the peaks of planes parallel to the surface will show a displacement corresponding to tensile deformation. The reason is that these planes are not subjected to the primary compressive stress, but to the perpendicular Poisson's expansion of the material. As a result, the diffraction line shifts towards lower angles without any change in broadening nor shape.

Microstresses arise from localized strains within the crystalline grains, resulting from factors such as dislocations, impurities, vacancies, and defects. The presence of microstress leads to the broadening of diffraction peaks, as the applied tension on the material is non-uniform, causing an increase in interplanar distance in some areas and a decrease in others. This phenomenon is illustrated in Figure 2-17 (top - right). Therefore, one can consider a single grain as consisting of multiple small regions, where the plane spacing remains largely constant within each region but differs from the spacing in neighbouring regions. These specific regions give rise to distinct, sharp diffraction lines depicted by dotted curves on the right. The broadened diffraction line, represented by the solid curve, would be formed by the contribution of these sharp lines, each slightly offset from the others.[238] The peak broadening is caused not only by the introduction of lattice distortions, but also by the crystallite size. There are different methods to measure the broadening such as Warren-Aberlach [240] and Williamson-Hall, [241] which we briefly describe now.

One can estimate the broadening of the peak by considering the combined effects of instrumental broadening, β_{inst}, which can be determined through experimental measurements, the broadening resulting from the size of the crystallite, β_D, which can be computed using the Scherrer equation, $\beta_D = \left(\frac{0.9\lambda}{D\cos\theta}\right)$ (Eq. 2-7), and the broadening caused by strain, $\beta_S = 4\varepsilon\tan\theta$ (Eq. 2-8). Contributions from instrumental effects, micro strain and crystallite size can be separated in a

straight-forward fashion if the peaks are Gaussian or Lorentzian shaped.[238] For Lorentzian peaks,

$$\beta = \beta_{inst} + \beta_S + \beta_D \quad \text{(Eq. 2-9)}$$

For Gaussian peaks,

$$\beta^2 = {\beta_{inst}}^2 + {\beta_S}^2 + {\beta_D}^2 \quad \text{(Eq. 2-10)}$$

In our case, the peaks fit better to a Lorentzian function. Therefore, we can write:

$$\beta = \beta_{inst} + 4\varepsilon \tan\theta + \frac{0.9\lambda}{D\cos\theta} \quad \text{(Eq. 2-11)}$$

When multiplying for $\cos\theta$, we obtain:

$$(\beta - \beta_{inst})\cos\theta = \frac{0.9\lambda}{D} + 4\varepsilon \sin\theta \quad \text{(Eq. 2-12)}$$

The plot depicted in Figure 2-18 allows for the distinction between size and strain components by plotting $(\beta - \beta_{inst})\cos\theta$ as a function of $\sin\theta$. This graphical representation is commonly referred to as a Williamson-Hall plot and operates under the implicit assumption that the peak shapes adhere to the Lorentzian distribution.[238]

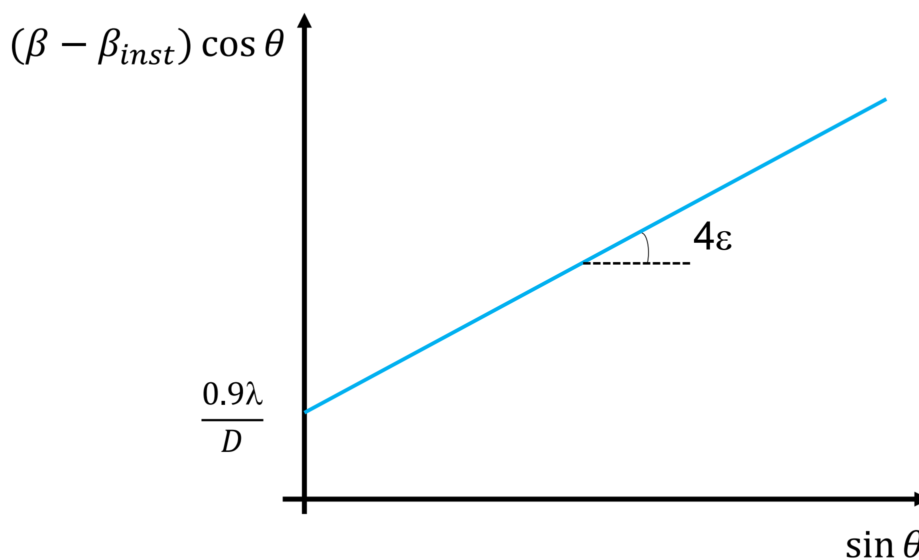

Figure 2-18 - Williamson-Hall plot, where the intersection of the fitting line with the y-axis represents the crystallite size, and the slope represents the microstrain.

Strictly speaking, we should distinguish between grain size and crystallite size. The latter typically refers to the ‘coherent diffraction domain size’, i.e., the size that could be estimated with the W-H method or with the Scherrer equation. However, it is possible than a grain would be formed by different crystallites. Nevertheless, such detailed studies are not carried out in this Thesis, and both terms would be used indistinctively.

In this Thesis, we focus on the deposition of Al_2O_3 thin films with thickness of 10-200 nm. For this reason, Grazing Incidence X-ray Diffraction (GIXRD) was chosen, since it has a lower penetration of the X-rays in the coatings, due to the use of a constant low incidence angle, close to the critical angle.

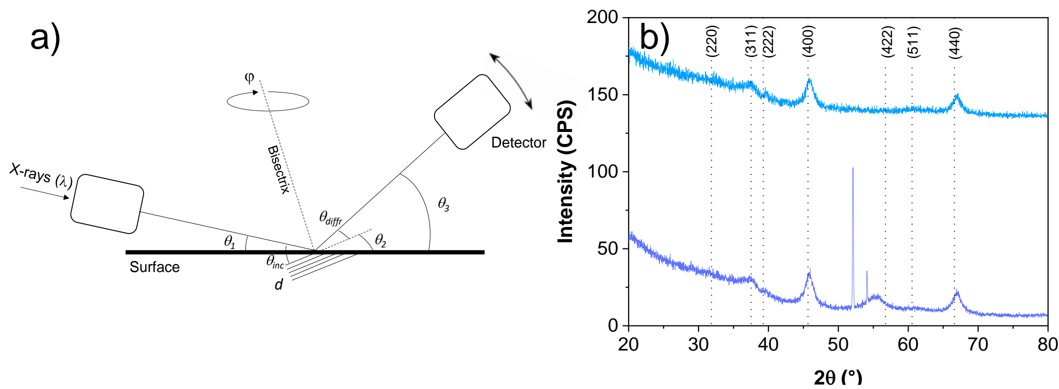

Figure 2-19 – a) Schematic of GIXRD. b) XRD pattern of a film with (dark purple line) and without (blue line) the Si (311) contribution.

In this Thesis, all the diffraction measurements were performed using GIXRD, whereby the detected planes exhibit a variable angle that changes with the surface. In the schematic on Figure 2-19a, the X-rays hit the sample surface under the small angle θ_1. In this Thesis, $\theta_1 = 0.5°$ and with this configuration the angles can be related by the following expressions:

$$\theta_{inc} = \theta_{diffr} \quad \text{(Eq. 2-13)}$$

$$\theta_2 = \theta_{inc} - \theta_1 \quad \text{(Eq. 2-14)}$$

$$\theta_3 = \theta_{diffr} + \theta_2 \quad \text{(Eq. 2-15)}$$

$$\theta_3 = 2\theta_{inc} - \theta_1 \quad \text{(Eq. 2-16)}$$

The Si substrate displays a sharp peak at ca. 53°, and a broader peak around 56°, with the former being identified as originating from Si(311) planes, see Figure 2-19b. The appearance of these Si contributions can be avoided by changing the orientation of the Si substrate against the incident beam. The intensity of this peak is maximum if the (100) wafer is oriented with the (110) plane towards the X-ray beam. In these circumstances, the 311 plane gives $\theta_2 = 25.2°$. Since the incident angle is 0.5°, the angle between the beam and the Si (311) plane in the substrate is $\theta_{inc} = \theta_2 + \theta_1 = 25.7°$, which agrees well with the observed peak at $2\theta = 51{,}4°$. Only the Si(311) Si planes create a substrate peak in the GIXRD pattern, since only this plane is hit by the grazing X-rays approximately under their Bragg angle θ.[242] However, a rotation of the Si substrate by an angle φ~45° around an axis perpendicular to it leads to the disappearance of that contribution, as it can be observed in Figure 2-19b (blue line).

It is important to find out why no other planes from the Si (100) substrate are not detected. The angle φ_1 between an *hkl* plane of the Si and the surface of the (100) wafer can be calculated using the scalar product of the vectors, as:

$$(h,k,l)\cdot(1{,}0{,}0) = (h+0+0) = \sqrt{h^2+k^2+l^2}\cdot\sqrt{1^2+0^2+0^2}\cdot cos\varphi_1$$

In addition, the Bragg's law has to be true for the interplanar distance of the *hkl* plane that we are considering (d_{hkl}). Therefore, we can calculate the Bragg's angle for that plane, φ_2, re-writing Eq. 2-5 as:

$$\varphi_2 = sin^{-1}\left(\frac{\lambda}{2d_{hkl}}\right)$$

The peak will be detected only if $\theta_{inc}=\varphi_1+0.5$ and φ_2 are relatively close.

Table 2-4 shows the values of these angles. It can be observed that the plane that shows the lowest value of angle difference is the (311), which explains why only that peak from the substrate is detected. An in-plane rotation of 45° of the wafer makes this peak disappear since the interplanar distance is not oriented properly respect to the incident beam.

Table 2-4 – Information about the peak position (2θ), plane spacing (d_{hkl}) and Miller indices (hkl) for Silicon (JCPDS Card No 00-005-0565). The angles with the (100) plane, and the difference with the Bragg's angle are calculated.

2θ (°)	d_{hkl} (Å)	h	k	l	$\theta_{inc}=\varphi_1+0.5$ (°)	Bragg's angle j_2 (°)	Difference (°)
28.419	3.138	1	1	1	55.2	14.2	41.0
47.305	1.92	2	2	0	45.5	23.7	21.8
56.102	1.638	3	1	1	25.7	28.1	2.3
69.171	1.357	4	0	0	0.5	34.6	34.1
76.37	1.246	3	3	1	47.0	38.2	8.8
88.056	1.1083	4	2	2	35.8	44.0	8.3
94.972	1.045	5	1	1	16.3	47.5	31.2
106.731	0.9599	4	4	0	45.5	53.4	7.9
114.126	0.9178	5	3	1	32.8	57.1	24.3
127.568	0.8586	6	2	0	18.9	63.8	44.9
136.925	0.8281	5	3	3	40.8	68.5	27.7

In this Thesis, GIXRD was performed in a Bruker D8 Discover in parallel beam configuration, using a Cu K_α source operated at 40 kV and 40 mA. All the measurements were acquired in grazing incidence mode (0.5º) from 2θ=20º to 75º, with a step size of 0.02º. XRD patterns were acquired at ϕ angles (rotation of the sample in the holder) of 0º and 45º to record or avoid the signal from the Si substrates (forbidden 311 reflections at 2θ~53º), respectively.[242,243]

2.4.2 Specular X-ray Reflectivity

Specular X-ray Reflectivity (XRR) is a non-destructive technique used to determine the thickness, surface and interface roughness, and density of films, whether they are single-layer or multilayer, regardless of the film's crystallinity.

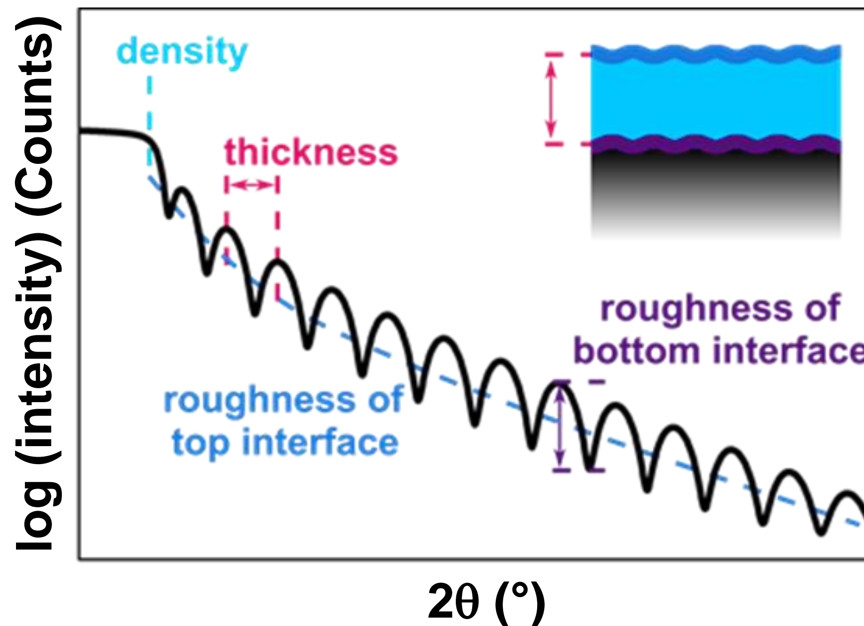

Figure 2-20 – XRR pattern and respective information that can be obtained from it. Adapted from [244].

XRR involves measuring the intensity of an X-ray beam reflected from a surface relative to the intensity of the incident beam, with a grazing angle (θ). When the incident beam is below the critical angle, total reflection of x-rays will occur. This corresponds to the edge in Figure 2-20, which gives information about the density of the film. However, if the incident beam is above the critical angle, some photons will penetrate the sample through refraction due to the differences in density, while others will be reflected at the surface. The Kiessig fringes are created through the interference of X-rays that have been partially reflected from both the air-film and film-substrate interfaces. When the surface roughness increases, the amplitude of these fringes decreases.[245] The frequency of the fringes seen in a XRR pattern is proportional to the thickness of the film (i.e. the thicker the film, the higher the frequency of the fringes). The roughness is given by the decay of the Kiessig fringes. When the surface of the film is rough, it

scatters the reflected X-rays and reduces the intensity of the fringes. Additionally, the reduction in fringe intensity is proportional to the roughness of the film surface. However, determining the thickness of a rough surface becomes challenging because the decrease in intensity masks the oscillation pattern.

In this Thesis, XRR was performed to analyse Al_2O_3 films using a PANalytical X'Pert Pro with Cu-K_α radiation (λ = 0.154 nm) equipped with a knife edge collimator, which avoids the inhomogeneity of the film by reducing the footprint of the beam. GenX 3.6.3 software was used to fit the data and obtain the density and thickness of the films. The measurements and data fitting were performed by Yves Fleming at LIST.

2.4.3 Ellipsometry

Ellipsometry is a non-destructive technique used to determine the optical properties of thin films. This technique relies on the change of polarization of light upon reflection or transmission at an interface. As a result of the interaction between the sample and the light, the polarization state of the reflected beam will be altered compared to its initial state, as seen in Figure 2-21a.

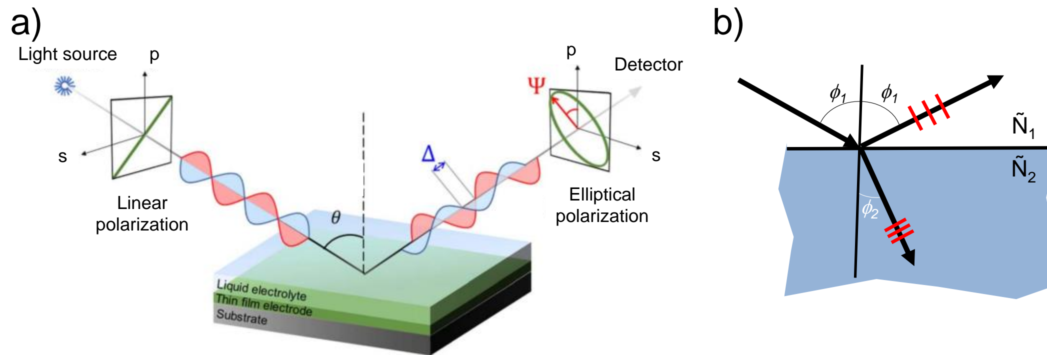

Figure 2-21 – a) Ellipsometry measurement demonstrates the use of linearly polarized light directed at the sample with both p- and s-components of polarization. As the light interacts with the sample, the reflected p- and s-polarizations exhibit varying amplitudes (Ψ, degrees) and phases (Δ, degrees), resulting in the generation of elliptically polarized light.[246] b) An incident light beam interacting with the interface separating air and a material characterized by a complex refractive index $\tilde{N}_2$. Adapted from [247]

When dealing with polarized light, the electric field can be split into two components, parallel and perpendicular to the plane of propagation, known as *p* and *s* polarization, respectively. Once the beam enters the second medium from the first, the reflection coefficients for p-waves and s-waves according to Fresnel are given by:[247]

$$r_s = \frac{\tilde{N}_2 \cos\phi_1 - \tilde{N}_1 \cos\phi_2}{\tilde{N}_2 \cos\phi_1 + \tilde{N}_1 \cos\phi_2} \quad \text{(Eq. 2-17)}$$

$$r_p = \frac{\tilde{N}_1 \cos\phi_1 - \tilde{N}_2 \cos\phi_2}{\tilde{N}_1 \cos\phi_1 + \tilde{N}_2 \cos\phi_2} \quad \text{(Eq. 2-18)}$$

Where $\tilde{N}_1$ and $\tilde{N}_2$ are the complex refractive indices from the first and second medium, respectively, see Figure 2-21b. The complex refractive index, $\tilde{N}$, is composed of both real and imaginary part, $\tilde{N} = n \pm ik$ (Eq. 2-19) being *n* the

refractive index, *k* the extinction coefficient and *i* the imaginary number. ϕ_1 and ϕ_2 represents the angles of incidence and refraction, the latter can be obtained using the Snell-Descartes equation. [247]

The change in polarization of the light is described using the ellipsometric parameters, Ψ (psi) and Δ (delta). Ψ is the amplitude ratio of the reflected or transmitted *p-polarized* light to the *s-polarized* light, while Δ is the phase difference between the two polarizations. These parameters are derived from these reflections' coefficients using the following equation:

$$-\frac{r_p}{r_s} = \tan(\psi)e^{i\Delta} \quad \text{(Eq. 2-20)}$$

Once a sample is measured, a model is developed to obtain the properties of the film. This model utilizes Fresnel's equations to calculate the expected response, incorporating the sample's thickness and optical constants. In cases where these values are unknown, initial estimates are used for preliminary calculations. The calculated values are then compared to the experimental data to assess the model's accuracy.

In this Thesis, the refractive index and the thickness of the films were measured using an Alpha-SE Ellipsometer from J.A. Woollam. The measurements were performed using angles of incidence of 75˚, 70˚ and 65˚ in reflection. The optical data was modelled and fitted using CompleteEASE software and taken at 632.8 nm. The model consisted in a three-tiered layer composed by the silicon substrate, followed by Al_2O_3 described by an absorbing film (B-Spline), and finally an effective medium approximation (EMA) to simulate the roughness of the film.

2.4.4 Stylus profilometry

Stylus profilometry is a widely used characterization method ideal for measuring the thickness of the film (height difference between the top of the film and substrate), and assessing the topography and roughness of the surface. In addition, the residual stress of the film can be measured, which is a critical factor to evaluate the stability of the coating and its adhesion to the substrate. This method involves measuring the vertical movement of the stylus as it is moved horizontally (scanned) across the sample surface.

Most films tend to generate a persistent state of stress caused by various factors including thermal stress (σ_{th}), intrinsic stress (σ_{int}), and extrinsic stress (σ_{ext}). The total stress is a sum of all these contributions.

$$\sigma_{total} = \sigma_{ext} + \sigma_{th} + \sigma_{int} \quad \text{(Eq. 2-21)}$$

Thermal stress occurs when a coating experiences a thermal gradient, resulting from a disparity in the thermal expansion coefficients between the substrate and the film material. The presence of intrinsic stress in thin films can be attributed to the microstructure of the coating, which is in turn influenced by the bonding between the substrate and the film.[248] There are misfit stresses arising from lattice mismatch, and impurities can cause contraction or expansion effects through the occurrence of point defects. Additionally, the stress can be influenced by factors such as the bombardment of working and reactive gases during the growth of the film, as well as the deposition process itself. Finally, extrinsic stress is due to external loading.[248]

Thermal and intrinsic stresses are a phenomenon that occur due to film deposition, which causes a substrate to bend and alter its original shape. If the film tends to contract parallel to its surface, then it results in tensile stress (Figure 2-22b), whereas expansion parallel to the surface causes compressive stress (Figure 2-22a). The magnitude and sign of this stress depend on various factors, including deposition rate, particle energy, film thickness, and the chemical and physical properties of the material incorporated.[249]

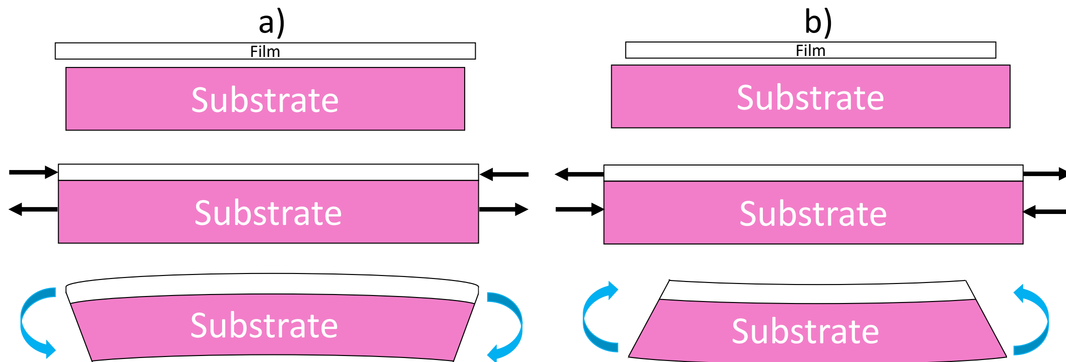

Figure 2-22–- Schematic of the residual stress present in thin films and how it affects the curvature of the substrate. When a film has a propensity to expand, it leads to the development of compressive stress (shown as (a)), while a film that has a tendency to shrink generates tensile stress (shown as (b)). Adapted from [250].

The amount of bending or deflection can be evaluated by determining the change in the substrate's curvature radius. The cantilever beam method, developed by G. Gerald Stoney, can then be utilized to estimate the residual stress (σ) by the following equation: [251]

$$\sigma = \frac{1}{6} \frac{E}{(1-\upsilon)} \frac{t_S^2}{t_f} \left[\frac{1}{R_F} - \frac{1}{R_S} \right] \quad \text{(Eq. 2-22)}$$

In the equation, t_s and t_f represent the thickness of the wafer and film, respectively. R_s and R_F denote the radius of curvature of the sample previous and after deposition, respectively. Lastly, E and υ stand for the Young's Modulus (130 GPa) and the Poisson's ratio (0.28) of the silicon substrate. [252][253]

In the present work, the residual stress in the films was quantified by evaluating the radius of curvature of the samples with a KLA Tencor P-17 benchtop stylus profiler system equipped with a diamond stylus operating at 20 μm/s scan speed, a 200 Hz sampling rate, and with an applied force of 2 mg. The scan length was 1 cm, and each sample was measured four times. Stoney's equation was utilized to calculate the surface stress created by the coating.

2.4.5 Atomic force microscopy

Atomic force microscopy (AFM) is a technique of surface analysis used to obtain images of micro/nanostructured films with resolutions on the order of fractions of nanometres. The basic working principle of AFM relies on a flexible cantilever with an integrated sharp tip (radius of around 10 to 50 nm) that scans the surface by means of a xyz scanner. Figure 2-23 shows a schematic with a representation of a typical AFM.

AFM is based on interacting forces between the sample and the tip influencing the bending of the cantilever. Such forces can be mechanical (due to contact), magnetic, electrostatic, Van der Waals, etc. The bending of the cantilever results in the displacement (or deflection) of the reflected laser beam position on the photo-detector with respect to its equilibrium position. The cantilever deflects downward and upward by net repulsive and attractive forces, respectively. The back reflected light is directed to a four-quadrant photodiode, which measures the cantilever deflection.

Tapping mode or AM mode is typically used for topography. This mode reduces the wear and damage of the tip. Since the tip contacts the sample during part of the cantilever oscillation cycle it enables high resolution and fast scanning. In the last years, there was a great development in the AFM field with the introduction of the bimodal amplitude modulation-frequency modulation (AM-FM). The AM-FM provides knowledge about viscoelastic information, and elastic information such contact stiffness and Young’s and storage modulus.[254][255]

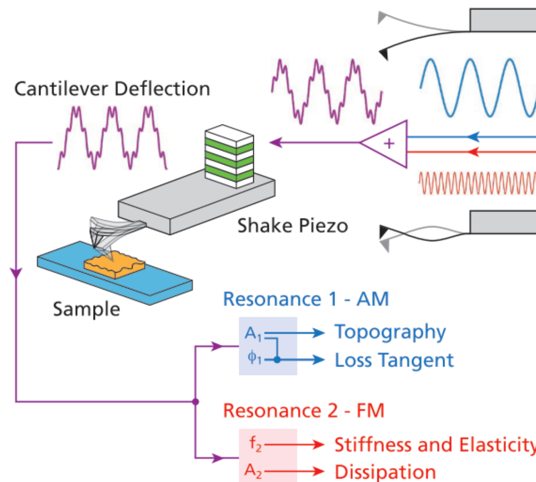

Figure 2-23 – Schematic of control in AM-FM Mode. Adapted from Hurley et al. [256].

In order to excite two cantilever resonances simultaneously, two distinct excitation signals represented by blue and red curves on the right are combined (Figure 2-23). The resulting cantilever deflection is depicted by the purple curve on the left and analysed to ascertain the response at each resonance. One of the resonances, Resonance 1, operates in normal tapping or AM mode as indicated by the blue box. The vertical feedback loop for standard tapping mode topography is controlled by the amplitude A_1. Additionally, the values for loss tangent are given by A_1 and the phase φ_1. Resonance 2 operates in FM mode denoted by the red box. Changes in resonance frequency determine elasticity and stiffness, while changes in the amplitude A_2 provide information about viscous or dissipation. [256]

Before the tip of the cantilever interacts with the sample, the first eigenmode of the cantilever is excited at or near its resonant frequency f_1 with a large amplitude (usually about $A_{1,free} \approx 100$ nm). Meanwhile, the second or higher eigenmode is excited near its resonant frequency f_2, but with a significantly smaller frequency. The first and second eigenmodes have different spring constants k_1 and k_2, and quality factors Q_1 and Q_2, respectively. As the cantilever approaches the sample, the deflection signal of the cantilever is measured and analysed by a lock-in amplifier. This analysis allows for the determination of the amplitude A_1 and ϕ_1 response of the first eigenmode, which is used to calculate the effective storage modulus of the interaction (E_{eff}) and the tip radius (r), which is calculated using the following equation: [257]

$$E_{eff} = \frac{\pi}{R}\sqrt{\frac{1}{6}}\left(\frac{k_1}{Q_1}\frac{A_{1,free}}{A_{1,set}}\cos\phi_1\right)^{-1/2}\left(\frac{2k_2\Delta f_2}{f_2}\right)^{3/2} \quad \text{(Eq. 2-23)}$$

During the measurements, the geometry of silicon AFM tip changes when used and tends to affect the measurement accuracy. In our case, this change is mostly caused by the alumina film that has a high stiffness. Since the tip was not calibrated, the values of the modulus varied with time and they were not fully reliable.

The AM-FM mode of the MFP-3D Infinity AFM from Asylum Research was utilized to obtain images of the nanomechanical and topography characteristics of the Al_2O_3 films coated with Au NPs. The measurements were performed under standard ambient conditions (at RT and relative humidity of approximately 50%) using a standard cantilever holder for air operation. 200x200 nm² and 50x50 nm² regions were imaged with a 256x256 pixel resolution at a scan rate of 3 Hz. The tip radius was calibrated (in the beginning and middle of the measurement for a set of samples) to achieve a value of 72.9 GPa for the Fused Silica reference, which corresponds to the deformation applied to the sample. To maintain repulsive intermittent contact mode, the amplitude setpoint was set to $A_{setpoint}/A_0$ ~ 0.7, ensuring the phase remained below 90°. The measurement of films was performed by João Paulo Cosas Fernandes at LIST. The software WSxM was used to plot 3D images and equalization.[258]

Height-Height correlation function

The AFM images have been analysed under the framework of the so-called *dynamic scaling theory*. Basically, the underlying idea is that the characteristics of a surface are constant regardless space dimension and deposition time if proper scaling factors are included. In other words, they would show *invariance under a change of scale*, which is a characteristic of *fractals*. Therefore, a surface is said to exhibit *self-similar scaling* if the scale factors in the horizontal (i.e. *x* or *y*) and vertical (*z*) directions are equal. In contrast, the surface is called *self-affine* if the scale factors are different in the vertical and horizontal directions. In addition, the surface is called *isotropic* if the statistical behaviour of a surface

does not depend on the direction in the surface (i.e., is the same in *x* than in *y*). If this is not the case, the surface is *anisotropic*, which can be the situation in case of e.g., the use of a beam bombardment on the surface.[259]

The surface morphology of the coatings was analysed with the height-height correlation function (HHCF, $H(r,t)$) in order to estimate the growth parameters of the deposits: roughness (w), correlation length (ξ) and Hurst parameter (α). This function represents the average height difference squared between any pair of points, separated by a distance r over an entire AFM micrograph:[260,261]

$$H(r,t) = \langle |h(r+r',t) - h(r',t)|^2 \rangle \quad \text{(Eq. 2-24)}$$

Where $h(r,t)$ is the surface height at a point r and time t. The calculation if the HHCF from the AFM images was performed with Gwyddion software. For a self-affine isotropic surface, it has been observed that the HHCF behaves differently in two distinct regions.[262] First, for small values of r, we obtain the following equation,

$$H(r < \xi) = 2w^2 \left(\frac{r}{\xi}\right)^{2\alpha} \quad \text{(Eq. 2-25)}$$

The Hurst parameter, also called roughness exponent, is directly related to the fractal dimension of the surface, as $D = 3 - \alpha \ (0 < \alpha < 1)$.

Second, for large values of r,

$$H(r \gg \xi) = 2w^2 \quad \text{(Eq. 2-26)}$$

Several analytic forms for HHCF have been proposed that satisfy the requirements for a self-affine surface and they are given in the previous two equations.[262] For an isotropic self-affine surface, the so-called K-correlation model and the functional form proposed by Sinha et al. [263] can be used. In this Thesis, because of its simplicity, we focus on the Sinha functional form:

$$H(r) = 2w^2 \left[1 - exp\left[-\left(\frac{r}{\xi}\right)^{2\alpha}\right]\right] \quad \text{(Eq. 2-27)}$$

The two regimes of the HHCF can be observed in Figure 2-24: the first region behaves following the power law ($r \ll \xi$), and the second as a constant ($r \gg \xi$).

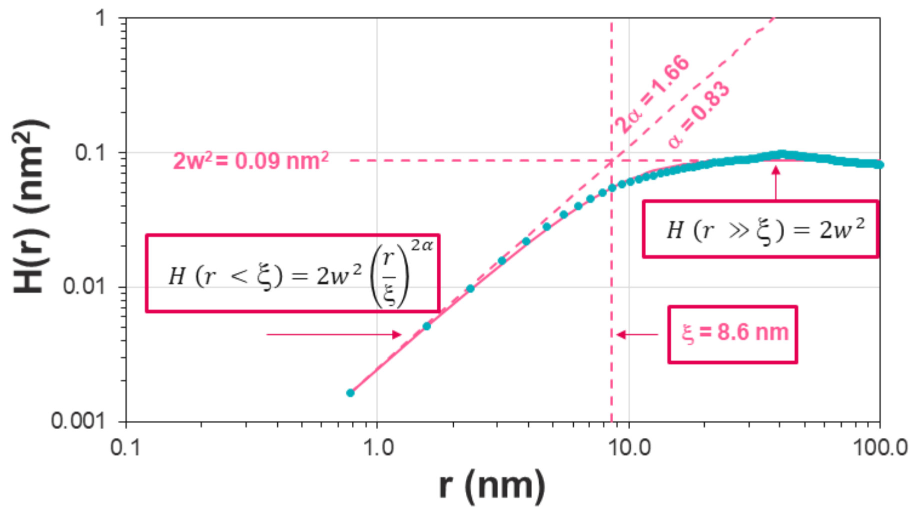

Figure 2-24 – Experimental fitting of the HHCF using Eq. 2-27, and physical meaning of the of the fitting parameters.

For similar values of *w*, a small value for the Hurst parameter ($\alpha \approx 0$) implies a locally rougher surface, while a higher value ($\alpha \approx 1$) is correlated with a smoother surface as seen in the following Figure 2-25a. The correlation length, ξ, is the limit between both regimes, and it represents the lateral distance within the surface heights of any two points that are correlated, also known as the feature size (see Figure 2-25b).

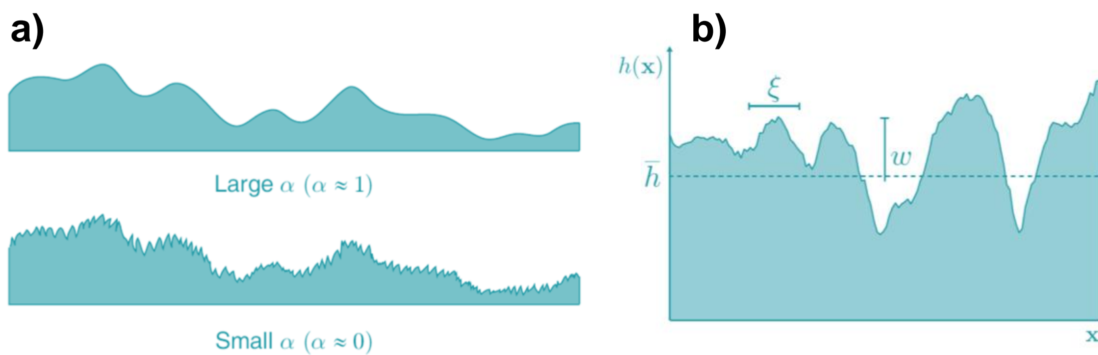

Figure 2-25 – Interpretation of the parameters obtained from the fitting of the HHCF. a) Comparison between the local surface morphology for surface with similar *w* but different α. b) Schematic of a rough surface with the mean heigh ($\bar{h}$), correlation length (ξ) and roughness (w). Adapted from [262].

These parameters (w, ξ and α) are obtained from the fitting of experimental HHCF curves to Eq. 2-27, as illustrated in Figure 2-26.

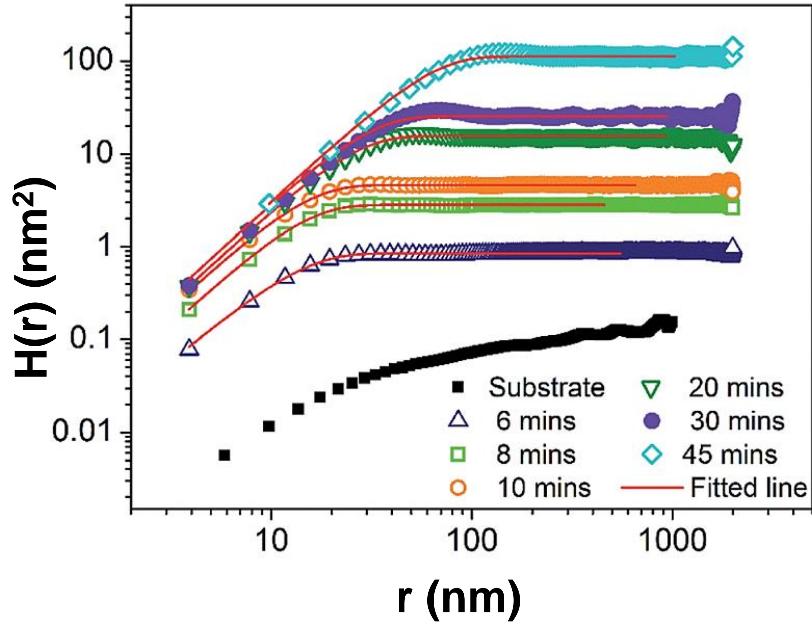

Figure 2-26 - log-log plot of HHCF, H(r,t) as a function of distance r for Cu thin films on glass substrate at different deposition times (0-45 minutes). Adapted from [260].

Combined, the three roughness parameters *w*, ξ, and α completely characterize a self-affine surface. They are independent, and they vary according to the process by which a surface is formed. It is common to observe a power-law behaviour for roughness with deposition time:

$$w(t) \sim t^{\beta} \quad \text{(Eq. 2-28)}$$

Where β is the so-called *growth exponent*. An equivalent correlation can be found for the correlation length:

$$\xi(t) \sim t^{1/z} \quad \text{(Eq. 2-29)}$$

Where *z* is referred to as the *dynamic exponent*. Self-affine surfaces under dynamic scaling show the following relationship between the different exponents:

$$z = \frac{\alpha}{\beta} \quad \text{(Eq. 2-30)}$$

This condition is called *stationary growth*. However, this theoretical relation is not generally observed experimentally. For instance, the roughness parameter α may vary with time, which leads also to the of local slope. In this case, the growth is called *non-stationary*. Some of the deviations from the theory are coming from

the so-called non-local effects. Thus, scaling arguments work well when the important growth effects in a deposition are "local", or only affect nearby surface heights. A typical example of that is atom diffusion to nearby locations, which depend on deposition conditions such as activation energy and temperature. In contrast, non-local effects are of much longer range than local effects. For instance, *shadowing* is a non-local process because it depends on the heights of all other surface features, not just those close. Another non-local effect is *re-emission*, which takes place when the sticking coefficient of species to the surface is lower than 1. In addition, other processes take place during the deposition of a film which can influence its growth (see Section 2.2).

2.4.6 Scanning electron microscopy

Scanning electron microscopy (SEM) is a popular technique that obtain images of the sample's surface or substrate-film interface by scanning it with a beam of highly energetic electrons produced by a cathode (electron probe) in a raster scan pattern. The electrons in the beam are accelerated towards the sample, where they collide with the atoms and molecules of the surface. When an electron beam strikes and passes through a sample, it is deflected by the specimen in either elastic scattering or inelastic scattering mode.[264] These collisions result in the emission of secondary electrons (SEs), backscattered electrons (BSEs), Auger electrons, and X-rays. The emission of SEs is mainly originated from the outmost layers of the sample, and therefore it provides information regarding the sample morphology and topography, while BSEs highlight differences in the atomic weight of the atoms present in the samples.[265]

Images of the cross-section of our films were obtained using a Hitachi SU-70 Field-Emission Scanning Electron Microscope (FE-SEM), operating at 15 kV. In order to reduce the charging effect, the alumina samples were connected with carbon and copper tape.

2.4.7 Transmission electron microscopy

Transmission electron microscopy (TEM) is a powerful imaging technique that uses a beam of electrons to examine the internal structure, at the atomic level at a very high resolution (higher than SEM). TEM is based on the acceleration of the electron with a higher voltage source (80-300 kV) under vacuum through a thin film (thickness < 100 nm) and forms an image (diffraction) from the transmitted electrons from the sample.

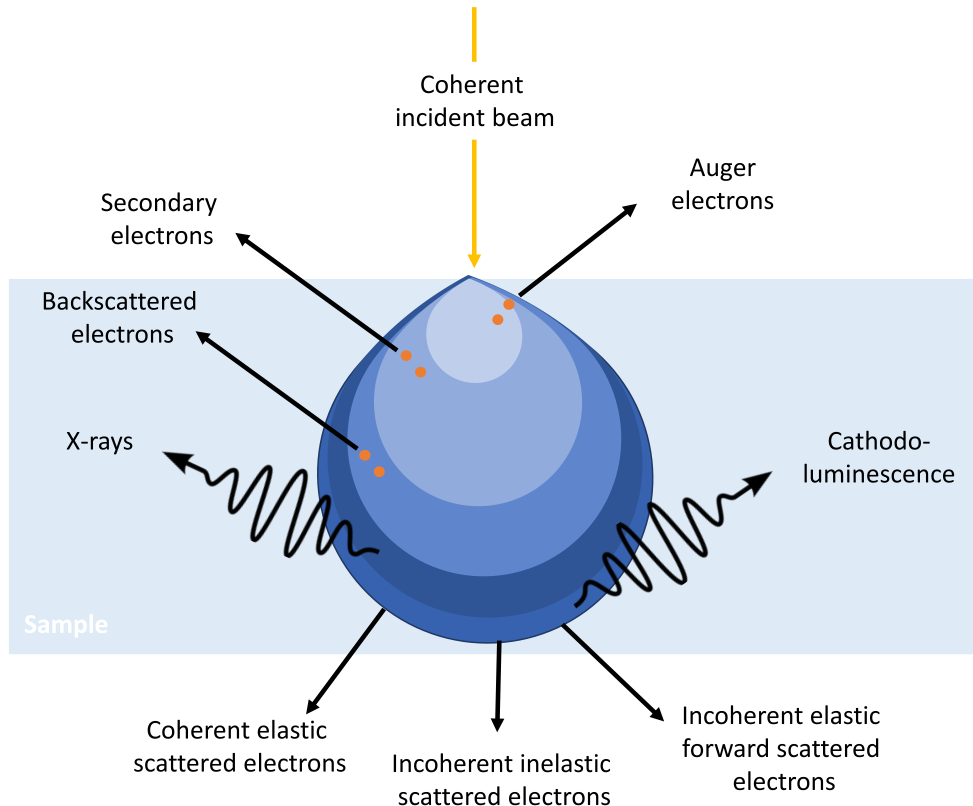

Figure 2-27 – Schematic of the interaction of the electrons with a sample.

When a specimen is struck by a beam, various possibilities can occur, see Figure 2-27. Some of the electrons collide with the atoms of the specimen and return in the opposite direction, resulting in what is known as *backscattered electrons*. These electrons can be detected and utilized to create an SEM image of the sample surface, which can offer insights into the material's composition and topography. Additionally, *secondary electrons* are those electrons that are produced when an incident electron excites an electron in the sample. When an electron leaves the atom, it creates a hole in the atom structure, and it is then filled by electrons from higher energy levels. This process can cause an excess

of energy in the atom, which is compensated by either the separation of an electron from the outer layer of the atom (*Auger electron*) and/or the emission of X-rays from the atom. The electrons that pass through the specimen (due to the small thickness) are the ones that are mostly used in TEM (*transmitted electrons*). These electrons can suffer deviations (variation on the outer angle), have different phase (incoherent elastic) and they can lose energy (incoherent inelastic).

The column of the microscope comprises a sequence of electromagnetic lenses and apertures which aim to concentrate the electron beam onto the specimen and magnify the TEM image onto the display screen or detectors. Nowadays, contemporary TEMs come with electronic sensors such as CCD detectors, alongside a retractable fluorescent viewing screen, to capture TEM images in a digital form.[266]

Bright field (BF-TEM) images are formed by the unscattered electrons (transmitted electrons) that have passed through the sample. The regions of the sample that absorb or scatter fewer electrons appear darker, while those that absorb or scatter more electrons appear brighter. Bright field images provide information about the overall structure and composition of the sample. On the other hand, dark field images are formed by the electrons that have been scattered by the sample. In dark field imaging, a small aperture is placed in the imaging plane that blocks the directly transmitted electrons. This allows only the scattered electrons to form the image, which appear as bright spots against a dark background. Dark field images provide information about the structural features of the sample that scatter electrons, such as defects, dislocations, or grains in crystalline materials. Also, high-resolution (HR-TEM) images reveal details of the atomic structure. It can be created by using both transmitted and diffracted electron beams to create an interference image and requires smaller sample thickness (<50 nm or even <10 nm).[267] Additionally, selected-area electron diffraction (SAED) is formed by the scattered electrons that meet the criteria of Bragg's condition. Then, they are used to form a diffraction pattern that

can be utilized to ascertain the lattice parameters, the crystal structure and orientation.

TEM observations in BF, HR and SAED modes were employed for the characterization of Al_2O_3 and the multilayer of Au-Al_2O_3. Cross-sections of the Al_2O_3 thin films deposited on silicon substrates were prepared following the conventional procedure of mechanical polishing followed by argon ion milling to electron transparency. Microstructural information was obtained using a LaB_6 microscope, JEO 2100 plus, operating at 200 kV. Additionally, the multilayers were carried out using a JEM - ARM 200F Cold FEG TEM/STEM operating at 200 kV and equipped with a spherical aberration (Cs) probe and image correctors (point resolution 0.12 nm in TEM mode and 0.078 nm in STEM mode). The measurements were performed by Cristina Rojas and Sylvie Migot at Instituto de Ciencia de Materiales de Sevilla and Institute Jean Lamour, respectively.

2.4.8 Electron energy loss spectroscopy

Electron energy loss spectroscopy (EELS) is a spectroscopic method that involves measuring the inelastic energy loss of the transmitted electrons by a specimen when interacts with an electron beam. EELS data consists of the energy loss spectral information from the specimen, and it can be divided into three regions, see Figure 2-28:

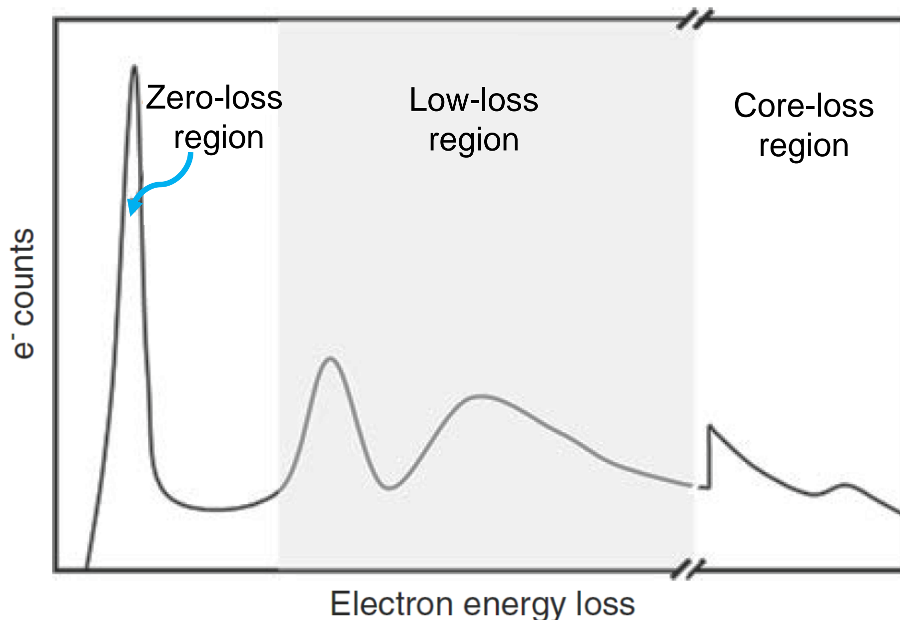

Figure 2-28 - Schematic diagram of electron energy loss spectrum showing typical regions of different energy losses. Adapted from [267].

1. Zero-loss peak: it is the most intense peak and occurs at 0 eV in the spectrum. This corresponds to the electrons that have no or negligible energy loss when passing through the sample.
2. Low-loss region: is located between 0-50 eV. It represents the energy that is lost by the electrons though excitation of valence electrons. There is also a broad peak, which represents the collective oscillations of free electrons also known as *plasmons*. Additionally, other peaks are observed in this area that corresponds to interband transitions.
3. Core-loss region: situated typically from 100 eV. Here the incident electron excites the inner-shell electrons (*core electrons*) to higher energy levels (unoccupied state above the Fermi level).

When an inner electron receives sufficient energy, it becomes excited but does not have enough energy to escape into the vacuum. As a result, the electron jumps to an empty level located above the Fermi level. However, the electron is not equally likely to occupy any of the available empty states, as the number of states with a particular energy level is greater than others. Therefore, the shape of the ionization edge is directly influenced by the distribution of energy levels available to the electron, which is described by the density of states (DOS), see Figure 2-29.[206] Two zones can be distinguished in an absorption edge: the energy loss near edge structure (ELNES) within ca. 50 eV of the edge onset which are due to bonding effects, and the extended energy loss fine structure (EXELFS) above some 100 eV the edge onset due to diffraction effects from the atoms surrounding the ionized atom. [267,268] ELNES can be used to identify phases like a fingerprint.

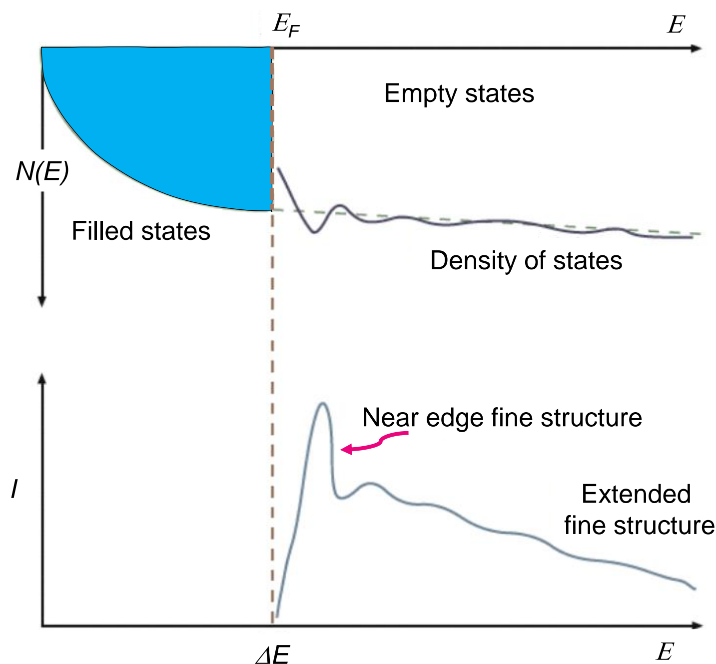

Figure 2-29 - Relationship between the DOS and the ELNES intensity in the ionization edge fine structure (Adapted from William and Carter et al. [267]).

The EELS spectra were recorded in TEM diffraction mode, with a spectrometer collection angle of 1.02 mrad and with low doses to minimize the damage produced to the sample. Under these conditions, the energy resolution of the couple microscope/spectrometer system was ~1 eV. After experimental acquisition, the data were processed using the Gatan Digital Micrograph

software. The measurements were made by Cristina Rojas at Instituto de Ciencia de Materiales de Sevilla.

2.4.9 X-ray photoelectron spectroscopy and method of Tougaard

X-Ray photoelectron spectroscopy (XPS) is a surface-sensitive analytical technique used to study the atomic composition, chemical bonding, electronic structure, and band structure of a sample. It provides information about the surface of a material by measuring the energies of photoelectrons emitted when a material is bombarded with X-rays. Additionally, the binding energy (BE) of a core-electron is a distinctive feature for elements in a specific chemical environment (chemical shift).

In XPS, an ejection of a core-electron from a sample takes place when an x-ray photon (with energy hv) is absorbed by an electron of the sample with a lower binding energy (BE, the energy retaining the electron to the nucleus), leading to a phenomenon called *photoionization*. As a result of this absorption, the core-electron will experience excitation to either a bound state (chemical bounds) or the continuum, where it will become a free particle. Then, the core-hole undergoes decay through either non-radiative or radiative processes such as emission of Auger electrons or fluorescence. In one scenario, the core hole is filled by an electron from an outer shell, and the surplus of energy is then transferred to another outer shell electron, causing its emission. This phenomenon is referred to as Auger decay. Alternatively, the core hole is filled by an electron from an outer shell, resulting in the simultaneous emission of a photon with energy equal to the difference in BE of the two levels involved in the electron transition. This is the well-known X-ray fluorescence.

When the energy of the photon is higher than the BE of the electron with the nucleus, this will lead to a surplus of energy of the emitted electron which is going to be converted in kinetic energy (E_k). The relation between the binding energy and the kinetic energy is given by the following equation (excluding the work functions of the sample and the detector):

$$BE = h\nu - E_K \quad \text{(Eq. 2-31)}$$

Conductors (such as metals) during the photoionization process, create a core-hole leaving a positive charge in the atom. However, the positive charge is rapidly neutralized as electrons from the surrounding covalent band transition into the core level, filling the vacant electronic state making the atom more stable. In contrast, in a case of an insulator sample (such as alumina) challenges arise in the ability of the sample to neutralise the positive charge created within the lifetime of the core-hole. Since there isn't a perfect electrical contact between the sample and the holder due to the presence of an insulator in between, the electrons will have difficulty to fill the core-hole left in the atoms and the surface of the sample charges. As a consequence, slightly lower kinetic energy is obtained, which in turn shifts the binding energy peak for higher energies.

In the literature, it was found that Au particles with sizes between 1.4 nm (clusters containing 55 gold atoms) [269] and 1.2 nm (cluster containing 33 gold atoms) [270] lead to a transition from a metallic state ("bulk-like") to an insulating molecular state, respectively. In our XPS results, the gold nanoparticles behave as bulk materials.

The Kratos Axis Ultra DLD system was used to conduct measurements on Au-Al_2O_3 samples. The surface sample was irradiated with a monochromatic Al K_α X-ray source (hv = 1486.7 eV) operating at a power of 150 W, with an analysis area of 700 µm x 300 µm. The measurements were performed by Jérôme Guillot at LIST. XPS analysis focuses on a depth of just a few nanometres. This small depth allows for a high level of sensitivity to the surface condition of the sample being studied. In fact, the technique is so sensitive that it can detect changes at the atomic level, expressed as atomic percentage.

QUASES-Analyze software was used to evaluate the characteristics of Au clusters on Al_2O_3 coatings (height and coverage). To do so, the shape of the XPS inelastic peak was analysed to study the growth of Au clusters on Al_2O_3 coatings using the method proposed by Tougaard.[271–273] A more detailed information is presented on the next section about this approach.

Method of Tougaard to analyze the shapes of the XPS peaks

The inelastic background in the energy distribution of emitted electrons depends strongly on the depth concentration profile. To illustrate this, Tougaard et al. [274] studied four distinct arrangements of copper (Cu) within gold (Au) and showed that the main difference among the shapes of the spectra was not found in the peaks, but in the backgrounds, see Figure 2-30.

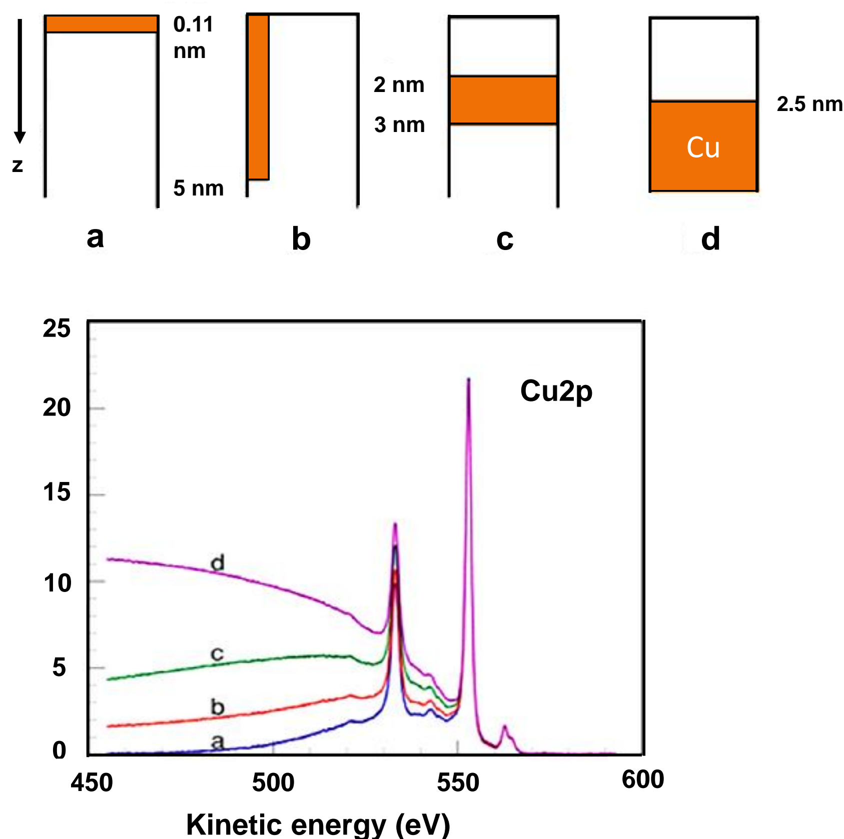

Figure 2-30 - Cu2p spectra from Cu atoms with different concentration distributions in an Au matrix. Adapted from [274].

The electrons in the four scenarios have covered distinct distances within the solid before exiting its surface, leading to variations in their energy distribution. When all copper (Cu) atoms are concentrated in a thin surface layer (as in situation a), only a small number of electrons lose energy, resulting in a high peak intensity and a low background. On the other hand, in situation d), where all Cu atoms are located at greater depths, most electrons lose energy and deviate from the peak energy, contributing to a background signal at lower energies.

Consequently, the background of electrons scattered inelastically exhibits significant fluctuations as is correlated with the height of the layer.[274]

The measured XPS spectrum $J(E,\Omega)$ is a function of the intrinsic distribution of the spectrum of a single atom $F(E,\Omega)$, the number of atoms per Å at depth z (c(z)), and the differential inelastic scattering cross section (K(T) the probability that an electron shall lose energy T per unit energy loss and per unit path length. In these expressions, *E* represents the kinetic energy of the electron, and Ω is the solid angle of the emission. For a reference sample where its depth distribution is known, the emission spectrum of a single atom $F(E,\Omega)$ can be calculated using the equation (Eq. 2-32). With the same equation, this spectrum is then used, for a quantitative analysis, to determine the spatial distribution of the same element but in a sample of unknown in-depth concentration profile. The signal attenuation is estimated from the inelastic scattering cross section, K(T) and the inelastic electron mean free path (IMFP) given/calculated by the TPP-2 M (Tanuma, Powell, Penn 2 Method) formula.[275,276]

$$F(E,\Omega) = \frac{1}{P_1}\left[J(E,\Omega) - \frac{1}{2\pi}\int dE' J(E',\Omega)\int ds e^{-is\,(E-E')}\left(1-\frac{P_1}{P(s)}\right)\right] \quad \text{(Eq. 2-32)}$$

Where,

$$P(s) = \int c(z) e^{\left(\frac{-z}{cos\theta}\right)\Sigma(s)}\, dz \quad \text{(Eq. 2-33)}$$

with

$$P_1 = \int_0^{\infty} c(z) e^{\frac{-z}{IMFP.\cos\theta}}\, dz \quad \text{(Eq. 2-34)}$$

Where T=(E-E') is the energy loss, c(z) is the number of atoms per unit volume at depth z, θ is the angle between surface normal and the detector, *z/cosθ* is the travelled distance, s is an integration variable without physical significance, $\Sigma(s)$ and P(s) are the Fourier transform of energy distribution functions. They are introduced solely for mathematical convenience and have no direct physical significance. The following expression for the cross-section K(T) was used,

$$IMFP \times K(T) = \frac{BT}{(C+T^2)^2} \quad \text{(Eq. 2-35)}$$

With C= 1643 ev^2 and B ≅ 3000 eV^2. [271]

The approach employed for the analysis of data is summarized in Figure 2-31 with the respective equations. In this Thesis, a bulk Au reference (Au foil) was included as a reference which was measured together with each group of samples. The experimental spectrum of the foil J(E), was first used to determine the spectrum (F(E)) emitted by a single atom, considering that the concentration profile c(z) is known for a bulk sample. A correct fit is obtained when $F(E) \approx 0$ after the background removal for a wide energy interval 50-150 eV on the low kinetic energy side of the peak.[277] To accomplish this, it is necessary to have the IMPF and K(T) as inputs. F(E) represents the single Au atom, and it should remain consistent between the reference (foil) and the sample. Therefore, it becomes possible to determine the concentration profile with depth (c(z)) for the sample, since the experimental spectrum J(E) of the sample had already been measured. To do so, the background of the spectrum is calculated in order to obtain F(E) from J(E). The background is calculated assuming a certain geometry of the Au islands. In our case, the simplest geometry was selected, which is defined as a rectangular island characterized by height (h) and coverage (c). Thus, the vertical and horizontal characteristics of islands can be described in terms of their height and coverage, respectively. It is worth noting that the coverage affects only the intensity of the spectra, while the height of the island influences not only the intensity of the peak, but also the distribution of energy in the background (i.e. the shape of the peak).

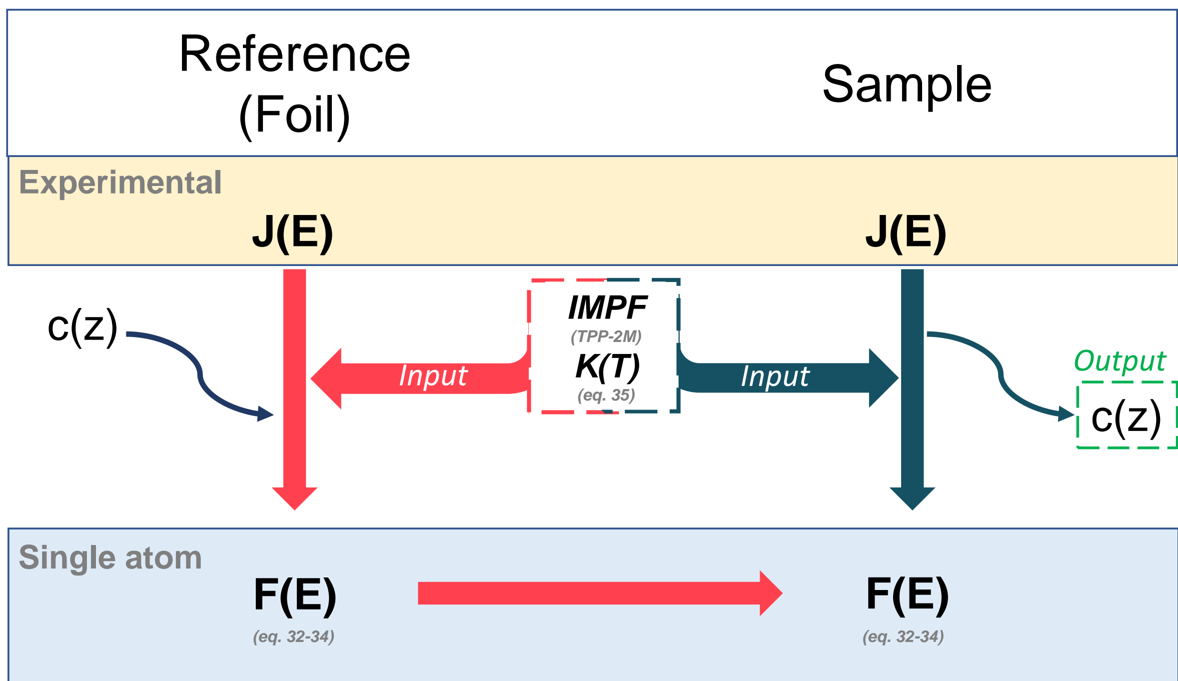

Figure 2-31 - Process for the determination of the height and coverage of the islands from XPS spectra using Tougaard method. The important equations are included.

The Au 4f peaks overlap with the Al 2p and Al 2s peaks and the associated background, making the analysis unreliable. Therefore, the Au 4d peaks were selected for the analysis. A buried-layer profile was selected for the determination of the clusters height and coverage, which lead to more efficient description of the initial steps of gold nanoparticle growth on alumina.

2.4.10 Time-of-Flight Secondary Ion Mass Spectrometry

ToF-SIMS stands out as a limited number of methods capable of precisely identifying individual compounds present on a surface. The fundamental principle behind ToF-SIMS is relatively straightforward: when a surface is bombarded with a primary ion beam, typically a beam of high-energy ions such as Cs^+, it induces the ejection of secondary ions, which can be analysed based on the time taken for them to fly from the sample to the detector by a time-of-flight mass analyser. The analyser measures the flight times of the secondary ions to determine their mass-to-charge ratios (m/z). According to classical physics principles, under a constant acceleration voltage, ions with lower m/z values will exhibit the highest velocities and reach the detector first, whereas ions with larger m/z values will travel at slower speeds and arrive at the detector later. The principal equation for the calculation of the mass/charge ratio from the time of flight is the following:

$$\frac{m}{z} = \left(\frac{2eV_s}{L^2}\right) t^2 \quad \text{(Eq. 2-36)}$$

Where m and z are the mass and the electric charge of the secondary ion, respectively. t is the time of flight, V_s the acceleration voltage (constant), L the flight distance and e the elementary charge.

This information allows the identification of the different chemical species present on the surface. By scanning the primary ion beam across the sample surface and analysing the emitted secondary ions at each point, ToF-SIMS can create detailed chemical maps of the sample's surface. In this Thesis, the measurements were done by SC-Ultra, with an impact energy of 1 keV, the primary beam intensity was 1 nA in a scanned area of 250×250 μm^2. The MCs_x^+ mode (M: element of interest, x = 1 or 2) was used with low mass resolution (400). The measurements were performed by Nathalie Valle at LIST.

2.4.11 Raman spectroscopy

Raman spectroscopy is a non-destructive technique for chemical analysis. It is based on the inelastic scattering of photons that occurs when a sample is irradiated by a monochromatic light with known frequency. Raman spectroscopy is a subfield within vibrational spectroscopy that enables a sensitive structural identification of small concentrations of chemicals. This is possible due to the different functional groups, which have distinctive vibrational energies, also known as molecular fingerprints.[278] This technique involves measuring the shift in frequency of scattered light from a sample. This shift occurs when an incident photon strikes a molecule, resulting in the production of a scattered photon. The scattered light can either have a higher or lower frequency corresponding to anti-Stokes and Stokes Raman scattering, respectively.[279] In the case where a molecule transitions from a ground state to a virtual state and then returns to a higher energy vibrational state, the scattered photon possesses less energy than the incident photon, resulting in a longer wavelength. This phenomenon is known as Stokes scattering. On the contrary, if the molecule is already in a vibrational state and transitions to its ground state after scattering, the scattered photon has more energy, which causes a shorter wavelength. This process is known as anti-Stokes scattering, which is the last common transition to take place, as it demands the molecule to be in a vibrationally excited state before the photon is incident upon it.[280] Nevertheless, Rayleigh scattering is the most frequent type of scattering since it does not require any changes to occur in the vibrational state of the molecule. [280]

The Surface Enhanced Raman Spectroscopy (SERS) effect of Au-Al_2O_3 samples was analysed using a Renishaw inVia micro-Raman spectrometer with a laser beam of 633 nm, power 10 mW, extended (total time) 10 s, grating 1200 and accumulation of 1 scan (i.e. no averaging of several spectra). It was focused on a 1 μm^2 area by a 50× objective lens on the top surface of the film. The measurements were carried out with several aqueous solutions of Rhodamine 6G (R6G) of different concentrations, which was dropped onto the Au-Al_2O_3 SERS substrates. The Raman spectra were measured ranging from 104 to 3200 cm^{-1}. The measurements were performed by Simon Bulou at LIST.

2.4.12 UV-Vis spectroscopy

The optical properties of Au-Al_2O_3 were investigated by ultraviolet-visible (UV-Vis) spectroscopy. The working principle of this method involves the emission of a broad range of wavelengths of light, which then passes through a monochromator to select a specific wavelength of light. The resulting beam passes though the sample, in this case, Au-Al_2O_3 or Au@Al_2O_3 films deposited on a glass substrate. When the beam interacts with the sample it can be absorbed (I_a), reflected (I_r) and the remaining light is transmitted (I_t). The incident light (I_0) can be expressed as the sum of the absorbed, reflected, and transmitted light:

$$I_0 = I_a + I_r + I_t \quad \text{(Eq. 2-37)}$$

Finally, the detector measures the intensity of the light passing through the sample and converts the amount of absorbed light into a spectrum. The Beer-Lambert law, also known as the law of absorption, states that the amount of radiation absorbed by the sample is directly proportional to the thickness of the absorbing layer.[281,282] The absorbance (A) of the coatings was calculated through the relation: $A = -\log T$ (Eq. 2-38) (being the transmittance T between 0 and 1). Therefore, if there is absorption in the region corresponding to the wavelength of the red colour, then the substance will be seen as green/blue because these are their complementary colours.

Optical properties such as transmittance and absorbance of Au-Al_2O_3 on glass were investigated using a Perkin Elmer LAMBDA 1050 UV/vis/NIR Spectrophotometer with a 150 mm InGaAs Integrating Sphere. Transmission and absorbance spectra were acquired in the range from 1500 to 250 nm. A spectrometer was used, which included a combination of tungsten-halogen and Deuterium lamps, as the light source, providing radiation in the visible, near UV and IR regions.

2.5 Localized surface plasmon resonance

The Au nanoparticles deposited on Al_2O_3 show absorbance peaks in the UV-Vis spectrum, due to the phenomenon of Localized Surface Plasmon Resonance (LSPR). Thus, when the electromagnetic field of the light reaches the metal nanoparticle, a part of the incident light is absorbed by moving the conduction electrons towards the NP surface, creating an electron oscillation as depicted in Figure 1-2.

The characteristics of the LSPR (intensity, position, width) depend on the characteristics of the nanoparticles (Au) and the underlying isolator (Al_2O_3). In this section we summarize briefly the origin of the LSPR peak and the influence of few characteristics of the materials.

When the size of metal particles (R) is much smaller than the wavelength of light (R << λ), a quasi-static approximation can be applied to nanoparticles of sizes between 10 to 40 nm.[283] This assumes that the electric field inside the particles is uniform and neglects any changes in phase of the external driving field as it passes through the metal particles. As a result, the conduction electrons inside the particles respond simultaneously and move in phase with each other. When the electrons are restricted within the NP, they gather on one side, resulting in an accumulation of negative charge, while the other side accumulates positive charge, creating an electric dipole. These polarized charges induce restoring forces, which depends on the amount and distribution of the accumulated charges and defines the frequency of the oscillations. By applying boundary conditions at the surface of the nanoparticle, let's assume a spherical shape, one can determine the polarization of the entire sphere resulting from the external field. The internal field E_i can then be calculated accordingly: [284]

$$E_i = E_0 \frac{3\varepsilon_m}{\varepsilon + 2\varepsilon_m} \quad \text{(Eq. 2-39)}$$

Where E_0 is the incident electric field, ε_m the dielectric constant of an embedding medium, and ε is the dielectric constant of the sphere. The dipole moment p induced by the external field can be calculated as $p = \varepsilon_m \alpha E_0$ (Eq. 2-40); the polarizability of a sphere, α, determines how strongly a particle scatters and

absorbs light, and also the degree to which the incident field is enhanced in the vicinity of the particle. The polarizability is defined as:[284,285]

$$\alpha = 4\pi\varepsilon_0 R^3 \frac{\varepsilon_1-\varepsilon_m}{\varepsilon_1+2\varepsilon_m} \quad \text{(Eq. 2-41)}$$

Where *R* is the radius of the nanoparticle and ε_1 is the dielectric constant of the nanoparticle. When a plane wave comes into contact with a NP, it undergoes three processes: partial transmission without deviation, partial absorption, and partial scattering. The total extinction is determined by the sum of the absorption in the NPs and of the scattering by the NPs. One can calculate the rates of energy absorption and scattering by the particle and express them in the form of absorption, scattering, and extinction cross-sections:

$$\sigma_{abs} = k_0\, Im(\alpha) \quad \text{(Eq. 2-42)}$$

$$\sigma_{scat} = \frac{k_0^4}{6\pi} |\alpha|^2 \quad \text{(Eq. 2-43)}$$

$$\sigma_{ext} = \sigma_{scat} + \sigma_{abs} \quad \text{(Eq. 2-44)}$$

Where k_0 is the wavenumber of light in vacuum and Im the imaginary part of the dielectric constant. The imaginary part is correlated with the loss factor (i.e. the energy dissipation of the matter).

The surface plasmon resonance possesses a distinct characteristic in that relies on various factors such as the metal's composition, the size of the nanoparticle, its shape/geometry, and the medium or environment in which it exists.

2.5.1 Effect of Nanoparticle Size

Nanoparticles can be categorized into two groups based on their size. In the case of small NPs (2R < 40 nm), the scattering cross section is minimal, and absorption is the dominant factor in extinction. On the contrary, larger NPs (2R > 40 nm) tend to have a more significant scattering cross section, which becomes increasingly important in the extinction cross section. In other words, as it can be appreciated in Figure 2-32, photon absorption or scattering are the most important phenomenon behind the overall absorbance peak for small and large nanoparticles, respectively (most of the overall extinction cross section is due to the absorbance or scattering cross section in Eq. 2-44). Additionally, a further increase leads to the broadening of the LSPR.[284] This effect between smaller and bigger particles can be also observed in Figure 2-32.

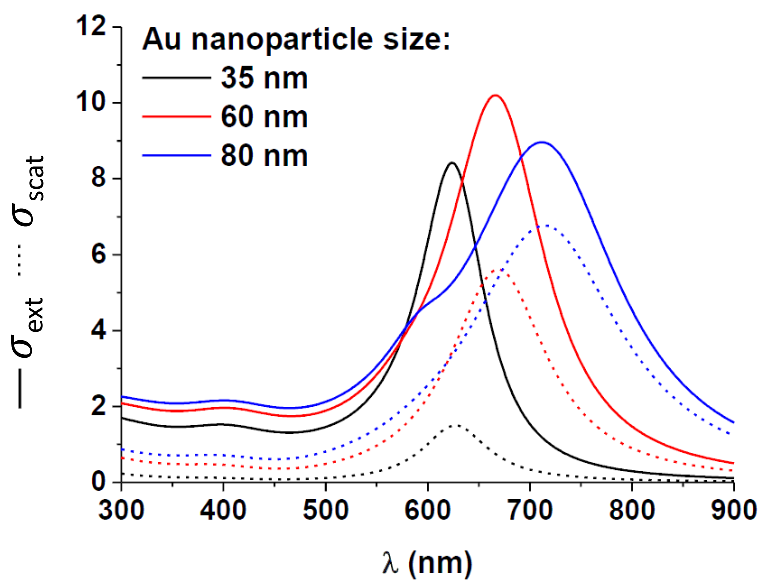

Figure 2-32 - Extinction efficiencies (σ_{ext}) and scattering cross section (σ_{scat}) of Au spherical NPs in a medium with a refractive index of 2.0 with an increasing in the NP size. Adapted from [115].

For small particles, phase retardation and effects of higher multipoles can be neglected, and the Mie formula is simplified considerably. Mie's expression for the extinction cross is described in the following equation:[284]

$$\sigma_{ext}(w) = \frac{9w\varepsilon_m^{3/2}V_0}{c}\frac{\varepsilon_2(w)}{[(\varepsilon_1(w)+2\varepsilon_m)^2]+\varepsilon_2(w)^2} \quad \text{(Eq. 2-45)}$$

Where $V_0 = \frac{4\pi}{3} R^3$ (Eq. 2-46) represents the volume of a particle, ε_1 and ε_2 denote the real and imaginary parts of the dielectric function of the particle's material, ε_m is the dielectric function of the surrounding medium and c is the speed of light and w is the angular frequency of the exciting radiation. As observed in the above expression, the cross section has a resonance at the frequency where the denominator $[(\varepsilon_1(w) + 2\varepsilon_m)^2] + \varepsilon_2(w)^2$ (Eq. 2-47) takes its minimum. This condition happens when $\varepsilon_1(w) = -2\varepsilon_m$ (Eq. 2-48). [284] The spectral characteristics, such as the resonance's position and shape, are not directly influenced by the particle radius R. Instead, they are indirectly affected by the size-dependent properties of $\varepsilon_{1,2}(w)$. [284] Consequently, the resonance's position, width, and height provide a viable means for investigating the size-related variations in the dielectric functions. [284] Specifically, the peak position relies on ε_1 , the peak height corresponds to ε_2 , and alterations in the band width are associated with changes in the refractive index. [284]

Figure 2-33 illustrates the connection between nanoparticle size and LSPR wavelength.

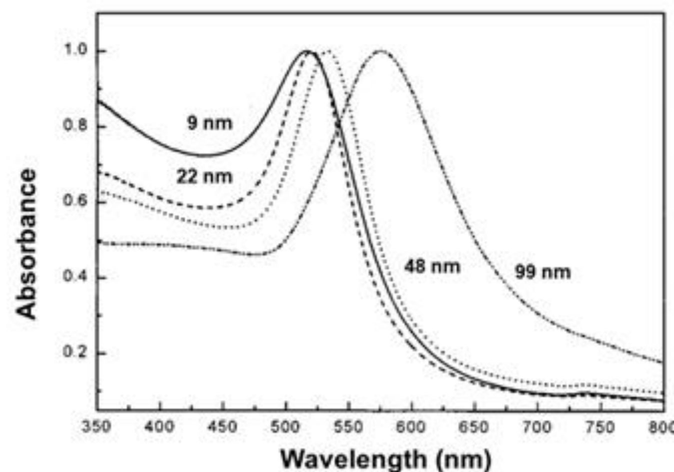

Figure 2-33 - Absorption spectra of 9 nm, 22 nm, 48 nm and 99 nm of Au nanoparticles. Adapted from [286].

Essentially, the red-shift of the plasmon resonance can be attributed to the decrease in the restoring force caused by an increase in distance between the positive ions and electrons in the conduction band. Moreover, larger nanoparticles result in the excitation of higher-order oscillation modes since the

electrons can no longer respond uniformly to the applied field due to retardation of the field across the nanoparticle. Additionally, another effect comes from the electromagnetic retardation which results in a broadening of the plasmon resonance band, which can be seen in Figure 2-33.

2.5.2 Effect of Nanoparticle Shape

Besides size, the LSPR is also highly dependent on the shape of the metal NP, which influences the line shape and position of the surface plasmon resonance.[287] The shape of the NPs is defined by the geometrical depolarization factors, L_i with i = a, b, c, and $L_a+L_b+L_c = 1$. In a sphere, these factors are defined as $L_a = L_b = L_c = \frac{1}{3} = 0.33$, in a spheroid by $L_a \neq L_b = L_c$ and a general ellipsoid $L_a \neq L_b \neq L_c$. Further information is found in Figure 1-9 in Section 1.2. The depolarization factors determine the electric polarizability along the corresponding principal axes. For ellipsoids, the electric polarizability α_i for field direction parallel to the principal axis i=a, b or c is given by the following equation:[284]

$$\alpha_i(w) = \varepsilon_0 \frac{\varepsilon(w)-\varepsilon_m}{\varepsilon_m+[\varepsilon(w)-\varepsilon_m]L_i} V_{cluster} \quad \text{(Eq. 2-49)}$$

The plasmon resonance condition occurs when the denominator is minimal, $\varepsilon\,(w) = \varepsilon_m\left(1 - \frac{1}{L_i}\right)$ (Eq. 2-50). For a prolate particle excited by an electric field along their long axis, the relevant polarization factor is L = 0.11 and is smaller than a sphere (L = 0.33). From the previous equation, we can see that L_i is inversely related to the permittivity, a smaller L_i value corresponds to a higher negative permittivity. Therefore, in the case of prolate nanoparticles, the lower L_i values lead to a higher negative permittivity compared to spherical nanoparticles. The resonance for such particle requires a more negative permittivity which, looking at Figure 2-34, will occur at longer wavelengths-the change in the shape results in the resonance being redshifted. In other words, the increase in the aspect ratio can be explained by reduced restoring forces between the charges at the end-sides (i.e. reduction in the depolarization factor) of a prolate. This causes a decrease in the resonance frequency leading to a red-shift.

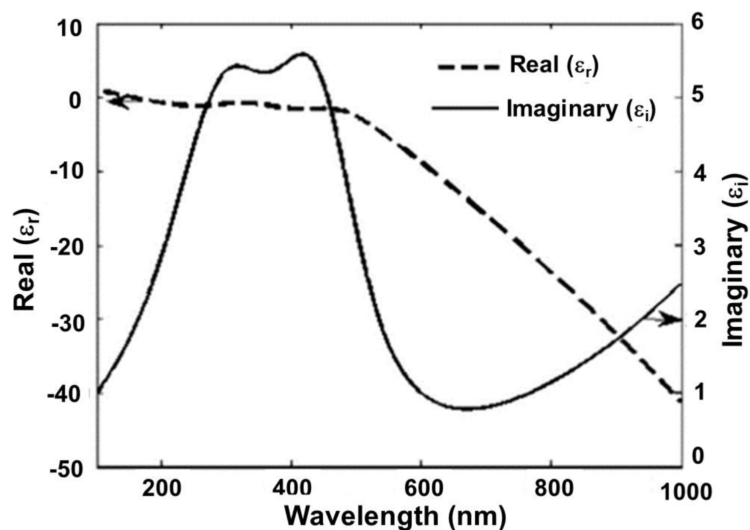

Figure 2-34 - Au dielectric permittivity for bulk gold as a function of wavelength. Adapted from [288].

As we can see, the surface plasmon resonance frequency is affected by the shape of the NP (through L). This changes in the particle shape led to different resonance conditions, illustrated in Figure 2-35.

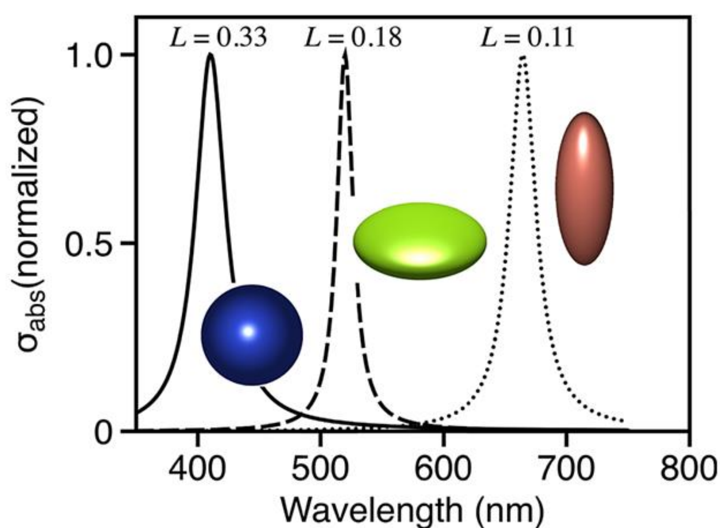

Figure 2-35 - Absorption spectra for a sphere, oblate and prolate. The relevant shape factors are shown. Adapted from [285].

Figure 2-36 shows the optical properties of Au nanostructures of various sizes and shapes that are stabilized with cationic surfactants in aqueous solutions. It is observed that Au nanospheres and nanocubes have a single surface plasmon peak. However, Au nanobranches, nanorods, and nanobipyramids show two significant surface plasmon peaks. One of these peaks corresponds to electron oscillation along the transverse direction, while the other corresponds to electron oscillation along the longitudinal direction.[287]

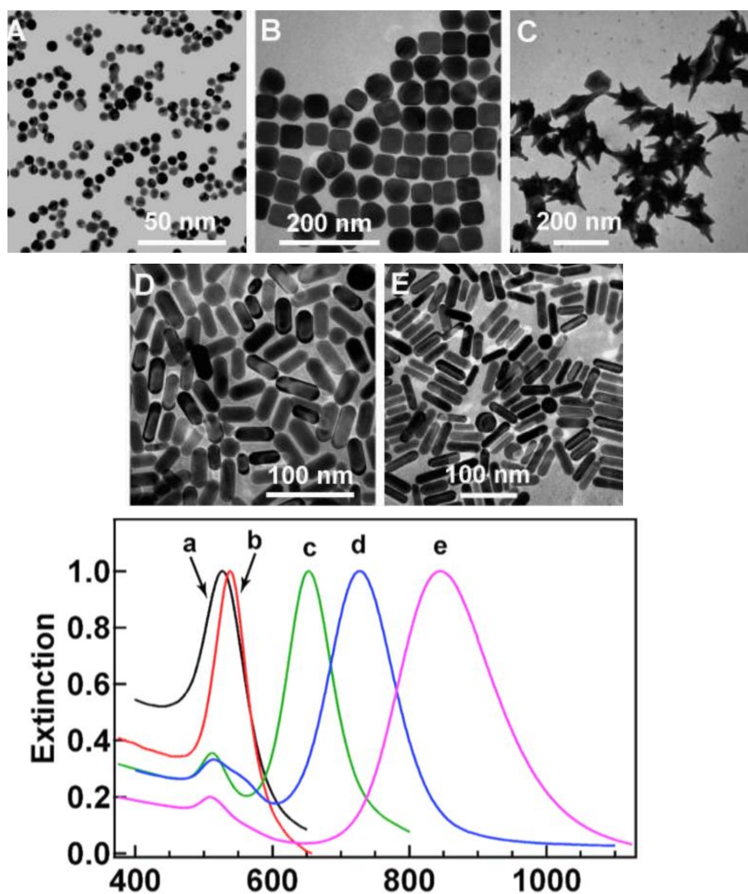

Figure 2-36 – (top) TEM images of Au nanoparticles with different shape and sizes a) Nanospheres b) nanocubes c) nanorods (AR = 2.4) d) nanorods (AR = 3.4) and e) nanorods (AR = 4.6), and (bottom) normalized extinction spectra from the above structures. Adapted from [287].

2.5.3 Material dependence

As it was previous mentioned, the dielectric properties of the NPs also alter their SPR. Nanoparticles with similar shapes and sizes exhibit plasmon resonances at different wavelength positions for different materials, which is the case of Au and Ag, for example. Both have the LSPR wavelength located in the visible region, but they have different dielectric constants, as we can see in Figure 2-37 (Ag) and in Figure 2-34(Au).

In general, the imaginary part of the dielectric constant affects the LSPR strength (LSPR peak intensity) and the real part the plasmon frequency (LSPR peak position).[289,290]

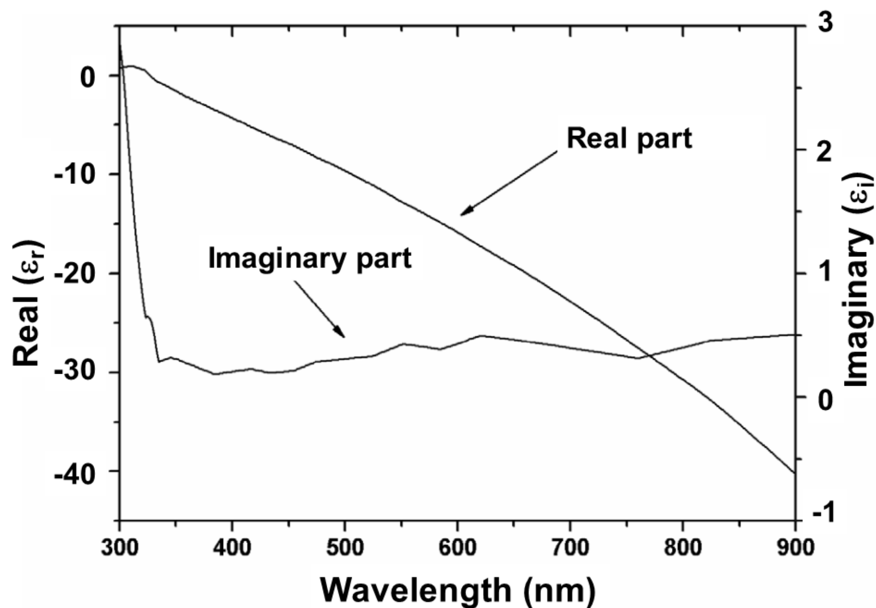

Figure 2-37 - Dielectric permittivity for silver bulk as a function of wavelength. Adapted from [291]

2.5.4 Effect of surrounding media

The frequency of plasmon resonance is strongly influenced by the dielectric characteristics of the medium surrounding the NP; the presence of electric fields around the NP surface also induces the polarization of the surrounding medium. As evident from the equation $\varepsilon_1(w) = -2\varepsilon_m$, (Eq. 2-48) if the dielectric constant ε_m of the surrounding medium is raised, it leads to a rise in the negative value of $\varepsilon_1(w)$ to satisfy the plasmon resonance requirement, consequently resulting in a displacement towards longer wavelengths, i.e., red-shift, of the plasmon resonance, as depicted in Figure 2-38. This means that an increase in the dielectric constant of the medium results in a lowering of the Coulombic restoring force on the displaced electron cloud, which causes a decline in the plasmon resonance frequency.

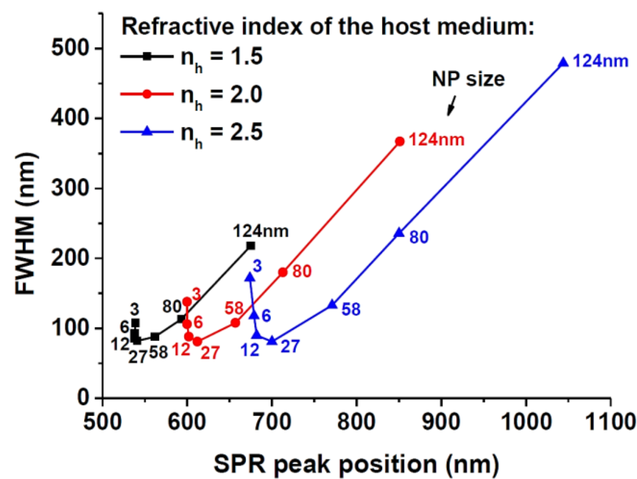

Figure 2-38 - Half-width of the dipolar resonances of different sizes of Au nanoparticles versus the respective peak position for a refractive index of 1.5, 2.0 and 2.5. Adapted from [115].

Understanding the impact of substrate interaction on plasmon resonance properties of nanoparticles is crucial, as nanoparticles are typically synthesized on surfaces. However, this introduces additional complexity to electromagnetic modelling, as the asymmetric environment (substrate-air) needs to be taken into consideration. To investigate the interaction between a 10 nm Ag sphere and a 10 nm thick mica substrate, Lance Kelly et al.[292] employed the discrete dipole approximation (DDA) method, which is used for isolated NPs of arbitrary shape

and complex surrounding environments. The sphere was surrounded by vacuum until it was fully encased by mica and observed the highest SPR peak. As depicted in Figure 2-39, the LSPR wavelength experiences a red-shift as the sphere transitions from being free to full embedded (100%). This demonstrates the influence of the substrate on the position of the LSPR peak, which can be essential in tuning the wavelength. [292]

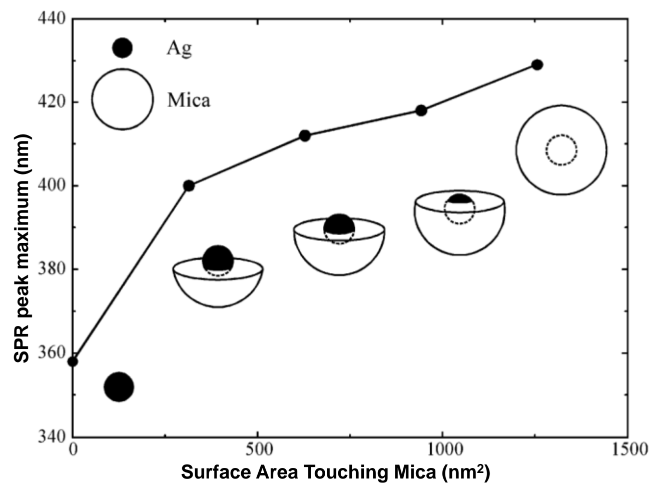

Figure 2-39 - The DDA findings involving a sinking sphere model that examines the displacement caused by a substrate. Specifically, a metal core is gradually submerged into a semi-spherical piece of mica, positioned at intervals of 0, 5, 10, and 15 nm from the edge, along the diameter of the core. Adapted from [292].

Chapter 3

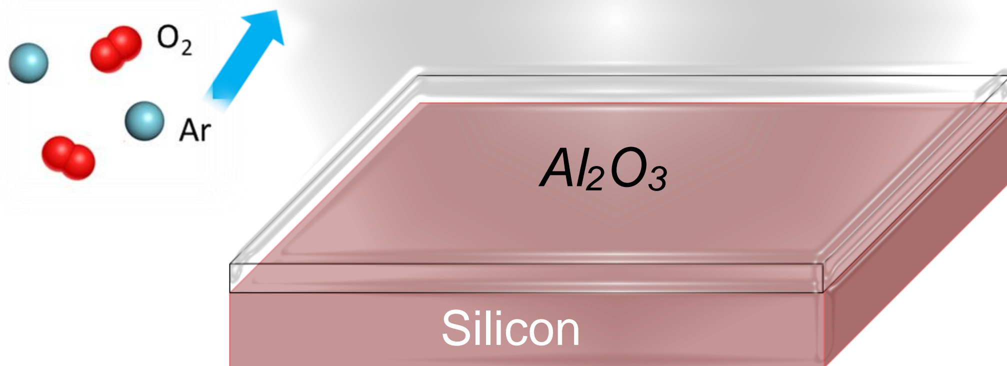

3. Alumina coatings

In this chapter, we focus on the deposition of Al_2O_3 using HiPIMS, MF, and MF+HiPIMS power sources, while implementing a feedback control system to regulate the O_2 flow and mitigate target poisoning. The research investigates how substrate temperature, sputtering power, and source type impact the properties of Al_2O_3 thin films. The presented work has been published recently in Surface and Coatings Technology, and it is entitled "Tuning the characteristics of Al_2O_3 thin films using different pulse configurations: Mid-frequency, high-power impulse magnetron sputtering, and their combination".

3.1. Deposition conditions

In the deposition of alumina two different power sources were used, namely High-Power Impulse Magnetron Sputtering (HiPIMS), and Mid-Frequency (MF). To achieve efficient deposition of stoichiometric Al_2O_3 films, an active feedback reactive sputtering controller (Speedflo, Gencoa Ltd.) was utilized, where the flow of O_2 was constantly adjusted to prevent the poisoning of the Al target and to achieve films with a high O concentration at an ideal deposition rate. For that, the hysteresis behaviour during HiPIMS and MF operation was recorded with plasma emission monitoring (PEM) technology.

In Figure 3-1 shows the hysteresis curve acquired during HiPIMS process (2000 W) in an Ar atmosphere (50 sccm) with the variation of O_2 from 0 to 50 and back to 0 sccm at a constant rate. The curve can be divided into three sections: metallic, compound, and poisoned modes. For the deposition of the alumina films, the setpoint was adjusted to 10% on the PEM sensor, and the deposition was carried out in the compound region. It is worth noting that this hysteresis exhibits the same shape as the one presented in Figure 2-5 of Chapter 2.

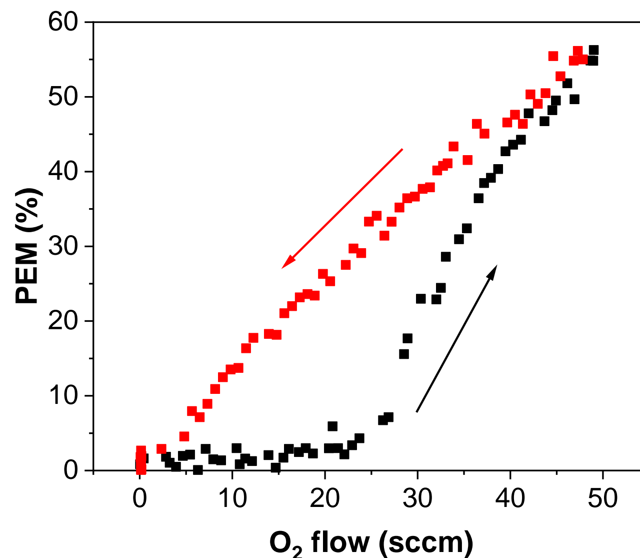

Figure 3-1 - Hysteresis plots (PEM signal vs O_2 flow) obtained for a HiPIMS process at 2000 W in an Ar/O_2 atmosphere at 450°C.

The depositions were performed at two different temperatures, namely 450°C for HiPIMS and 200°C and 450°C for MF, with three different power

settings: 2000 and 2500 W for both HiPIMS and MF, and 3500 W for MF. During the experimental process, the current and voltage were continuously monitored using a Teledyne Lecroy HDO4054 oscilloscope. The discharge-current waveforms for HiPIMS, MF, and MF+HiPIMS were obtained and are shown in Figure 3-2. The current oscillations observed during MF operation were relatively small in comparison to the high intensity of each peak during HiPIMS deposition. For clarity, the MF signal (Figure 3-2b) was amplified by a factor of 10. As shown in Figure 3-2a, one HiPIMS pulse was applied every millisecond, while 40 pulses were applied during the same period in the case of MF (Figure 3-2b).

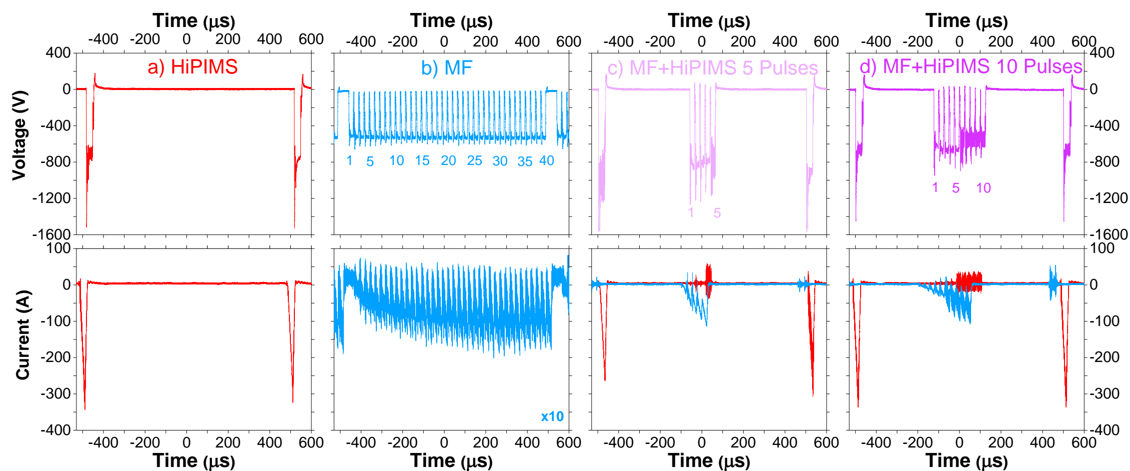

Figure 3-2 - The waveforms of the target and current were recorded for different operations. a) HiPIMS. b) MF with the current multiplied by a factor of 10. c) shows MF+HiPIMS with 5 MF pulses. d) shows MF+HiPIMS with 10 MF pulses. The average power for each source was set at 2500 W.

The MF+HiPIMS setups (Figure 3-2c and d)) combine both sources, operating at 2500 W each, resulting in a total power of 5000 W. To achieve this, MF pulses (5 and 10) were alternated during the off-time between consecutive HiPIMS pulses. Thus, the power of individual MF peaks in the MF+HiPIMS setup is 8 and 4 times greater than in the MF alone condition, respectively (as evident from the higher current and voltages in Figure 3-2c and d as compared to Figure 3-2b. It should be noted that in the MF+HiPIMS configuration, there is a slight disturbance in the current of both MF and HiPIMS sources when the other source is in operation (as shown in the lower part of Figure 3-2c and d). This is a result of the experimental setup of the sources and the oscilloscope and does not imply that either of the sources is supplying current to the targets when they are not in operation.

Table 3-1 sums up the main deposition conditions for the two power sources and several features of the Al_2O_3 films at different temperatures, such as deposition rate, grain size estimated from the broadening of the (400) and (440) Al_2O_3 peaks, residual stress, refractive index (for λ = 632.8 nm) and density.

Table 3-1 – Information on the synthesis conditions and characteristics of Al_2O_3 films, including the grain size calculation from the broadening of the 400 and 440 diffraction peaks of Al_2O_3.

<table>
<tr><th>Source</th><th>Power (W)</th><th>Voltage (V)</th><th>Average Current (A)</th><th>Temperature (˚C)</th><th>Thickness (nm)</th><th>Deposition rate (nm/min)</th><th>Grain size (nm) (400)</th><th>Grain size (nm) (440)</th><th>Residual stress (GPa)</th><th>Refractive index (λ=632.8 nm)</th><th>Density (g/cm^3)</th></tr>
<tr><td>MF</td><td>3500</td><td>350</td><td>9.2</td><td>200</td><td>386</td><td>6.4</td><td>-</td><td>-</td><td>- 2.0 ± 0.1</td><td>1.628</td><td>2.99 ± 0.08</td></tr>
<tr><td>MF</td><td>2000</td><td>341</td><td>5.4</td><td>450</td><td>193</td><td>7.6</td><td>6</td><td>7</td><td>- 0.7 ± 0.3</td><td>1.706</td><td>2.99 ± 0.08</td></tr>
<tr><td>MF</td><td>2500</td><td>349</td><td>6.8</td><td>450</td><td>185</td><td>9.8</td><td>7</td><td>7</td><td>- 0.5 ± 0.1</td><td>1.689</td><td>2.96 ± 0.08</td></tr>
<tr><td>MF</td><td>3500</td><td>364</td><td>8.9</td><td>450</td><td>202</td><td>12.9</td><td>7</td><td>7</td><td>- 5.3 ± 0.5</td><td>1.708</td><td>3.20 ± 0.08</td></tr>
<tr><td>HiPIMS</td><td>2000</td><td>840</td><td>2.3</td><td>450</td><td>194</td><td>1.6</td><td>6</td><td>5</td><td>- 6.9 ± 0.2</td><td>1.706</td><td>3.38 ± 0.09</td></tr>
<tr><td>HiPIMS</td><td>2500</td><td>931</td><td>2.5</td><td>450</td><td>205</td><td>1.8</td><td>5</td><td>5</td><td>- 10 ± 1.6</td><td>1.740</td><td>3.54 ± 0.09</td></tr>
<tr><td rowspan="2">MF+HiPIMS
5 Pulses</td><td>MF 2500</td><td>440</td><td>5.10</td><td rowspan="2">450</td><td rowspan="2">168</td><td rowspan="2">4.7</td><td rowspan="2">5</td><td rowspan="2">5</td><td rowspan="2">- 4.51 ± 1.3</td><td rowspan="2">-</td><td rowspan="2">-</td></tr>
<tr><td>HiPIMS 2500</td><td>909</td><td>2.62</td></tr>
<tr><td rowspan="2">MF+HiPIMS
10 Pulses</td><td>MF 2500</td><td>386</td><td>5.95</td><td rowspan="2">450</td><td rowspan="2">227</td><td rowspan="2">9.1</td><td rowspan="2">6</td><td rowspan="2">6</td><td rowspan="2">- 4.10± 0.6</td><td rowspan="2">-</td><td rowspan="2">-</td></tr>
<tr><td>HiPIMS 2500</td><td>905</td><td>2.62</td></tr>
</table>

3.2. XRD analysis

Figure 3-3a shows grazing incidence patterns of Al_2O_3 films deposited at different temperatures and powers using both sources, where the diffraction peaks of γ-Al_2O_3 reference (JCPDS Card No. 00-050-0741) are indicated by vertical lines. All the patterns have similar backgrounds. The narrow peaks and the hump between approximately 50° and 56° are due to forbidden diffractions of the Si substrate. These peaks can be effectively eliminated by rotating the samples by 45º in the holder, as shown in the patterns of the rotated samples in Figure 3-3b.

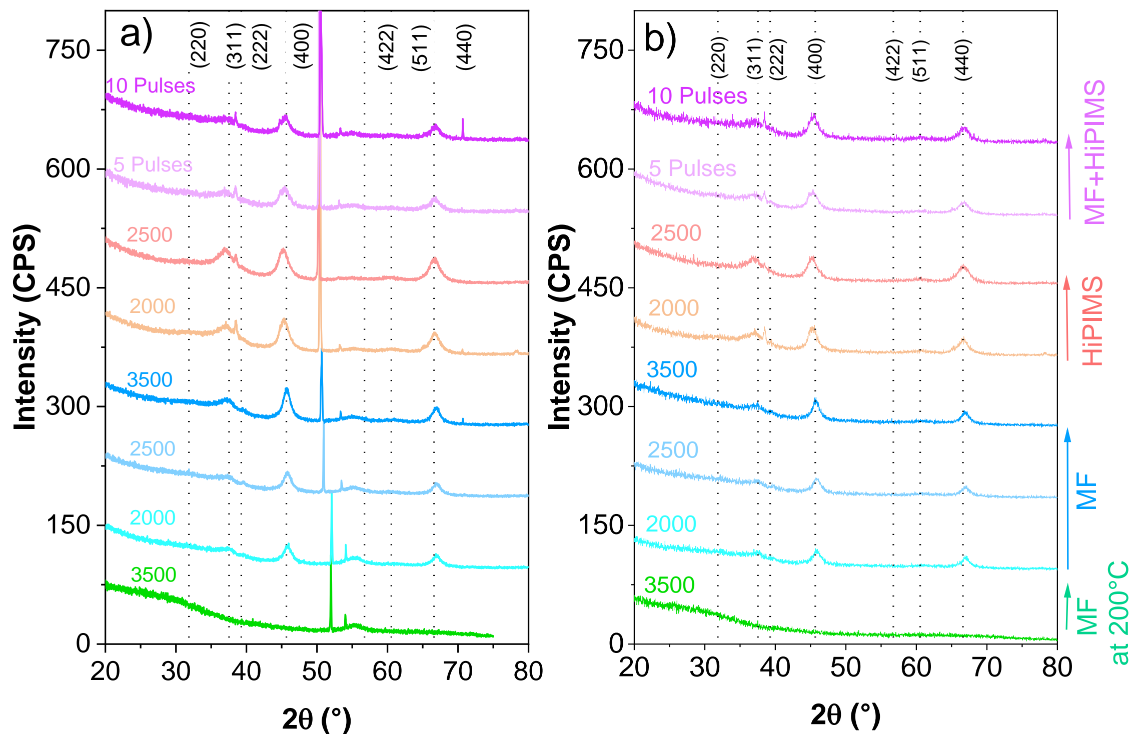

Figure 3-3 – XRD patterns of Al_2O_3 films deposited by MF, HIPIMS and MF+HiPIMS at various temperatures (450ºC, except indicated otherwise) and powers (indicated in W next to each pattern). The position of a reference of γ-Al_2O_3 is indicated by dotted lines. In the case of MF+HiPIMS an average power of 2500 W was set for each source for both 5 and 10 pulses. a) without rotation b) with rotation of 45°.

Except for the MF sample deposited at 200°C, which remained amorphous even after a higher power deposition (3500 W), all the patterns display peaks that agree with the γ-phase reference. This suggests that the degree of crystallization is greatly influenced by the substrate temperature. The (311), (400), and (440)

planes of γ-Al_2O_3 can be identified from the three peaks observed at approximately 37.5°, 45.6°, and 66.6°, respectively. Zhou et al. [293] obtained similar findings for Al_2O_3 films deposited via twin targets reactive HiPIMS. Regardless of the source and power used, all films deposited at 450ºC (cf. Table 3-1) exhibited similar grain sizes (5-7 nm) for the (400) and (440) planes, suggesting that the influence of these parameters on the grain size is limited. This observation aligns with the significant variation in grain size resulting from a decrease in deposition temperature to 200ºC. Moreover, the contribution of microstrain to peak broadening is likely insignificant, as the grain size calculated for two distinct peaks is comparable. The integrated intensity of the main peaks of alumina and the Si hump, after background subtraction, is depicted in Figure 3-4.

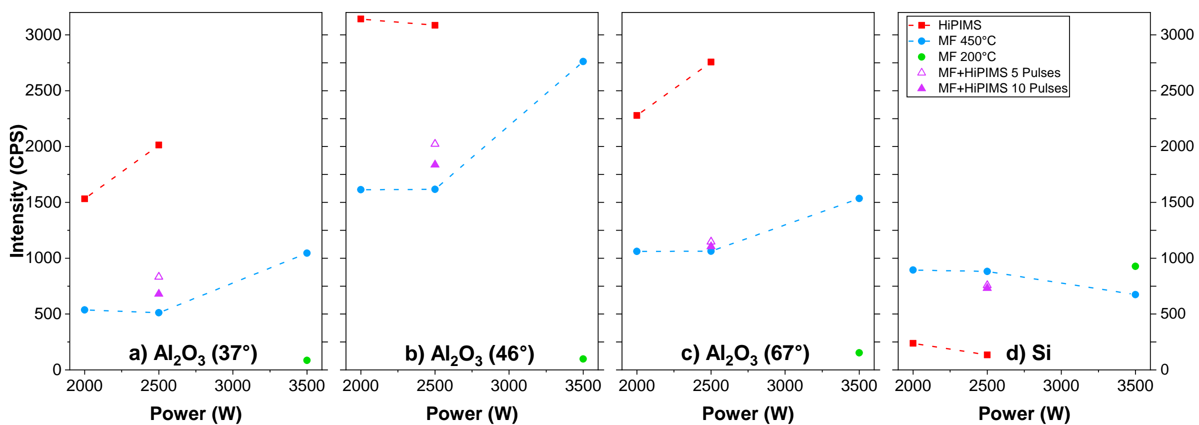

Figure 3-4 – Integrated intensity of peaks of Al_2O_3 located at a) 37°, b) 46° and c) 67°, and d) for the silicon peak from Figure 3-3.

The intensity of the Al_2O_3 peaks undergoes a significant increase for films deposited by MF at 3500 W when the deposition temperature is elevated from 200ºC (green point) to 450ºC (light blue line). This disparity indicates a contrast between two films of varying characteristics (amorphous versus nanocrystalline). The increase of MF power from 2000 to 3500 W also induces an increase of the intensity of the diffraction peaks (cf. all blue line in Figure 3-4) for films deposited at 450ºC. Nevertheless, the effect of varying MF power on the intensity of the Al_2O_3 peaks is less pronounced than that of temperature, underscoring the greater influence of deposition temperature on the crystallinity of Al_2O_3 films

relative to deposition power. The resemblance between the intensity of peaks for films deposited at 2000 and 2500 W suggests that the impact of magnetron power is insignificant relative to substrate heating under those sputtering conditions. Films deposited by HiPIMS exhibit a further increase in the intensity of all the Al_2O_3 peaks, particularly at higher deposition power (red line in Figure 3-4). Notably, the intensity of all Al_2O_3 peaks evolves consistently, i.e. there is no redistribution of intensities among peaks or nor presence of new peaks in the patterns. This implies that the changes in Al_2O_3 peak intensities cannot be attributed to effects of modified texture or preferential growth. Given that all films possess equivalent thickness and similar grain size (i.e. peak broadening), the most plausible explanation for this observation is that films deposited by HiPIMS and/or higher deposition power exhibit a higher density of diffracting elements (i.e. grains). Figure 3-5 provides a visual representation of this concept. It shows two films with identical thickness and comparable texture and grain size, but with differing grain density. This model accounts for the behaviours of the Si peak, which declines concurrently with the growth of the Al_2O_3 peaks (cf. Figure 3-4d). The explanation is that the greater presence of diffracting elements in Al_2O_3 films diminishes the amount of radiation that reaches and/or leaves the Si substrate.

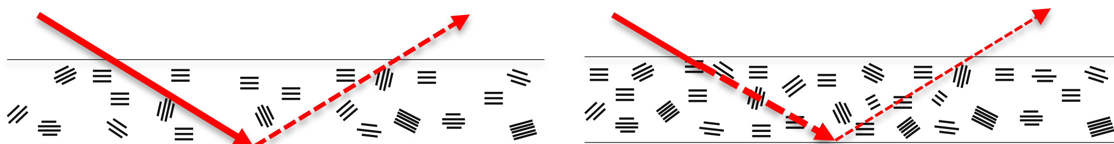

Figure 3-5 – Schematics of two films with identical texture, thickness, and grain size, but different grain density. An increase in the density of γ-Al_2O_3 grains, from left to right, is observed in films deposited by HIPIMS rather than MF or at higher deposition powers. The red arrows represent the incoming and outgoing X-ray beams. It is illustrated how increased grain density contributes to a reduction in the amount of radiation that reaches and/or leaves the Si substrate.

The intensity of Al_2O_3 peaks in the MF+HiPIMS configuration (represented by purple triangles in Figure 3-4) falls between the HiPIMS and MF at 2500 W configurations but is closer to the MF configuration even for the Si peak. Moreover, the sample with 5 pulses has a higher grain density when compared to the one with 10 pulses. The XRD patterns reveal a shift of the diffraction peaks among films, which can be attributed to the induction of residual stress during the deposition process.[293] [294] Figure 3-6 provides an example illustrating the

shift to lower angles of the (400) Al_2O_3 peak for a film deposited by HiPIMS, when compared with one deposited by MF. This shift suggests a higher compressive residual stress in the former sample. This phenomenon will be discussed in detail later.

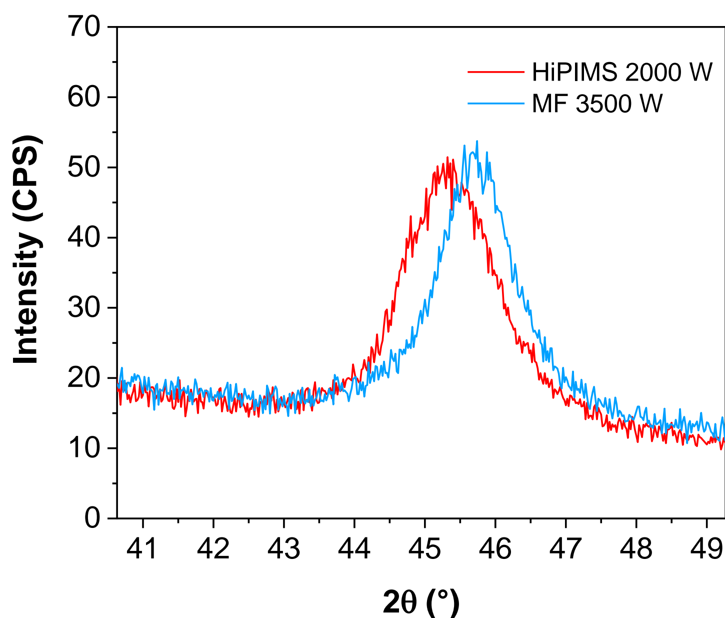

Figure 3-6 – A close-up view of the (400) peak of alumina for films deposited under various power conditions by HIPIMS and MF.

3.3. TEM analysis

In order to conduct a more thorough investigation of the model depicted in Figure 3-5, HRTEM and EELS analyses were performed on select samples (MF-3500W-200ºC, MF-2500W-450ºC, MF-3500W-450ºC, and HiPIMS-2500W-450ºC). Figure 3-7 displays HRTEM images of these films, along with the corresponding FFT patterns. The results are consistent with those obtained from XRD (Figure 3-3). Specifically, the film deposited at 200ºC (Figure 3-7a) is found to be amorphous, as evidenced by the presence of only a diffuse halo in the FFT and the absence of any identifiable alumina planes. On the other hand, the other three images indicate that the films are polycrystalline, with various planes being directly measurable in the images (e.g. 1.98, 2.38 and 4.48 Å), which correspond well with the interplanar distances reported for the (400), (311) and (111) planes

of γ-Al_2O_3 [JCPDS Card No. 00-050-0741]. In fact, the FFT patterns display distinct points that align with the reference of γ-Al_2O_3 (dashed red lines). However, the number of points detected in the FFTs increases when higher deposition power (Figure 3-7c) or HiPIMS (Figure 3-7d) is employed, in agreement with the XRD results (Figure 3-4). In fact, for these two films, points located in diffraction rings corresponding to the (511) plan can be identified, which are hardly discernible in the film deposited with MF at 2500W and 450ºC (Figure 3-7b).

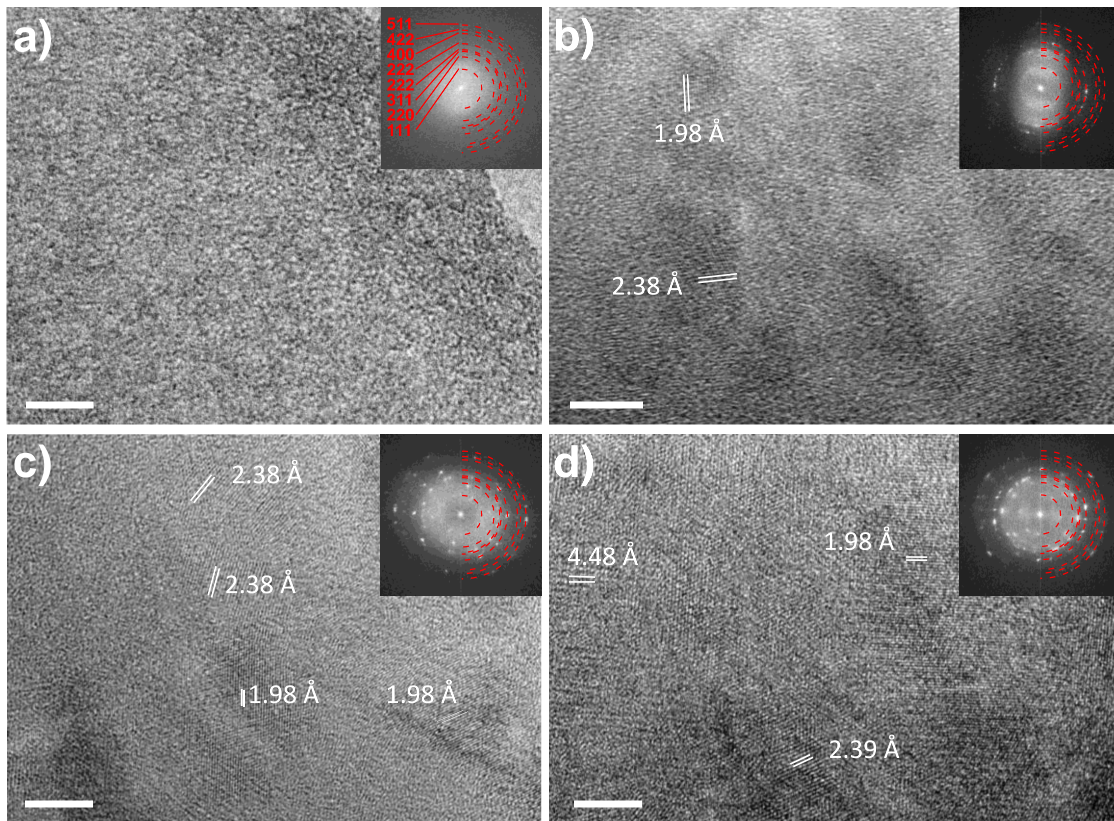

Figure 3-7 – High resolution TEM images of selected films deposited under varying conditions. a) MF at 3500W and 200ºC. b) MF at 2500W and 450ºC. c) MF at 3500W and 450ºC. d) HiPIMS-2500W-450ºC. Insets are shown in the images, displaying FFTs from the HRTEM images and the red dashed semi-circumferences highlight the position of the first 8 planes of γ-Al_2O_3 reference [JCPDS Card No. 00-050-0741]. The Miller Indexes of these planes are labelled in (a). The scale bars in all images represent 5 nm.

3.4. EELS analysis

In Figure 3-8, the Al-L edge of the films is compared to a reference of γ-Al_2O_3 measured by EELS. The shape of this edge is complex and influenced not only by the Al_2O_3 phase, [295] but also by the coordination of the Al atom [295,296] or the presence of defects or vacancies. [296] In addition, the electron beam can also affect alumina.[295] During the experiment, the occurrence of a pre-peak in the O-K edge, which is commonly linked to sample damage,[297–299] was prevented (spectra not shown). However, it should be noted that other causes for this peak have also been reported. [300] The shape of the Al-L edge of γ-Al_2O_3 is consistent with literature reports. [296] The Al-L edge is composed of two regions depending on the energy level of the excited electron (2p or 2s), with the $L_{2,3}$ and L_1 edges located at energy losses of approximately 75 and 115 eV and approximately 115 and 130 eV, respectively. [295,301] In the $L_{2,3}$ region, three peaks can be distinguished, two of which are characteristic of Al spinels such as γ-Al_2O_3 located at ca. 79 and 83 eV, as well as a broad symetric peak at 100 eV, which the position/shape is common for many alumina phases. [295] The shape of the spectra of the films reflects the crystallization process, as interpreted from Figure 3-4.

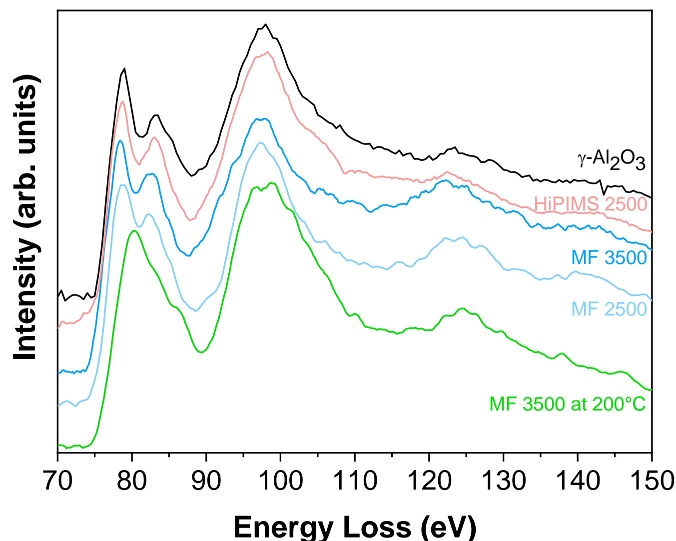

Figure 3-8 – EELS measurement of the Al-L edge of selected films at various temperatures (450ºC, except indicated otherwise) and powers (indicated in W next to each pattern) with a reference of γ-Al_2O_3 included at the top.

3.5. SEM analysis

Cross-sectional SEM images of selected films deposited at 450ºC by HiPIMS (top) and MF (bottom) are presented in Figure 3-9. The left-hand side displays the films deposited at the lowest power (2000 W), while the right-hand side shows the films deposited at the highest powers (2500 W and 3500 W). Due to the low conductivity of alumina, the image quality is poor, resulting in charging effects. Despite this, it appears that the films deposited at 2000 W (left column) exhibit a columnar growth pattern. In contrast, the images for higher powers (right column) show a V-shaped structure, which is related to an increase in energy provided to the films. These findings align with observations made by Anders et al. [302] in zone T and zone 2. It is noteworthy that films deposited at the same power using different sources exhibit similar microstructure, which may be attributed to the high deposition temperature.

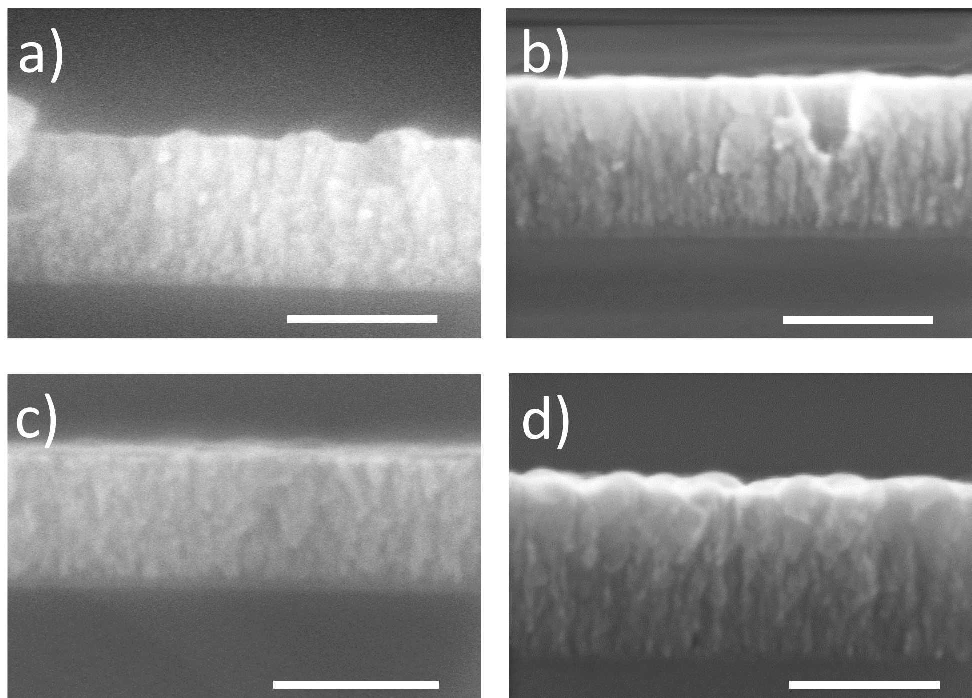

Figure 3-9 – SEM images of cross-sections of Al_2O_3 films produced by (a) HiPIMS at 2000 W, (b) HiPIMS at 2500 W, (c) MF at 2000 W and (d) MF at 3500 W at 450°C. The scale bars for all images correspond to 200 nm.

3.6. Additional structural properties of the coatings

Additional characteristics of the films and processes can be observed in Figure 3-10 and summarized in Table 3-1.

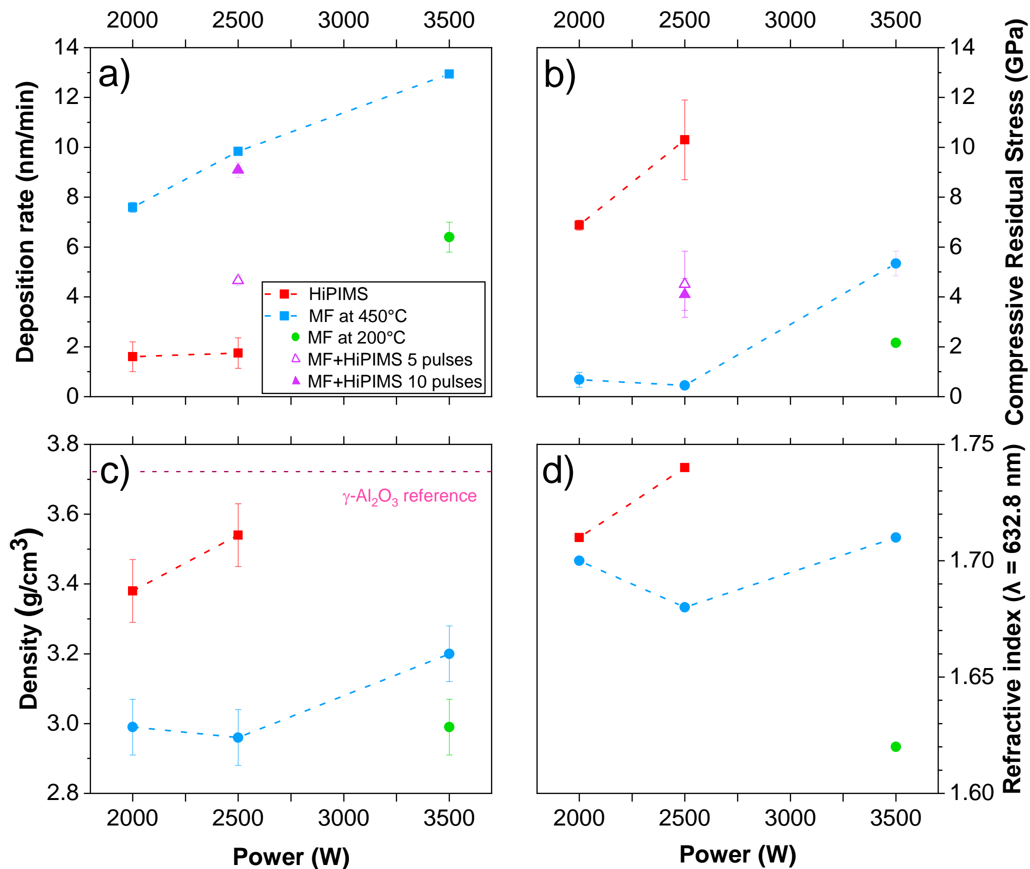

Figure 3-10 – Characteristics of the deposited alumina films by MF, HiPIMS and MF+HiPIMS at various temperatures and powers. a) Deposition rate. b) compressive residual stress. c) density. d) refractive index. The reference value for the density of γ-Al_2O_3 [JCPDS Card No. 00-050-0741] is indicated by a horizontal line in (c).

Figure 3-10a demonstrates that the deposition rates for HiPIMS-deposited films (1.6 – 1.8 nm/min) are inferior to those deposited by MF, which progressively increase from 7.6 to 12.9 nm/min with increasing power. This finding is consistent with the lower deposition rates typically observed for HiPIMS, which is a drawback of this power source. [188] Furthermore, a comparison of the films deposited by MF at 3500 W highlights the impact of the angle amplitude during dynamic mode deposition. Specifically, the deposition rate for the sample

deposited at 200ºC is approximately half of that for the other samples (6.4 vs. 12.9 nm/min) because it was deposited at an angle amplitude of 70° instead of 15°. As a result, the lower exposure of that sample to the target results in a reduced deposition rate. The implementation of the MF+HiPIMS setup significantly improves the deposition rate to 4.7 nm/min (5 MF pulses) and 9.1 nm/min (10 MF pulses) compared to the HiPIMS setup (improvements by factors of 2.6 and 5.1, respectively). It is noteworthy that a higher number of MF peaks (i.e., lower energy per MF peak) results in a doubled improvement in deposition rate compared to the HiPIMS-only configuration, almost approaching the values obtained with MF alone. Since the average power used in the MF discharge is the same in both cases, this indicates that it is more efficient to distribute the energy among more MF peaks rather than concentrating it on a few ones.

Figure 3-10b shows that all of the samples exhibit compressive residual stress, which in general tends to increase with deposition power. The films created using HiPIMS have the highest values of 6.9 ± 0.2 and 10 ± 1.6 GPa for those deposited at 2000 and 2500 W, respectively. On the other hand, films created by MF at the same power range have significantly lower values of 0.5 ± 0.1 GPa, which suggests that the intrinsic contribution to stress is not significant at these MF powers. In fact, both measurements agree well with the value that can be calculated for thermal stress (σ_{th}=-0.61 GPa) using the following expression: [303]

$$\sigma_{th} = \frac{E_f}{1-\nu_f}\int_{T_1}^{T_2}(\alpha_s - \alpha_f)dT \quad \text{(Eq. 3-1)}$$

where E_f and ν_f are the elastic modulus and Poisson's ratio of the Al_2O_3 film (E_f = 125 GPa, ν_f = 0.2),[304] T_1 and T_2 are the initial and final temperatures (450 and 25ºC), and α_f and α_s are the linear thermal expansion coefficients of γ-Al_2O_3 (average α_f = 12.8×10^{-6} K^{-1} up to 450ºC))[305] and Si substrate (α_s varies between 2.6×10^{-6} K^{-1} at 25ºC and 4.1×10^{-6} K^{-1} at 450ºC).[303]

The varying behaviour of MF and HIPIMS can be attributed to the characteristics of the deposition process. HiPIMS deposition has a higher energy and density of ions, coupled with a low deposition rate, which results in higher compressive stress. [306] In contrast, the MF+HiPIMS process has a higher deposition rate

connected to the MF pulses and subsequent lower ratio of ions impinging the surface per deposited atom, which leads to a lower compressive stress of approximately -4 GPa (60% less than HiPIMS alone). These findings suggest that the MF+HiPIMS configuration can mitigate the stress by balancing the ion density and deposition rate. The film deposited with 10 MF pulses exhibits a stress level that is comparable to the film deposited with only 5 pulses, despite a much larger difference in deposition rate. In fact, when using MF+HiPIMS with 10 MF pulses, the deposition rate is similar to that of the MF film (cf. Figure 3-10a).This suggests that there may be a limit to the reduction of compressive stress achievable through the increase of deposition rate by incorporating a secondary power source between HiPIMS pulses in the form of MF.

The residual stress increases from -0.5 GPa to approximately -5 GPa as the MF deposition power increases from 2500 W to 3500 W. However, decreasing the temperature from 450ºC to 200ºC under this condition reduces the residual stress to approximately -2 GPa (green point in Figure 3-10b). It appears that the deposition power has a greater impact on the residual stress than the temperature, implying that the nature of the residual stress is more intrinsic than thermal. However, it is important to note that the decrease in stress to -2 GPa may not be solely attributed to the deposition temperature (as the thermal contribution to stress is low), but may also be due to the lower deposition rate of that sample caused by the wider angle amplitude during deposition (as shown in Figure 3-10a). The findings are consistent with those reported by Zywitzki et al. [126], who studied the compressive residual stress in alumina films deposited on sheet steel substrates using pulsed magnetron sputtering with a dual magnetron in the power range of 11-17 kW. The results showed a slight decrease in compressive residual stress from 0.64 to 0.60 GPa when the temperature was increased from 290-350°C. Additionally, for films deposited at substrate temperatures of 550-560°C, the compressive residual stress increased with power in the range of 2.0 to 9.4 GPa, indicating the influence of power on residual stress. However, these findings conflict with those reported by Kohout et al. [124], who investigated residual stress in amorphous alumina films deposited on Si stripes using HiPIMS at 3 mTorr with an average power of 440 W and a

frequency of 10 kHz. The results showed a low compressive residual stress of approximately 200 MPa, which may be attributed to the higher deposition rate (30 nm/min, 15 times higher than the present study), resulting in fewer ions impinging on the substrate per unit time and thus generating lower compressive residual stress.

In Figure 3-10c, the density of both the MF and HiPIMS films exhibits a similar trend to the compressive stress observed before. The density of the amorphous film is 2.99±0.08 g/cm^3, which is within the range reported in literature (between 2.66 and 3.07±0.05 g/cm^3). [307] Films deposited at MF at 450ºC with 2000 and 2500 W exhibit similar density values, with the γ phase detected. At the highest power, the MF film deposited at 450ºC exhibits a density of 3.20±0.08 g/cm^3, indicating an increase in density. Films deposited using HiPIMS have a higher density that increases with the sputtering power. The highest density value (3.54 ± 0.09 g/cm^3) is close to the reference value of γ-Al_2O_3 (represented by the dashed horizontal line in Figure 3-10c, which is in agreement with the gradual increase of γ-Al_2O_3 grain density in the films. Finally, the refractive index values of the films at 632.8 nm are summarized in Figure 3-10d. The amorphous films exhibited a relatively low value of n, approximately 1.62. However, by increasing the temperature to 450ºC, higher values of n (approximately 1.675-1.708) were obtained, as well as by changing the power source to HiPIMS, which resulted in even higher values of n (approximately 1.706-1.740). This behaviour is likely due to the increased crystallinity of the samples, which involves a trade-off between the contribution of the amorphous and γ phases, and the higher density of the HiPIMS-produced films (3.54 ± 0.09 g/cm^3) compared to amorphous films (2.99 ± 0.08 g/cm^3), as shown in Table 3-1.[294]

The outcomes of our study are consistent with those of Houska et al., who demonstrated that the refractive index (n) at 632 nm is dependent on the phase of Al_2O_3. Specifically, n values range from approximately 1.49-1.65 for amorphous Al_2O_3, to higher values of approximately 1.46-1.69 for γ-Al_2O_3, and up to 1.77 for α-Al_2O_3. [308] Notably, the maximum refractive index values obtained in our research (n~1.740) were observed in a sample characterized as γ-Al_2O_3, but the value is very similar to those reported for α-Al_2O_3. This finding suggests

that films containing the γ-Al_2O_3 phase may also achieve the refractive index range typical of α-Al_2O_3.

In addition, the Lorentz-Lorenz equation [309] often relates the refractive index (n) and density (ρ) of a material through the follow equation:

$$\frac{n^2-1}{n^2+2} = K\rho \quad \text{(Eq. 3-2)}$$

Where K is a constant influenced by the polarizability of the material through a relation that, for a dielectric, can be expressed as:

$$K = \frac{N_A \alpha}{3\varepsilon_0 M} \quad \text{(Eq. 3-3)}$$

The molecular weight (M) and polarizability (α) of a material, as well as Avogadro's constant (N_A) and the permittivity of the vacuum (ε_0), are involved in the given equation. For Al_2O_3, its polarizability can be estimated as the sum of the polarizabilities of its constituent parts, namely Al^{3+} and O^{2-} ions. The polarizability values for these ions are 6.0×10^{-42} and 1.6×10^{-40} $C{\cdot}m^{-2}{\cdot}V^{-1}$, respectively, [310] which gives an overall polarizability for Al_2O_3 of 5.0×10^{-40} $C{\cdot}m^{-2}{\cdot}V^{-1}$.

Figure 3-11 illustrates the correlation between the refractive index of the films and their measured densities. The Lorentz-Lorentz equation (Eq. 3.2), which employs the previously mentioned value for the polarizability of alumina, is represented by the solid orange line. This equation exhibits an approximately linear behaviour within the given range.

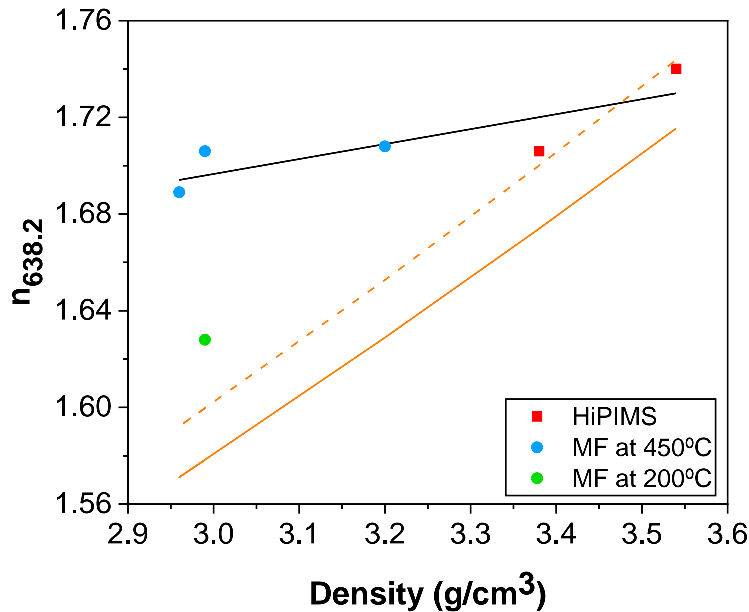

Figure 3-11 – Refractive index (n) of the films measured at a wavelength of 632.8 nm in function of the density. The back line represents a linear fitting of all the samples, excluding the amorphous film deposited at 200ºC. The orange lines correspond to the Lorentz-Lorenz equation (Eq. 3.2), using polarizabilities of Al_2O_3 of 5.0×10^{-40} C·m^{-2}·V^{-1} (solid line) and 5.14×10^{-40} C·m^{-2}·V^{-1} (dashed line).

To analyse our samples, a linear fitting was fitted to the observed values, with the exception of the amorphous film that was deposited at 200ºC. The trend shows an increase in refractive index with density, consistent with the behaviour predicted by the Lorentz-Lorenz equation. Nonetheless, the slope of that fit (represented by the black line) is considerably lower than the anticipated trend (orange line), indicating that the rise in refractive index should be greater in proportion to the observed changes in density. The discrepancy between the observed and anticipated trends could be attributed to experimental errors and/or the non-applicability of the equation to this particular case. However, the samples created through HiPIMS (represented by the red squares) exhibit an increase in refractive index with density, with a slope that appears to align with the Lorentz-Lorenz expression. In fact, a slight increase (3%) in the polarizability of alumina (from 5.0×10^{-40} to 5.14×10^{-40} C·m^{-2}·V^{-1}, which causes a variation of K from 0.111 to 0.114 cm^3/g) causes a shift in the plot (represented by the dashed orange line), bringing it in close agreement with the behaviour of the HiPIMS-deposited films.

The main results of this study are illustrated in Figure 3-12, which depicts a map of the samples. The plot consists of multiple squares, each representing a single sample. The X axis summarizes the deposition source and temperature of

the sample, while the Y axis displays the deposition power. The red arrows in the plot illustrate the general trend of compressive residual stress, film density, grain density, and refractive index, which increase simultaneously when the deposition temperature and power are elevated or when changing the deposition source from MF to HiPIMS. Put differently, these four parameters of the films tend to rise with the energy level involved in the deposition process.

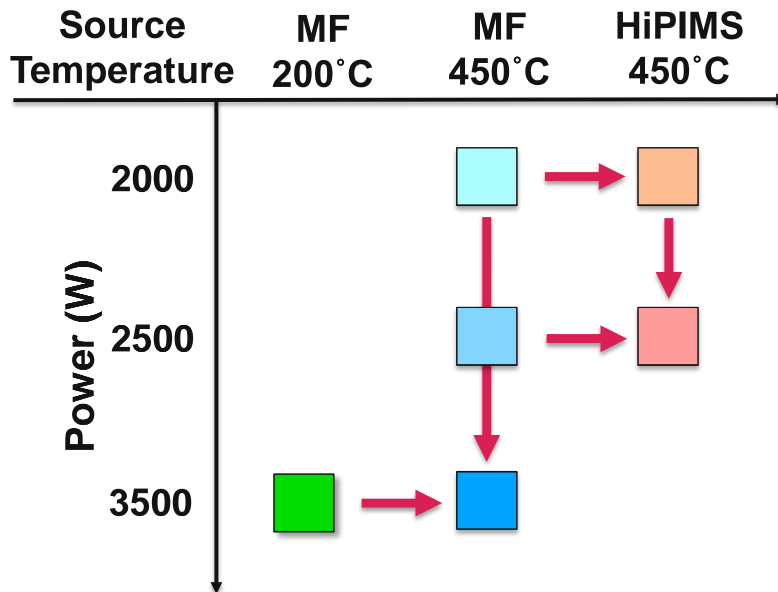

Figure 3-12 – Map of samples influenced by the power source, power and deposition temperature. The direction of the arrow indicates the general trend of the increase in grain size, residual stress, film density, and refractive index. The colour code using in this Figure is coherent with the colours employed for each sample in previous figures.

The combined use of MF and HiPIMS can be considered as an intermediate approach that has a significant impact on both the deposition rate and the reduction of residual stress, in comparison to using only HiPIMS.

3.7. Conclusion

Alumina thin films were deposited onto silicon (100) substrates using HiPIMS and MF magnetron sources with an active feedback reactive sputtering controller in dynamic mode at different temperatures and powers. Amorphous alumina was obtained at 200°C for MF, even at higher power values of 3500 W. However, raising the temperature to 450°C resulted in the formation of γ-Al_2O_3 with similar grain sizes (5-7 nm) regardless of the source configuration and power used. As there were no noticeable texture effects and the film thickness remained consistent, the observed fluctuations in the intensity of the diffraction peaks were attributed to changes in the density of γ-Al_2O_3 grains within the films. The films exhibited a columnar growth for low powers (2000 W) and a V-shaped structure for 2500 W. However, the microstructure of films deposited using both power sources was similar, which was attributed to the relatively high temperatures of the deposition process.

As the energy involved in the deposition process increased (i.e., higher deposition temperature, source power, and use of HiPIMS instead of MF), the grain density, compressive residual stress, film density, and refractive index increased in parallel. The films deposited at lower powers (2000 and 2500 W) using MF demonstrated the lowest values of compressive stress (-0.5 GPa), which were attributed to thermal effects. On the other hand, films deposited using HiPIMS showed significantly higher values, reaching up to -10±1.6 GPa (mostly intrinsic), for the same deposition powers. The reason for this was attributed to the lower deposition rate of HiPIMS (around 5 times lower) and the increased energy and density of the ions bombarding the substrate. The hybrid MF+HiPIMS configuration enabled the reduction of stress down to 4.10±0.6 GPa, partly due to the increased deposition rate. It was observed that increasing the number of MF pulses from 5 to 10 resulted in a significant improvement in the deposition rate, approaching the values obtained with MF alone, while the residual stress remained nearly constant. Therefore, there may be a limit to the potential reduction of residual stress in films deposited by HiPIMS through intercalation of pulses of other sources between HiPIMS pulses. Finally, films deposited by HiPIMS showed the highest grain and film density, approaching values close to

the bulk γ-Al_2O_3 reference. Furthermore, the refractive index showed an increase up to $n_{632.8}$ = 1.740, which was in close proximity to the values documented for α-Al_2O_3. A correlation was observed between density and refractive index in these films, in agreement with the behaviour predicted by the Lorentz-Lorenz equation.

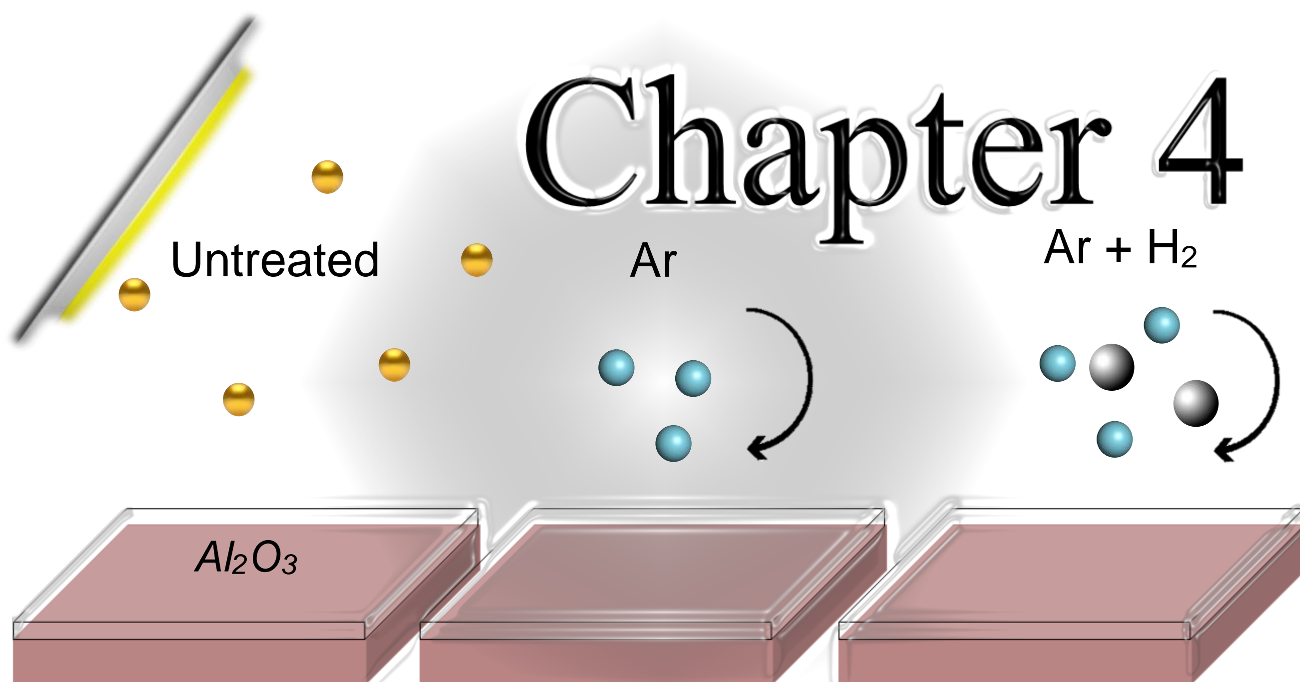

4. Selection and optimization of Au/Al_2O_3 deposition conditions

In the previous chapter, different approaches for alumina deposition were presented. This chapter is devoted to set some general parameters for the deposition of gold in alumina. In that regard, Chapter 4 bridges the connection between Chapter 3, alumina films, with Chapter 5, influence of the surface treatment on the Au growth on alumina. Therefore, this chapter is sub-divided into two sections. In the first one, some considerations regarding the deposition of Al_2O_3 *are discussed. In the second one, a quick screening across different deposition parameters of Au on* Al_2O_3 *is carried out.*

4.1 Optimization of the alumina surface properties for Au NPs deposition

For the preparation of alumina films with Au nanoparticles on top, the first decision is about which power source will be used for alumina deposition, either MF or HiPIMS. As HiPIMS is a newer technology and there is limited literature available on its use, HiPIMS was chosen to deposit it. However, the surface of alumina films prepared using HiPIMS shows several features which are correlated with the HiPIMS process (see Figure 4-1). Thus, few spots are observed in the surface of the film deposited by MF (Figure 4-1b), while the areal density of defects in the surface of a film deposited by HIPIMS is much higher (Figure 4-1a).

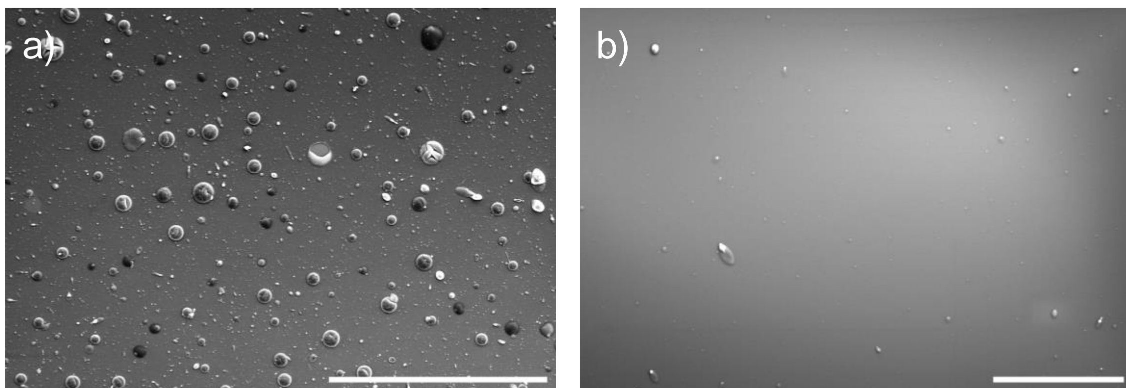

Figure 4-1 – Top-view SEM images of a) HiPIMS film and b) MF film, both deposited at 450°C with 200 nm of thickness. Both scales represent 100 μm.

Two different types of defects can be identified in the top of the surfaces deposited by HiPIMS (see Figure 4-2a); in one hand, we find smaller particles with irregular shape (pink arrow), which can be explained by the droplets emission from the target caused by the arcing occurring during the deposition process, even under the feedback control (cf. Figure 3-1 of the previous chapter). In the other hand, there are larger features with regular circular shape (blue arrow in Figure 4-2a), whose origin is connected with the high levels of residual stress were measured for HiPIMS films (cf. Figure 3-10 of previous chapter). Figure 4-2b shows a x-section TEM image of the same film, where a local delamination can be identified. In these points, the residual stress overcome the adhesion of the silicon substrate and the alumina film, and spherical 'bubbles' are originated as a consequence.

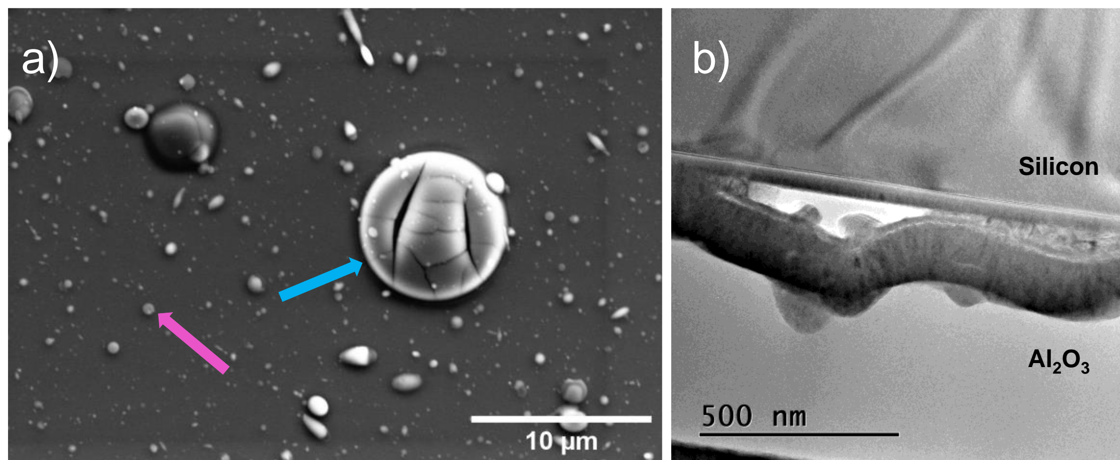

Figure 4-2 – Closer look to the surface of Alumina deposited by HiPIMS a) Top-view SEM image with two types of features: first, irregular particles from the discharge (indicated by the pink arrow); secondly, circles that are related to punctual adhesion issues and large stress, resulting from a large ion bombardemnet during HiPIMS (indicated by the blue arrow). b) TEM image highlights this local delamination.

The high level of stress causes a large curvature of the coated substrates, which can be appreciated in Figure 4-3a, where the profiles of the as-deposited substrates (height as a function of the scanning length of 1 cm) by HiPIMS (red line) and by MF (blue lines) are depicted. The stress level is much higher for HIPIMS (- 10 ± 1.6 GPa) leading to a larger curvature compared with MF at 2000 W (- 0.7 ± 0.3 GPa). In addition, to the larger curvature of the HiPIMS profile, many "spikes" are detected during that scan, as a consequence of the issues reported before. To quantify the roughness of the samples, a polynomial function was subtracted from the raw data, leading to the profile illustrated in Figure 4-3b. Finally, a smoothed profile (adjacent averaging of 1000 points over a profile that contains 50 000 points for 1 cm length, black line in b) was subtracted to eliminate the long-range oscillations still present in the profile. The overall result of this procedure is illustrated in Figure 4-3c, where a horizontal profile can be appreciated.

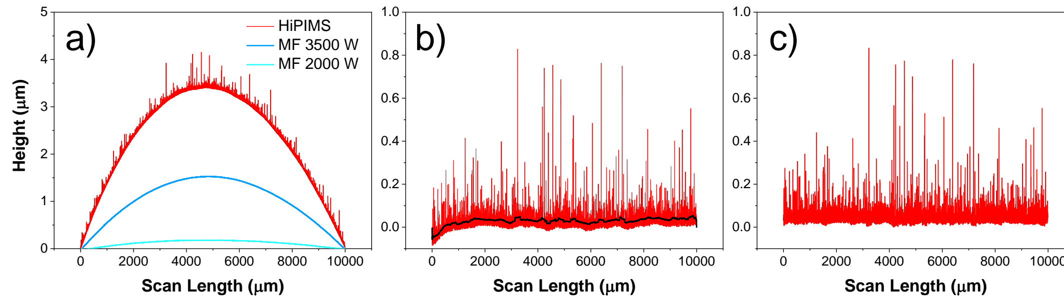

Figure 4-3 – a) Profilometer scan on an Al_2O_3 surface produced using HiPIMS 2500W and MF 2500W and 3500W at 450°C. b) scan after subtraction of a polynomial function c) scan after subtraction of an average line (black line in b)).

The histogram of Figure 4-3 is illustrated in Figure 4-4, together with others corresponding to profiles of coatings produced by both MF and MF+HiPIMS. It is important to note that the histograms were not plotted with equal bin sizes, thus, direct comparisons among them (e.g. areas) are not valid.

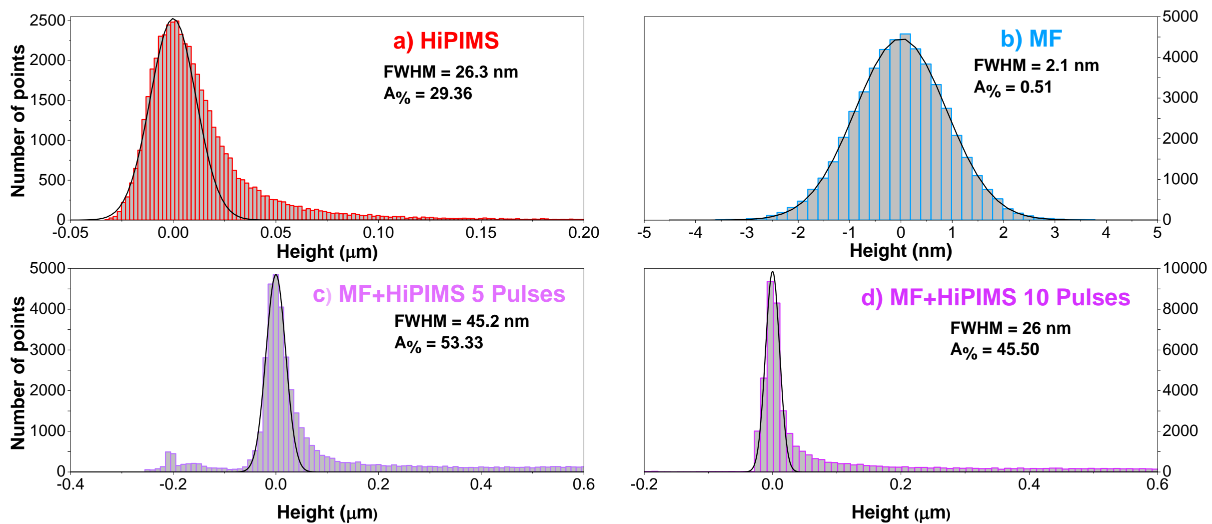

Figure 4-4 – Histograms of the height profiles for different depositions. a) HiPIMS b) MF c) MF+HiPIMS with 5 pulses and d) MF+HiPIMS with 10 pulses. Black solid lines represent Gaussian fittings. The histograms were displaced horizontally to set the position of the Gaussian curves to zero. Each histogram has different bin size.

It is observed that the histogram of the coating deposited by MF is symmetric (Figure 4-4b), and it can be fitted nicely to a Gaussian function (black lines in Figure 4-4). That Gaussian represents the roughness of the coating, which can be accounted by its full width at half maximum (FWHM). In contrast, the other histograms are clearly asymmetric, due to the presence of these features. In these cases, Gaussian functions were also fitted to each histogram (represented

by black solid lines), trying to reproduce the overall behaviour of the peak, particularly the left side (i.e. valleys of the roughness, which are not affected by particles or droplets). In order to understand better these two surface behaviours, a schematic was drawn, Figure 4-5. The Gaussian curve represents the “natural roughness” of the film and the tail of the curve corresponds to the droplets/contaminations of the surface.

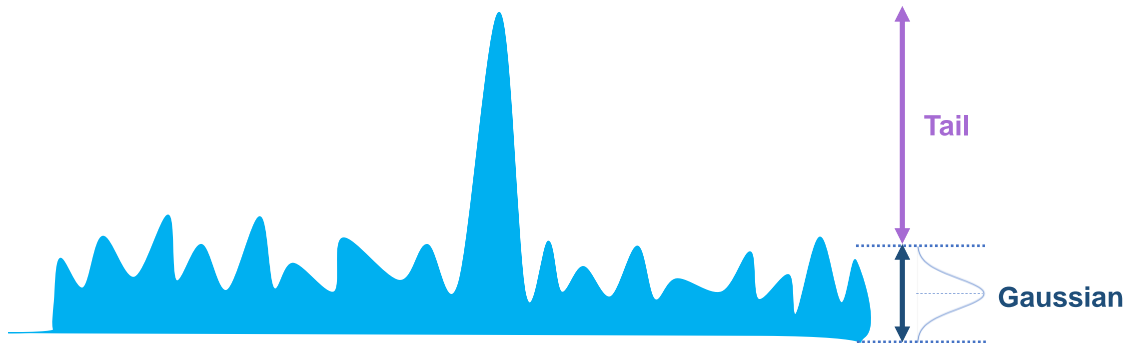

Figure 4-5 – Schematic representing the "natural roughness” given by the Gaussian curve, as well as the effect of particles and droplets, which are represented by the tail of the same curve.

These results indicate that the ‘natural roughness’ (i.e. excluding particles and droplets effects) of the film deposited by MF (2.1 nm) is a factor 10 lower than the film deposited by HiPIMS (26.3 nm). This may be connected to the lower crystallinity of MF films, or to a different film growth. In addition, the film deposited by MF+HIPIMS (10 pulses) shows a similar FWHM than HiPIMS (26 nm), while it is almost doubled (45.2 nm) for the film MF+HIPIMS (5 pulses).

Other interesting features can be interpreted from the histogram plots. For instance, the delamination of the films can also be seen in Figure 4-4c, where a small peak at -0.2 μm, corresponding to the film thickness, is present. In fact, the % area of the histogram not covered by the Gaussian function ($A_{\%}$) serves as a measurement of the presence of particles or droplets in the surface of the films. That parameter changes from 0.51% to 29.36% when transitioning from MF to HiPIMS. The corresponding values are even higher for MF+HiPIMS, where 5 pulses lead to 53.33% and 10 pulses to 45.50%. This suggests a lower adhesion or a higher instability during the MF+HiPIMS deposition, where more droplets were ejected from the target onto the substrate compared with MF and HiPIMS

alone. For a realistic comparison between all the histograms, Figure 4-6a represents the histograms of these profiles calculated using the same bin size. Consequently, the areas under each histogram are the same, since all the profilometry data was scanned with the same length and number of points. However, this cannot be appreciated in Figure 4-6, since a logarithmic scale is used in the Y axis to gain insights from the plots. For instance, if a linear scale would be used, the histogram of the MF sample (which is very narrow and 'intense', max at 3×10^4) would dominate the features of the others (max. at 7×10^3).

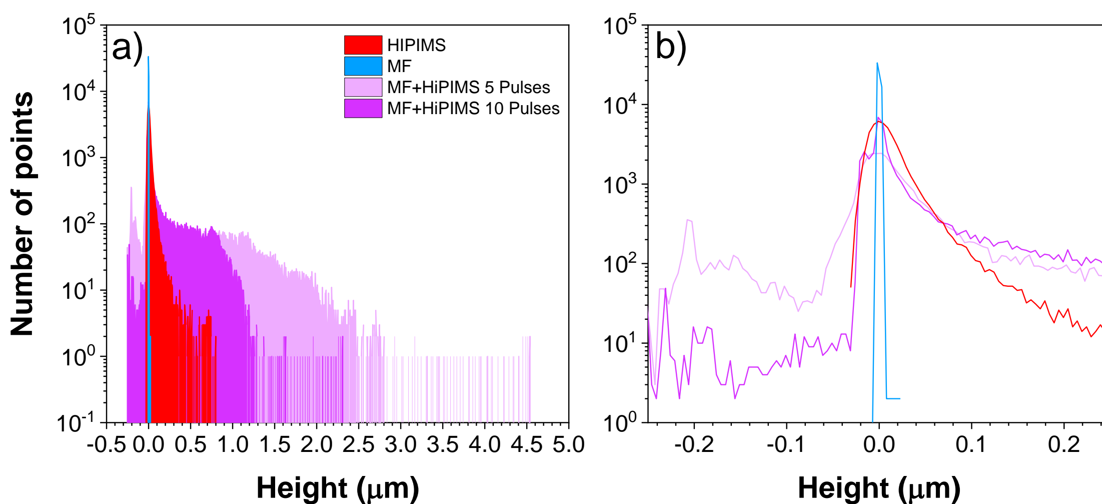

Figure 4-6 – a) Histograms of Figure 4-4 re-calculated using the same bin size and represented in a logarithmic scale b) Detailed view of the around the origin.

In this plot we can observe the MF coating (in blue) has a much sharper peak than any of the others, indicating the much lower roughness, compared to the HiPIMS (red) and MF+HiPIMS (purple) coatings. In addition, points are found up to really high values of particle size (up to 4.5 μm for the film deposited with MF+HiPIMS with 5 pulses), which is remarkable considering that the thickness of these films is about 200 nm. In fact, these values of thickness can be inferred from the detailed view of the histograms of Figure 4-6b, where both films deposited using the MF+HiPIMS configuration show points at x=-0.2 μm, which correspond to points where film delaminated. In that figure, the much narrower nature of histogram of the film deposited using MF (lower surface roughness) can be clearly appreciated. To minimize these issues detected when HiPIMS is used, we decided to reduce the deposition time, and the thickness of the films.

Figure 4-7 illustrates HiPIMS films produced at room temperature with a low thickness (approximately 10 nm), where a reduced number of droplets is observed, resulting in smoother films. In one hand, the reduction of process time reduces the density of particles originated by target arcing. In the other hand, the lower thickness of the films reduces the likelihood of delamination, since residual stress operates in a lower amount of deposited material. As a result, fewer circular features are observed in these deposits. For this reason, alumina films will be produced at room temperature with a thickness of around 10 nm for the deposition of gold nanoparticles. The use of room temperature for deposition avoids any thermal influence on the subsequent gold deposition, and at it becomes the only viable choice when depositing Au@Al_2O_3 multilayers.

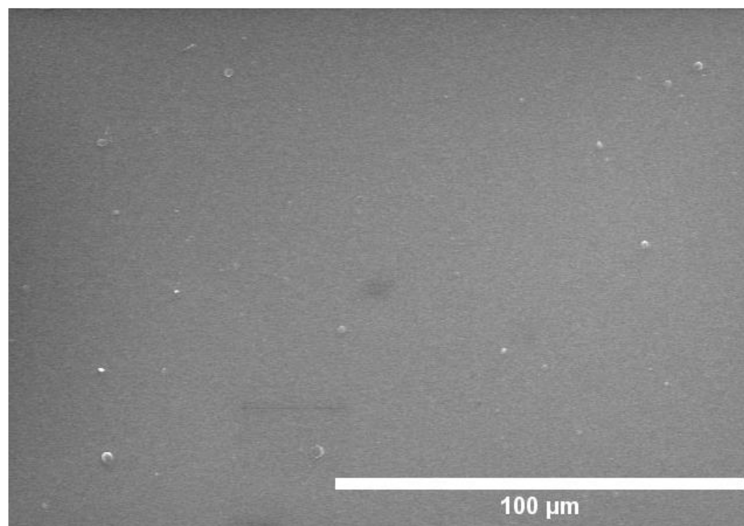

Figure 4-7 – Top-view SEM images of a 10 nm thin film deposited by HiPIMS at room temperature.

In any case, the presence of these particles does not have any major influence of the deposition of Au; when depositing gold nanoparticles on these thin layers of alumina, we can identify three different regions, as seen in Figure 4-8. The first region is a dark area, which consists of alumina without Au NPs (which were removed by scratching the surface). In the second region, Au NPs can be detected. In the third region we can identify an Al_2O_3 bubble coated with Au NPs, and no significant difference from the previous region can be observed.

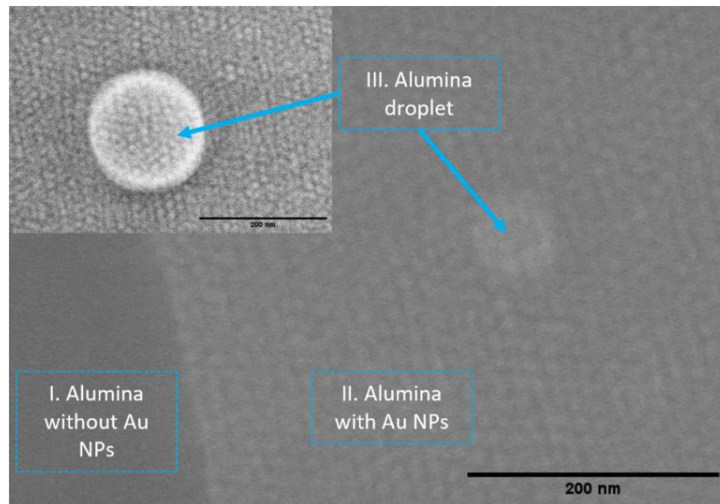

Figure 4-8 – Top-view SEM images with different zones I) Alumina without Au II) Alumina with Au NPs and III) Au NPs in a droplet. Both scales represent 200 nm.

These droplets can also be detected when scanning the surface of the Au/Al_2O_3 films by AFM, as seen in the bottom-right corner of Figure 4-9a and b). In these cases, the lines where the particle is located (from y=0 to y~50 in this example) are not considered in the further analysis.

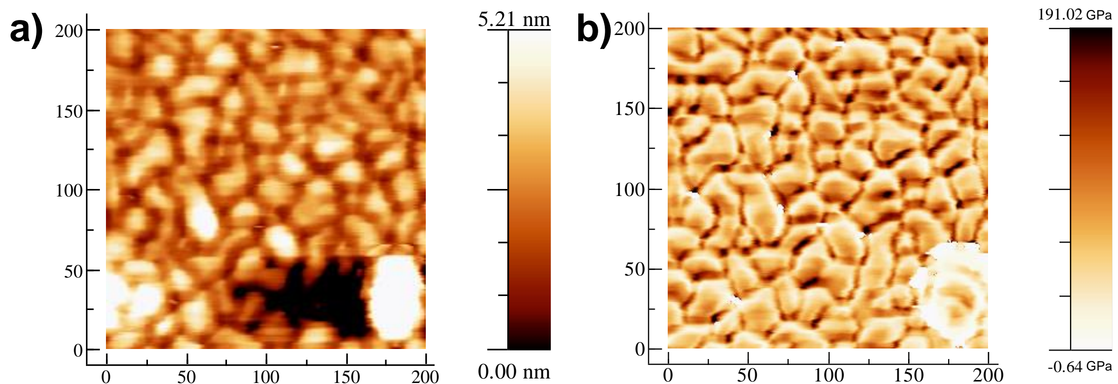

Figure 4-9 – AFM images of Au NPs deposited on alumina. a) Topography. b) Stiffness. The units of the x and y axes are nm. A particle or droplet can be observed in the bottom-right corner.

4.2 Conditions of deposition of Au nanoparticles deposition parameters

The following chapters of this Ph.D. Thesis focus on the study of Au NPs deposited on Al_2O_3 surfaces. Table 4-1 summarizes the deposition conditions of Au in the samples studied in this Ph.D., and the different colours indicate the location of each one. The influence of two major experimental conditions has been explored, which are connected to i) the plasma treatment of the Al_2O_3 surface prior Au deposition and ii) the Au sputtering. Therefore, the three left columns of Table 4-1 summarize the sputtering conditions of Au (source type, power and duty cycle). The conditions of Ar+H_2 plasma treatment of the Al_2O_3 surface prior Au deposition (H_2 flow and duration of the treatment in mins) are indicated on the fourth column and the top row of the four right columns. The values included in these columns indicate the duration of Au deposition in seconds (between 10 and 80 s). Au has been always deposited on Al_2O_3 films deposited by HiPIMS at room temperature (i.e. amorphous Al_2O_3), except two samples where a temperature of 450ºC has been used (i.e. γ-Al_2O_3). In these two cases, the deposition of Au was delayed, to allow the alumina film to cool down back to room temperature. All the coatings were deposited in dynamic mode, which involves moving the substrates in an oscillating motion in front of the target (with a rotation speed of 5 rpm). The amplitude of the movement was 70° and 15° for Au and Al_2O_3, respectively. On the other hand, the Ar+H_2 plasma treatment was performed in static mode. Finally, the term 'ML' indicates the deposition of Au@Al_2O_3 multilayers. To select the most interesting conditions, a quick screening of different parameters was carried out. To do so, the absorbance of the samples was compared, while trying to find conditions where a good LSPR can be obtained.

Table 4-1 – Deposition parameters of Au explored in this Ph.D. Sputtering conditions (source type, power and duty cycle), and characteristics of the Ar+H_2 plasma treatment of the Al_2O_3 surface (flow of H_2 and duration). The values of the cells represent the deposition time of Au in seconds (all between 10 to 80 s), and the dash (-) indicates that such condition was not explored. Au was grown on alumina deposited at room temperature in all cases, except 2 samples where the deposition temperature was 450ºC. The term 'ML' indicates 'multilayer'. Colours indicate that samples are included in Chapter 4 (Figure 4-10, Figure 4-11, and Figure 4-12), Chapter 5 and Chapter 6.

Power Source	**Power (W)**	**Duty Cycle (%)**	**H_2 flow (sccm)**	**Ar+H_2 plasma treatment time (min)**			
				30	**20**	**10**	**0**
DC	67	100	-	-	-	-	10,20,30,40
	32	100	0	-	60	-	60 (450°C)
			1.5	30	30	30	
			3.0	30	60 (450°C) 10,20,30,40, 50,60,70,80 ML(10,30,60)	30	10,20,30, 40,50,60
Pulsed DC	43-58	40	3.0	-	30	-	30
		20		-	30	-	30
		4.1		-	30	-	30
		1.5		-	30	-	30

In the next section, the effects of the following process conditions on the deposition of gold nanoparticles will be investigated: the power at 67 and 32 W, conditions of surface pre-treatment, and alumina produced at 450°C.

Figure 4-10 shows the influence of deposition power 67W and 32W on Au films deposited at different deposition times from 10-40 s and 10-60 s, respectively. This parameter is important, since it controls the deposition rate of Au. The depositions were carried out in dynamic mode. The UV-Vis absorbance is shown in Figure 4-10, and it is calculated with the expression $A = -log\ T$, where A is the absorbance and T the transmittance (between 0 and 1) with the maximum SPR peaks attributed to each deposition time.[311] For the films deposited at 67 W (Figure 4-10a), it is observed that the LSPR peak starts to broaden and lose the peak definition for films deposited at around ca. 20 s due to the beginning of percolation film growth mechanism. In contrast, for films deposited at 32 W (minimum value that the DC generator can apply),

Figure 4-10b, this behaviour only starts to appear around 50 s. This indicates that the percolation phenomena is delayed, and a higher control of the NPs deposition is attained. For this reason, all the following depositions of Au in DC will be carried out at 32 W.

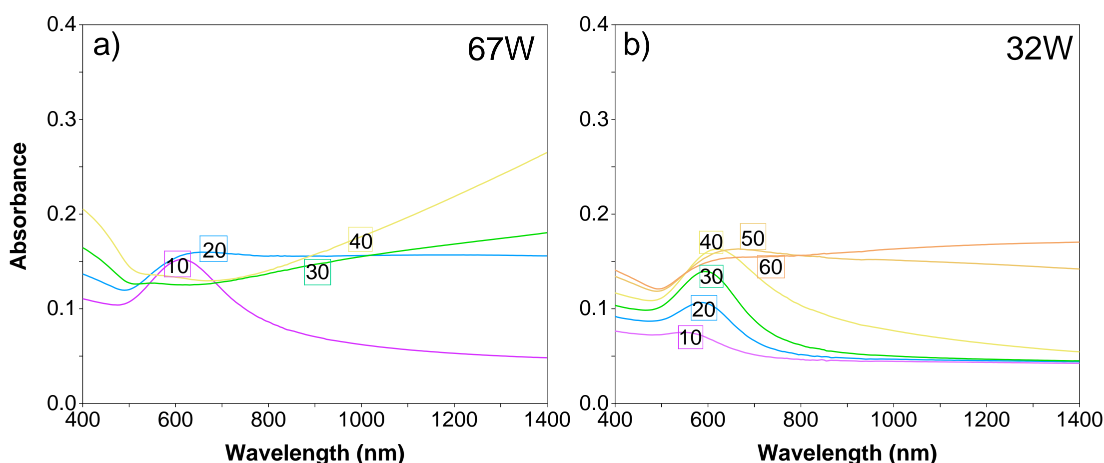

Figure 4-10 –The absorption spectra of gold clusters deposited on Al_2O_3 coatings with two distinct powers a) 67 W and b) 32W for different deposition times indicated in the figure. The squares indicate the SPR position of the maximum.

Figure 4-11 illustrates the influence of the deposition temperature of Al_2O_3 and its plasma surface treatment on the absorbance of different Au coated samples deposited for 60 s. The plasma was generated by 3 microwave antennas with a mixture of Ar (50 sccm) and H_2 (3 or 0 sccm).

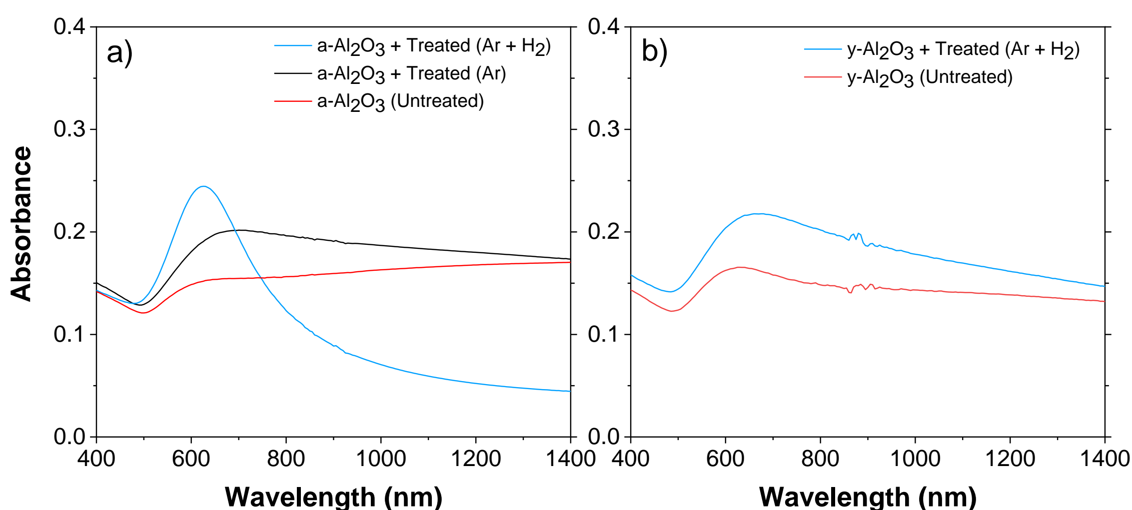

Figure 4-11 – The absorption spectra of gold clusters on a) amorphous Al_2O_3 at room temperature and b) γ- Al_2O_3 at 450°C with/without Ar and H_2 treatment.

The influence of the surface treatment is very relevant on amorphous alumina, as it can be observed in Figure 4-11a. The sample deposited with a treatment of $Ar+H_2$ reveals a pronounced LSPR peak with even higher absorbance (0.244) making this treatment the most suitable for the growth of Au clusters. In contrast, no peak is present in a film grown without plasma treatment. The film treated with Ar plasma shows a slightly better shape than the untreated sample, although the shape of the peak is clearly less defined than when H_2 is employed in the mixture; this result reveals that the presence of H_2 in the plasma treatment is crucial to obtain optimal results. Ondok et al.[5] indicated that when hydrogen is added up on the discharge, it favourably bonds to oxygen based on bond enthalpy. Consequently, it will disrupt the Me-O bond by forming O-H bond. Thus diminishes the content of oxygen atoms, which are bonded to Me atoms in such manner that oxygen deficiencies are produced and stoichiometry of MeO films is deteriorated.[5]

The deposition temperature of alumina controls if the film is amorphous or crystalline (cf. Chapter 3), and it is important for the following studies on depositing the Au NPs. Alumina deposited at 450ºC lead to the formation of γ-Al_2O_3 films (Figure 4-11b), where the $Ar+H_2$ plasma treatment has a much more limited effect. Both samples show similar spectra, although a higher intensity is observed for the sample that suffered the plasma treatment. It is worth mentioning that the untreated γ-Al_2O_3 shows a better spectrum than the amorphous (both red lines Figure 4-11). However, the amorphous alumina is clearly more sensitive to the $Ar+H_2$ plasma treatment than γ-Al_2O_3, leading to a distinct LSPR peak (both blue lines in Figure 4-11). This could be caused due to a higher structural stability of the (nano)crystalline form of alumina vs. the amorphous one. Therefore, alumina films deposited at room temperature were preferred (i.e., amorphous). In addition, lower values of surface energy are reported for amorphous alumina (0.97 J/m^2) than crystalline alumina (1.5 to 1.7 J/m^2), which is much closer to Au (1.51 J/m^2), so amorphous alumina is expected to promote the growth of nanoparticles instead continuous films (cf. Section 2.2). Finally, the deposition of a-Al_2O_3 facilitates the experimental operations (particularly important for deposition of multilayers) and reduces the thermal stress.

Finally, an optimization of the hydrogen treatment (H_2 flux and treatment length) was performed for Au films deposited for 30 s. The flux of H_2 was varied between 1.5 and 3 sccm, and the treatment time between 10 and 30 min, as it is depicted in Figure 4-12. The results are compared with untreated surfaces with Au deposition time of 20 s and 30 s. The objective was to find the best conditions which shift the LSPR peak to lower wavelengths, specifically close to the sample of 20 s, in order to obtain the smallest possible particle sizes and the most spherical clusters.[115,312,313] The best result was obtained with 3 sccm of H_2 with 20 and 30 minutes of treatment, where SPR changed from 615 nm (30 s without treatment) to 580 nm. Therefore, 20 minutes of plasma treatment were chosen to reduce the length of the treatment time.

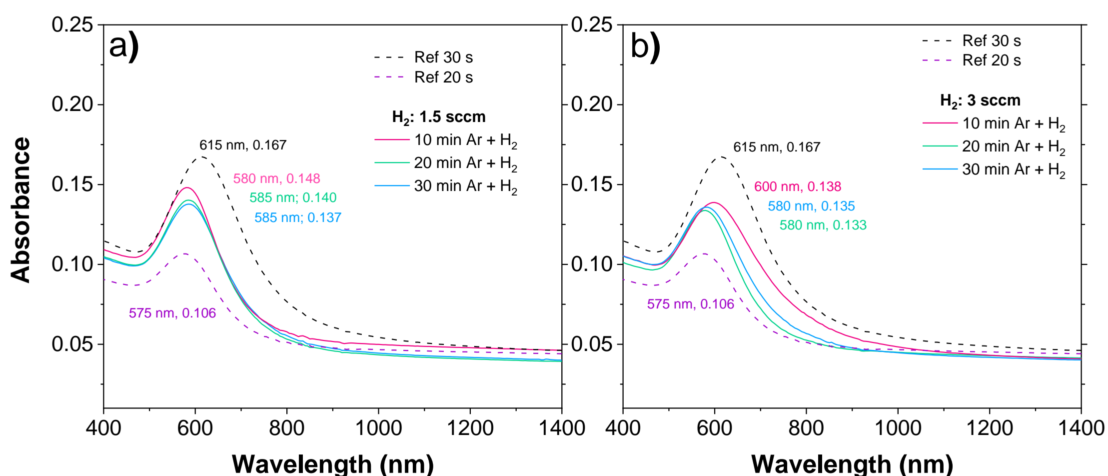

Figure 4-12 – Absorption spectra of alumina films deposited for 30 s and treated with argon and different fluxes of hydrogen a) 1.5 sccm and b) 3 sccm during 10, 20 and 30 minutes.

In the following chapter, alumina films will be produced by HiPIMS at room temperature with 10 nm of thickness. After, gold nanoparticles will be deposited by DC at 32 W at room temperature with different time depositions ranging from 10 s to 80 s, depending on the pre-treatment. The treatment of Ar (50 sccm) and H_2 (3 sccm) for 20 minutes was chosen, and such samples will be referred as <u>treated</u>. Samples without any surface treatment will be called <u>untreated</u>.

4.3 Conclusion

In this chapter, the optimal conditions for depositing gold nanoparticles onto alumina surfaces are determined. First, it was observed that alumina films deposited using HiPIMS at 450°C exhibited droplets, resulting in rough surface that is not ideal to the deposition of gold NPs. On the other hand, films deposited at room temperature (amorphous) had smoother surfaces (reduced occurrence of droplets), lower risk of delamination, and absence of thermal effects during subsequent gold deposition. Moreover, in the process of depositing gold nanoparticles (Au NPs) on γ-Al_2O_3, it was observed that gold percolation occurred more rapidly in crystalline films compared to amorphous films. For this reason, alumina films deposited at room temperature were selected. Additionally in this chapter, various factors were investigated during the gold deposition process on alumina. These factors included power settings and the utilization of argon and hydrogen pre-treatment. Regarding power settings, it was noted that lower values (32 W) yielded superior results, as they prolonged the time required for percolation, thereby enhancing control over the growth of gold. Regarding the pre-treatment aspect, it was demonstrated that the utilization of a mixture of argon and hydrogen resulted in a decrease in percolation compared to an untreated surface (without pre-treatment) and to coatings conducted solely with argon. The optimal parameters were chosen and studied in Chapter 5.

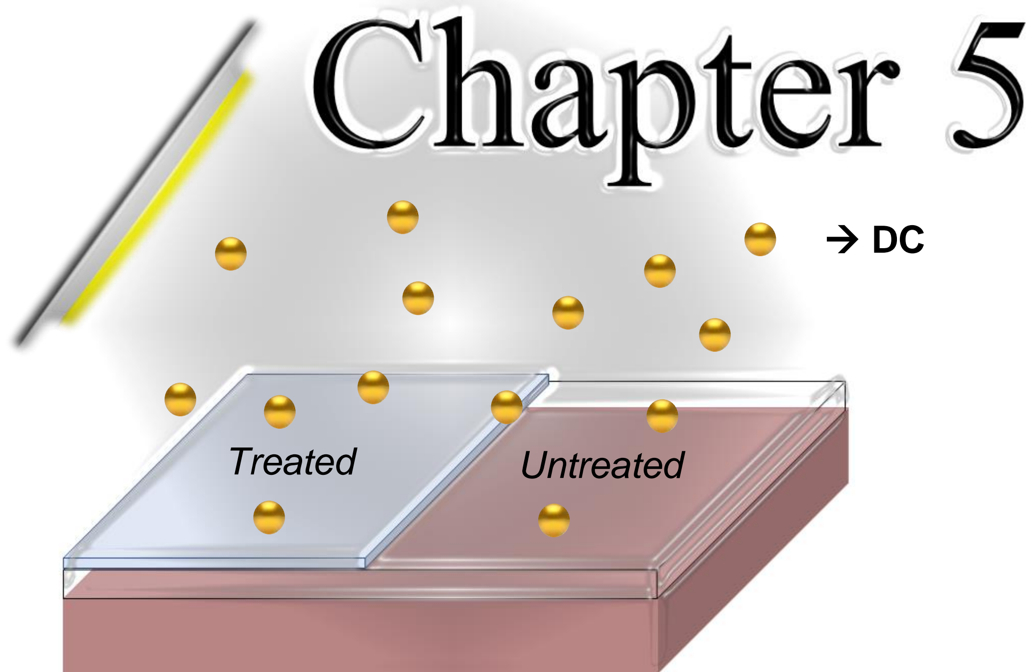

5. Deposition of Au/Al_2O_3 films

The objective of this chapter is to utilize the conditions selected in the previous one to deposit Au on Al_2O_3 with and without plasma treatment and analyse the growth of Au nanoparticles through the analysis of XPS spectra and AFM images using the method of Tougaard and the Height-Height correlation function, respectively. Finally, the optical properties of the samples are explained as a function of their growth characteristics.

For this study, two sets of samples were produced, with the only difference of the application or not of an Ar/H_2 plasma treatment on the Al_2O_3 coating prior to the deposition of Au. Thus, the first set (labelled as *Untreated*) was prepared without any pre-treatment on the alumina surface. In the second set (labelled as *Treated*), a pre-treatment of Ar and H_2 was performed before the deposition of Au by DC.

5.1 XPS results and analysis based on Tougaard method

The analysis of the photoelectron peak shapes provides information about the growth mode (i.e. layer-by-layer or islands, cf. Figure 2-8), the height and coverage of the particles formed on the surface of the substrate according to the Tougaard's method.[271,273,314–317] The Au 4f peaks overlap with the Al 2p and Al 2s peaks and the associated background, making the analysis unreliable. Therefore, the Au 4d peaks were analysed instead. Figure 5-1a and b) show the evolution of the Au 4d peak deposited on Al_2O_3 by increasing the Au deposition time for untreated and treated surfaces, respectively.

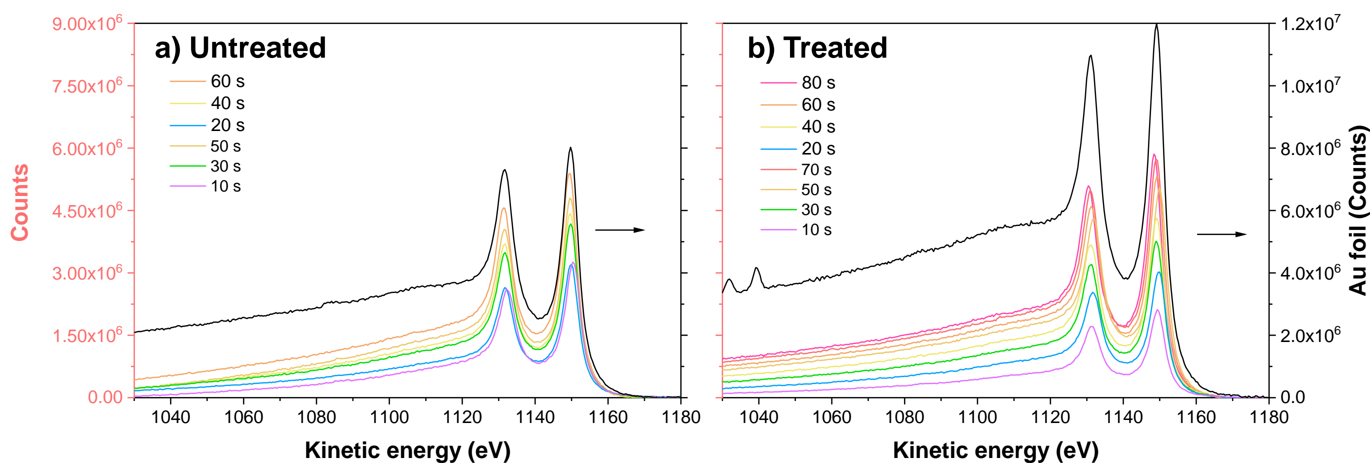

Figure 5-1 – Experimental Au 4d spectrum of gold deposited on a) untreated and b) treated alumina coatings for different deposition times, which are indicated in the figure. The black spectra represent the Au foil (reference) with the respective units on the right axis.

These spectra clearly show that the intensity ratio between the inelastic background (appearing at low kinetic energies, see e.g. 1050 eV) and the zero-loss peak (located at 1149 eV) increases as the amount of deposit (i.e. higher deposition time) increases. Further, for same deposition time, the background is higher for treated surfaces (cf. the intensity at 1050 ev), which indicates

qualitatively that the treated samples tend to grow more ‘vertically’ (i.e, island growth, Volmer-Weber), while the untreated samples tend to grow more ‘horizontally’ (layer-by-layer, Frank-Van der Merwe). These variations of the spectra with increasing the deposition time is due to a change in the inelastic-scattering processes that the Au electrons experience when they travel out of the material. This enables assessment of the average island height (h) and the surface coverage (c) of the deposit, as explained in Methods (Figure 2-31). The values of height and coverage were extracted from the distribution model used to fit the spectra (Figure 5-2). To do so, the experimental spectrum of the Au foil reference (J(E)) is analysed first, and the single-atom-spectrum (F(E)) can be obtained, since the Au concentration distribution is known (Figure 5-2). Then, the island height for the sample is calculated by the creation of a background whose subtraction from J(E) would lead to obtain a spectrum whose shape is consistent with the F(E) obtained from the foil reference Figure 5-2b. In other words, the background in Figure 5-2b is designed in such a way that the shape of the subtracted spectra (black line in Figure 5-2b) is as close as possible to the shape of the corresponding reference spectra (black line in Figure 5-2a). The coverage can be calculated by dividing the maxima of the subtracted spectra of the sample and the Au reference foil (i.e. a coverage of 100% would show the same intensities of the F(E) of the reference and the sample).

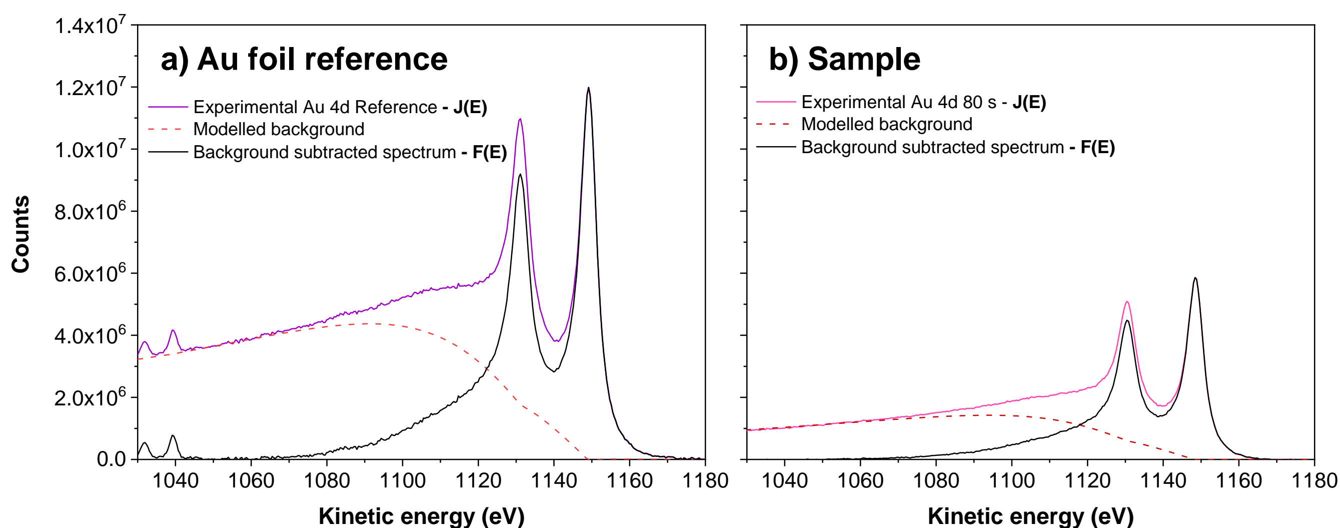

Figure 5-2 – Fitting of the experimental Au 4d spectrum with the modelled background and the subtracted spectrum for a) Au reference foil and b) Treated Al_2O_3 sample with Au deposited for 80 s. J(E) represents the experimental data and F(E) the subtracted background, i.e. the single atom spectrum.

Figure 5-3 shows the experimental spectra of the different samples and the Au foil references together with their corresponding backgrounds. It is clear the increase in background intensity over time. Moreover, it is evident that the background on the treated surfaces is higher when compared to the untreated surfaces. This observation is attributed to the greater island heights, which are associated with increased inelastic scattering when the deposition time is extended for the treated samples. In addition, it can be observed that the spectra of the untreated samples are closer to the Au reference than the treated samples; this reflects that the maximum coverage of the untreated samples is higher than in the treated samples (higher intensity ratios sample/reference).

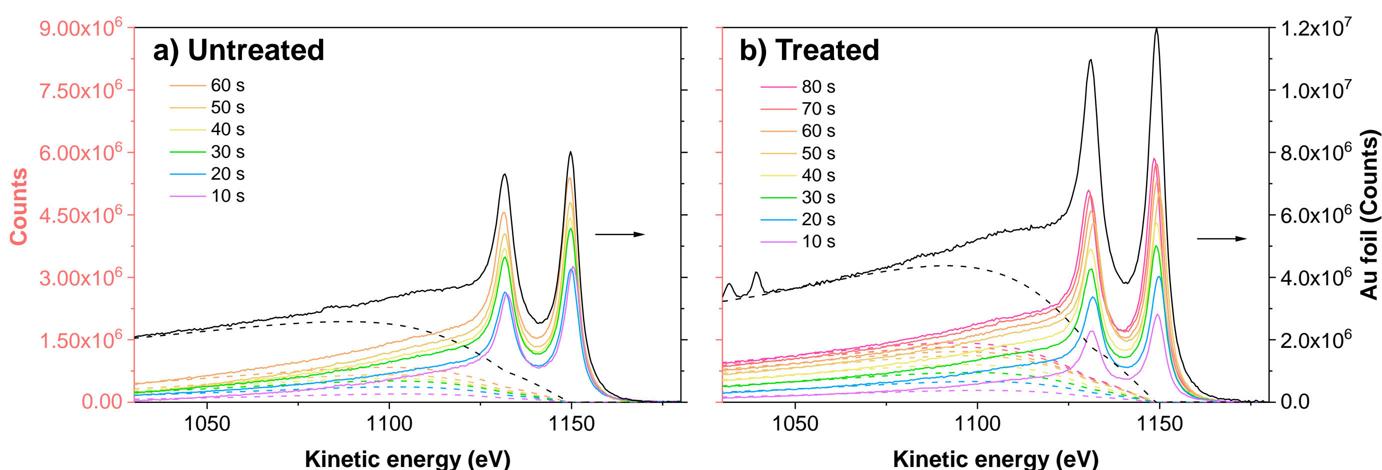

Figure 5-3 – Experimental spectrum for a) untreated and b) treated surfaces with their respective associated background. The black line represents the Au foil (reference) with the respective units on the right axis.

From the quantitative analyses of these spectra, the values of coverage and height are obtained, and they are plotted in Figure 5-4a depicts the amount of substance (AOS) vs. deposition time, defined as $AOS = c \times h$ (Eq. 5-1), which represents the Au volume measured in 'nm of full surface coverage'. It is clearly seen that treated surfaces show a higher linear slope compared with untreated surfaces, which reflects a higher deposition rate at longer deposition times.

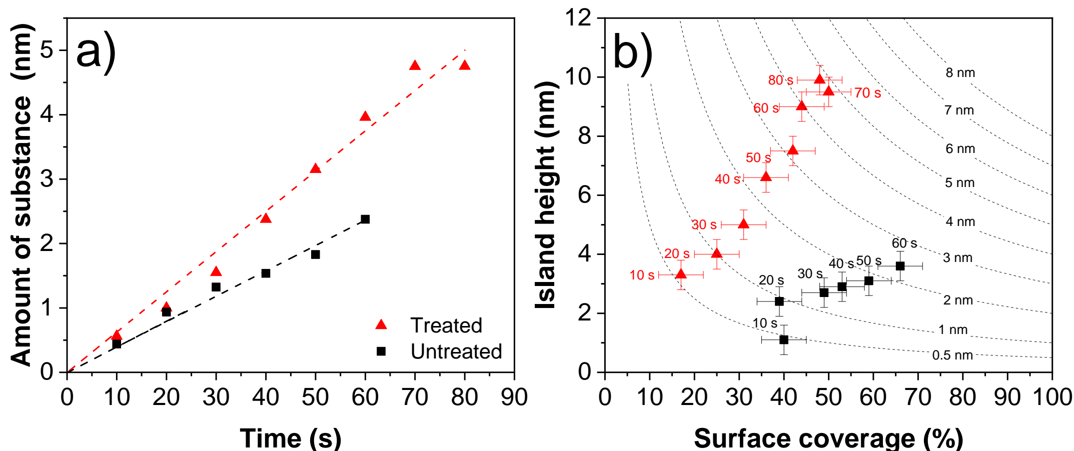

Figure 5-4 – Data obtained after XPS peak-shape analysis of spectra in Figure 5-3 for treated and untreated alumina surfaces. a) amount of substance (AOS) as a function of time, where the dashed lines represent linear fittings going through origin. b) island height vs. surface coverage. The dashed lines represent AOS isolines.

Figure 5-4b illustrates the variation of surface height and coverage depending on the amount of Au deposited for both surfaces. Additionally, the series of dashed curves represent isolines for a fixed deposited (AOS). [318] A point situated over a dashed line (e.g., 2 nm) indicates that the amount of material is equivalent to a film of 2 nm thickness with 100% coverage, although the distribution could be different (e.g., 4 nm height with 50% coverage or 8 mm height with 25% coverage). The Au deposited in treated surfaces have a tendency to grow more *vertically* (i.e. perpendicular to the substrate), i.e., stronger variation in height. In contrast, Au grown in untreated surfaces shows lower values of height and higher values of coverage, indicating a growth more '*horizontal*' i.e., parallel to the substrate.

5.2 SEM results

The SEM images of the untreated and treated samples are shown in Figure 5-5. The images indicate a growth in the cluster size with sputtering time.

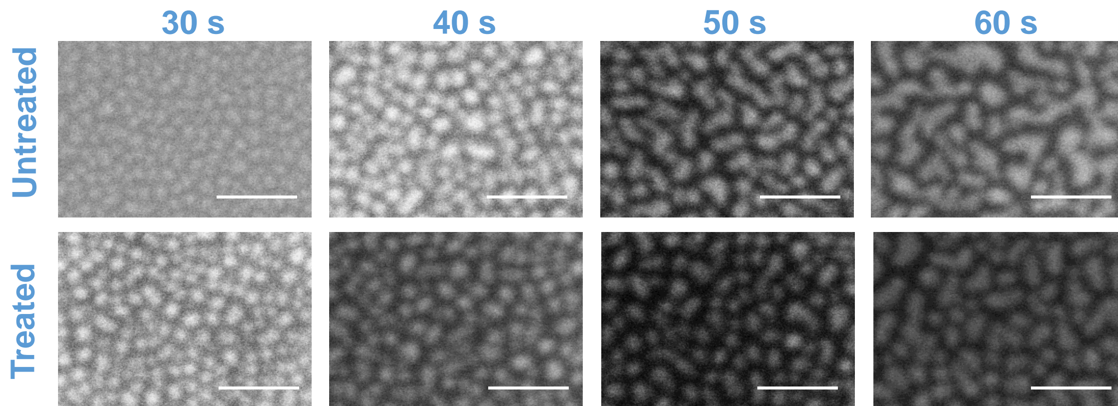

Figure 5-5 – Top view SEM images of Au nanoparticles deposited on Al_2O_3 films with depositions times from 30 s to 60 s. All the scale bars represent 50 nm.

Additionally, for deposition times less or equal than 40 s, more spherical shapes are attained. On the contrary, when increasing the sputtering time, the Au clusters tend to grow and coalesce between them and “worm-like” structures are observed, approaching a continuous film. The Au clusters are spread relatively homogeneously over all the samples. This growth is better explained by the Volmer Weber growth mode, which occurs when the adatoms have a strong affinity with each other instead of with the substrate, due to the high surface energy of metals. It is also observed that the images are very noisy. The reason is that alumina is an excellent electrical isolator, which leads to large charging under the electron beam. As a consequence, AFM analyses were carried out to characterize these films, and also gain information about the cluster height (Z coordinate).

5.3 AFM results and HHCF

The surface morphology of the samples was characterized using AFM, which allows obtaining high lateral resolution with low vertical noise.[319] Figure 5-6 represents the stiffness and topographic maps of gold clusters on treated and untreated surfaces. For each condition, at least three images were recorded, but only one of them was plotted after equalization (adjustment of the colour scale to represent the actual width of the height histogram). The surfaces are composed by rounded particles, which tend to agglomerate with deposition time, and create wider clusters, in agreement with SEM observations. It is worth mentioning that the colouring of the stiffness maps is inverted, with light colours representing the low value of stiffness. This is because gold, which is located on the top of the samples, has lower stiffness than alumina. As a consequence, it is expected that the minimum stiffness of the samples decreases with deposition time (higher coverage of samples with Au), which is observed. However, the maximum stiffness is not constant, as it would be expected since it reflects the value of the substrate. To analyse this behaviour in detail, the histograms of the stiffness images were calculated, and plotted in Figure 5-7.

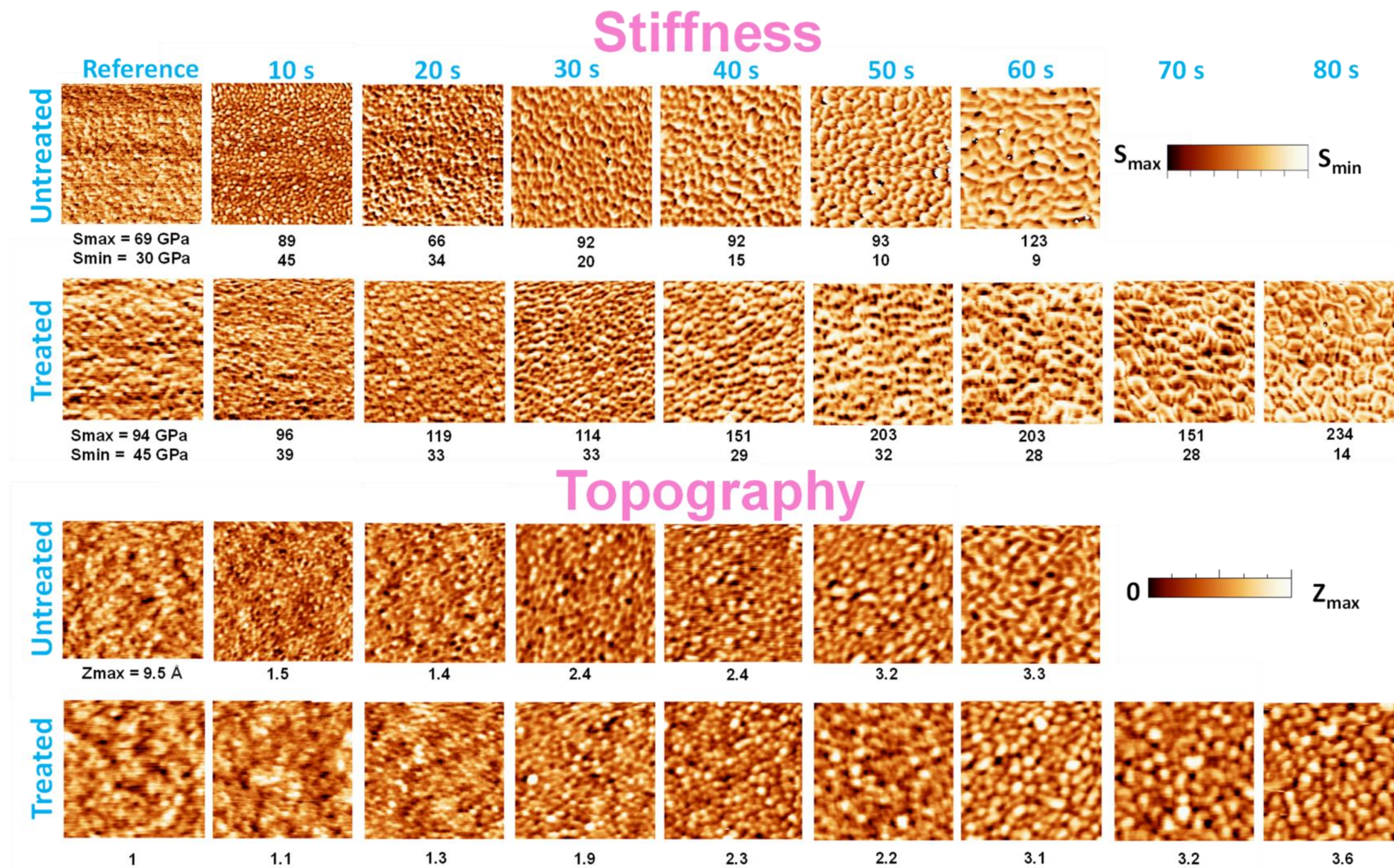

Figure 5-6 – Selected AFM stiffness and topography maps of 200x200 nm^2 scan area of the Au clusters deposited on untreated and treated alumina from 10 s to 80 s. The values of S_{max} and S_{min} (in GPa) and Z_{max} (in nm) are included below each image.

5.3.1 Analysis of the stiffness images

In Figure 5-7, it is observed a general broadening and leftward shift in the histograms for higher Au deposition times. Additionally, in both cases, increasing the deposition time resulted in an increase in the right tail of the histogram, which is particularly evident in the case of treated samples (Figure 5-7b). This is unexpected, since the highest values of stiffness should correspond to the alumina, and it should be constant.

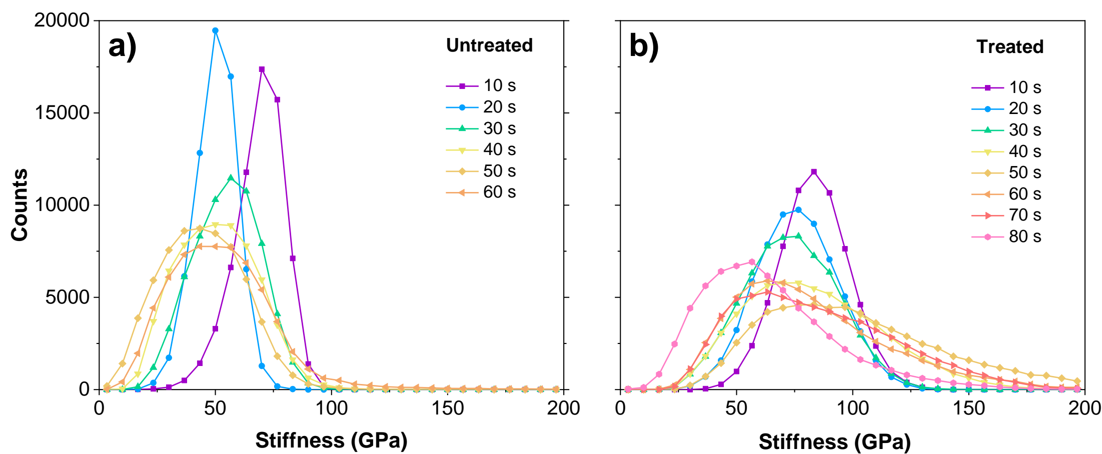

Figure 5-7 – Histograms of the stiffness images from Figure 5-6 for a) untreated and b) treated samples.

Therefore, the right side of the histograms provided unreliable information about the behaviour of the stiffness of the films, and it is likely an artifact of the measurement. Therefore, to monitor the evolution of surfaces with deposition time, we examined the left side of the histograms in detail, which represent the contribution of Au (and not the alumina substrate). To facilitate the analysis of the data on untreated and treated surfaces, the histograms were integrated, as shown in Figure 5-8. It should be noted that all points converge to the same value, as it represents the maximum number of points in an AFM image ($256 \times 256 = 65536$ points).

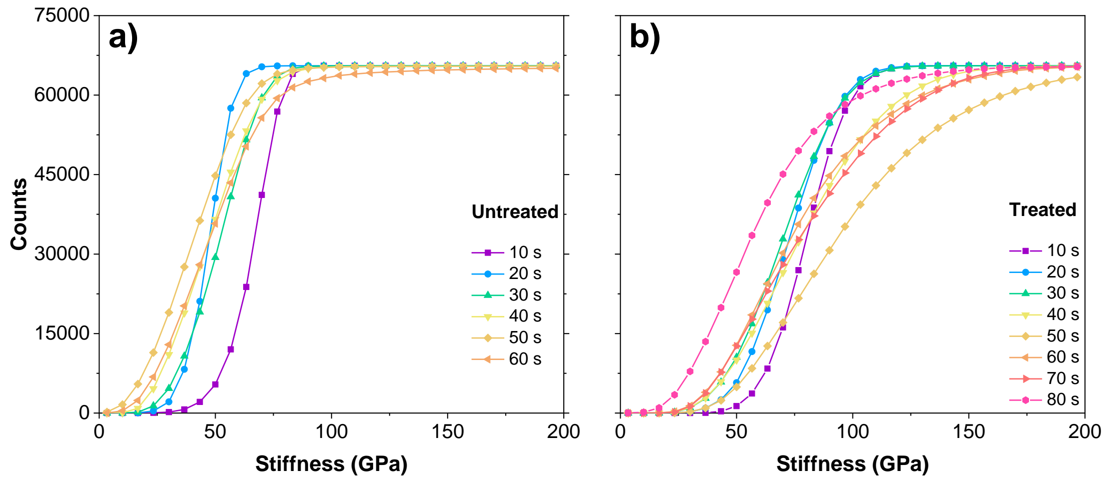

Figure 5-8 – Integrals of histograms of Figure 5-7 for a) untreated and b) treated samples.

To analyse the data and represent the behaviour of each curve, a threshold at 1% of accumulated counts was defined (ca. 655 counts). To determine its location (the stiffness where the threshold of 1% counts is located, defined as $S_{1\%}$), a linear line (dotted black line) was created between two consecutive points of the curve immediately below and over that threshold, as shown in Figure 5-9.

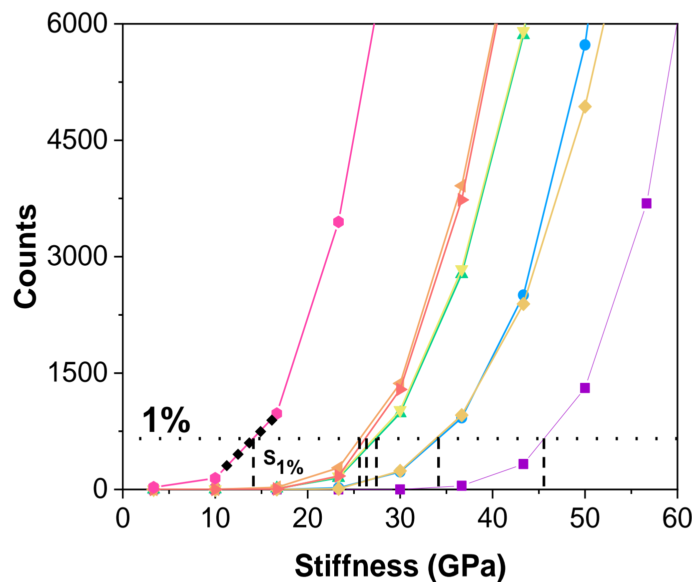

Figure 5-9 – Detailed view of the integrated curves of the stiffness histograms of the treated samples (Figure 5-8). The horizontal dotted line represents the threshold of 1% counts, which is used to characterize each sample. The values of $S_{1\%}$ for each sample are illustrated with vertical dashed lines.

The values of $S_{1\%}$ for each sample depending on the deposition time were plotted in Figure 5-10. In Figure 5-10a, all measurements conducted for the stiffness images are depicted. In general, a large dispersion of data is observed. The hollow squares and triangles indicate samples that exhibit defects (i.e. droplets) and/or have lack of quality of the image. Figure 5-10b displays the average value for each condition considering all the points. Due to the dispersion of data, the error bars are very large for some conditions. Therefore, a new plot was created (Figure 5-10c) where the doubtful data (hollow points in Figure 5-10a) were excluded from the averaging.

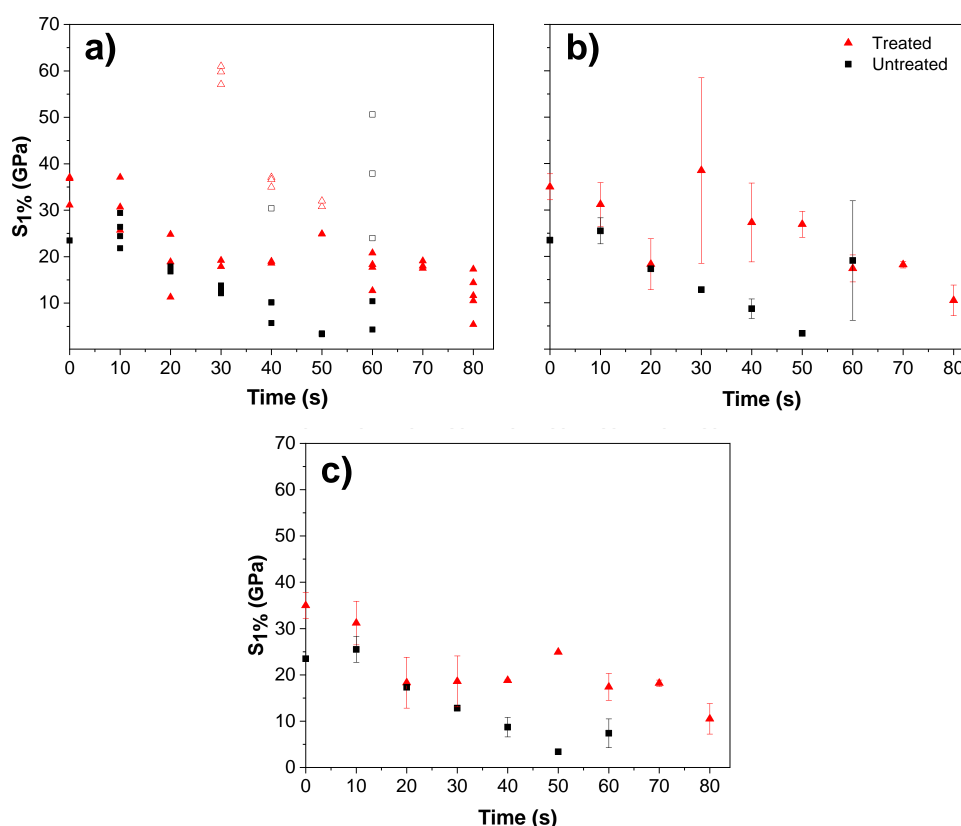

Figure 5-10 – Stiffness at 1% for untreated and treated surfaces at different deposition times. a) Measurement of all the images. b) average of each condition, considering all the datapoints in (a). c) average of each condition, excluding the hollow points in (a).

It appears to be a general trend of decreasing stiffness values as deposition time increases, following a higher amount of deposited Au. In addition, the values of untreated samples are lower than the treated ones, in agreement with the larger coverages observed for the untreated samples by XPS. Nonetheless, the trends are noisy, and there are certain points that do not follow the overall trends. This

can be explained by the influence of the AFM tip on the measurement; the measurements were conducted using a silicon AFM tip, whose geometry was altered due to usage, leading to a potential impact on measurement accuracy. In this particular case, the presence of a high modulus alumina film was likely the primary cause of this change. Since the tip was not calibrated, it resulted in an increase in modulus values, rendering the measured data unreliable for future analysis. Nevertheless, a similar effect is not noticeable in topography images depicted in Figure 5-6. In fact, stiffness and topographical images reveal equivalent microstructural details, as it can be easier observed in Figure 5-11, which compares both type of images from untreated and treated surfaces. In both cases, the microstructure of the films is the same regardless the image used, and we can clearly identify any sample using any of the images (stiffness or topographical). Therefore, the problem of the stiffness images is not a modification of lateral resolution (i.e., the images are equivalent), but a lack of accuracy of the values of stiffness (i.e. a doubtful colour coordinate). As a consequence, the stiffness images will not be utilized for future analysis, and our attention will be focused on topographical images.

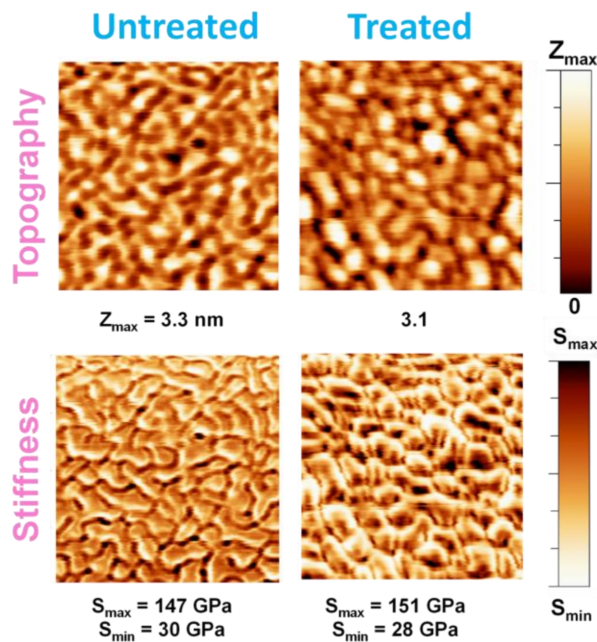

Figure 5-11 – Stiffness and topography for untreated and treated alumina surfaces with Au deposited for 60 s and 70 s, respectively.

5.3.2 Analysis of the topographical images using the height-height correlation function

Figure 5-12 shows the log-log plot of $H(r,t)$ obtained from selected untreated and treated AFM images as a function of distance, *r*. In addition, the fittings to Eq. 2-27 are illustrated.

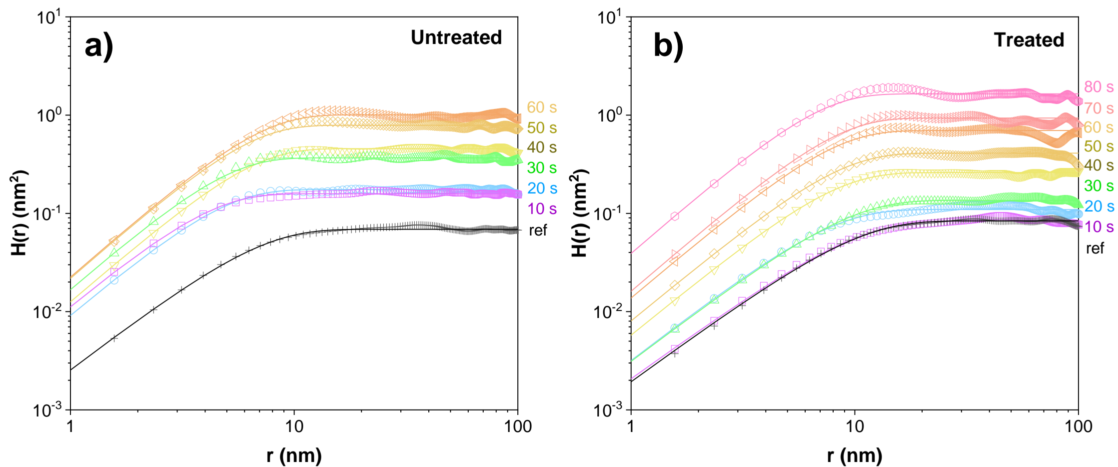

Figure 5-12 – log-log plot of the HHCF for gold clusters deposited on a) untreated and b) treated alumina surfaces with deposition times from 0 s to 80 s. The solid lines represent the fittings to Eq. 2-27.

The equilibrium value of $H(r,t)$ increases for higher Au deposition time, indicating the increase in the RMS roughness. The values of w, ξ and α were obtained from the fittings of the HHCF using Eq. 2-27, as shown in Figure 5-13. The error bars correspond to the standard deviation of values obtained from HHCF fittings of several AFM images (at least 3) for each condition.

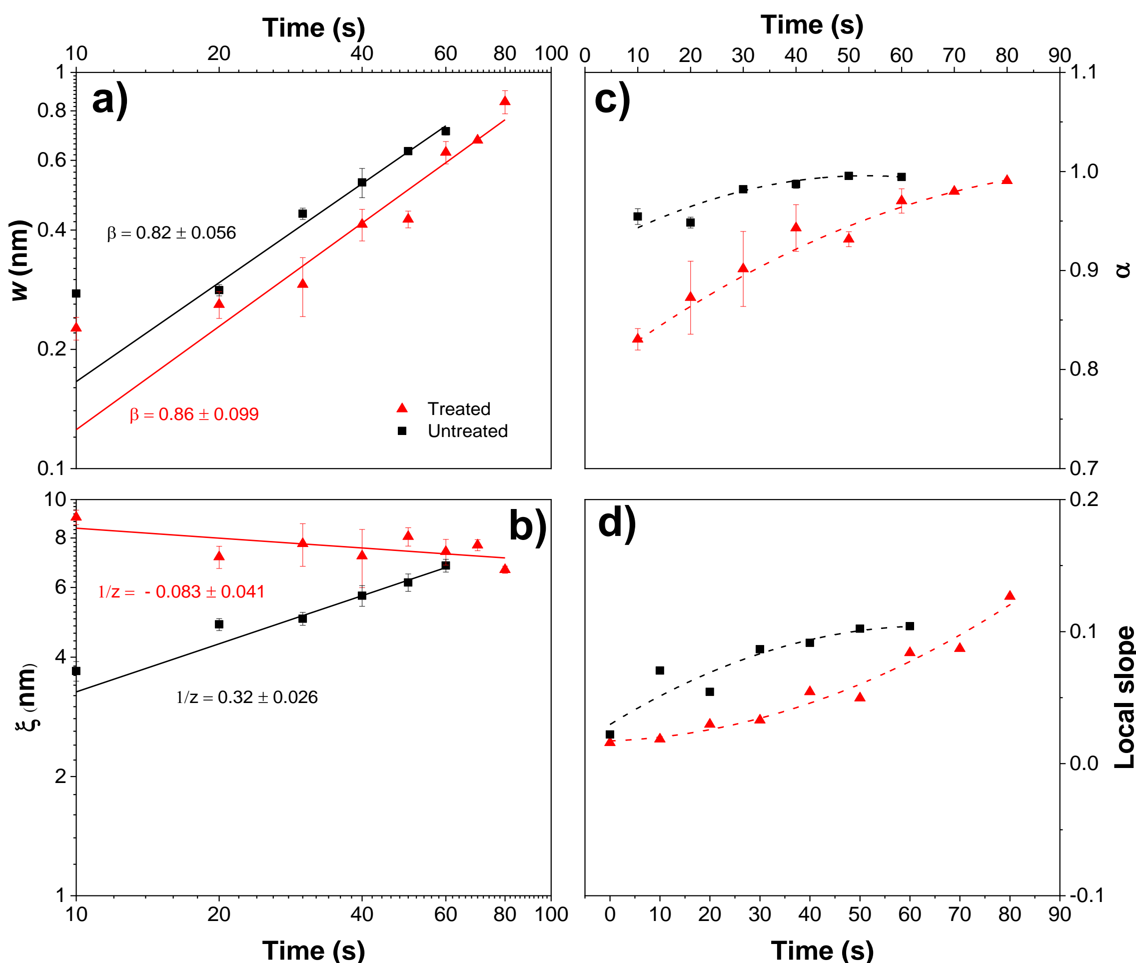

Figure 5-13 – The variation of a) roughness (w), b) correlation length (ξ), c) Hurst parameter (α) and d) local slope with deposition time. Straight lines in (a) and (b) represent linear fittings, and dashed lines in (c) and (d) are guides to the eye.

Figure 5-13a shows the increasing nature of *w* with time from 0.23 to 0.84 nm. The roughness of the untreated samples is slightly higher than the treated samples for same deposition times. Figure 5-13b, reveals an increase of ξ with t for untreated samples, indicating a lateral growth of the Au clusters. In contrast, ξ is almost constant for treated samples. The parameters w and ξ typically show a power law dependence [262],as $w \sim t^{\beta}$ and $\xi \sim t^{\frac{1}{z}}$, where β and z are the so-called growth and dynamic exponents, respectively. These two exponents serve to describe the behaviour of the surface. [262] There is also α from the short-range behaviour of the height-height correlation function. These 3 scaling exponents can be related by $z = \frac{\alpha}{\beta}$ for a self-affine surfaces. [262] The growth parameter β is similar in both cases (similar slopes), with values of β = 0.82 ± 0.056 and β = 0.86 ± 0.099 for untreated and treated samples, respectively. In

contrast, the behaviour of the dynamic parameter z is very different in both cases, 1/z = 0.32 ± 0.026 and 1/z = -0.083 ± 0.041.

The Hurst parameter describes the undulation, and it lies between 0 and 1, which represents a rougher and a smother local surface profile, respectively. Figure 5-13b, shows a large increase in the Hurst parameter in the treated samples from 0.83 at 10 s to 0.99 at 80 s. In contrast, untreated samples show a much lower variation of α, from 0.95 at 10 s to 0.99 at 60 s. This indicates that treated surfaces shows a 'pointier' growth at early stages of growth. This observation is linked to the effect of Ar/H_2 bombardment, which increases the traveling of Au adatoms on the alumina surface and promotes a locally rougher growth of gold compared to the untreated surface, where the α values are higher. However, as the deposition time increases, the α value for treated surfaces approaches unity, in agreement with the values observed for the untreated surface. For additional characterization of the growth mode, the local slope, $m \sim \frac{w^{\frac{1}{\alpha}}}{\xi}$ was plotted in function of time, as illustrated in Figure 5-13d. A higher variation on the slope with time is seen for treated surfaces. However, both set of samples change with time, a behaviour referred as nonstationary growth.[261] Additionally, an up-shift is seen for $H(r)$ with increasing the deposition time, which indicates an increase in the local slope confirming the nonstationary growth.[260,261,320]

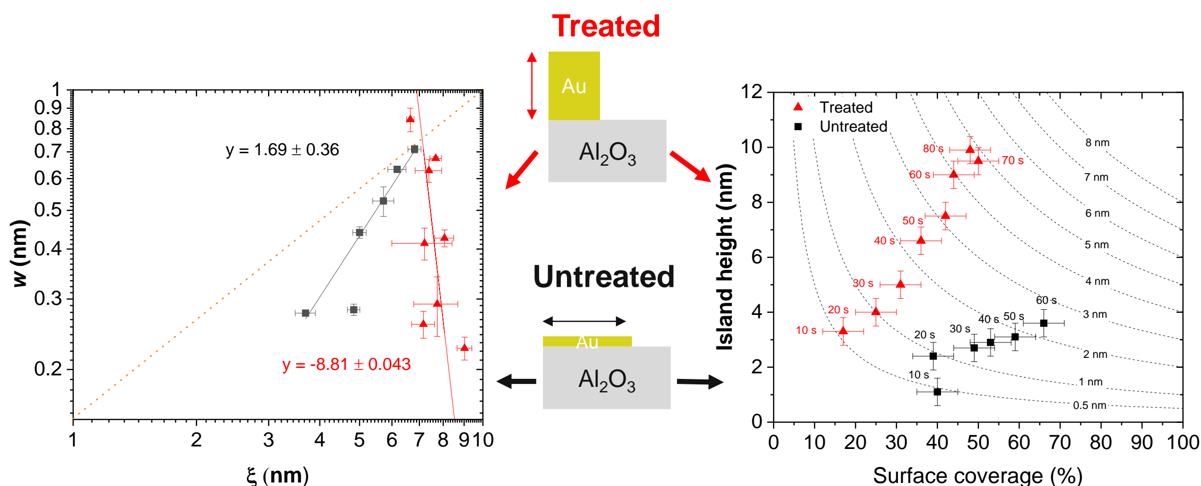

Figure 5-14 – Plots of 'vertical' vs. 'horizontal' parameters by AFM and XPS. a) *w* vs. ξ from AFM. b) island height vs. surface coverage from XPS. A scheme illustrating the growth of Au on treated and untreated Al_2O_3 coatings is also included.

Figure 5-14a shows a log-log plot of w vs. ξ. The relation between both parameters can be written as $w \sim \xi^{\gamma}$, with γ an exponent that predicts the competition between lateral and vertical growth. The values of γ were found to be 1.70±0.37 and -8.88±0.044 for untreated and treated surfaces, respectively. This indicates that treated surfaces tend to have a much higher variation in w compared with ξ, which is almost constant. In contrast, untreated samples shows a clear variation of ξ together with w with deposition time. In other words, Au nanoparticles deposited on plasma treated alumina surfaces tend to grow more vertically (perpendicular to the substrate), while Au nanoparticles deposited on untreated alumina treated tend to grow more horizontally (parallel to the substrate), as showed in the schematic of Figure 5-14. This conclusion is in agreement with the previous results obtained by the Tougaard analysis of XPS data, Figure 5-14b. Both analyses reveal the same behaviour in both growth directions (parallel and perpendicular to the surface) but use different characterization parameters to define them.

5.4 Geometrical models of Au growth

The parameters obtained by XPS and AFM serve not only to reach the same conclusions about the film's growth, but also they can be combined to create geometrical models that represent that process. Therefore, to illustrate the average growth of the films, 2D profiles were created using the data from ξ, h and c from AFM and XPS.

Figure 5-15 shows the evolution of the growth when increasing the deposition time for untreated and treated surfaces. The comparison of both set of samples highlights the different growth behaviour: lateral growth with many short wide islands for untreated samples, versus the vertical growth with less taller islands for plasma treated surfaces.

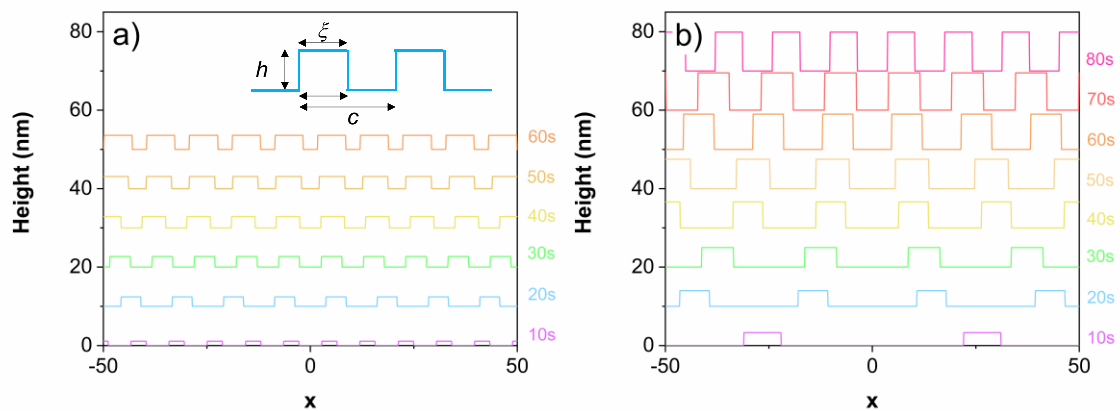

Figure 5-15 – Profile of a) untreated and b) treated surfaces with time depositions from 10 s to 80 s.

This 2D model has been expanded into a 3D model for a more realistic visualization. To do so, Au NPs were characterized using a two-dimensional Gaussian function, as seen in Figure 5-16. This function, is denoted by $f(x,y) = A\exp\left(-\left(\frac{(x-x_0)^2}{2\sigma_X^2}+\frac{(y-y_0)^2}{2\sigma_Y^2}\right)\right)$, where x_0 and y_0 are the coordinates of the center of each Gaussian, A is the height (h) given by XPS, σ_X and σ_y are the standard deviations in x and y, respectively. In our scenario, the isotropic nature of our surface results in the equality of the standard deviations, $\sigma_X = \sigma_y = \sigma$. It is worth mentioning that σ is not the FWHM of the Gaussian function, but they are related as: $FWHM = 2\sqrt{2\ln 2}\ \sigma \approx 2.355\ \sigma$. For this model, the standard deviation of the Gaussian functions is connected with the correlation length obtained from AFM,

and it is calculated with the expression $\xi = 2\sigma$. In other words, the width of the Gaussian is similar to the correlation length from AFM. This approach was verified by comparing the values of ξ with the particle sizes observed from SEM (Figure 5-5). Therefore, the shape of the Gaussian is determined using the parameters h and ξ.

The distribution of these Gaussians in a surface need to comply with the surface coverage (*c*) calculated by XPS. To do that, the Gaussians were distributed in the surface using a regular hexagonal packaging. For simplicity, the Gaussian-Gaussian distance was calculated using cylinders of radius *r* with the same volume and height that the Gaussian function:

$$V_{cyl} = h \cdot \pi r^2, V_G = h \cdot 2\pi\sigma^2; r = \sqrt{2}\sigma = \frac{\sqrt{2}}{2}\xi$$

Finally, the distance (d) between two closest cylinders (or Gaussians) depends on the coverage as $d^2 = \frac{2\pi r^2}{c \times \sqrt{3}} = \frac{\pi \xi^2}{c \times \sqrt{3}}$.

For each condition of treated and untreated samples, regular surfaces composed by Gaussian functions were created using the average experimental values of ξ, h and c. The roughness calculated from these modelled surfaces were in good agreement with the experimental values from AFM, in particular for the untreated samples. This is surprising, considering the simplicity of the geometrical model. Segments of each of these images were extracted and plotted together to illustrate the growth of untreated and treated surfaces depending on deposition time, which is plotted in Figure 5-16. It is evident from this model that the size of the NPs and coverage increase as the deposition time increases. However, the coverage is higher for the untreated samples, while particle height is more relevant for treated surfaces. This model allows illustrating the importance of the pre-treatment of Ar and H_2 plasma on the growth of the NPs.

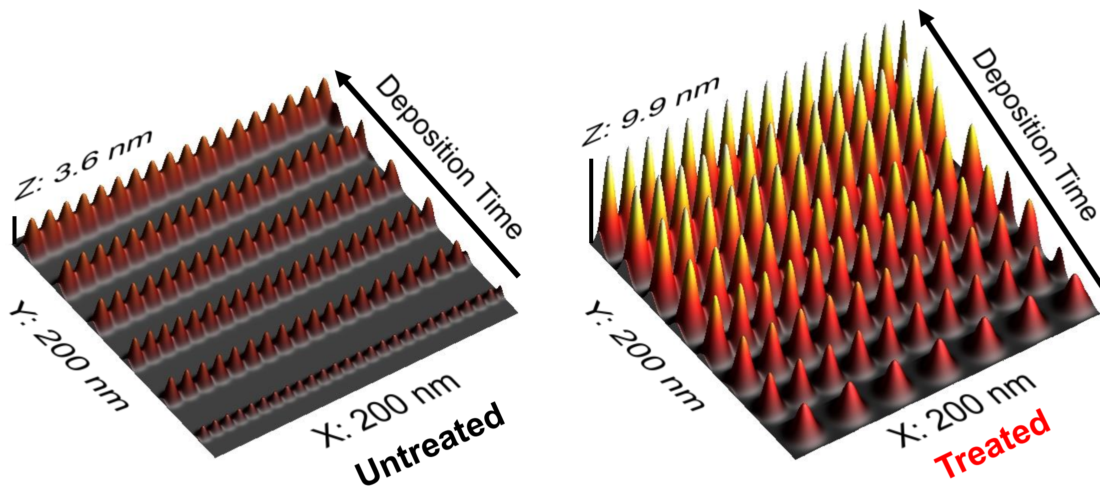

Figure 5-16 – 3D geometrical model illustrating the growth of untreated and treated surfaces for different Au deposition times.

5.5 Optical properties

The coloration of the Au-Al_2O_3 coatings can be seen in Figure 5-17. In both cases, increasing the deposition time of Au will lead to more absorption centres (Au NPs) that can interact with the incident light. Consequently, the primary impact of this factor is observed by an increase in the intensity of SPR absorption (Figure 5-18), leading to a notable reduction in the colour's brightness. Overly prolonged deposition times may cause a complete extinction within the visible spectrum, resulting in darker colours as seen in Figure 5-17.

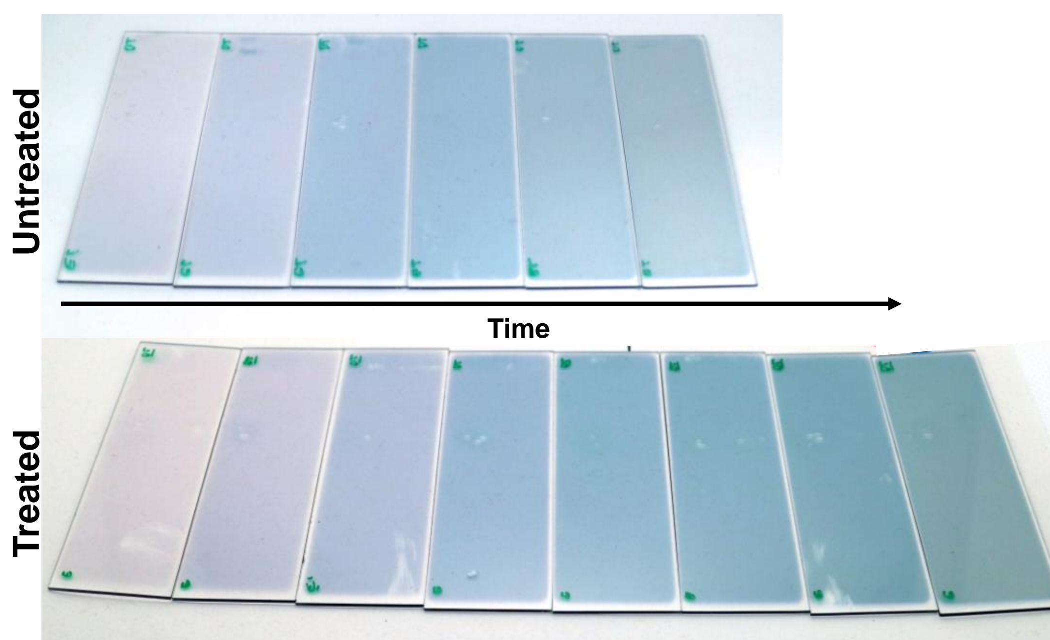

Figure 5-17 - Colours of Au-Al_2O_3 for untreated and treated surfaces deposited with different deposition times of gold on glass substrates.

The optical properties of the samples were measured using UV-Vis. The absorbance of each sample is shown in Figure 5-18 for both set of films, calculated with the expression $A = -\log T$, where A is the absorbance and T the transmittance (between 0 and 1). [311] The location of the maximum of the SPR peak is indicated with a hollow square. It is observed that the absorbance of the peak increases with the deposition time. This is a consequence of a higher Au content, which leads to the growth of the number and size of absorption centres (Au clusters) which interact with the incoming light, causing an increase in the intensity of the absorbance peak.[28] In addition, for higher deposition times, the peak is shifted to higher wavelengths because the particle shape changes progressively from spherical towards wormlike structure (cf. SEM images in

Figure 5-5) as well due to effects of size and local environment of the nanoparticle.[321,322] For untreated samples, a broad peak is seen at 50 s, and a similar optical response is obtained for 60 s. This is related with the transition from a morphology formed by Au clusters to a continuous film (percolation). Therefore, the plasma treatment allows to increase the range of the plasmonic effect, making it easier to control the nanoparticle growth. As a result, Au deposited on treated alumina show a clear LSPR peak up to 80 s of deposition, although the shape of the peak already reveals some signs of percolation. Nevertheless, it is worth mentioning that the deposition rate is much higher for treated than untreated samples (cf. Figure 5-4a); in fact, the treated film at 70 s (which shows no percolation) has ca. 2.5 more times more Au than the untreated sample at 50 s (where percolation is already observed). In other words, the plasma treatment allows accommodating at least 2.5 more times Au in the Al_2O_3 surface while avoiding the loss of the LSPR peak.

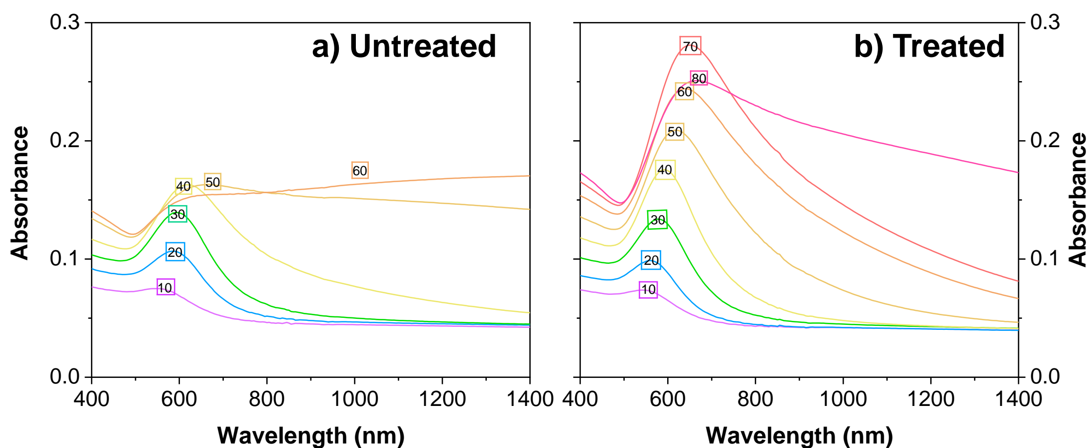

Figure 5-18 – Absorption spectra of Au clusters deposited on a) untreated and b) treated Al_2O_3 surfaces for different deposition times indicated in the figure. The squares indicate the position of the SPR maxima.

As a consequence, the absorbance is higher for treated alumina, where we can obtain a maximum of 0.28 at 650 nm compared with 0.16 at 610 nm for untreated alumina, leading to a 75% rise. This difference is caused mainly by the height of the Au clusters. A red shift of the maximum of the SPR peak is observed from 610 nm (untreated) to 650 nm (treated), since the nanoparticles have higher aspect ratio due to the higher vertical growth and lower lateral size on treated surfaces.[285] The intensity of the absorbance peak was plotted in function of its

wavelength (coordinates of the squares from Figure 5-18) in Figure 5-19a. Two different behaviours are observed depending on whether the surface is treated or untreated. Initially, a linear behaviour is seen in both cases, followed by a saturation point for each trend. The point of saturation is more pronounced in untreated surfaces, as it initiates at approximately 40 seconds of deposition, whereas in treated surfaces, it commences after 70 seconds. This indicates the transition from Au clusters to a continuous film being the linear zone higher for treated surfaces.

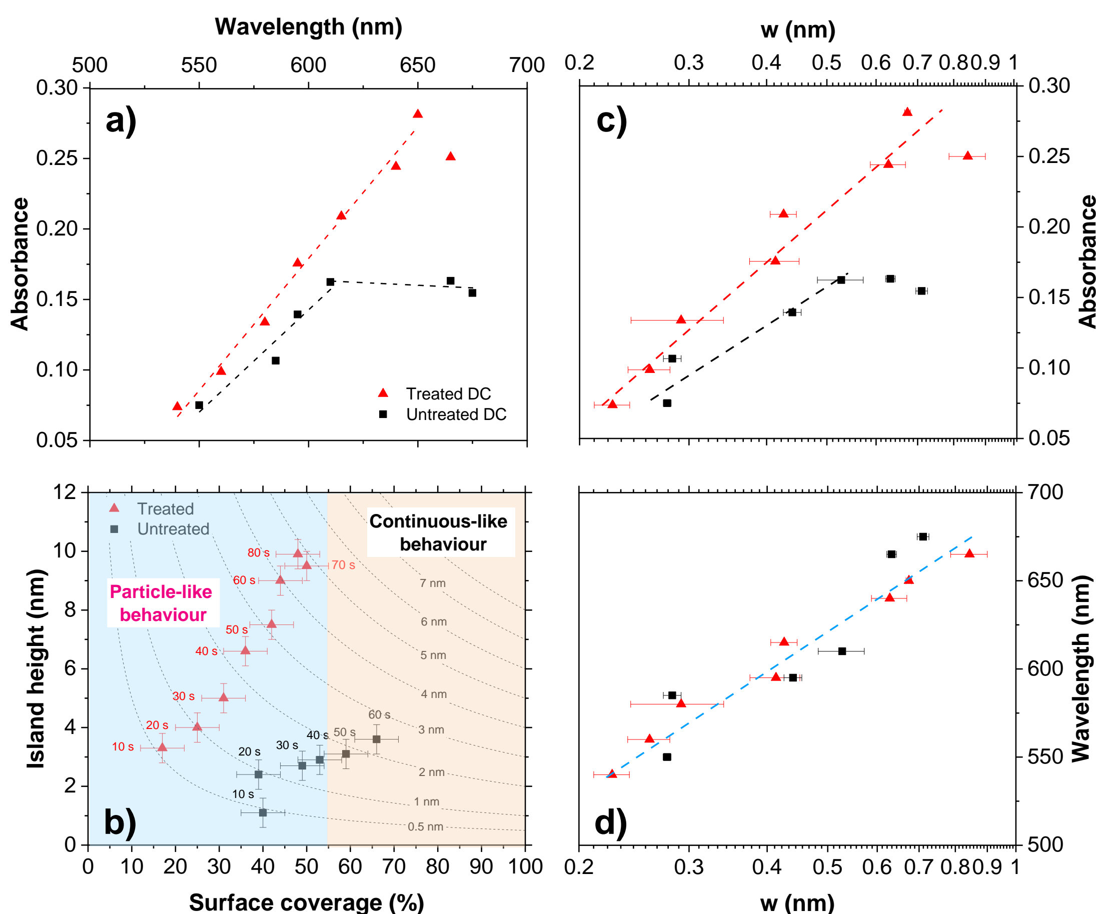

Figure 5-19 – a) Values of absorbance of the SPR peak in function SPR peak position. b) Island height as a function of surface coverage, divided into two zones: Particle-like behaviour (blue zone) and Continuous-like behaviour (orange zone). c) Absorbance of the SPR peak in function of the roughness of the coatings (w). d) Wavelength of the SPR peak in function of roughness (w) for untreated and treated samples. Dashed lines are guides to the eye.

The observations from absorbance are in excellent agreement with the results from the coverage obtained by XPS. Therefore, Figure 5-4b can be divided into two sections (cf. Figure 5-19b): the initial section corresponds to the particle-like

behaviour zone (blue zone) for lower coverages, while the second section represents the continuous-like behaviour zone (orange region) for higher coverages. The point of transition would be located at a surface coverage of ca. 55%. Therefore, samples with higher coverage than this threshold are already in the percolation region (both untreated samples prepared at 50 and 60 s), and samples near this threshold may show some effects (treated sample at 80 s). Figure 5-19c and d represent the correlation between characteristics of the LSPR peak (absorbance and wavelength) and roughness. In general, the absorbance increases with roughness (i.e., vertical size of the particles), provided that percolation is not reached. Such limit is reached for untreated samples at ca. 0.5 nm, and about 0.7 nm for treated ones, and from these values the absorbance does not increase. In other words, absorbance increases with the vertical size of the cluster, provided that the deposition is still 'clustered' and not 'film-like'. Figure 5-19d shows that the position of the SPR peak shifts to longer wavelengths for both surfaces with increasing the deposition time. Both sets of samples seem to share an approximately common correlation between roughness and position of the SPR peak. Therefore, it was observed that the increase of *w,* which gives information about the cluster height, the peaks shift from 540 nm to 675 nm due to combined effect of changes in the size, shape of Au NPs as well as in the interparticle distance.

5.6 Origin of the influence of the Ar/H_2 plasma pre-treatment on the film growth

So far, it has been demonstrated that the use of an Ar/H_2 plasma treatment in the alumina has a strong effect in the growth and properties of Au nanoparticles. However, the ultimate reason behind this behaviour, i.e. the nature of the modification induced by the Ar/H_2 plasma in the alumina, has been not discussed yet. Firstly, in section 4.2 (Figure 4-11a) it was demonstrated that the presence of H_2 in the plasma treatment was necessary to induce large changes of the LSPR peak, since a plasma using argon alone produces less noticeable effects.

A consequence of the plasma treatment could be a modification of the topography of the alumina surface. To check that hypothesis, Figure 5-20 illustrates the three-dimensional images depicting the topography of untreated (w = 0.16 nm) and treated references of Al_2O_3 with Ar (w = 0.16 nm) and Ar/H_2 plasma (w = 0.18 nm). The images and the values of roughness (w) are very similar, indicating that the differential growth of Au nanoparticles in the treated samples is not attributed to a structural change.

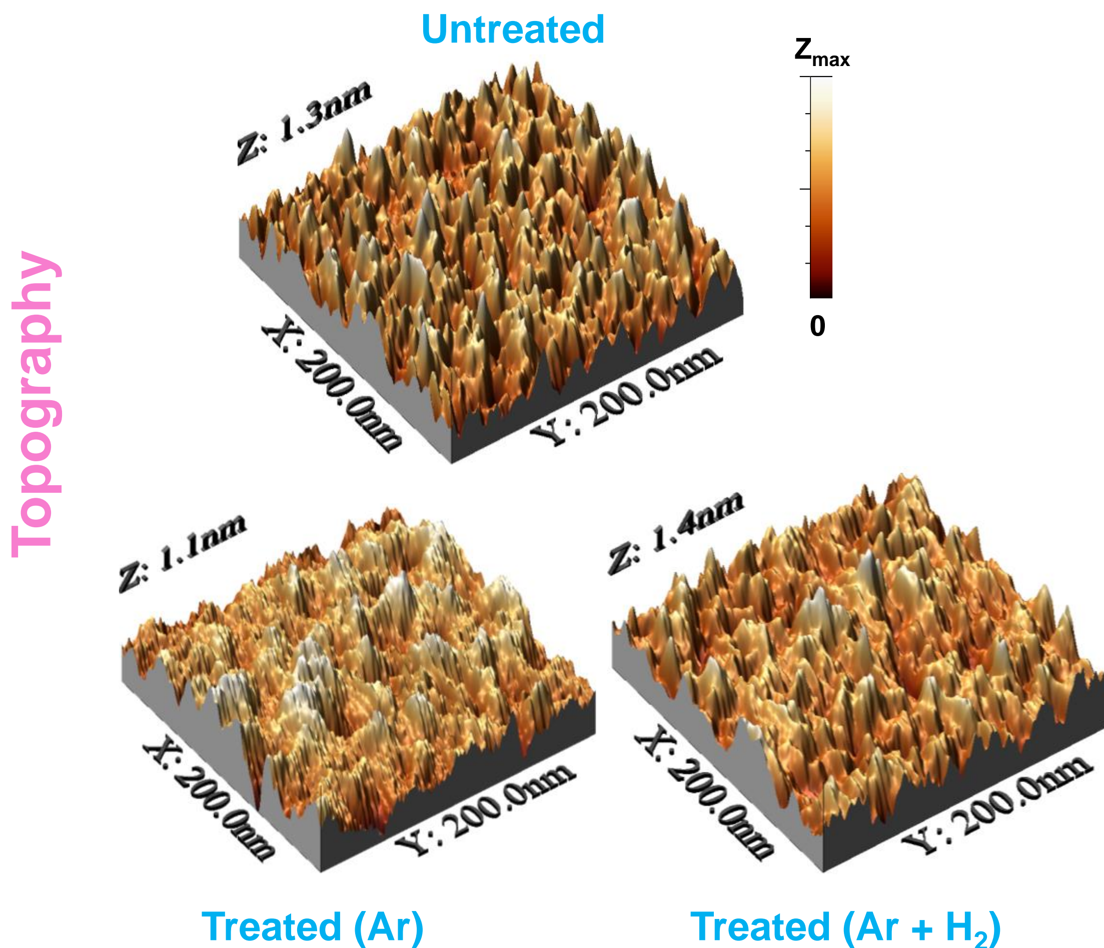

Figure 5-20 – Topographic 3D images for alumina surfaces with different plasma treatments: untreated (Z = 1.3 nm), treated with Ar (Z = 1.1 nm), and Ar/H_2 (Z = 1.4 nm) reference.

Therefore, the plasma may have induced a chemical change on the surface of alumina. To evaluate such possibility, different coatings were studied by SIMS. Thus, to elucidate the influence of the Ar/H_2 bombardment on Al_2O_3, 5 alumina coatings were deposited and subjected to 5 different treatments (see Table 5-1). Before leaving the sputtering chamber and being exposed to air, these samples were coated with a protective Au film (50 nm) which was deposited to 'encapsulate' them and avoid environmental modifications. Afterwards, the samples were rapidly transferred to a SIMS chamber for subsequent analysis.

Table 5-1 - Samples prepared for SIMS analysis. The samples were prepared in the sequence S1-S5.

Sample	Treatment
S1	None (reference sample)
S2	Exposure to Ar/H_2 during 20 min
S3	Plasma under Ar/H_2 during 20 min
S4	Exposure to Ar/D_2 during 20 min
S5	Plasma under Ar/D_2 during 20 min

Before Au encapsulation and SIMS analyses, alumina coatings were subjected to three types of treatment: no treatment, exposure to a mixture of Ar/H_2 without plasma, and Ar/H_2 plasma treatment. In addition, treatments were performed twice, using conventional hydrogen (H_2) and deuterium (D_2). The reason for using D_2 is that there are additional sources of hydrogen in the sputtering chamber, such as water adsorbed in the walls, or hydrogen in the atmosphere which is not removed by the turbomolecular pumping. In contrast, D_2 cannot be confused with these contaminants, and it is chemically equivalent to H_2.

Figure 5-21 shows the SIMS depth profiles of the samples of Table 5-1, where 6 elements are depicted: H, D, O, Al, Si and Au. The intensity of other monitored elements, such carbon, is negligible. The depth has been normalized selecting as zero the point where the intensity of the Si is half of the maximum (cf. Figure 5-21l). Three different regions can be identified in all the profiles; Au capping layer (left), the Si substrate (right), and the alumina coating in the center of both. In the alumina region, H (and D in S5, Fig. Figure 5-21e) can be detected in addition to Al and O. In fact, hydrogen is already detected in sample S1, which was not exposed nor treated with H_2. Therefore, this H has to be incorporated from H_2O or hydrogen traces present in the deposition chamber during deposition. Nevertheless, this 'H trapping' is a characteristic of alumina, since significant H signals are not observed in the Si substrate nor in the Au capping layer. Therefore, the signal of H observed in the alumina region for films only exposed to H_2 or D_2 (S2 and S4) is caused by the same effect. In fact, film S4

does not show any presence of D in the alumina, although it was exposed to D_2. In contrast, a small signal of deuterium in the Au layer is detected (intensity ca. 10), which is probably trapped during the deposition of the Au capping layer after the presence of D_2 in the chamber. Similar intensities of H and D signals are observed in the Au layer in other samples, indicating that such absorption process takes place in Au, although at a much lower extent than in alumina. Therefore, for samples where no plasma treatment was performed (S1, S2 and S4), the presence of H and D in the alumina and/or Au layers is caused by the presence of these elements in the sputtering atmosphere during the alumina deposition, and it is not a consequence of a posterior diffusion in the coatings. Coating S5 is the only film where a distinct D signal is appreciated. Such deuterium signal covers the whole thickness of the alumina layer, indicating that the Ar/H_2 plasma is able to introduce H species well below the surface of the alumina.

The chemical profiles of the different elements are compared in the right column of Figure 5-21. It can be observed that the Au profiles are not aligned, which indicates that the thickness of alumina is not constant assuming similar sputtering rates in SIMS (from thinner to thicker: reference (S1), plasma treated (S3 and S5), and exposed (S2 and S4)). Since the intensity is plotted in linear scale, the distinct shape of the different peaks can be better appreciated. In general, each element has a characteristic peak shape regardless of sample, particularly coincident near the Si interface. H shows a sharp peak near the Si interface (Figure 5-21i), and a lower broader peak towards the Au capping layer. The sharp peak may be caused by a large absorption of H species at the beginning of the alumina deposition, or due to an artifact due to the interface effect with Si. The shape of the second broad peak divides the samples into two groups. Thus, exposed samples (S2 and S4, red and green lines) show a decrease of intensity in 'two steps' towards Au. In contrast, the reference and treated sample (S1, S3 and S5, black, blue and purple lines) shows a simpler peak, whose intensity decreases normally towards the Au layer. Nevertheless, this second peak seems to show a higher broadening near the Au region for plasma treated samples, probably due to the influence of some internal re-arrangement process. In fact, the intensity of the H signal in sample S5 is much lower than in the others (Figure 5-21i), which is likely a consequence of the

replacement of H by D during Ar/D_2 plasma treatment (cf. D profile in Fig. Figure 5-21k).

The O signal (Fig. Figure 5-21h) shows a plateau near the Si substrate, and a peak next to the Au capping layer, maybe because a certain interface effect. Nevertheless, the intensity of these maxima is lower for the films subjected to plasma treatment (blue and purple lines). The profile of Aluminium shows a progressive increase from the Si interface up to a depth of ca -0.5; from this point, untreated samples (green and red lines) show a reduction of intensity, while treated surfaces (blue and purple lines) show the opposite behaviour. Therefore, the results of O and Al profiles indicate that the Ar/H_2 plasma treatment causes a reduction of the O/Al ratio near the alumina surface. In other words, plasma treatment leads to a preferential sputtering of the O atoms from the surface of the alumina, a process that is likely facilitated by the presence of H_2. This explains the comparatively much lower effect of the Ar plasma on alumina, since the chemical driving force to form water molecules is not present. Such chemical modification of the alumina surface explains the differences of Au growth between plasma treated and untreated alumina.

Figure 5-21 - Left: SIMS profiles of the 5 samples under study, in log scale. Right: comparison of the SIMS profiles per element, in linear scale. The reference depth is illustrated with a vertical black line situated in zero.

Another process that could contribute to the chemical modification of the alumina surface could be the formation of -OH (hydroxide) species due to the plasma treatment. Nevertheless, this process is probably minor. Figure 5-22 shows the SIMS profiles of Al, O and D for sample S5 in linear scale. The intensities have been modified to allow a proper comparison among profiles. It is observed that the D signal does not increase together with the O and Al near the Au interface, and a horizontal shift is observed instead. In other words, it seems that there is less D near the alumina surface than in the bulk, which is the opposite of what expected if plasma would have induced a significant hydroxide formation in the alumina surface.

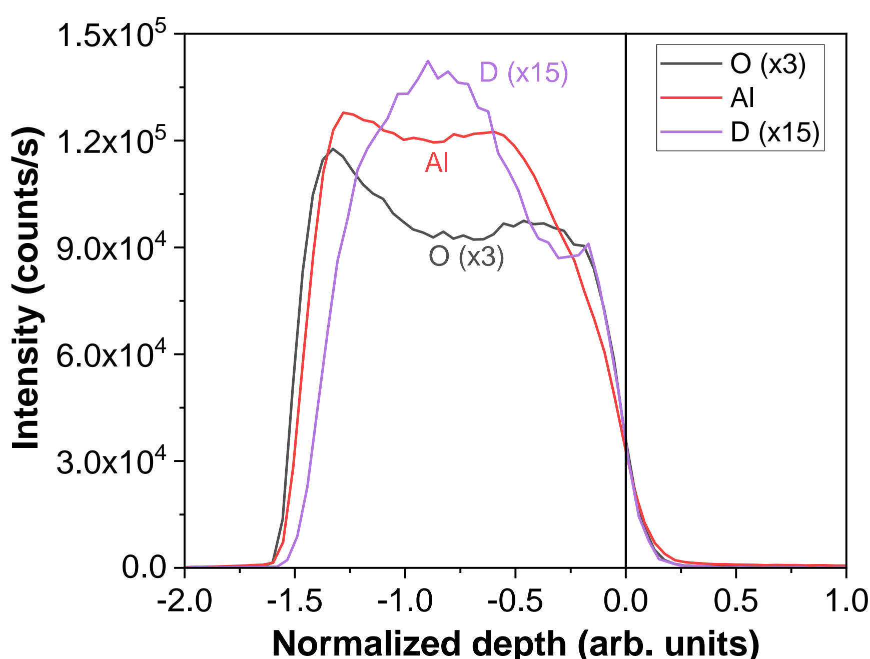

Figure 5-22 - Detail of the SIMS profiles of sample S5.

As previous discussed in Section 4.2, amorphous alumina exhibits lower surface energy values (0.97 J/m^2) compared with Au (1.51 J/m^2). As a result, amorphous alumina is anticipated to facilitate the vertical growth of nanoparticles (non-wetting gold-phobic behaviour) rather than the formation of continuous films. However, when the surface is treated with Ar/H_2, it is observed that the Au nanoparticles tend to grow more vertically than horizontally compared with untreated surfaces. This suggests that the surface energy of the alumina surface is further reduced when the plasma pre-treatment is applied as a consequence

of the reduction of the O/Al ratio in the surface, leading to a more significant gold-phobic behaviour and the promotion of the growth of vertically oriented Au nanoparticles.

5.7 Growth mechanisms of Au NPs

To understand the growth mechanisms at different deposition times, a schematic of the growth diagram (Figure 5-23) was created to depict the Au growth on both untreated and treated alumina surfaces. The left column illustrates the influence of the plasma treatment on the alumina surface. The topography is not modified (cf. Figure 5-20), and the chemical modifications on amorphous alumina are represented on a deformed γ-Al_2O_3 cell. As demonstrated in Figure 5-21, the surfaces treated with Ar/H_2 plasma reduce the O/Al ratio, which is represented with higher amount of O vacancies than Al vacancies.

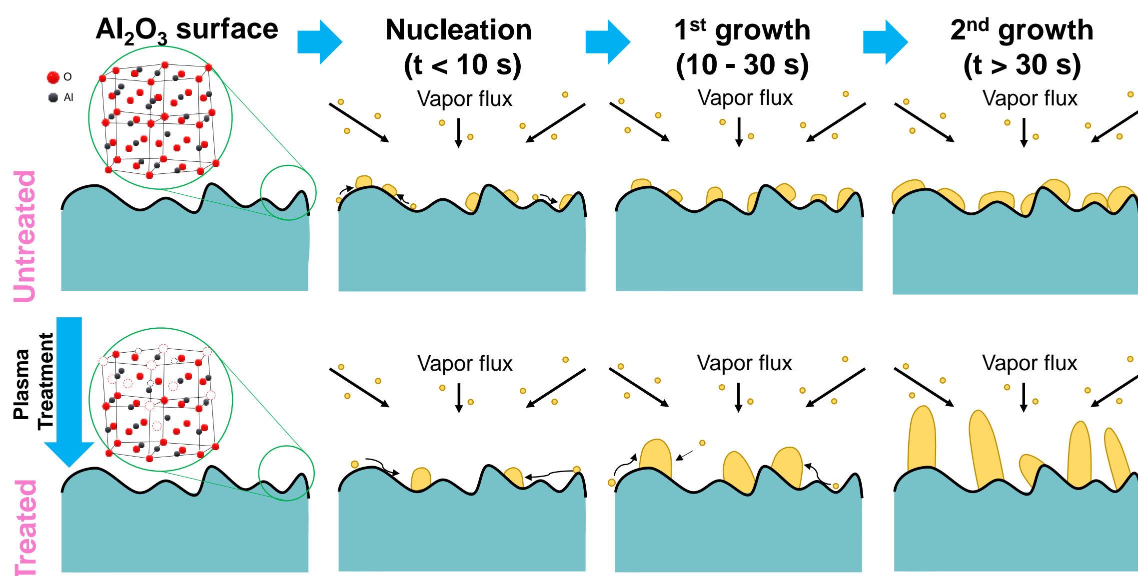

Figure 5-23 – Schematic of the growth mechanisms of Au on an untreated and treated alumina surface at different stages of the Au deposition.

The Au nucleation stage is represented in the second column. Thus, for deposition times below 10 seconds, adatoms tend to exhibit longer traveling distances on the plasma pre-treated alumina surface (resulting in non-wetting behaviour) due to its lower surface energy compared to an untreated surface. Consequently, the adatoms create a lower density of larger nuclei with preferential vertical growth, leading to higher local roughness i.e., lower values of the Hurst parameter. In contrast, untreated surfaces show higher wetting the

alumina surface, which leads to a higher density of smaller nuclei with smaller height. In this last the NPs tend to grow horizontally, resulting in higher coverages.

After nucleation, we can distinguish two different growth stages; thus, up to 30 s of deposition, the deposition rate on both substrates is pretty similar (cf.Figure 5-4), i.e. the area covered by gold particles in the 3rd column of Figure 5-23 is the same regardless the treatment of the surface. In this stage, the untreated surface growths horizontally (higher coverage), nucleating more small islands and growing those already existing horizontally (higher correlation lengths). In contrast, treated surfaces tend to grow vertically, increasing roughness while keeping correlation length more or less constant. However, for deposition times larger than 30 s, the deposition rate of treated surfaces is higher (cf. Figure 5-4); this is likely because the topography of the deposited Au starts to dominate over the original Al_2O_3 topography; the vertical range of the untreated alumina is about 1 nm (Figure 5-20), which is in the range of the island height up to ca. 30 s (Figure 5-4); from that point, the islands heights of the treated surface would dominate the contributions to the topography, while the islands of the untreated surface would mostly follow the topography of the surface, starting to show coalesce processes (cf. Figure 5-18 and Figure 5-19); this is all illustrated in the right columns of Figure 5-23; up to 30 s of growth, gold has similar deposition probability in both cases, since the topography is similar; however, after 30 s, both situations are no longer equivalent, and the more vertical islands present in the treated surfaces increase the surface area available for the deposition, leading to higher deposition rates. In contrast, due to the horizontal growth of untreated surfaces, Au islands start touching each other and percolation effects begin to appear (cf. particles on the right).

5.8 Application of samples for SERS

Selected Au-Al_2O_3 coatings were tested with Rhodamine 6G (R6G) for Surface-enhanced Raman spectroscopy (SERS) applications. The objective of the study was to create a specific region within the sample surface with and without Au nanoparticles (Au NPs) by deliberately scratching the surface, seen in Figure 5-24 and Figure 4-8. The objective was to evaluate the presence/absence of the SERS phenomenon in close locations of each sample.

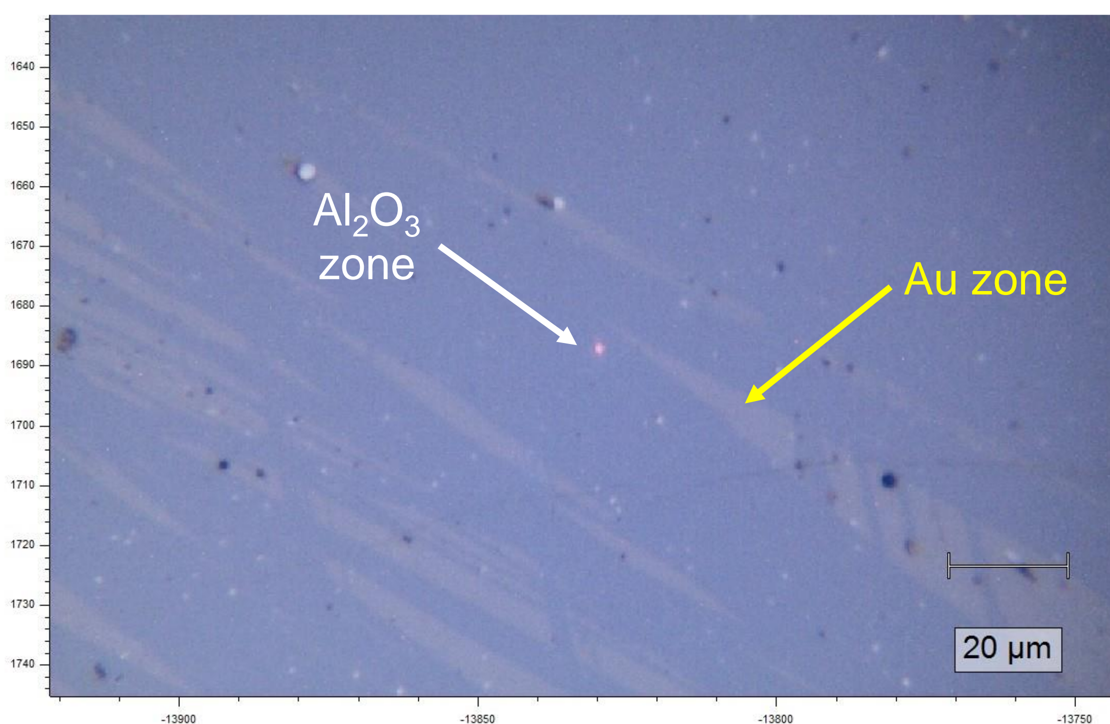

Figure 5-24 – Optical microscope image of Au-Al_2O_3 coatings with two distinct zone: presence and absence of Au nanoparticles.

Raman Spectroscopy was used to measure the untreated and treated samples, using a concentration of 10^{-5} mol/L R6G. In Figure 5-25a is possible to see that untreated samples have much lower peak intensity when compared with treated samples. This observation validates that the utilization of plasma pre-treatment enhances R6G detection by inducing alterations in Au growth. Additionally, another measurement was made with three Au deposition times: 30, 50, and 70 s, using a concentration of 10^{-3} mol/L R6G. Figure 5-25b illustrates the Raman spectra for the three different samples. In the Al_2O_3 zone, three peaks

are observed, which correspond to the silicon peak of the substrate at 301, 520, and between 935 and 990 cm^{-1}.[323] In contrast, the spectra of the R6G can be clearly observed in the regions of the samples covered with Au particles, which confirms the SERS capabilities of these samples. The results reveal that the signal experiences enhancement as the deposition time of Au increases, with the highest enhancement observed at 70 seconds of deposition.

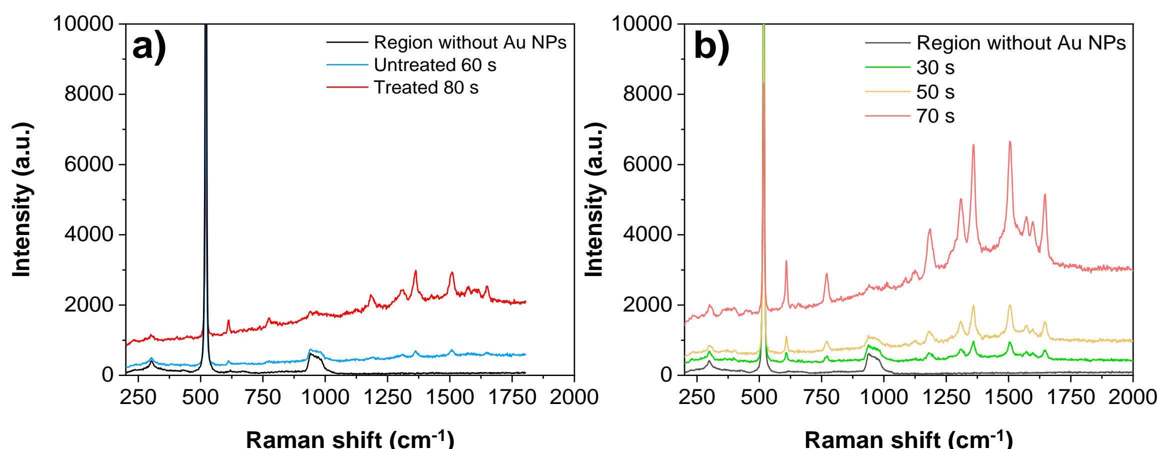

Figure 5-25 - Raman spectra of a) R6G analyte (10^{-5} M) for untreated (60 s) and treated (80 s) surfaces. b) R6G analyte (10^{-3} M) in treated surfaces at different deposition times (30 s, 50 s and 70 s). A reference of an area without Au NP is also plotted for comparison.

Another important factor is determining a robust SERS substrate its lifetime. In our cases, all the coatings were measured more than 2 years after the deposition of the samples. Samples were stored in boxes under air, without any specific protection nor precaution. This indicates that samples are able to show a strong SERS effect even after long periods of time, which is an advantage for potential commercial applications. This is probably due to the high chemical stability of the constituents (Alumina and Au) against oxidation and other processes of environmental degradation.

The enhancement factor (EF) was estimated according to the following expression:

$$EF = \frac{I_{SERS}}{I_{Raman}} \times \frac{N_{Raman}}{N_{SERS}}$$

I_{SERS} and I_{Raman} denotes the intensity of the specific peak corresponding to the analytes that are adsorbed on the surface of the coating and the conventional

Raman signal, respectively. N_{Raman} and N_{SERS} represent the analyte concentration in the Raman and SERS measurements respectively. In our case, EF values have been estimated around 10^4.

To ensure reproducibility, the measurements were conducted twice, and the results depicted below exhibit consistent shape and intensity, thus confirming excellent reproducibility, see Figure 5-26.

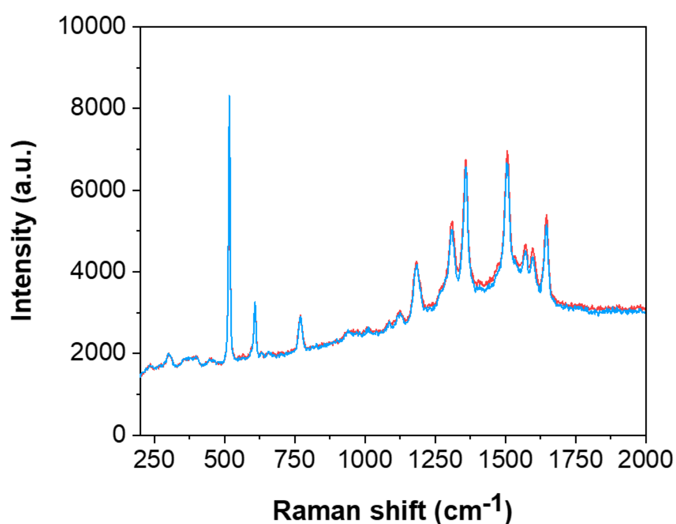

Figure 5-26 – Reproducibility of SERS using a concentration of 10^{-3} M of R6G 2 different areas of treated surfaces with Au deposition time of 70 s.

5.9 Conclusions

Magnetron sputtering provides a flexible way of depositing various materials into the oxide matrix. Au nanoparticles were effectively deposited through DC sputtering in dynamic mode.

The influence of Ar/H_2 plasma treatment on the growth of Au nanoparticles is significant, leading to a transformation from 'horizontal' (parallel to the Al_2O_3 surface) to 'vertical' growth (perpendicular to the Al_2O_3 surface). This effect is observed consistently through two different techniques: XPS and AFM, and results are also supported with SEM images. Furthermore, the plasma treatment induces a higher deposition rate of Au nanoparticles compared with untreated surfaces. Therefore, the Ar/H_2 plasma treatment induces a chemical modification in the surface of Al_2O_3, which likely induces a lower surface energy of alumina and lower wetting of Au. As a consequence, we would obtain higher traveling distances of Au adatoms, leading to lower densities of larger islands that tend to grow vertically. In contrast, untreated surfaces lead to higher densities of smaller particles that tend to growth horizontally. This difference of growth with time leads to different topographies, which ultimately explain the different deposition rates observed for both cases at longer deposition times. Geometrical models have been developed to illustrate the distinct growth patterns observed in each case, providing a visual representation of the effects of plasma treatment on the morphology of the nanoparticles.

The optical properties of treated and untreated surfaces also differ significantly. The plasma treatment allows for a higher accommodation of Au on the surface without percolation, approximately a factor of 2.5 times more Au compared to untreated surfaces. The optical behaviour of the films can be understood based on their characteristics. The saturation of the SPR peak occurs at coverages above approximately 55%, indicating a transition from cluster-like structures to film-like formations. Additionally, the absorbance of the films shows a linear growth trend with roughness, reflecting an increased amount of absorbing material. This is maintained until percolation is reached, resulting in the degradation of the SPR behaviour.

A common trend between wavelength and roughness is observed for both sets of samples, suggesting a correlation between the optical properties and the surface roughness. This highlights the importance of surface morphology in determining the optical characteristics of the films.

The variation in growth and optical properties of Au on treated and untreated Al_2O_3 surfaces is firstly attributed to a chemical modification and at higher deposition times to a topographical change. The formation of aluminium hydroxide species appears to be minimal in this context. However, it was observed that the O/Al ratio decreases on the surface of alumina following Ar/H_2 plasma treatment, explaining the inefficiency of Ar plasma. The presence of H_2 significantly facilitates the extraction of O from alumina, leading to the formation of water species.

The reduction in the O/Al ratio likely results in a further decrease in the surface energy of amorphous alumina, leading to a more Au-phobic behaviour. Consequently, gold adatoms on the treated alumina surface can travel greater distances, resulting in a lower density of high Au islands that tend to grow perpendicular to the substrate. On the other hand, gold deposition on untreated alumina surfaces leads to a higher density of small particles with lower heights, which tend to grow more parallel to the alumina surface. A topographical alteration becomes significant when deposition times exceed 30 seconds, as treated surfaces, characterized by their pronounced vertical growth, develop protrusions that enhance the attachment of additional gold adatoms. This phenomenon contributes to higher deposition rates compared with untreated surfaces.

Overall, this study demonstrates the profound influence of Ar/H_2 plasma treatment on the growth, morphology, and optical properties of Au nanoparticles, providing valuable insights into the fabrication and characterization of nanoscale materials for various applications such as SERS. This Ph.D. Thesis achieved an enhancement factor of 10^4 with excellent reproducibility, which has been achieved even two years after the deposition of the samples.

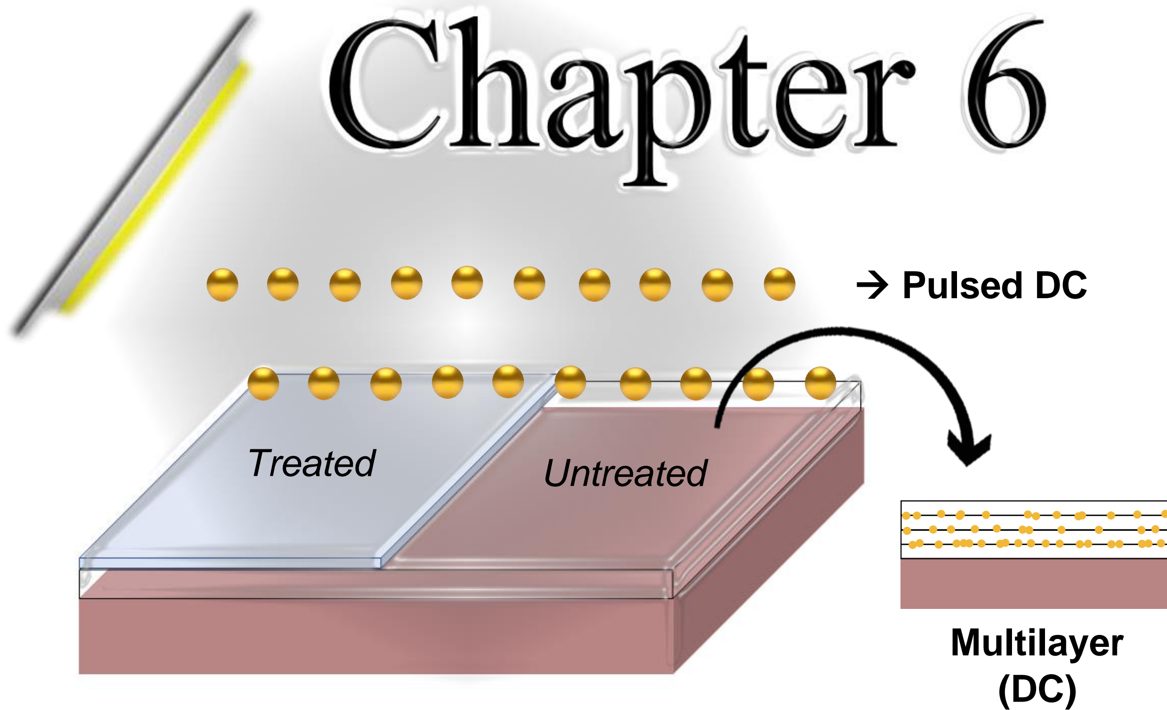

6. Advanced synthesis of Au/Al_2O_3 films

In the previous chapter, we studied the influence of Ar/H_2 plasma surface treatment of Al_2O_3 on the growth of Au islands deposited by continuous DC magnetron sputtering. In this chapter, we will expand that knowledge into two directions. Thus, in the first section we will compare these results with equivalent samples where Au was sputtered using a Pulsed DC source, where the duty cycle and frequency were varied. In the second section, a multilayer architecture (i.e. $Au-Al_2O_3-Au-Al_2O_3$) instead a unique deposition of Au on Al_2O_3 will be studied.

6.1. Au/Al_2O_3 monolayers using pulsed DC sputtering for Au

The Au clusters studied in this chapter were deposited by Pulsed DC for 30 s onto alumina coatings deposited at room temperature. The detailed conditions are displayed in Table 4-1 and Table 6-1.

Table 6-1 - Characteristics of Pulse DC operation for a deposition time of 30 s of Au on treated and untreated alumina.

Duty cycle (%)	T_{on} (µs)	T_{off} (µs)	Frequency (kHz)	Average power (W)
40	95	145	4.2	42
20	50	200	4.0	44
4.1	15	350	2.7	50
1.52	15	50	15	53

The results of these samples will be compared with the samples described in Chapter 5, which will be used as references.

6.1.1. Tougaard analysis of XPS results

The samples with 20% and 40% of duty cycle with and without treatment were measured by XPS. Figure 6-1a depicts a comparison of the amount of substance between Pulsed DC and continuous DC.

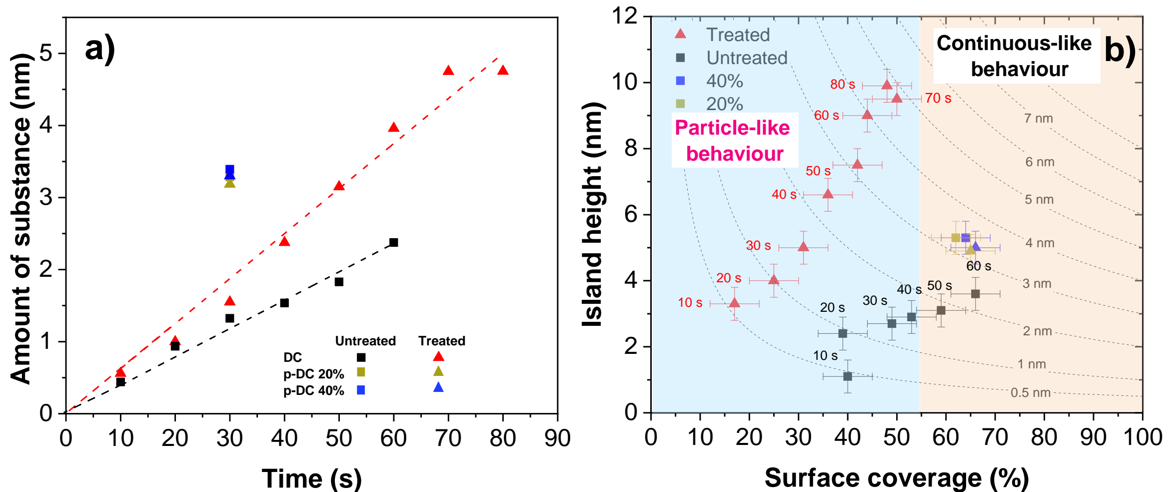

Figure 6-1 – Data obtained after XPS peak-shape Tougaard analysis for treated and untreated alumina surfaces using Pulsed DC. a) amount of substance (AOS) as a function of Au deposition time, where the dashed lines represent linear fittings b) island height vs. surface coverage.

It is evident that Pulsed DC leads to a significantly higher amount Au for the same deposition time (30 s) compared to DC. Considering that the average power is the same as in DC, this means that the high peak power overcomes the lack of sputtering during the off-time, leading to a higher deposition rate. Surprisingly, all four samples (marked in blue and yellow) are closely grouped together. In addition, all the samples appeared together in the growth map of Figure 6-1b, all of them located in the 'continuous-like behaviour region'. This is unexpected, since two of them underwent plasma pre-treatment, and higher deposition rates and island heights were expected. Nevertheless, it is worth mentioning that these results of XPS are probably not precise due to the large surface contaminations of these samples; thus, a large C1s peak was measured in these samples by XPS, which was quantified between 50-54%, in contrast to <10% measured in the samples analysed in the previous Chapter.

6.1.2. AFM measurements

All the samples were measured by AFM, and then the HHCF analysis was performed. Figure 6-2 shows the different parameters (w, ξ, α and m) obtained for Pulsed and continuous DC in function of the time. In general, no clear trends are observed with duty cycle nor application of plasma treatment.

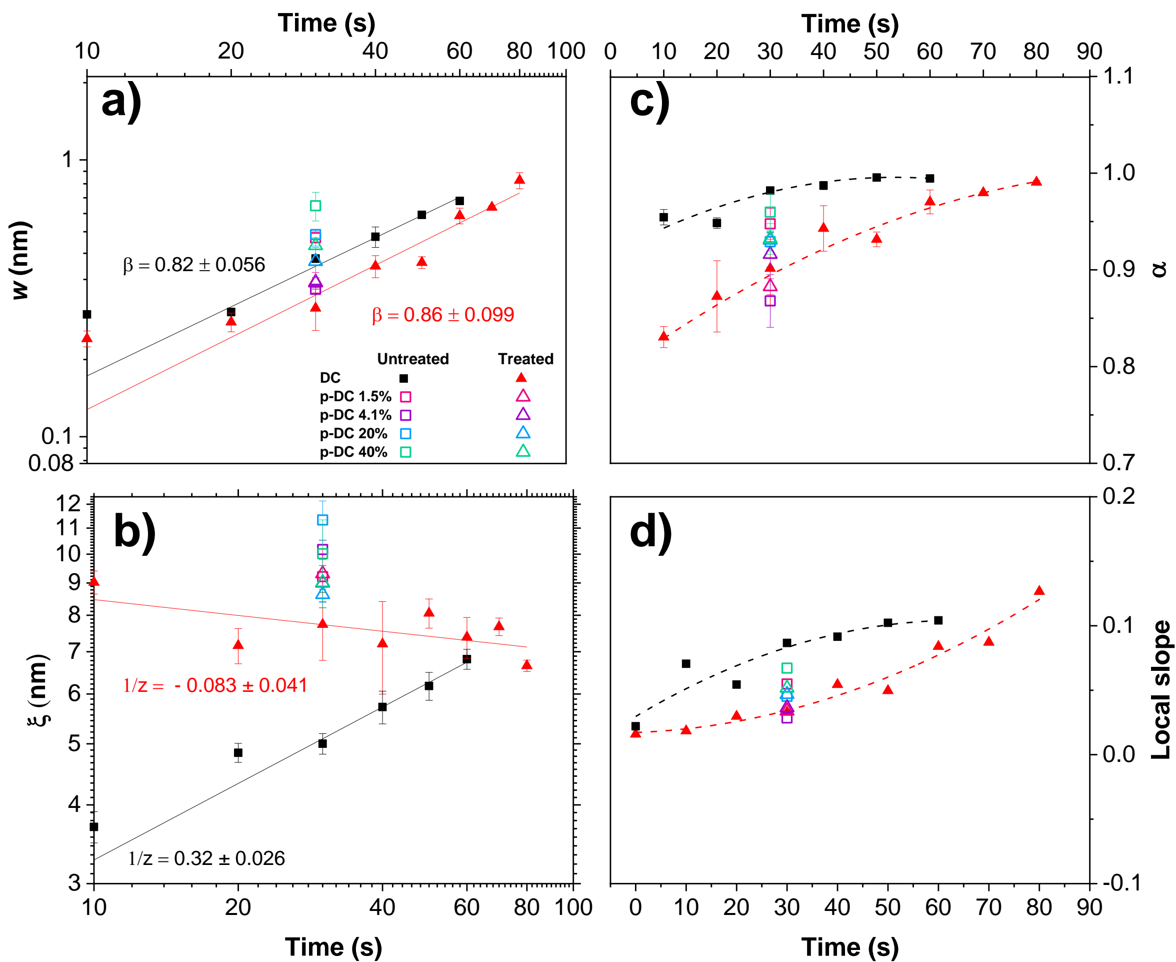

Figure 6-2 – The variation of a) roughness (w), b) correlation length (ξ), c) Hurst parameter (α) and d) local slope with deposition time for Au deposits prepared by Pulsed and continuous DC (hollow and filled symbols, respectively) on plasma treated and untreated alumina surfaces (triangles and squares, respectively).

Figure 6-2a shows that untreated surfaces using pulsed DC tend to have higher roughness compared with samples prepared by continuous DC for same deposition times. Such increase may be connected to higher deposition rates. In fact, values of roughness are comparable with samples prepared by continuous DC for longer deposition times. Figure 6-2b shows the main influence of the use

of pulsed-DC source, since the values of correlation length are clearly higher than those of samples grown with DC power source. Finally, the values of Hurst parameter and local slope (Figure 6-2c and d) are basically located between the samples prepared by continuous DC for 30 s. Therefore, the use of pulsed DC source did not cause any major variation of these growth parameters either.

The roughness was plotted in function of the correlation length in Figure 6-3 (representing growth perpendicular vs. parallel to the substrate). All samples prepared with p-DC appear in a separate region, grouped at higher correlation lengths. In this group, treated samples deposited with p-DC (hollow triangles) are closer to the corresponding samples prepared with continuous DC (solid triangles) than the untreated samples deposited with p-DC (hollow squares) to the corresponding samples deposited with continuous DC (solid squares). Therefore, in general, the main morphological modification induced by the use p-DC was the increase of correlation length, while the values of roughness are similar. This effect could be connected to the higher deposition rate and/or to a higher energy provided by the p-DC discharge to the adatoms traveling across the alumina surface. These phenomena would lead to higher correlation lengths, particularly in the case of untreated substrates, since there is more material to grow nanoparticles parallel to the substrate, and/or higher ad-atom energy to travel across the surface and form larger nanoparticles.

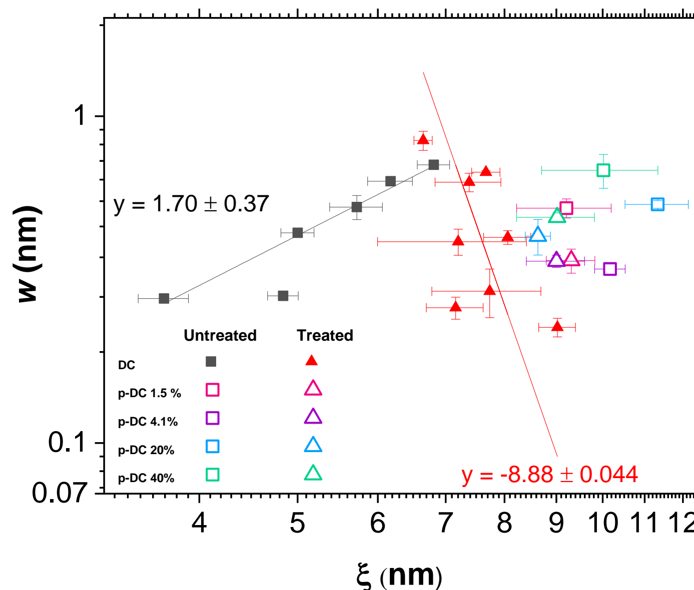

Figure 6-3 – Roughness (w) as function of correlation length (ξ) for samples prepared by Pulsed and continuous DC (hollow and solid symbols, respectively).

6.1.3. Optical properties

The UV-Vis absorbance for samples deposited on untreated and treated surfaces using Pulsed DC is shown in Figure 6-4. It is clearly observed that the absorbance peak increases following the higher values of duty cycle, likely due to a higher Au content in the samples.

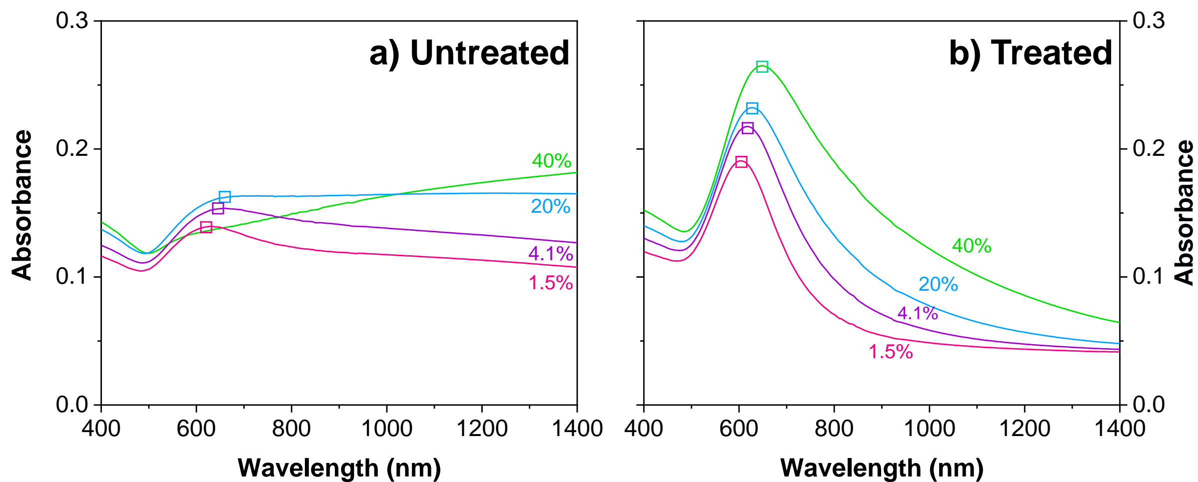

Figure 6-4 – UV-Vis absorption spectra of Au clusters deposited by Pulsed DC on a) untreated and b) treated Al_2O_3 coatings using different deposition conditions (duty cycles indicated in the plot). The squares indicate the position of the maximum of the SPR peak.

A shift for higher wavelengths is also seen. As it happened with nanoparticles deposited using continuous DC, samples deposited on plasma-treated surfaces have higher absorbance and better peak definition than those deposited in untreated alumina (cf. Figure 5-17). This result indicates again the significance of Ar/H_2 plasma pre-treatment in increasing the LSPR range.

Figure 6-5 plots the coordinates of the maximum of SPR peak for Au clusters deposited with continuous and pulsed DC. It is observed that points corresponding to samples deposited by Pulsed DC lay on top of the corresponding trends defined in Chapter 5 for Au deposited using continuous DC. In other words, the plasma treatment is the critical synthesis condition which controls the characteristics and properties of the films, while the conditions of the Au sputtering are of less importance. It is also observed that all the samples

deposited on untreated alumina using Pulsed DC are in percolation or close (cf. the shapes of the peaks in Figure 6-4). This result is in agreement with the high values of correlation length observed for these samples, and also with the location of these films in the growth map obtained by XPS (Figure 6-1b).

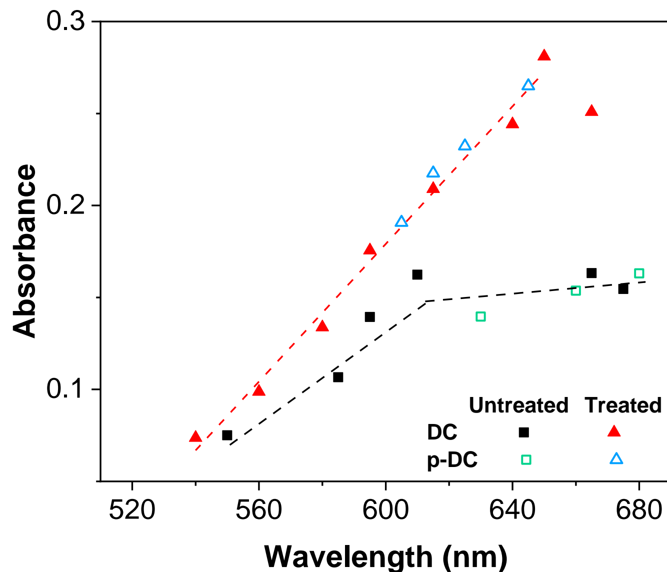

Figure 6-5 – Maximum absorbance vs. wavelength of the SPR peak for different samples.

Figure 6-6 depicts the correlation of the characteristics of the SPR peak (wavelength and absorbance) and the sample roughness.

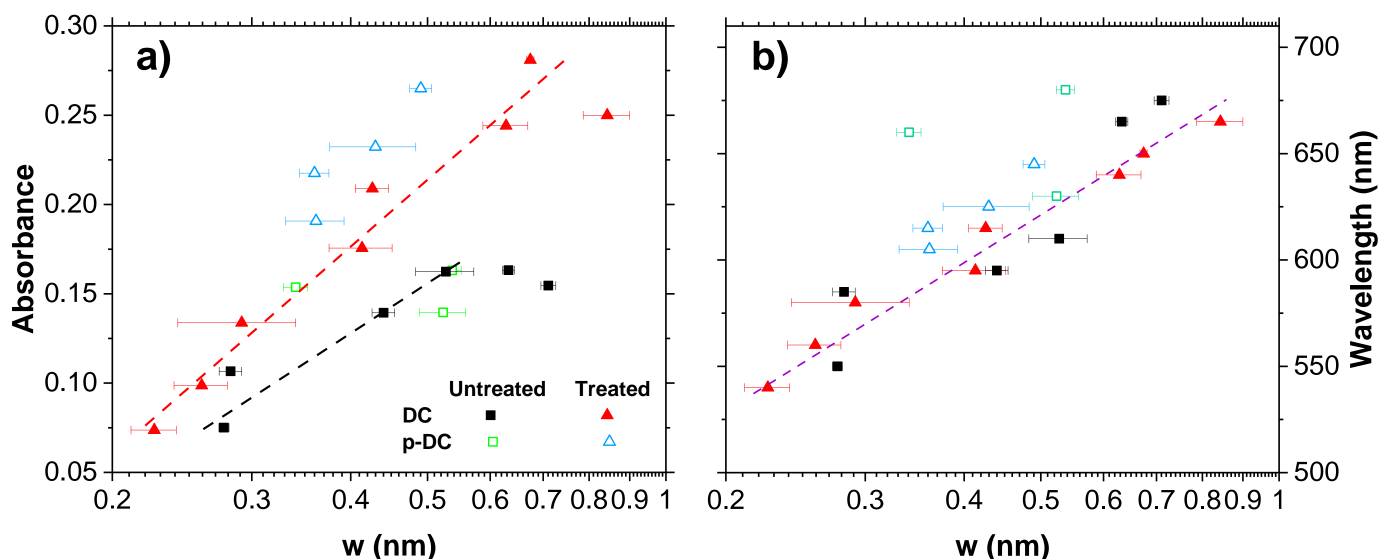

Figure 6-6 – Correlation of the characteristics of the SPR peak with the roughness of samples. a) Absorbance. b) Wavelength.

In general, the samples deposited using Pulsed DC follow the trends observed by the samples prepared by continuous DC. Therefore, the use of a different power source (Pulsed DC instead continuous DC) does not induce any major advantage for the process. As a consequence, the sputtering of Au in the multilayers described in the following section was carried out using conventional continuous DC, as in Chapter 5.

6.2. Au@Al_2O_3 multilayers using continuous DC sputtering for Au

To enhance the absorbance and protect the Au NPs, we embedded gold on alumina by creating coatings with multilayer architecture. As depicted in the schematic of Figure 6-7, these multilayers consisted of 4 alternating layers of alumina with a 3 Ar/H_2 plasma pre-treatment of 20 min in each (i.e., not performed for the last layer of alumina), and 3 Au NPs layers deposited using continuous DC. The deposition time of Al_2O_3 was set to 10 minutes, and it was varied between 10, 30 and 60 s for Au.

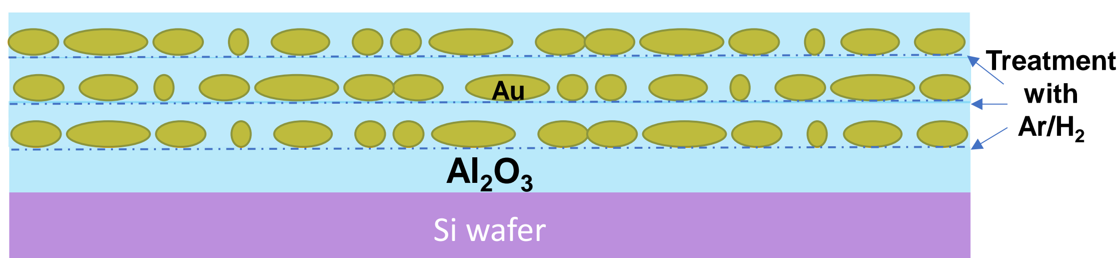

Figure 6-7 – Schematic of a multilayer composed of alumina (4),Au NPs (3) layers and 3 pre-treatments of Ar/H_2.

6.2.1 Microstructure of the multilayers evaluated by TEM

The coatings were analysed by TEM. Figure 6-8 shows the microstructure of the multilayer prepared with 30 s of Au deposition time. The native thin SiO_2 layer (ca 6.5 nm) can be observed on top of the Si substrate in Figure 6-8a. The Au layers show a thickness of ca. 7 nm, which is also the value of the initial Al_2O_3 layer. However, the thickness other Al_2O_3 layers is significantly reduced to 3.5-4 nm. This is probably because the Au layers are not continuous (actually, they are formed by individual nanoparticles), although it is difficult to appreciate in x-section images. As a consequence, during each Al_2O_3 deposition, the gaps among the Au nanoparticles need to be filled, leading to lower observed thickness of the Al_2O_3 layers.

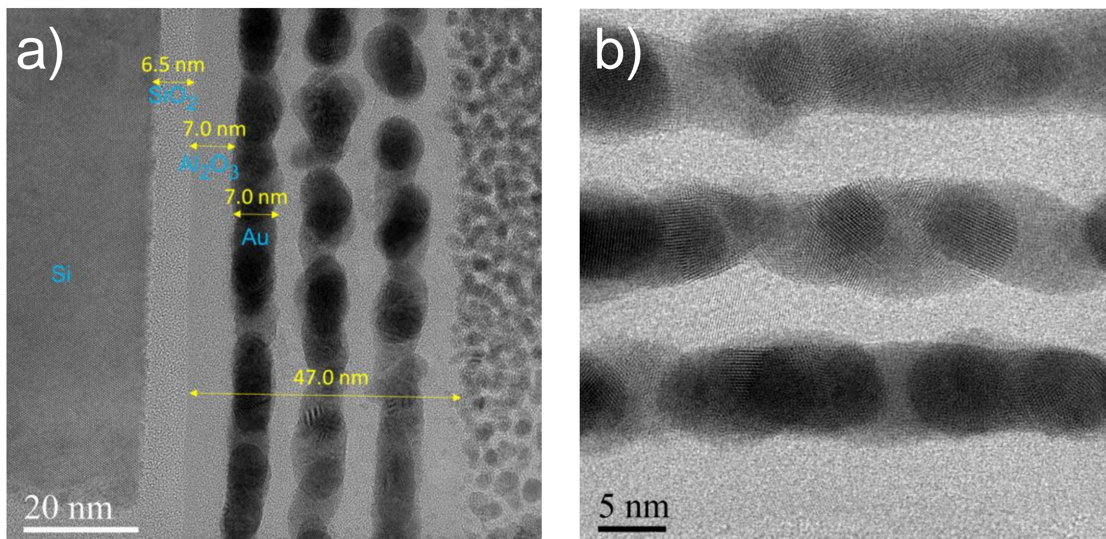

Figure 6-8 – TEM micrographs of the Au/Al_2O_3 multilayer with 30 s of Au deposition a) STEM b) HRTEM.

A cross section HRTEM micrograph of that multilayer is shown in Figure 6-8b. This image reveals the presence of planes in the Au nanoparticles, but also in some areas of Al_2O_3. To evaluate the interplanar distances of these planes, a Fourier transformation (FFT) analysis was carried out in Figure 6-9. Specifically, the (400) plane of γ-Al_2O_3 (0.198 nm), and the (111), (200) and (220) planes to Au (0.235, 0.239, and 0.144 nm) can be identified. The detection of Al_2O_3 planes is noticeable, since these alumina layers are deposited at room temperature, and their structure is mostly amorphous (cf.Figure 3-3).

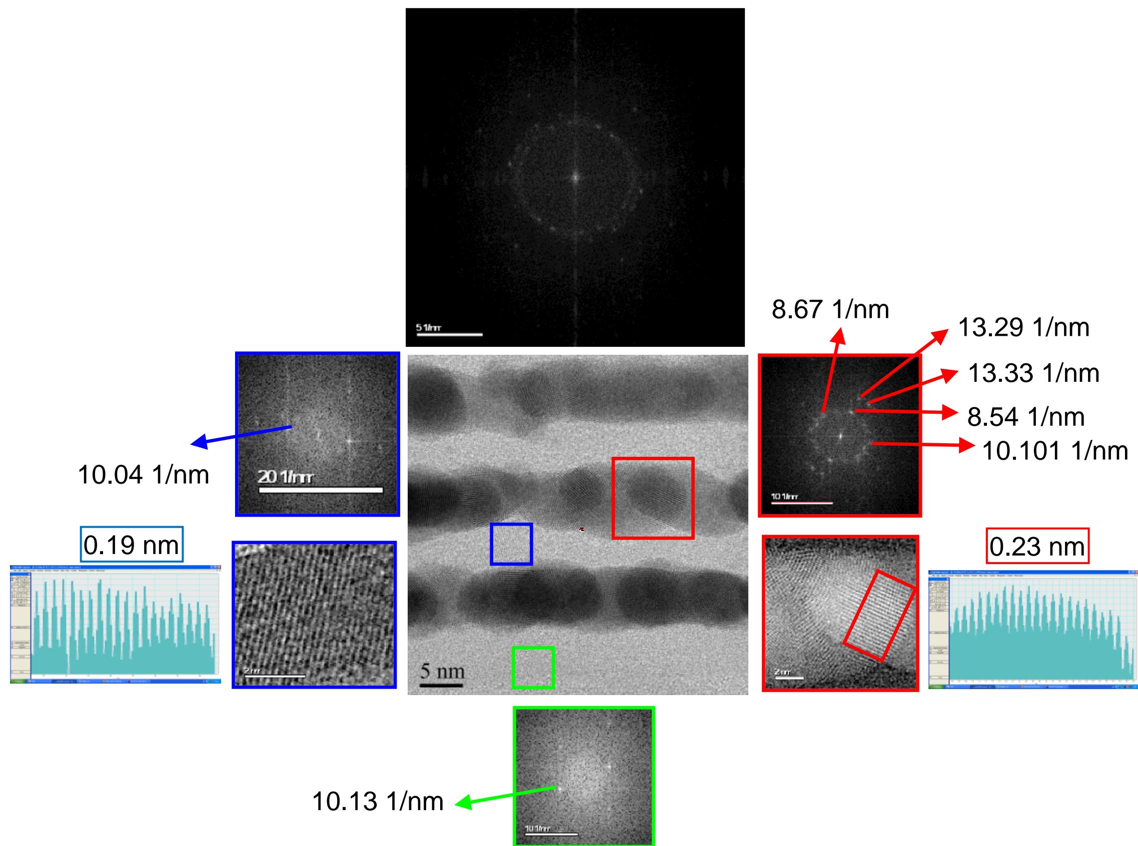

Figure 6-9 – FFT analysis of the micrograph in Figure 6-8b. Top: overall FFT of the image. Bottom: FFT of a region where Al_2O_3 planes were observed. Left and right: FFT images of the regions where planes can be observed in alumina (blue square, left) and Au (red square, right). The distances of the different points in the FFTs are indicated. Inverse FFT images highlighting the planes (by selecting the diffraction points in the FFTs) are also shown. Finally, colour profiles of these images are also depicted, where the wavelength (interplanar distance) is indicated.

The FFT of the whole image (Figure 6-9 top) was radially integrated and converted into a diffractogram pattern equivalent to that measured with CuK_a (i.e. a diffractogram with intensity in function of 2θ, Figure 6-10. There is some overlapping of peaks corresponding to Au and Al_2O_3 references. As a consequence, since Au peaks dominate the pattern, the peaks of Al_2O_3 are difficult to identify. However, a small doublet can be observed at ca. 45°, which corresponds to the (400) γ-Al_2O_3 peak and the (200) of Au.

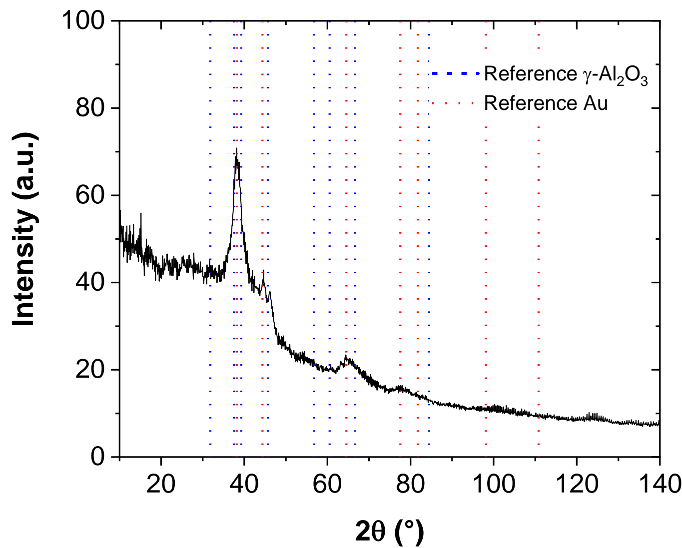

Figure 6-10 – Diffractogram obtained from the radial integration of the FFT of the whole image of Figure 6-9 top. Vertical lines represent the positions of Au and γ-Al_2O_3 references.

A chemical mapping (Figure 6-11) was also performed on the multilayer, revealing the distribution of Si, Ar, Al, O, and Au in the multilayer. First, the Si substrate is seen in the bottom. Additionally, the three layers of Au are easily distinguishable, and in these regions a slightly higher concentration of trapped Ar from the sputtering process is also detected. Finally, Al and O fill are detected in the whole coating, since Au NPs are embedded within the alumina.

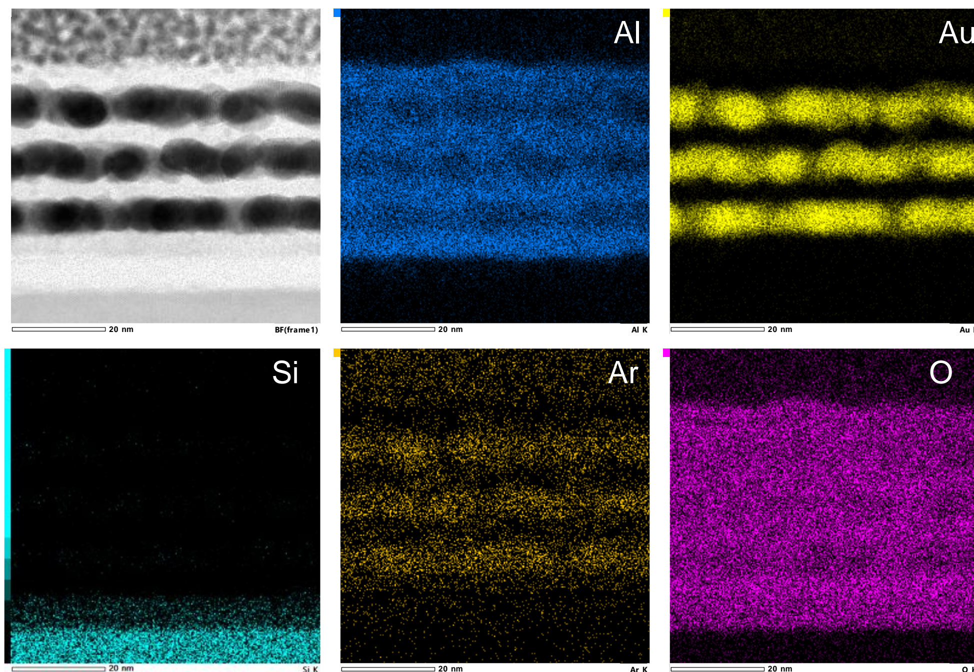

Figure 6-11 – Chemical mapping of the multilayer deposited at 30 s for Au. The top-left image depicts a STEM image of the analysed area.

6.2.2 Optical properties

The UV-Vis absorbance spectra is shown in Figure 6-12 for Au@Al_2O_3 multilayers deposited at 10, 30 and 60 s. An increase in the intensity of absorbance and the wavelength of the maxima is seen when increasing the Au deposition time, likely connected to the increasing number and size of Au nanoparticles.

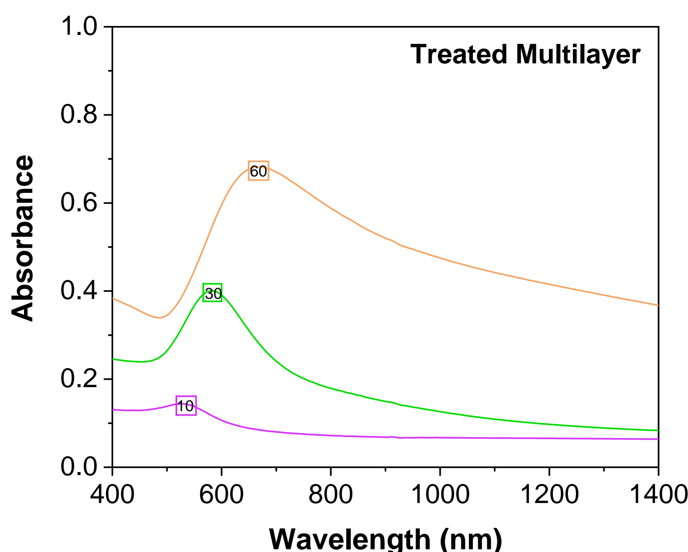

Figure 6-12 –Absorption spectra of Au@Al_2O_3 multilayers with deposition times of 10, 30 and 60 s of Au. The squares indicate the position of the maximum of the SPR peak.

In order to compare the treated multilayer with the untreated and treated monolayers, the coordinates of the maximum of the SPR peaks were taken and analysed in Figure 6-13. The multilayers samples show an absorbance which is a factor 2-3 higher than the corresponding monolayers, in agreement with the higher amount of Au in the samples. The position of the LSPR peak of the multilayer prepared for 30 s is very close corresponding monolayer. However, multilayers with Au deposition time of 10 and 60 s reveal shifts to lower and higher wavelengths, respectively. Those shifts indicate that the multilayer cannot be simply interpreted as a ‘combination of monolayers’. At higher deposition times, the nanoparticles are larger, but the relative surface area of contact between Au and Al_2O_3 respect to the overall particle size decreases. These factors are probably controlling the observed behaviour of the multilayers.

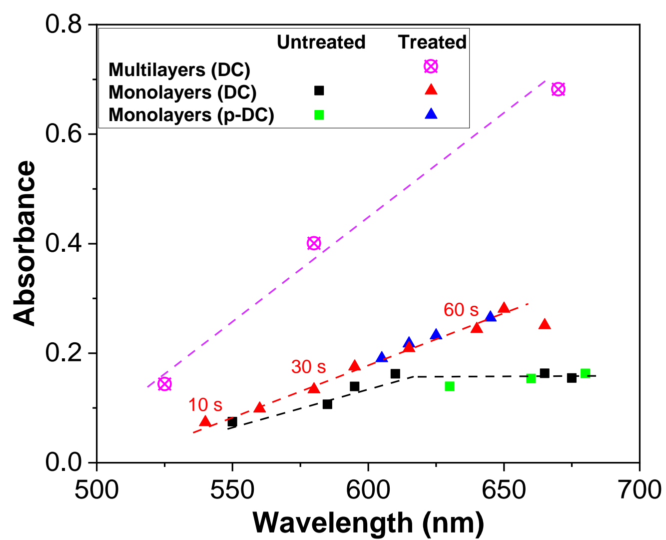

Figure 6-13 – Absorbance of the Multilayer coatings for deposition times of 10, 30 and 60 s compared with untreated and treated samples for DC and Pulsed DC from Figure 6-5. Dashed lines are guides to the eye.

6.3. Conclusion

It was observed that pulsed DC leads to higher deposition rates, resulting in increased amounts of Au material obtained compared to untreated and treated surfaces using continuous DC. Additionally, higher correlation lengths were observed for these samples, particularly for untreated alumina surfaces. This could be attributed to the higher deposition rates during the pulse and/or higher energy of the Au adatoms traveling in the Al_2O_3 surface. Nevertheless, no clear trends were observed regarding the growth deposition mechanism in sputtering parameters. This suggests that these parameters may not have a significant impact on the deposition process under the investigated conditions. In fact, they exhibited similar trends optical properties to those prepared using continuous DC, indicating that the plasma pre-treatment of Al_2O_3 surfaces plays a more crucial role than the modification of Au sputtering conditions.

In the investigation of the multilayers, it was found both Au and Al_2O_3 planes were detected by TEM. These multilayers exhibited higher absorbance compared to monolayers, owing to the higher nanoparticle density. Nevertheless, the location of the LSPR peak changes respect to the corresponding monolayers, which likely indicates the influence of other parameters in the optical behaviour of the samples.

7. Conclusions and perspectives

This Ph.D. dissertation is focused on the deposition of gold nanoparticles onto alumina films using physical vapor-phase deposition. Additionally, the dissertation includes an analysis of the film properties and the optimization of nanoparticle growth. The Thesis was structured into several chapters that investigate the various stages involved in the production of these coatings.

First of all, the production and optimization of alumina films using different sputtering techniques was investigated. It was found that alumina films below 200°C are amorphous, while at temperatures around 450°C, they transition to a crystalline phase (γ-Al_2O_3). HiPIMS sputtering resulted in higher crystallite density compared to MF sputtering due to increased ion energy and density. However, HiPIMS films exhibited a lower deposition rate and higher residual stress. In general, when increasing the energy put in the film (higher power, or temperature, and using HiPIMS instead of MF), several film properties such as grain density, refractive index, compressive stress, and film density were simultaneously increased.

Films produced using a combination of MF and HiPIMS showed characteristics intermediate between HiPIMS and MF alone. HiPIMS sputtering presented some challenges like local delamination and microdroplets caused by arcing, but these issues were minor at lower thicknesses, and they could be identified in characterization. HiPIMS films deposited at room temperature with lower thickness exhibited smoother surfaces with fewer droplets. They offered advantages such as a lower risk of delamination due to lower thermal stress, and no thermal effects during subsequent Au deposition.

The use of an Ar/H_2 plasma treatment of the alumina surface prior Au deposition resulted in Au/Al_2O_3 films with an increased absorbance peak compared to untreated surfaces, and those treated with argon only. The enhancement of the Ar/H_2 pre-treatment of the LSPR peak was similar regardless

the hydrogen concentration and exposure time. This treatment caused a shift from 'horizontal' to 'vertical' growth (i.e., from more parallel to more perpendicular to the surface), as observed through detailed analysis of AFM and XPS results. On the one hand, treated surfaces showed a quite constant correlation length (ξ) when increasing roughness (w), but in the case of untreated surfaces showed a remarkable variation of correlation length (horizontal growth). On the other hand, untreated surfaces showed lower Au deposition rates, higher coverages, and lower heights in XPS analysis, while the opposite was observed for treated surfaces. In short, both techniques (XPS and AFM) analyses revealed similar behaviour in terms of growth directions (parallel and perpendicular to the surface) but employing different characterization parameters to describe them.

These growing parameters not only reveal the same growth patterns for both set of samples, but they can be also combined into geometrical models to illustrate the distinct growth patterns observed in each case. This analysis provides an average visual representation of the effects of plasma treatment on the morphology of the nanoparticles.

In terms of optical properties, two distinct trends of absorbance vs wavelengths could be appreciated depending on the plasma treatment, which is kept even for films with Au deposited using a pulsed source. For untreated samples, the LSPR peak starts to vanish at a relatively low Au deposition time. This is because the coverage of the samples reaches ca. 55%, i.e. more continuous film than individual nanoparticles. In contrast treated surfaces exhibited higher absorbances at higher wavelengths, demonstrating an increased capacity for accommodation of Au before percolation, up to ca. 2.5 times more Au compared with untreated surfaces. Multilayers exhibit even higher absorbances due to the higher increase of surface density of Au NPs. Both coordinates of the LSPR peaks increase with roughness; in case of absorbance, such trend is valid until percolation. In contrast, the position of the LSPR peak shows a common trend with roughness for both sets of samples regardless of the percolation effect, suggesting that surface morphology plays a key role to determine the wavelength of the LSPR. In case of multilayers, position of the

peak is shifted in comparison with the corresponding monolayers, likely due alumina encapsulation.

The different growth and optical properties of Au on treated and untreated Al_2O_3 is likely caused by a chemical variation of its surface, which leads to a different Au wetting behaviour, which ultimately leads on a topographical difference at higher depositions times (> 30 s). The formation of aluminium hydroxide species is probably minor. In contrast, the O/Al ratio was found to decrease in the surface of alumina after Ar/H_2 plasma treatment, which explains the inefficiency of Ar plasma; the presence of H_2 facilitates dramatically the O extraction from alumina to form water species. The reduction of the O/Al ratio probably leads to a further reduction of the surface energy of alumina, which turns it to be more gold-phobic. As a consequence, gold adatoms can travel farther distances in the treated alumina, leading to a lower density of high Au islands, which tend to grow perpendicularly to the substrate. In contrast, gold deposited in untreated alumina leads to a high density of small particles with low height, which tend to grow more parallel to the alumina surface.

After ca. 30 seconds of deposition, the characteristics of the Au deposit start to dominate over the initial topographical characteristics of the alumina. From that point, the topographical differences between both types of samples lead to the higher deposition rate observed for treated samples, as a consequence of the higher surface area and higher aspect ratio of the Au nanoparticles.

Switching from DC to pulsed DC Au sputtering resulted in higher correlation lengths, particularly on untreated samples. This can be attributed to the higher deposition rates (i.e. nanoparticles had more material to grow in parallel to the substrate) and/or higher energy of the Au adatoms (which would allow them to traveling farther across the Al_2O_3 surface). However, no clear trends were observed regarding the influence of particular sputtering parameters.

For an application point of view, Au-Al_2O_3 coatings were tested for their suitability in SERS applications using Rhodamine 6G dye. The coatings exhibited an enhancement factor at least of 10^4, and good reproducibility was shown even after 2 years of sample storage.

Overall, the study demonstrated the significance of plasma pre-treatment in controlling the growth of Au nanoparticles and optimizing the optical and morphological properties of alumina films. The findings open up new possibilities for practical applications, such as the detection of substances like cocaine, and provide insights into the tunability of Au nanoparticles for SERS applications.

There are two lines areas to consider when looking at future developments of this work: academia and entrepreneurship. In academia, the first objective would be to expand and consolidate our understanding of how pre-treatment affects the surface of alumina. The goal is to verify our mechanism for gold growth. To achieve this, we need to conduct simulations, specifically atomistic simulations, on both treated (with O vacancies) and untreated alumina surfaces. These simulations will provide insights into the surface of alumina, and the different behaviour of Au adatoms when travel across these surfaces. These simulations will be performed by Hassan Ohubi and Matthias Rupp at LIST. The second objective is to correlate semi-quantitatively the absorbance peaks (peak position, width) with the characteristics of the films obtained from XPS and AFM data. This will be done through simulations that estimate the absorbance of the samples depending on their characteristics, which are currently underway with positive results in collaboration with Nuno Figueiredo from the University of Coimbra in Portugal. Third, it would be interesting to use another function known as PSDF (Power Spectral Density Function) to analyze the AFM images in order to compare with the results obtained with HHCF. The PSDF function incorporates sensitivity to order, and the outputs would complement the results obtained from HHCF. However, PSDF analysis and fitting is less straightforward than the HHCF. Finally, another interesting point would be to study the effect of hydrogen and argon plasma on the growth of other elements in alumina (e.g. Ag) or Au on other oxides, such as TiO_2 or SiO_2.

In addition to academia, we have found that the use of H_2/Ar plasma pre-treatment to enhance the SERS response of Au/Al_2O_3 may have a potential commercial application. In that regard, when this Ph.D. is being finished (July 2023), we are preparing a patent to protect these findings: characteristics of the

i) plasma treatment and ii) the obtained surfaces. Actually, a literature revision already performed by a patent attorney found nothing close to our findings; in fact, the closest result is an article from Costa et al. [174], which indicates that Au/Al_2O_3 samples do not show SERS effects. The patent preparation is the main reason behind the delay in the publication of results samples including Au nanoparticles (the paper of alumina is already published).

The patent will allow me to prepare and submit a project to a new internal LIST call called YES, whose intention is to promote entrepreneurship. Thus, this is the first year, LIST will grant 200 k€ to an individual holding a PhD or Post-doctoral position who has developed a patent or trade secret within MRT-LIST. The person awarded will be announced by the end of October 2023. This grant will cover all expenses associated with research, entrepreneurship courses, conferences, salaries, and consumables required to advance the idea towards commercialization. Some of the points to investigate/develop in the framework of this project are e.g. i) to perform the depositions on substrates with higher roughness (for example etched glass) since it is proven on the literature that higher roughness leads to better enhancement factors on SERS; ii) deposition of SERS samples in cheaper substrates (e.g. plastic). iii) design and development of prototypes (casettes).

Finally, another direction that we would like to explore would be the application of a JUMP project to FNR in Luxembourg, probably in any of the 2 calls in 2024. That call would be the natural continuation of the YES program, and it is oriented to consolidate and expand the entrepreneurship activities.

8. References

[1] S. Bayda, M. Adeel, T. Tuccinardi, M. Cordani, F. Rizzolio, The history of nanoscience and nanotechnology: From chemical-physical applications to nanomedicine, Molecules. 25 (2020) 1–15. https://doi.org/10.3390/molecules25010112.

[2] S. Vilayurganapathy, Localized Surface Plasmon Resonance Induced Structure-Property Relationships of Metal Nanostructures, 2013. https://scholarworks.wmich.edu/dissertations.

[3] M.L. García-Betancourt, S.I.R. Jiménez, A. González-Hodges, Z.E.N. Salazar, I.L. Escalante-García, J.R. Aparicio, Low Dimensional Nanostructures: Measurement and Remediation Technologies Applied to Trace Heavy Metals in Water, in: M.A. Murillo-Tovar, H. Saldarriaga-Noreña, A. Saeid (Eds.), Trace Metals in the Environment, IntechOpen, Rijeka, 2020. https://doi.org/10.5772/intechopen.93263.

[4] S. Vilayurganapathy, Localized Surface Plasmon Resonance Induced Structure- Property Relationships of Metal Nanostructures, 2013.

[5] C. Durkan, M.E. Welland, Size effects in the electrical resistivity of polycrystalline nanowires, Phys Rev B. 61 (2000) 14215–14218. https://doi.org/10.1103/PhysRevB.61.14215.

[6] D. Guo, G. Xie, J. Luo, Mechanical properties of nanoparticles: Basics and applications, J Phys D Appl Phys. 47 (2014). https://doi.org/10.1088/0022-3727/47/1/013001.

[7] E. Arzt, Size effects in materials due to microstructural and dimensional constraints: a comparative review, Acta Mater. 46 (1998) 5611–5626. https://doi.org/10.1016/S1359-6454(98)00231-6.

[8] A.I. Boukai, Y. Bunimovich, J. Tahir-Kheli, J.K. Yu, W.A. Goddard, J.R. Heath, Silicon nanowires as efficient thermoelectric materials, Nature. 451 (2008) 168–171. https://doi.org/10.1038/nature06458.

[9] A. Vahl, J. Strobel, W. Reichstein, O. Polonskyi, T. Strunskus, L. Kienle, F. Faupel, Single target sputter deposition of alloy nanoparticles with adjustable composition via a gas aggregation cluster source, Nanotechnology. 28 (2017). https://doi.org/10.1088/1361-6528/aa66ef.

[10] D. Daniel, Marie-Christine; Astruc, Gold Nanoparticles: Assembly, Supramolecular Chemistry, Quantum-Size-Related Properties, and Applications toward Biology, Catalysis, and Nanotechnology., 2004.

[11] C. Louis, O. Pluchery, Gold Nanoparticles for Physics, Chemistry and Biology, IMPERIAL COLLEGE PRESS, 2012. https://doi.org/10.1142/p815.

[12] M. Loos, Carbon Nanotube Reinforced Composites, 2015. https://doi.org/10.1016/B978-1-4557-3195-4.00001-1.

[13] P.P. Edwards, J.M. Thomas, Gold in a metallic divided state - From Faraday to present-day nanoscience, Angewandte Chemie - International Edition. 46 (2007) 5480–5486. https://doi.org/10.1002/anie.200700428.

[14] G. Mie, Beiträge zur Optik trüber Medien, speziell kolloidaler Metallösungen, Ann Phys. 330 (1908) 377–445. https://doi.org/10.1002/andp.19083300302.

[15] G. Barbillon, Plasmonics and its applications, Materials. 12 (2019). https://doi.org/10.3390/ma12091502.

[16] R.E. Messersmith, G.J. Nusz, S.M. Reed, Using the localized surface plasmon resonance of gold nanoparticles to monitor lipid membrane assembly and protein binding, Journal of Physical Chemistry C. 117 (2013) 26725–26733. https://doi.org/10.1021/jp406013q.

[17] K.L. Kelly, E. Coronado, L.L. Zhao, G.C. Schatz, The optical properties of metal nanoparticles: The influence of size, shape, and dielectric environment, Journal of Physical Chemistry B. 107 (2003) 668–677. https://doi.org/10.1021/jp026731y.

[18] L. Novotny, B. Hecht, Principles of Nano-Optics, Cambridge University Press, 2012. https://doi.org/10.1017/CBO9780511794193.

[19] V.G. Kravets, A. v. Kabashin, W.L. Barnes, A.N. Grigorenko, Plasmonic Surface Lattice Resonances: A Review of Properties and Applications, Chem Rev. 118 (2018) 5912–5951. https://doi.org/10.1021/acs.chemrev.8b00243.

[20] K. Watanabe, Photochemistry on nanoparticles, in: Encyclopedia of Interfacial Chemistry: Surface Science and Electrochemistry, Elsevier, 2018: pp. 563–572. https://doi.org/10.1016/B978-0-12-409547-2.13211-1.

[21] Y. Danan, Y. Ramon, J. Azougi, A. Douplik, Z. Zalevsky, Decoupling and tuning the light absorption and scattering resonances in metallic composite nanostructures, Opt Express. 23 (2015) 29089. https://doi.org/10.1364/oe.23.029089.

[22] N. Ajdari, C. Vyas, S.L. Bogan, B.A. Lwaleed, B.G. Cousins, Gold nanoparticle interactions in human blood: a model evaluation, Nanomedicine. 13 (2017) 1531–1542. https://doi.org/10.1016/j.nano.2017.01.019.

[23] R.F. Aroca, R.A. Alvarez-Puebla, N. Pieczonka, S. Sanchez-Cortez, J. v. Garcia-Ramos, Surface-enhanced Raman scattering on colloidal nanostructures, Adv Colloid Interface Sci. 116 (2005) 45–61. https://doi.org/10.1016/j.cis.2005.04.007.

[24] K.Q. Lin, J. Yi, J.H. Zhong, S. Hu, B.J. Liu, J.Y. Liu, C. Zong, Z.C. Lei, X. Wang, J. Aizpurua, R. Esteban, B. Ren, Plasmonic photoluminescence for recovering native chemical information from surface-enhanced Raman scattering, Nat Commun. 8 (2017). https://doi.org/10.1038/ncomms14891.

[25] S. Wei, M. Zheng, Q. Xiang, H. Hu, H. Duan, Optimization of the particle density to maximize the SERS enhancement factor of periodic plasmonic nanostructure array, Opt Express. 24 (2016) 20613. https://doi.org/10.1364/oe.24.020613.

[26] D.P. O'Neal, L.R. Hirsch, N.J. Halas, J.D. Payne, J.L. West, Photo-thermal tumor ablation in mice using near infrared-absorbing nanoparticles, Cancer Lett. 209 (2004) 171–176. https://doi.org/10.1016/j.canlet.2004.02.004.

[27] C.S. Kealley, M.B. Cortie, A.I. Maaroof, X. Xu, The versatile colour gamut of coatings of plasmonic metal nanoparticles, Physical Chemistry Chemical Physics. 11 (2009) 5897. https://doi.org/10.1039/b903318a.

[28] N.M.R. de Figueiredo, Nanocomposite coatings based on metal nanoparticles exhibiting Surface Plasmon Resonance deposited by sputtering techniques, 2018. http://hdl.handle.net/10316/79523.

[29] L. Qiao, D. Wang, L. Zuo, Y. Ye, J. Qian, H. Chen, S. He, Localized surface plasmon resonance enhanced organic solar cell with gold nanospheres, Appl Energy. 88 (2011) 848–852. https://doi.org/10.1016/j.apenergy.2010.09.021.

[30] K.A. Willets, R.P. van Duyne, Localized surface plasmon resonance spectroscopy and sensing, Annu Rev Phys Chem. 58 (2007) 267–297. https://doi.org/10.1146/annurev.physchem.58.032806.104607.

[31] F.B. Arango, A. Femius Koenderink, Polarizability tensor retrieval for magnetic and plasmonic antenna design, New J Phys. 15 (2013). https://doi.org/10.1088/1367-2630/15/7/073023.

[32] C.D. Geddes, J.R. Lakowicz, Metal-Enhanced Fluorescence concentrating the local field and subsequently increasing, 2002.

[33] A.M. Wilson, J. Mazzaferri, É. Bergeron, S. Patskovsky, P. Marcoux-Valiquette, S. Costantino, P. Sapieha, M. Meunier, In Vivo Laser-Mediated Retinal Ganglion Cell Optoporation Using KV1.1 Conjugated Gold Nanoparticles, Nano Lett. 18 (2018) 6981–6988. https://doi.org/10.1021/acs.nanolett.8b02896.

[34] T. Chen, B.M. Reinhard, Assembling Color on the Nanoscale: Multichromatic Switchable Pixels from Plasmonic Atoms and Molecules, Advanced Materials. 28 (2016) 3522–3527. https://doi.org/10.1002/adma.201506179.

[35] Z. Xie, W. Yu, T. Wang, H. Zhang, Y. Fu, H. Liu, F. Li, Z. Lu, Q. Sun, Plasmonic Nanolithography: A Review, Plasmonics. 6 (2011) 565–580. https://doi.org/10.1007/s11468-011-9237-0.

[36] X. Zhang, Y.L. Chen, R.S. Liu, D.P. Tsai, Plasmonic photocatalysis, Reports on Progress in Physics. 76 (2013). https://doi.org/10.1088/0034-4885/76/4/046401.

[37] E. Kazuma, T. Tatsuma, Photoinduced reversible changes in morphology of plasmonic Ag nanorods on TiO2 and application to versatile photochromism, Chemical Communications. 48 (2012) 1733–1735. https://doi.org/10.1039/c2cc16589a.

[38] A. Boltasseva, H.A. Atwater, Low-loss plasmonic metamaterials, Science (1979). 331 (2011) 290–291. https://doi.org/10.1126/science.1198258.

[39] P. Wang, M.E. Nasir, A. v. Krasavin, W. Dickson, Y. Jiang, A. v. Zayats, Plasmonic Metamaterials for Nanochemistry and Sensing, Acc Chem Res. 52 (2019) 3018–3028. https://doi.org/10.1021/acs.accounts.9b00325.

[40] I. Goykhman, B. Desiatov, J. Khurgin, J. Shappir, U. Levy, Locally oxidized silicon surface-plasmon Schottky detector for telecom regime, Nano Lett. 11 (2011) 2219–2224. https://doi.org/10.1021/nl200187v.

[41] M.W. Knight, H. Sobhani, P. Nordlander, N.J. Halas, Photodetection with Active Optical Antennas, Science (1979). 332 (2011) 702–704. https://doi.org/10.1126/science.1203056.

[42] B.A. Kairdolf, A.M. Smith, T.H. Stokes, M.D. Wang, A.N. Young, S. Nie, Semiconductor quantum dots for bioimaging and biodiagnostic applications, Annual Review of Analytical Chemistry. 6 (2013) 143–162. https://doi.org/10.1146/annurev-anchem-060908-155136.

[43] X. Huang, Z.P. Aguilar, H. Xu, W. Lai, Y. Xiong, Membrane-based lateral flow immunochromatographic strip with nanoparticles as reporters for detection: A review, Biosens Bioelectron. 75 (2015) 166–180. https://doi.org/10.1016/j.bios.2015.08.032.

[44] Quantum Dots & Nanoparticles , (n.d.). https://chem.beloit.edu/edetc/background/quantum_dots/index.html (accessed March 13, 2023).

[45] M. Quinten, Optical Properties of Nanoparticle Systems, Wiley, 2011. https://doi.org/10.1002/9783527633135.

[46] S.P. Goutam, G. Saxena, D. Roy, A.K. Yadav, R.N. Bharagava, Green Synthesis of Nanoparticles and Their Applications in Water and Wastewater Treatment, in: Bioremediation of Industrial Waste for Environmental Safety, Springer Singapore, 2020: pp. 349–379. https://doi.org/10.1007/978-981-13-1891-7_16.

[47] K. Hachem, M.J. Ansari, R.O. Saleh, H.H. Kzar, M.E. Al-Gazally, U.S. Altimari, S.A. Hussein, H.T. Mohammed, A.T. Hammid, E. Kianfar, Methods of Chemical Synthesis in the Synthesis of Nanomaterial and Nanoparticles by the Chemical Deposition Method: A Review, Bionanoscience. 12 (2022) 1032–1057. https://doi.org/10.1007/s12668-022-00996-w.

[48] S. Iravani, H. Korbekandi, S. v Mirmohammadi, B. Zolfaghari, Synthesis of silver nanoparticles: chemical, physical and biological methods, 2014.

[49] K. Ravichandran, P.K. Praseetha, T. Arun, S. Gobalakrishnan, Synthesis of Nanocomposites, in: Synthesis of Inorganic Nanomaterials: Advances and Key Technologies, Elsevier, 2018: pp. 141–168. https://doi.org/10.1016/B978-0-08-101975-7.00006-3.

[50] A.V. Laura Prati, Gold Catalysis: Preparation, Characterization, and Applications, CRC Press. (2016).

[51] D.I. Meira, R.P. Domingues, M.S. Rodrigues, E. Alves, N.P. Barradas, J. Borges, F. Vaz, Thin films of Au-Al2O3 for plasmonic sensing, Appl Surf Sci. 500 (2020). https://doi.org/10.1016/j.apsusc.2019.144035.

[52] N.M. Figueiredo, F. Vaz, L. Cunha, Y.T. Pei, J.M.T. De Hosson, A. Cavaleiro, Optical and microstructural properties of Au alloyed Al-O sputter deposited coatings, Thin Solid Films. 598 (2016) 65–71. https://doi.org/10.1016/j.tsf.2015.11.060.

[53] J. Wang, W.M. Lau, Q. Li, Effects of particle size and spacing on the optical properties of gold nanocrystals in alumina, J Appl Phys. 97 (2005). https://doi.org/10.1063/1.1868052.

[54] S. Cho, S. Lee, S.-G. Oh, S.J. Park, W.M. Kim, B.-K. Cheong, M. Chung, K.B. Song, T.S. Lee, S.G. Kim, Optical properties of Au nanocluster embedded dielectric films, 2000.

[55] G. De, S. Bhattacharyya, Au nanoparticles in alumina sols and coatings, J Mater Chem. 18 (2008) 2816–2824. https://doi.org/10.1039/b802156b.

[56] Y. Takeda, O.A. Plaksin, H. Wang, K. Kono, N. Umeda, N. Kishimoto, Surface Plasmon Resonance of Au Nanoparticles Fabricated by Negative Ion Implantation and Grid Structure toward Plasmonic Applications, Opt Rev. 13 (2006) 231–234. https://doi.org/10.1007/s10043-006-0231-2.

[57] Y. Takahashi, T. Tatsuma, Electrodeposition of thermally stable gold and silver nanoparticle ensembles through a thin alumina nanomask, Nanoscale. 2 (2010) 1494–1499. https://doi.org/10.1039/c0nr00230e.

[58] J. He, C. Huang, N. Dai, D. Zhu, Study of surface plasmon resonance of Au nanoparticles coated with dielectric layers, in: International Symposium on Photoelectronic Detection and Imaging 2011: Sensor and Micromachined Optical Device Technologies, SPIE, 2011: p. 81910N. https://doi.org/10.1117/12.899870.

[59] N.M. Figueiredo, T. Kubart, J.A. Sanchez-García, R. Escobar Galindo, A. Climent-Font, A. Cavaleiro, Optical properties and refractive index sensitivity of reactive sputtered oxide coatings with embedded Au clusters, J Appl Phys. 115 (2014). https://doi.org/10.1063/1.4861136.

[60] P.R. Ohodnicki, C. Wang, S. Natesakhawat, J.P. Baltrus, T.D. Brown, In-situ and ex-situ characterization of TiO 2 and Au nanoparticle incorporated TiO 2 thin films for optical gas sensing at extreme temperatures, J Appl Phys. 111 (2012). https://doi.org/10.1063/1.3695380.

[61] N.A. Joy, P.H. Rogers, M.I. Nandasiri, S. Thevuthasan, M.A. Carpenter, Plasmonic-based sensing using an array of Au-metal oxide thin films, Anal Chem. 84 (2012) 10437–10444. https://doi.org/10.1021/ac3026477.

[62] J. Borges, T. Kubart, S. Kumar, K. Leifer, M.S. Rodrigues, N. Duarte, B. Martins, J.P. Dias, A. Cavaleiro, F. Vaz, Microstructural evolution of Au/TiO2 nanocomposite films: The influence of Au concentration and thermal annealing, Thin Solid Films. 580 (2015) 77–88. https://doi.org/10.1016/j.tsf.2015.03.024.

[63] M.S. Rodrigues, D. Costa, R.P. Domingues, M. Apreutesei, P. Pedrosa, N. Martin, V.M. Correlo, R.L. Reis, E. Alves, N.P. Barradas, P. Sampaio, J. Borges, F. Vaz, Optimization of nanocomposite Au/TiO 2 thin films towards LSPR optical-sensing, Appl Surf Sci. 438 (2018) 74–83. https://doi.org/10.1016/j.apsusc.2017.09.162.

[64] E. Pedrueza, J.L. Valdés, V. Chirvony, R. Abargues, J. Hernández-Saz, M. Herrera, S.I. Molina, J.P. Martínez-Pastor, Novel method of preparation of gold-nanoparticle-doped TiO2 and SiO2 plasmonic thin films: Optical characterization and comparison with Maxwell-Garnett modeling, Adv Funct Mater. 21 (2011) 3502–3507. https://doi.org/10.1002/adfm.201101020.

[65] K. Kawaguchi, S. Yamamoto, M. Yoshikawa, K. Takahiro, Plasmonic cyclohexane-sensing by sputter-deposited Au nanoparticle array on SiO2, Thin Solid Films. 562 (2014) 648–652. https://doi.org/10.1016/j.tsf.2014.04.092.

[66] S. Zhu, T.P. Chen, Y.C. Liu, Y. Liu, Electroluminescence from SiO2 thin film embedded with self-assembled gold nanoparticles, Nanoscience and

Nanotechnology Letters. 5 (2013) 857–860. https://doi.org/10.1166/nnl.2013.1631.

[67] H.B. Liao, W. Wen, G.K.L. Wong, Preparation and optical characterization of Au/SiO2 composite films with multilayer structure, J Appl Phys. 93 (2003) 4485–4488. https://doi.org/10.1063/1.1560569.

[68] P.R. Ohodnicki, M.P. Buric, T.D. Brown, C. Matranga, C. Wang, J. Baltrus, M. Andio, Plasmonic nanocomposite thin film enabled fiber optic sensors for simultaneous gas and temperature sensing at extreme temperatures, Nanoscale. 5 (2013) 9030–9039. https://doi.org/10.1039/c3nr02891g.

[69] N.M. Figueiredo, Y.T. Pei, J.T.M. De Hosson, A. Cavaleiro, Structural and functional properties of nanocomposite Au-WO3 coatings, Surf Coat Technol. 280 (2015) 201–207. https://doi.org/10.1016/j.surfcoat.2015.08.057.

[70] G.M. Veith, A.R. Lupini, S.J. Pennycook, A. Villa, L. Prati, N.J. Dudney, Magnetron sputtering of gold nanoparticles onto WO3 and activated carbon, Catal Today. 122 (2007) 248–253. https://doi.org/10.1016/j.cattod.2007.01.010.

[71] M. Proença, J. Borges, M.S. Rodrigues, R.P. Domingues, J.P. Dias, J. Trigueiro, N. Bundaleski, O.M.N.D. Teodoro, F. Vaz, Development of Au/CuO nanoplasmonic thin films for sensing applications, Surf Coat Technol. 343 (2018) 178–185. https://doi.org/10.1016/j.surfcoat.2017.08.033.

[72] M. Proenca, M. Rodrigues, F. Vaz, J. Borges, Carbon Monoxide (CO) Sensor Based on Au Nanoparticles Embedded in a CuO Matrix by HR-LSPR Spectroscopy at Room Temperature, IEEE Sens Lett. 5 (2021). https://doi.org/10.1109/LSENS.2021.3074603.

[73] M. Ando, T. Kobayashi, S. Iijima, M. Haruta, Optical CO sensitivity of Au-CuO composite film by use of the plasmon absorption change, Sens Actuators B Chem. 96 (2003) 589–595. https://doi.org/10.1016/S0925-4005(03)00645-2.

[74] H.C. Barshilia, P. Kumar, K.S. Rajam, A. Biswas, Structure and optical properties of Ag–Al2O3 nanocermet solar selective coatings prepared using unbalanced magnetron sputtering, Solar Energy Materials and Solar Cells. 95 (2011) 1707–1715. https://doi.org/10.1016/j.solmat.2011.01.034.

[75] G. Schmidl, J. Dellith, H. Schneidewind, D. Zopf, O. Stranik, A. Gawlik, S. Anders, V. Tympel, C. Katzer, F. Schmidl, W. Fritzsche, Formation and characterization of silver nanoparticles embedded in optical transparent materials for plasmonic sensor surfaces, Mater Sci Eng B Solid State Mater Adv Technol. 193 (2015) 207–216. https://doi.org/10.1016/j.mseb.2014.12.001.

[76] J. Borges, C.G. Ferreira, J.P.C. Fernandes, M.S. Rodrigues, M. Proença, M. Apreutesei, E. Alves, N.P. Barradas, C. Moura, F. Vaz, Thin films of Ag-Au nanoparticles dispersed in TiO2: Influence of composition and microstructure on the LSPR and SERS responses, J Phys D Appl Phys. 51 (2018). https://doi.org/10.1088/1361-6463/aabc49.

[77] X. Zhou, E. Wang, S. Zhou, H. Yuan, Y. Wang, Q. Wang, Controlling size and distribution of Ag nanoparticles in near surface of SiO 2 glass by low-energy ion implantation , Materials Express. 11 (2022) 2010–2014. https://doi.org/10.1166/mex.2021.2115.

[78] M. Proença, M.S. Rodrigues, J. Borges, F. Vaz, Gas sensing with nanoplasmonic thin films composed of nanoparticles (Au, Ag) dispersed in a CuO matrix, Coatings. 9 (2019). https://doi.org/10.3390/COATINGS9050337.

[79] A.L. Stepanov, V.N. Popok, D.E. Hole, I.B. Khaibullin, Ion synthesis and laser annealing of Cu nanoparticles in Al2O3, Appl Phys A Mater Sci Process. 74 (2002) 441–446. https://doi.org/10.1007/s003390101076.

[80] R. Serna, A. Suárez-García, C.N. Afonso, D. Babonneau, Optical evidence for reactive processes when embedding Cu nanoparticles in Al2O3 by pulsed laser deposition, Nanotechnology. 17 (2006) 4588–4593. https://doi.org/10.1088/0957-4484/17/18/010.

[81] T. Bhatia, M. Aindow, N.P. Padture, Formation of a self-assembled Cu-γ-Al2O3 nanocomposite, Philos Mag Lett. 83 (2003) 135–142. https://doi.org/10.1080/0950083021000056614.

[82] Z. Zhao, J. Sun, G. Zhang, L. Bai, The study of microstructure, optical and photocatalytic properties of nanoparticles(NPs)-Cu/TiO2 films deposited by magnetron sputtering, J Alloys Compd. 652 (2015) 307–312. https://doi.org/10.1016/j.jallcom.2015.08.117.

[83] O. Mekasuwandumrong, N. Jantarasorn, J. Panpranot, M. Ratova, P. Kelly, P. Praserthdam, Synthesis of Cu/TiO2 catalysts by reactive magnetron sputtering deposition and its application for photocatalytic reduction of CO2 and H2O to CH4, Ceram Int. 45 (2019) 22961–22971. https://doi.org/10.1016/j.ceramint.2019.07.340.

[84] M. Bernareggi, G.L. Chiarello, G. West, M. Ratova, A.M. Ferretti, P. Kelly, E. Selli, Cu and Pt clusters deposition on TiO2 powders by DC magnetron sputtering for photocatalytic hydrogen production, Catal Today. (2019) 15–21. https://doi.org/10.1016/j.cattod.2018.07.011.

[85] F. Gao, J. Jiang, L. Du, X. Liu, Y. Ding, Stable and highly efficient Cu/TiO2 nanocomposite photocatalyst prepared through atomic layer deposition, Appl Catal A Gen. 568 (2018) 168–175. https://doi.org/10.1016/j.apcata.2018.10.006.

[86] G.H. Chan, J. Zhao, E.M. Hicks, G.C. Schatz, R.P. van Duyne, Plasmonic properties of copper nanoparticles fabricated by nanosphere lithography, Nano Lett. 7 (2007) 1947–1952. https://doi.org/10.1021/nl070648a.

[87] P. Asanithi, S. Chaiyakun, P. Limsuwan, Growth of silver nanoparticles by DC magnetron sputtering, J Nanomater. 2012 (2012). https://doi.org/10.1155/2012/963609.

[88] E. Körner, M.H. Aguirre, G. Fortunato, A. Ritter, J. Rühe, D. Hegemann, Formation and distribution of silver nanoparticles in a functional plasma polymer matrix and related Ag+ release properties, Plasma Processes and Polymers. 7 (2010) 619–625. https://doi.org/10.1002/ppap.200900163.

[89] M.K. Hedayati, F. Faupel, M. Elbahri, Review of plasmonic nanocomposite metamaterial absorber, Materials. 7 (2014) 1221–1248. https://doi.org/10.3390/ma7021221.

[90] P.R. West, S. Ishii, G. v. Naik, N.K. Emani, V.M. Shalaev, A. Boltasseva, Searching for better plasmonic materials, Laser Photon Rev. 4 (2010) 795–808. https://doi.org/10.1002/lpor.200900055.

[91] D. Gerard, S.K. Gray, Aluminium plasmonics, J Phys D Appl Phys. 48 (2015). https://doi.org/10.1088/0022-3727/48/18/184001.

[92] H. Yu, Y. Peng, Y. Yang, Z.-Y. Li, Plasmon-enhanced light–matter interactions and applications, NPJ Comput Mater. 5 (2019) 45. https://doi.org/10.1038/s41524-019-0184-1.

[93] Y. Gutiérrez, A.S. Brown, F. Moreno, M. Losurdo, Plasmonics beyond noble metals: Exploiting phase and compositional changes for manipulating plasmonic performance, J Appl Phys. 128 (2020). https://doi.org/10.1063/5.0020752.

[94] B. Samransuksamer, M. Horprathum, P. Eiamchai, V. Patthanasettakul, A. Wisitsoraat, C. Chananonnawathorn, D. Phokharatkul, P. Chindaudom, T. Jutarosaga, W. Rakreungdet, S. Dumrongrattana, Decoration of gold nanoparticles on TiO2 thin films for enhanced response of ethanol gas sensors, in: Adv Mat Res, Trans Tech Publications Ltd, 2014: pp. 251–254. https://doi.org/10.4028/www.scientific.net/AMR.979.251.

[95] P.C. Lansåker, J. Backholm, G.A. Niklasson, C.G. Granqvist, TiO2/Au/TiO2 multilayer thin films: Novel metal-based transparent conductors for electrochromic devices, Thin Solid Films. 518 (2009) 1225–1229. https://doi.org/10.1016/j.tsf.2009.02.158.

[96] G.M. Veith, A.R. Lupini, S.J. Pennycook, G.W. Ownby, N.J. Dudney, Nanoparticles of gold on γ-Al2O3 produced by dc magnetron sputtering, J Catal. 231 (2005) 151–158. https://doi.org/10.1016/j.jcat.2004.12.008.

[97] J. Borges, R.M.S. Pereira, M.S. Rodrigues, T. Kubart, S. Kumar, K. Leifer, A. Cavaleiro, T. Polcar, M.I. Vasilevskiy, F. Vaz, Broadband Optical Absorption Caused by the Plasmonic Response of Coalesced Au Nanoparticles Embedded in a TiO2 Matrix, Journal of Physical Chemistry C. 120 (2016) 16931–16945. https://doi.org/10.1021/acs.jpcc.6b03684.

[98] A. Schleunitz, H. Steffes, R. Chabicovsky, E. Obermeier, Optical gas sensitivity of a metaloxide multilayer system with gold-nano-clusters, Sens Actuators B Chem. 127 (2007) 210–216. https://doi.org/10.1016/j.snb.2007.07.017.

[99] C. Markert, D. Lützenkirchen-Hecht, R. Frahm, Structural and electrical properties of thin d.c. magnetron-sputtered gold films deposited on float glass, in: Surface and Interface Analysis, 2006: pp. 715–718. https://doi.org/10.1002/sia.2258.

[100] L. Armelao, D. Barreca, A. Gasparotto, E. Pierangelo, E. Tondello, S. Polizzi, Preparation of gold nanoparticles on silica substrate by radio frequency sputtering, J Nanosci Nanotechnol. 5 (2005) 259–265. https://doi.org/10.1166/jnn.2005.027.

[101] S. Terauchi, N. Koshizaki, H. Umehara, Fabrication of Au nanoparticles by radio-frequency magnetron sputtering, Nanostructured Materials. 5 (1995) 71–78. https://doi.org/10.1016/0965-9773(95)00011-3.

[102] P. Sangpour, O. Akhavan, A.Z. Moshfegh, M. Roozbehi, Formation of gold nanoparticles in heat-treated reactive co-sputtered Au-SiO2 thin films, Appl Surf Sci. 254 (2007) 286–290. https://doi.org/10.1016/j.apsusc.2007.07.095.

[103] M. Hirasawa, H. Shirakawa, H. Hamamura, Y. Egashira, H. Komiyama, Growth mechanism of nanoparticles prepared by radio frequency sputtering, J Appl Phys. 82 (1997) 1404–1407. https://doi.org/10.1063/1.365917.

[104] S. Tuscharoen, W. Hicheeranun, C. Chananonnawathorn, M. Horprathum, J. Kaewkhao, Effect of Sputtered Pressure on Au Nanoparticles Formation Decorated ZnO Nanowire Arrays, Mater Today Proc. 43 (2021) 2624–2628. https://doi.org/10.1016/j.matpr.2020.04.626.

[105] A. Sivasankar Reddy, N.M. Figueiredo, A. Cavaleiro, Nanocrystalline Au:Ag:SnO2 films prepared by pulsed magnetron sputtering, Journal of Physics and Chemistry of Solids. 74 (2013) 825–829. https://doi.org/10.1016/j.jpcs.2013.01.023.

[106] S. Biswasi, D. Gogoi, A.R. Pal, Gold Nanoparticle-Crystalline rubrene hybrid nanocomposite via plasma processing and realization of Plasmon-enhanced organic thin film transistor with high responsivity, Appl Surf Sci. 599 (2022). https://doi.org/10.1016/j.apsusc.2022.153883.

[107] G.R. Bamwenda, H. Arakawa, The visible light induced photocatalytic activity of tungsten trioxide powders, 2001.

[108] S. Sawada and G. C. Danielson, Optical Indices of Refraction of WO3, (1959). https://doi.org/10.1103/PhysRev.113.1008.

[109] J.L. Enriquez-Carrejo, M.A. Ramos, J. Mireles-Jr-Garcia, A. Hurtado-Macias, Nano-mechanical and structural study of WO3 thin films, Thin Solid Films. 606 (2016) 148–154. https://doi.org/10.1016/j.tsf.2016.03.054.

[110] N.M. Figueiredo, Y.T. Pei, J.T.M. de Hosson, A. Cavaleiro, Structural and functional properties of nanocomposite Au-WO3 coatings, Surf Coat Technol. 280 (2015) 201–207. https://doi.org/10.1016/j.surfcoat.2015.08.057.

[111] A.H. Jayatissa, K. Guo, A.C. Jayasuriya, Fabrication of cuprous and cupric oxide thin films by heat treatment, Appl Surf Sci. 255 (2009) 9474–9479. https://doi.org/10.1016/j.apsusc.2009.07.072.

[112] A. Bendavid, P.J. Martin, H. Takikawa, Deposition and modification of titanium dioxide thin films by filtered arc deposition, n.d. https://doi.org/10.1016/S0040-6090(99)00937-2.

[113] M.Z. Ghori, S. Veziroglu, A. Hinz, B.B. Shurtleff, O. Polonskyi, T. Strunskus, J. Adam, F. Faupel, O.C. Aktas, Role of UV Plasmonics in the Photocatalytic Performance of TiO2 Decorated with Aluminum Nanoparticles, ACS Appl Nano Mater. 1 (2018) 3760–3764. https://doi.org/10.1021/acsanm.8b00853.

[114] I. Tanahashi, H. Inouyeþand, A. Mito, Effect of Dielectric Matrices on Femtosecond Nonlinear Optical Properties of Au/Dielectric Composite Thin Films, n.d. https://doi.org/10.2109/jcersj.111.288.

[115] C. Figueiredo, Nuno Miguel Rodrigo de and Kubart, Tomas and Albano, Nanocomposite coatings based on metal nanoparticles exhibiting Surface Plasmon Resonance deposited by sputtering techniques, University of Coimbra, 2017. http://weekly.cnbnews.com/news/article.html?no=124000.

[116] V. Tiron, I.L. Velicu, T. Matei, D. Cristea, L. Cunha, G. Stoian, Ultra-short pulse HiPIMS: A strategy to suppress arcing during reactive deposition of SiO2 thin films with enhanced mechanical and optical properties, Coatings. 10 (2020). https://doi.org/10.3390/coatings10070633.

[117] P. Ramakrishnan, Alumina cutting tools, Transactions of the Indian Ceramic Society. 31 (1972) 106–112. https://doi.org/10.1080/0371750X.1972.10840811.

[118] B. Zhang, Y. Liu, S. Agarwala, M.L. Yeh, H.E. Katz, Structure, sodium ion role, and practical issues for β-alumina as a high-k solution-processed gate

layer for transparent and low-voltage electronics, ACS Appl Mater Interfaces. 3 (2011) 4254–4261. https://doi.org/10.1021/am2009103.

[119] M. Saito, M. Kirihara, T. Taniguchi, M. Miyagi, Micropolarizer made of the anodized alumina film, Appl Phys Lett. 55 (1989) 607–609. https://doi.org/10.1063/1.101572.

[120] T. Kohara, H. Tamagaki, Y. Ikari, H. Fujii, Deposition of α-Al2O3 hard coatings by reactive magnetron sputtering, Surf Coat Technol. 185 (2004) 166–171. https://doi.org/10.1016/j.surfcoat.2003.11.017.

[121] R.S. Roy, H. Guchhait, A. Chanda, D. Basu, M.K. Mitra, Improved sliding wear-resistance of alumina with sub-micron grain size: A comparison with coarser grained material, J Eur Ceram Soc. 27 (2007) 4737–4743. https://doi.org/10.1016/j.jeurceramsoc.2007.02.205.

[122] S. Vuorinen, L. Karlsson, Phase transformation in chemically vapour-deposited κ-alumina, Thin Solid Films. 214 (1992) 132–143. https://doi.org/10.1016/0040-6090(92)90761-Y.

[123] O. Zywitzki, G. Hoetzsch, Correlation between structure and properties of reactively deposited Al2O3 coatings by pulsed magnetron sputtering, Surf Coat Technol. 94–95 (1997) 303–308. https://doi.org/10.1016/S0257-8972(97)00341-1.

[124] J. Kohout, E. Bousser, T. Schmitt, R. Vernhes, O. Zabeida, J. Klemberg-Sapieha, L. Martinu, Stable reactive deposition of amorphous Al2O3 films with low residual stress and enhanced toughness using pulsed dc magnetron sputtering with very low duty cycle, Vacuum. 124 (2016) 96–100. https://doi.org/10.1016/j.vacuum.2015.11.017.

[125] N. Reddy, P. Bera, V.R. Reddy, N. Sridhara, A. Dey, C. Anandan, A.K. Sharma, XPS study of sputtered alumina thin films, Ceram Int. 40 (2014) 11099–11107. https://doi.org/10.1016/j.ceramint.2014.03.133.

[126] O. Zywitzki, G. Hoetzsch, Influence of coating parameters on the structure and properties of Al2O3 layers reactively deposited by means of pulsed magnetron sputtering, Surf Coat Technol. 86–87 (1996) 640–647. https://doi.org/10.1016/S0257-8972(96)02992-1.

[127] J. -E. Sundgren, H.T.G. Hentzell, A review of the present state of art in hard coatings grown from the vapor phase, Journal of Vacuum Science & Technology A: Vacuum, Surfaces, and Films. 4 (1986) 2259–2279. https://doi.org/10.1116/1.574062.

[128] K. Wefers, C. Misra, Oxides and Hydroxides of Aluminum, n.d.

[129] T.K. Phung, C. Herrera, M.Á. Larrubia, M. García-Diéguez, E. Finocchio, L.J. Alemany, G. Busca, Surface and catalytic properties of some γ-Al2O3 powders, Appl Catal A Gen. 483 (2014) 41–51. https://doi.org/10.1016/j.apcata.2014.06.020.

[130] L. Samain, A. Jaworski, M. Edén, D.M. Ladd, D.K. Seo, F. Javier Garcia-Garcia, U. Häussermann, Structural analysis of highly porous γ-Al2O3, J Solid State Chem. 217 (2014) 1–8. https://doi.org/10.1016/j.jssc.2014.05.004.

[131] J.M. Andersson, E. Wallin, V. Chirita, E.P. Münger, U. Helmersson, Ab initio calculations on the effects of additives on alumina phase stability, Phys Rev B Condens Matter Mater Phys. 71 (2005). https://doi.org/10.1103/PhysRevB.71.014101.

[132] A.B. Belonoshko, R. Ahuja, B. Johansson, Mechanism for the k-Al2O3 to the alpha-Al2O3 transition and the stability of k-Al2O3 under volume expansion, n.d. https://doi.org/10.1103/PhysRevB.61.3131.

[133] and -Al, B. Holm, R. Ahuja, Y. Yourdshahyan, B. Johansson, B.I. Lundqvist, Elastic and optical properties of alpha- and k-Al2O3, n.d. https://doi.org/10.1103/PHYSREVB.59.12777.

[134] I. Levin, D. Brandon, Metastable Alumina Polymorphs: Crystal Structures and Transition Sequences, Journal of the American Ceramic Society. 81 (2005) 1995–2012. https://doi.org/10.1111/j.1151-2916.1998.tb02581.x.

[135] J. Müller, M. Schierling, E. Zimmermann, D. Neuschütz, Chemical vapor deposition of smooth α-Al2O3 films on nickel base superalloys as diffusion barriers, Surf Coat Technol. 120–121 (1999) 16–21. https://doi.org/10.1016/S0257-8972(99)00333-3.

[136] J.M. Schneider, W.D. Sproul, A.A. Voevodin, A. Matthews, Crystalline alumina deposited at low temperatures by ionized magnetron sputtering, Journal of Vacuum Science & Technology A: Vacuum, Surfaces, and Films. 15 (1997) 1084–1088. https://doi.org/10.1116/1.580434.

[137] E. Dörre, H. Hübner, Alumina: Processing, Properties, and Applications, Springer Berlin Heidelberg, 2011. https://books.google.lu/books?id=ghRtMQEACAAJ.

[138] J.M. Andersson, E. Wallin, V. Chirita, E.P. Münger, U. Helmersson, Ab initio calculations on the effects of additives on alumina phase stability, Phys Rev B Condens Matter Mater Phys. 71 (2005) 1–14. https://doi.org/10.1103/PhysRevB.71.014101.

[139] W.D. Sproul, M.E. Graham, M.S. Wong, S. Lopez, D. Li, R.A. Scholl, Reactive direct current magnetron sputtering of aluminum oxide coatings, Journal of Vacuum Science & Technology A: Vacuum, Surfaces, and Films. 13 (1995) 1188–1191. https://doi.org/10.1116/1.579859.

[140] J. Jaiswal, S. Mourya, G. Malik, R. Chandra, Tunable optical properties of plasmonic Au/Al2O3 nanocomposite thin films analyzed by spectroscopic ellipsometry accounting surface characteristics, Journal of

the Optical Society of America A. 35 (2018) 740. https://doi.org/10.1364/JOSAA.35.000740.

[141] J.M. Andersson, E. Wallin, U. Helmersson, U. Kreissig, E.P. Münger, Phase control of Al2O3 thin films grown at low temperatures, Thin Solid Films. 513 (2006) 57–59. https://doi.org/10.1016/j.tsf.2006.01.016.

[142] G. Angarita, C. Palacio, M. Trujillo, M. Arroyave, Synthesis of Alumina Thin Films Using Reactive Magnetron Sputtering Method, in: J Phys Conf Ser, Institute of Physics Publishing, 2017. https://doi.org/10.1088/1742-6596/850/1/012022.

[143] P. Jin, G. Xu, M. Tazawa, K. Yoshimura, D. Music, J. Alami, U. Helmersson, Low temperature deposition of α-Al2O3 thin films by sputtering using a Cr2O3 template, Journal of Vacuum Science & Technology A: Vacuum, Surfaces, and Films. 20 (2002) 2134. https://doi.org/10.1116/1.1513641.

[144] N.M. Figueiredo, C. Louro, R.E. Galindo, A. Climent-Font, A. Cavaleiro, Structural and mechanical properties of Au alloyed AlO sputter deposited coatings, Surf Coat Technol. 206 (2012) 2740–2745. https://doi.org/10.1016/j.surfcoat.2011.11.008.

[145] G. Hoetzsch, Correlation between structure and properties of reactively deposited Al2O3 coatings by ,pulsed magnetron sputtering, 1997. https://doi.org/10.1016/S0257-8972(97)00341-1.

[146] J.M. Schneider, W.D. Sproul, R.W.J. Chia, M.-S. Wong, A. Matthews, Very-high-rate reactive sputtering of alumina hard coatings, Surf Coat Technol. 96 (1997) 262–266. https://doi.org/10.1016/S0257-8972(97)00152-7.

[147] G. Hoetzsch, Influence of coating parameters on the structure and properties of Al2O3, layers reactively deposited by means of pulsed magnetron sputtering, 1996.

[148] H. Gerdes, R. Bandorf, D. Loch, G. Bräuer, Reactive sputter deposition of alumina coatings, in: IOP Conf Ser Mater Sci Eng, 2012. https://doi.org/10.1088/1757-899X/39/1/012009.

[149] Q. Wang, L. Fang, Q. Liu, L. Chen, Q. Wang, X. Meng, H. Xiao, Target voltage hysteresis behavior and control point in the preparation of aluminum oxide thin films by medium frequency reactive magnetron sputtering, Coatings. 8 (2018). https://doi.org/10.3390/coatings8040146.

[150] A. Belkind, A. Freilich, G. Song, Z. Zhao, R. Scholl, E. Bixon, Mid-frequency reactive sputtering of dielectrics: Al2O3, Surf Coat Technol. 174 (2003) 88–93. https://doi.org/10.1016/S0257-8972Ž03.00369-4.

[151] E. Wallin, T.I. Selinder, M. Elfwing, U. Helmersson, Synthesis of α-Al2O3 thin films using reactive high-power impulse magnetron sputtering, EPL. 82 (2008). https://doi.org/10.1209/0295-5075/82/36002.

[152] J. Lin, High rate reactive sputtering of Al2O3 coatings by HiPIMS, Surf Coat Technol. 357 (2019) 402–411. https://doi.org/10.1016/j.surfcoat.2018.10.024.

[153] E. Wallin, U. Helmersson, Hysteresis-free reactive high power impulse magnetron sputtering, Thin Solid Films. 516 (2008) 6398–6401. https://doi.org/10.1016/j.tsf.2007.08.123.

[154] M. Aiempanakit, T. Kubart, P. Larsson, K. Sarakinos, J. Jensen, U. Helmersson, Hysteresis and process stability in reactive high power impulse magnetron sputtering of metal oxides, Thin Solid Films. 519 (2011) 7779–7784. https://doi.org/10.1016/j.tsf.2011.06.021.

[155] G. Zhou, L. Wang, X. Wang, Y. Yu, Deposition of nanostructured crystalline alumina thin film by twin targets reactive high power impulse magnetron sputtering, Appl Surf Sci. 455 (2018) 310–317. https://doi.org/10.1016/j.apsusc.2018.05.153.

[156] F. Schmaljohann, D. Hagedorn, F. Löffler, Electrical insulation performance of aluminum oxide layers on metallic substrates – HiPIMS compared to RF-MS, Surf Coat Technol. 361 (2019) 119–122. https://doi.org/10.1016/j.surfcoat.2019.01.010.

[157] J. Houska, J. Blazek, J. Rezek, S. Proksova, Overview of optical properties of Al2O3 films prepared by various techniques, Thin Solid Films. 520 (2012) 5405–5408. https://doi.org/10.1016/j.tsf.2012.03.113.

[158] J. Wang, W.M. Lau, Q. Li, Effects of particle size and spacing on the optical properties of gold nanocrystals in alumina, J Appl Phys. 97 (2005). https://doi.org/10.1063/1.1868052.

[159] Y. Hosoya, T. Suga, T. Yanagawa, Y. Kurokawa, Linear and nonlinear optical properties of sol-gel-derived Au nanometer-particle-doped alumina, J Appl Phys. 81 (1997) 1475–1480. https://doi.org/10.1063/1.363983.

[160] S. Hazra, A. Gibaud, C. Sella, Tunable absorption of Au-Al2O3 nanocermet thin films and its morphology, Appl Phys Lett. 85 (2004) 395–397. https://doi.org/10.1063/1.1774250.

[161] N.M. Figueiredo, T. Kubart, J.A. Sanchez-García, R. Escobar Galindo, A. Climent-Font, A. Cavaleiro, Optical properties and refractive index sensitivity of reactive sputtered oxide coatings with embedded Au clusters, J Appl Phys. 115 (2014). https://doi.org/10.1063/1.4861136.

[162] A. Belahmar, A. Chouiyakh, Influence of the Fabrication Conditions on the Formation and Properties of Gold Nanoparticles in Alumina Matrix Produced by Cosputtering, International Journal of Nano and Material Sciences Journal Homepage:Www.ModernScientificPress.Com Int. J.

Nano & Matl. Sci. 3 (2014) 16–29. www.ModernScientificPress.com/Journals/ijnanos.aspx.

[163] S. Peng, J.M. McMahon, G.C. Schatz, S.K. Gray, Y. Sun, Reversing the size-dependence of surface plasmon resonances, Proceedings of the National Academy of Sciences. 107 (2010) 14530–14534. https://doi.org/10.1073/pnas.1007524107.

[164] G. Weick, G.L. Ingold, R.A. Jalabert, D. Weinmann, Surface plasmon in metallic nanoparticles: Renormalization effects due to electron-hole excitations, Phys Rev B Condens Matter Mater Phys. 74 (2006). https://doi.org/10.1103/PhysRevB.74.165421.

[165] J.R. Heath, Size&ependent surface-plasmon resonances of bare silver particles, n.d.

[166] S. Fedrigo, W. Harbich, J. Buttet, Collective dipole oscillations in small silver clusters embedded in rare-gas matrices, n.d.

[167] A. Perez, P. Mélinon, V. Dupuis, L. Bardotti, B. Masenelli, F. Tournus, B. Prével, J. Tuaillon-Combes, E. Bernstein, A. Tamion, N. Blanc, D. Taïnoff, O. Boisron, G. Guiraud, M. Broyer, M. Pellarin, N. del Fatti, F. Vallée, E. Cottancin, J. Lermé, J.L. Vialle, C. Bonnet, P. Maioli, A. Crut, C. Clavier, J.L. Rousset, F. Morfin, Functional nanostructures from clusters, Int J Nanotechnol. 7 (2010) 523–574. https://doi.org/10.1504/IJNT.2010.031733.

[168] I. Tanahashi, A. Mito, Linear and femtosecond optical nonlinear properties of Au/Al 2O3 thin films prepared by a sputtering method, Jpn J Appl Phys. 50 (2011). https://doi.org/10.1143/JJAP.50.105001.

[169] C.H. Zhao, B.P. Zhang, S.J. Wang, P.P. Shang, C. Chen, Microstructure and optical absorption properties of Au/NiO thin films, International Journal of Minerals, Metallurgy and Materials. 18 (2011) 115–120. https://doi.org/10.1007/s12613-011-0409-x.

[170] M.A. Rahman, S.M.K. Vivek, S.H. Kim, J.Y. Byun, Polarizonic-interference colouration of stainless steel surfaces by Au-Al2O3 nanocomposite thin film coating, Appl Surf Sci. 505 (2020). https://doi.org/10.1016/j.apsusc.2019.144428.

[171] Robert N. WENZEL, Theory of Wetting Action at Solid Surfaces, n.d. https://doi.org/10.1021/ie50320a024.

[172] S. Gao, N. Koshizaki, H. Tokuhisa, E. Koyama, T. Sasaki, J.K. Kim, J. Ryu, D.S. Kim, Y. Shimizu, Highly stable au nanoparticles with tunable spacing and their potential application in surface plasmon resonance biosensors, Adv Funct Mater. 20 (2010) 78–86. https://doi.org/10.1002/adfm.200901232.

[173] M. Ando, T. Kobayashi, S. Iijima, M. Haruta, Optical CO sensitivity of Au-CuO composite film by use of the plasmon absorption change, Sens Actuators B Chem. 96 (2003) 589–595. https://doi.org/10.1016/S0925-4005(03)00645-2.

[174] D. Costa, J. Oliveira, M.S. Rodrigues, J. Borges, C. Moura, P. Sampaio, F. Vaz, Development of biocompatible plasmonic thin films composed of noble metal nanoparticles embedded in a dielectric matrix to enhance Raman signals, Appl Surf Sci. 496 (2019). https://doi.org/10.1016/j.apsusc.2019.143701.

[175] A.S.H. Makhlouf, Current and advanced coating technologies for industrial applications, in: Nanocoatings and Ultra-Thin Films, Elsevier, 2011: pp. 3–23. https://doi.org/10.1533/9780857094902.1.3.

[176] R.D. Arnell, P.J. Kelly, Recent advances in magnetron sputtering, 1999.

[177] M. Hala, Characterization of High Power Impulse Magnetron Sputtering Discharges, 2011.

[178] J.T. Gudmundsson, D. Lundin, Introduction to magnetron sputtering, in: High Power Impulse Magnetron Sputtering: Fundamentals, Technologies, Challenges and Applications, Elsevier, 2019: pp. 1–48. https://doi.org/10.1016/B978-0-12-812454-3.00006-1.

[179] J.T. Gudmundsson, D. Lundin, Introduction to magnetron sputtering, 2019. https://doi.org/10.1016/B978-0-12-812454-3.00006-1.

[180] Plasma-Assisted Surface Coating, 2011. https://www.researchgate.net/publication/258154795.

[181] I. Petrov, A. Myers, J.E. Greene, J.R. Abelson, Mass and energy resolved detection of ions and neutral sputtered species incident at the substrate during reactive magnetron sputtering of Ti in mixed Ar+N 2 mixtures , Journal of Vacuum Science & Technology A: Vacuum, Surfaces, and Films. 12 (1994) 2846–2854. https://doi.org/10.1116/1.578955.

[182] A. Belkind, A. Freilich, J. Lopez, Z. Zhao, W. Zhu, K. Becker, Characterization of pulsed dc magnetron sputtering plasmas, New J Phys. 7 (2005). https://doi.org/10.1088/1367-2630/7/1/090.

[183] M. Hala, Characterization of High Power Impulse Magnetron Sputtering Discharges, 2011.

[184] S. Schiller, K. Goedicke, J. Reschke, V. Kirchhoff, S. Schneider, F. Milde, Pulsed magnetron sputter technology, 1993.

[185] U. Helmersson, M. Lattemann, J. Bohlmark, A.P. Ehiasarian, J.T. Gudmundsson, Ionized physical vapor deposition (IPVD): A review of

technology and applications, Thin Solid Films. 513 (2006) 1–24. https://doi.org/10.1016/j.tsf.2006.03.033.

[186] V. Kouznetsov, K. MacÁk, J.M. Schneider, U. Helmersson, I. Petrov, A novel pulsed magnetron sputter technique utilizing very high target power densities, Surf Coat Technol. 122 (1999) 290–293. https://doi.org/10.1016/S0257-8972(99)00292-3.

[187] K. Sarakinos, J. Alami, S. Konstantinidis, High power pulsed magnetron sputtering: A review on scientific and engineering state of the art, Surf Coat Technol. 204 (2010) 1661–1684. https://doi.org/10.1016/j.surfcoat.2009.11.013.

[188] J.T. Gudmundsson, N. Brenning, D. Lundin, U. Helmersson, High power impulse magnetron sputtering discharge, Journal of Vacuum Science & Technology A: Vacuum, Surfaces, and Films. 30 (2012) 030801. https://doi.org/10.1116/1.3691832.

[189] A. Anders, Discharge physics of high power impulse magnetron sputtering, Surf Coat Technol. 205 (2011) S1–S9. https://doi.org/10.1016/j.surfcoat.2011.03.081.

[190] A. Anders, Tutorial: Reactive high power impulse magnetron sputtering (R-HiPIMS), J Appl Phys. 121 (2017). https://doi.org/10.1063/1.4978350.

[191] M. Samuelsson, D. Lundin, J. Jensen, M.A. Raadu, J.T. Gudmundsson, U. Helmersson, On the film density using high power impulse magnetron sputtering, Surf Coat Technol. 205 (2010) 591–596. https://doi.org/10.1016/j.surfcoat.2010.07.041.

[192] A. Anders, Deposition rates of high power impulse magnetron sputtering: Physics and economics, Journal of Vacuum Science & Technology A: Vacuum, Surfaces, and Films. 28 (2010) 783–790. https://doi.org/10.1116/1.3299267.

[193] J. Emmerlich, S. Mráz, R. Snyders, K. Jiang, J.M. Schneider, The physical reason for the apparently low deposition rate during high-power pulsed magnetron sputtering, Vacuum. 82 (2008) 867–870. https://doi.org/10.1016/j.vacuum.2007.10.011.

[194] J. Vlček, K. Burcalová, A phenomenological equilibrium model applicable to high-power pulsed magnetron sputtering, Plasma Sources Sci Technol. 19 (2010). https://doi.org/10.1088/0963-0252/19/6/065010.

[195] D. Lundin, P. Larsson, E. Wallin, M. Lattemann, N. Brenning, U. Helmersson, Cross-field ion transport during high power impulse magnetron sputtering, Plasma Sources Sci Technol. 17 (2008). https://doi.org/10.1088/0963-0252/17/3/035021.

[196] K. Sarakinos, J. Alami, M. Wuttig, Process characteristics and film properties upon growth of TiOx films by high power pulsed magnetron

sputtering, J Phys D Appl Phys. 40 (2007) 2108–2114. https://doi.org/10.1088/0022-3727/40/7/037.

[197] K. Sarakinos, J. Alami, C. Klever, M. Wuttig, Process stabilization and enhancement of deposition rate during reactive high power pulsed magnetron sputtering of zirconium oxide, Surf Coat Technol. 202 (2008) 5033–5035. https://doi.org/10.1016/j.surfcoat.2008.05.009.

[198] E. Wallin, U. Helmersson, Hysteresis-free reactive high power impulse magnetron sputtering, Thin Solid Films. 516 (2008) 6398–6401. https://doi.org/10.1016/j.tsf.2007.08.123.

[199] D. Depla, S. Heirwegh, S. Mahieu, J. Haemers, R. De Gryse, Understanding the discharge voltage behavior during reactive sputtering of oxides, J Appl Phys. 101 (2007). https://doi.org/10.1063/1.2404583.

[200] D. Güttler, B. Abendroth, R. Grötzschel, W. Möller, D. Depla, Mechanisms of target poisoning during magnetron sputtering as investigated by real-time in situ analysis and collisional computer simulation, Appl Phys Lett. 85 (2004) 6134–6136. https://doi.org/10.1063/1.1835002.

[201] D. Depla, R. De Gryse, Target poisoning during reactive magnetron sputtering: Part I: The influence of ion implantation, Surf Coat Technol. 183 (2004) 184–189. https://doi.org/10.1016/j.surfcoat.2003.10.006.

[202] D. Depla, S. Mahieu, R. De Gryse, Depositing Aluminium Oxide: A Case Study of Reactive Magnetron Sputtering, (2008) 153–197. https://doi.org/10.1007/978-3-540-76664-3_5.

[203] E. Mikmeková, Enhanced properties of carbon based coatings, n.d.

[204] J. Sarkar, Sputtering and Thin Film Deposition, in: Sputtering Materials for VLSI and Thin Film Devices, Elsevier, 2014: pp. 93–170. https://doi.org/10.1016/b978-0-8155-1593-7.00002-3.

[205] J.L. Shohet, Encyclopedia of Plasma Technology, 2016.

[206] Diego Martínez Martínez, Recubrimientos protectores autolubricantes con estructura “Nanocomposite” TIC/a-C Y derivados nitrogenados preparados por Pulverización catódica, Universidad de Sevilla, 2007.

[207] F. Cemin, Élaboration de couches minces par HiPIMS: propriétés structurales et aspects énergétiques, (2018). https://www.theses.fr/2018SACLS417.

[208] L. ZHU, G. LU, S. MAO, J. CHEN, D.A. DIKIN, X. CHEN, R.S. RUOFF, Ripening of silver nanoparticles on carbon nanotubes, Nano. 02 (2007) 149–156. https://doi.org/10.1142/S1793292007000507.

[209] Y. Fukamori, M. König, B. Yoon, B. Wang, F. Esch, U. Heiz, U. Landman, Fundamental insight into the substrate-dependent ripening of monodisperse Clusters, ChemCatChem. 5 (2013) 3330–3341. https://doi.org/10.1002/cctc.201300250.

[210] J. Tang, P. Photopoulos, A. Tserepi, D. Tsoukalas, Two-dimensional nanoparticle self-assembly using plasma-induced Ostwald ripening, Nanotechnology. 22 (2011). https://doi.org/10.1088/0957-4484/22/23/235306.

[211] J.A. Venables, Introduction to Surface and Thin Film Processes, Cambridge University Press, 2000. https://doi.org/10.1017/CBO9780511755651.

[212] I. Petrov, P.B. Barna, L. Hultman, J.E. Greene, Microstructural evolution during film growth, Journal of Vacuum Science & Technology A: Vacuum, Surfaces, and Films. 21 (2003) S117–S128. https://doi.org/10.1116/1.1601610.

[213] Peter M. Martin, Handbook of deposition technologies for films and coatings: science, applications and technology, 2010. http://elsevier.com/locate/permissions,.

[214] J.A. Venables, T. Spiller, M. Hanbucken, Nucleation and growth of thin films, 1984. http://iopscience.iop.org/0034-4885/47/4/002.

[215] C.I. Fornari, G. Fornari, P.H. de O. Rappl, E. Abramof, J. dos S. Travelho, Monte Carlo Simulation of Epitaxial Growth, in: Epitaxy, InTech, 2018. https://doi.org/10.5772/intechopen.70220.

[216] K. Oura, M. Katayama, A. V. Zotov, V.G. Lifshits, A.A. Saranin, Growth of Thin Films, in: 2003: pp. 357–387. https://doi.org/10.1007/978-3-662-05179-5_14.

[217] A.H. Tavakoli, P.S. Maram, S.J. Widgeon, J. Rufner, K. Van Benthem, S. Ushakov, S. Sen, A. Navrotsky, Amorphous alumina nanoparticles: Structure, surface energy, and thermodynamic phase stability, Journal of Physical Chemistry C. 117 (2013) 17123–17130.

[218] S. Halas, T. Durakiewicz, J.J. Joyce, Surface energy calculation – metals with 1 and 2 delocalized electrons per atom, Chem Phys. 278 (2002) 111–117. https://doi.org/10.1016/S0301-0104(02)00379-8.

[219] C.T. Campbell, Ultrathin metal films and particles on oxide surfaces: structural, electronic and chemisorptive properties, n.d.

[220] C.T. Campbell, Ultrathin metal films and particles on oxide surfaces: structural, electronic and chemisorptive properties, Surf Sci Rep. 27 (1997) 1–111. https://doi.org/10.1016/S0167-5729(96)00011-8.

[221] B.A. Movchan, A. V Demchishin, Structure and properties of thick condensates of nickel, titanium, tungsten, aluminum oxides, and zirconium dioxide in vacuum, Fiz. Metal. Metalloved. (1969). https://www.osti.gov/biblio/4181669.

[222] Rointan F. Bunshah, Handbook of Hard Coatings, 2001.

[223] O.O. Abegunde, E.T. Akinlabi, O.P. Oladijo, S. Akinlabi, A.U. Ude, Overview of thin film deposition techniques, AIMS Mater Sci. 6 (2019) 174–199. https://doi.org/10.3934/MATERSCI.2019.2.174.

[224] J.A. Thornton, Influence of apparatus geometry and deposition conditions on the structure and topography of thick sputtered coatings, Journal of Vacuum Science and Technology. 11 (1974) 666–670. https://doi.org/10.1116/1.1312732.

[225] R. Messier, A.P. Giri, R.A. Roy, Revised structure zone model for thin film physical structure, Journal of Vacuum Science & Technology A: Vacuum, Surfaces, and Films. 2 (1984) 500–503. https://doi.org/10.1116/1.572604.

[226] P.J. Kelly, R.D. Arnell, Development of a novel structure zone model relating to the closed-field unbalanced magnetron sputtering system, Journal of Vacuum Science & Technology A: Vacuum, Surfaces, and Films. 16 (1998) 2858–2869. https://doi.org/10.1116/1.581432.

[227] P.B. Barna, M. Adamik, Fundamental structure forming phenomena of polycrystalline films and the structure zone models, 1998.

[228] A. Anders, A structure zone diagram including plasma-based deposition and ion etching, Thin Solid Films. 518 (2010) 4087–4090. https://doi.org/10.1016/j.tsf.2009.10.145.

[229] F.A. Smidt, Use of ion beam assisted deposition to modify the microstructure and properties of thin films, International Materials Reviews. 35 (1990) 61–128. https://doi.org/10.1179/095066090790323975.

[230] R.M. Bradley, J.M.E. Harper, D.A. Smith, Theory of thin-film orientation by ion bombardment during deposition, J Appl Phys. 60 (1986) 4160–4164. https://doi.org/10.1063/1.337499.

[231] J.A. Thornton, High Rate Thick Film Growth, Annual Review of Materials Science. 7 (1977) 239–260. https://doi.org/10.1146/annurev.ms.07.080177.001323.

[232] M. Marinov, Effect of ion bombardment on the initial stages of thin film growth, Thin Solid Films. 46 (1977) 267–274. https://doi.org/10.1016/0040-6090(77)90182-1.

[233] J. Pelleg, L.Z. Zevin, S. Lungo, N. Croitoru, Reactive-sputter-deposited TiN films on glass substrates, Thin Solid Films. 197 (1991) 117–128. https://doi.org/10.1016/0040-6090(91)90225-M.

[234] G.N. Van Wyk, H.J. Smith, Crystalline reorientation due to ion bombardment, Nuclear Instruments and Methods. 170 (1980) 433–439. https://doi.org/10.1016/0029-554X(80)91053-8.

[235] D. Manova, J.W. Gerlach, S. Mändl, Thin film deposition using energetic ions, Materials. 3 (2010) 4109–4141. https://doi.org/10.3390/ma3084109.

[236] Gencoa, Controlling reactive processes, (2023). https://www.gencoa.com/resources/documents/controlling_reactive_processes.pdf (accessed May 15, 2023).

[237] D. Kiselman, The 777 nm oxygen triplet in the Sun and solar-type stars, and its use for abundance analysis, Astron Astrophys. 275 (1993) 269–282.

[238] B. D. Cullity, S. R. Stock, Elements of X-Ray Diffraction, Third, Pearson, 2014.

[239] C. Mansilla, Structure, microstructure and optical properties of cerium oxide thin films prepared by electron beam evaporation assisted with ion beams, Solid State Sci. 11 (2009) 1456–1464. https://doi.org/10.1016/j.solidstatesciences.2009.05.001.

[240] B.E. Warren, B.L. Averbach, The Separation of Cold-Work Distortion and Particle Size Broadening in X-Ray Patterns, J Appl Phys. 23 (1952) 497–497. https://doi.org/10.1063/1.1702234.

[241] G.K. Williamsont, W.H. Hallt, X-RAY LINE BROADENING FROM FILED ALUMINIUM AND WOLFRAM, Acta Metallurgica. 1 (1953) 22–31. https://doi.org/10.1016/0001-6160(53)90006-6.

[242] C. Weiss, New Silicon Nanocrystal Materials for Photovoltaic Applications, Friedrich-Schiller-Universität Jena, 2017. https://doi.org/10.4229/28THEUPVSEC2013-1AV.3.3.

[243] Dipl.-P.C. Weiss, Structural, electronic and optical properties of group-IV honeycomb crystals, n.d.

[244] Phenwisa Niyamakom, Influence of deposition parameters on morphology, growth and structure of crystalline and amorphous organic thin films-(the case of perylene and α-NPD), Fakult ̈at f ̈ur Mathematik, Informatik und Naturwissenschaftender RWTH Aachen University , 2008.

[245] rigaku, X-RAY REFLECTOMETRY (XRR) , Https://Rsmd.Rigaku.Com/Techniques/Xrr. (n.d.).

[246] M. Cazorla Soult, V. Siller, X. Zhu, R. Gehlhaar, P.J. Wojcik, A. Morata, A. Tarancón, P.M. Vereecken, A. Hubin, Spectroscopic Ellipsometry for Operando Monitoring of (De)Lithiation-Induced Phenomena on LiMn2O4

and LiNi0.5Mn1.5O4 Electrodes, J Electrochem Soc. 169 (2022) 040501. https://doi.org/10.1149/1945-7111/ac5ceb.

[247] J.N.H. Harland G. Tompkins, Spectroscopic ellipsometry : practical application to thin film characterization, n.d. http://ebookcentral.proquest.com/lib/unilu-ebooks/detail.action?docID=4205920.

[248] Joaquim O. Carneiro, Vasco Teixeira, S. Azevedo, Encyclopedia of Thermal Stresses, Springer Netherlands, Dordrecht, 2014. https://doi.org/10.1007/978-94-007-2739-7.

[249] G.N. Strauss, S. Schlichtherle, H.K. Pulker, Mechanical stress in optical coatings, 2005. www.phystech-coating.com.

[250] Kurt E. Sickafus, Eugene A. Kotomin, Blas P. Uberuaga, Radiation Effects in Solids, 2007. http://www.nato.int/science.

[251] The tension of metallic films deposited by electrolysis, Proceedings of the Royal Society of London. Series A, Containing Papers of a Mathematical and Physical Character. 82 (1909) 172–175. https://doi.org/10.1098/rspa.1909.0021.

[252] Mechanical Properties of Monocrystalline Silicon, (n.d.). https://www.universitywafer.com/mechanical-properties-monocrystalline-silicon.html.

[253] P. Profilers, Thin Film Stress Measurements using KLA-Tencor Stylus Based Profilers, (n.d.).

[254] O. Instruments, Fast-Quantitative-AFM-Nanomechanical-Measurements-Using-AM-FM-Viscoelastic-Mapping-Mode, (2015).

[255] O. Instruments, AM-FM Viscoelastic Mapping Mode, Nano Lett. 4 (2017) 1–8.

[256] M.K.I.R.B.O. and R.P. Donna Hurley, Fast, quantitative AFM nanomechanical measurements using AM-FM Viscoelastic Mapping Mode, 2015. http://www.microscopy-analysis.com/user/loginWeb:www.microscopy-analysis.com.

[257] M. Kocun, A. Labuda, W. Meinhold, I. Revenko, R. Proksch, Fast, High Resolution, and Wide Modulus Range Nanomechanical Mapping with Bimodal Tapping Mode, ACS Nano. 11 (2017) 10097–10105. https://doi.org/10.1021/acsnano.7b04530.

[258] I. Horcas, R. Fernández, J.M. Gómez-Rodríguez, J. Colchero, J. Gómez-Herrero, A.M. Baro, WSXM: A software for scanning probe microscopy and a tool for nanotechnology, Review of Scientific Instruments. 78 (2007). https://doi.org/10.1063/1.2432410.

[259] C. Mansilla, P. Philipp, T. Wirtz, Roughening of silicon (1 0 0) surface during low energy Cs+ ion bombardment, in: Nucl Instrum Methods Phys Res B, 2011: pp. 905–908. https://doi.org/10.1016/j.nimb.2010.11.063.

[260] R. Kesarwani, P.P. Dey, A. Khare, Correlation between surface scaling behavior and surface plasmon resonance properties of semitransparent nanostructured Cu thin films deposited via PLD, RSC Adv. 9 (2019) 7967–7974. https://doi.org/10.1039/C9RA00194H.

[261] T.-M.L. Matthew Pelliccione, Evolution of Thin Film Morphology, Springer New York, New York, NY, 2008. https://doi.org/10.1007/978-0-387-75109-2.

[262] Matthew. Pelliccione, T.-M. (Toh-M. Lu, Evolution of thin film morphology : modeling and simulations, Springer, 2008.

[263] S.K. Sinha, E.B. Sirota, S. Garoff, H.B. Stanley, X-ray and neutron scattering from rough surfaces, Phys Rev B. 38 (1988) 2297–2311. https://doi.org/10.1103/PhysRevB.38.2297.

[264] A. Ul-Hamid, Contrast Formation in the SEM, in: A Beginners' Guide to Scanning Electron Microscopy, Springer International Publishing, 2018: pp. 77–128. https://doi.org/10.1007/978-3-319-98482-7_3.

[265] K. Akhtar, S.A. Khan, S.B. Khan, A.M. Asiri, Scanning electron microscopy: Principle and applications in nanomaterials characterization, in: Handbook of Materials Characterization, Springer International Publishing, 2018: pp. 113–145. https://doi.org/10.1007/978-3-319-92955-2_4.

[266] nanoScience, Transmission Electron Microscopy, (n.d.). https://www.nanoscience.com/techniques/transmission-electron-microscopy/ (accessed March 16, 2023).

[267] Transmission Electron Microscopy A Textbook for Materials Science, n.d.

[268] I. MacLaren, K.J. Annand, C. Black, A.J. Craven, EELS at very high energy losses, Microscopy. 67 (2018) i78–i85. https://doi.org/10.1093/jmicro/dfx036.

[269] H.G. Boyen, G. Kästle, F. Weigl, B. Koslowski, C. Dietrich, P. Ziemann, J.P. Spatz, S. Riethmüller, C. Hartmann, M. Möller, G. Schmid, M.G. Garnier, P. Oelhafen, Oxidation-resistant gold-55 clusters, Science (1979). 297 (2002) 1533–1536. https://doi.org/10.1126/science.1076248.

[270] S.B. DiCenzo, S.D. Berry, E.H. Hartford, Photoelectron spectroscopy of single-size Au clusters collected on a substrate, Phys Rev B. 38 (1988) 8465–8468. https://doi.org/10.1103/PhysRevB.38.8465.

[271] S. Tougaard, Universality classes of inelastic electron scattering cross-sections, Surface and Interface Analysis. 25 (1997) 137–154.

https://doi.org/10.1002/(SICI)1096-9918(199703)25:3<137::AID-SIA230>3.0.CO;2-L.

[272] S. Tougaard, Quantitative analysis of the inelastic background in surface electron spectroscopy, Surface and Interface Analysis. 11 (1988) 453–472. https://doi.org/10.1002/sia.740110902.

[273] S. Tougaard, Energy loss in XPS: Fundamental processes and applications for quantification, non-destructive depth profiling and 3D imaging, J Electron Spectros Relat Phenomena. 178–179 (2010) 128–153. https://doi.org/10.1016/j.elspec.2009.08.005.

[274] S. Tougaard, Surface nanostructure determination by x-ray photoemission spectroscopy peak shape analysis, Journal of Vacuum Science & Technology A: Vacuum, Surfaces, and Films. 14 (1996) 1415–1423. https://doi.org/10.1116/1.579963.

[275] S. Tanuma, C.J. Powell, D.R. Penn, Calculations of electron inelastic mean free paths. V. Data for 14 organic compounds over the 50-2000 eV range, Surface and Interface Analysis. 21 (1994) 165–176. https://doi.org/10.1002/sia.740210302.

[276] H. Shinotsuka, S. Tanuma, C.J. Powell, D.R. Penn, Calculations of electron inelastic mean free paths. X. Data for 41 elemental solids over the 50eV to 200keV range with the relativistic full Penn algorithm, Surface and Interface Analysis. 47 (2015) 871–888. https://doi.org/10.1002/sia.5789.

[277] S. Hajati, S. Tougaard, What nano-physical properties can be determined by analysis of elastic peak accompanied by its inelastic background tail in XPS and AES spectra?, 2006.

[278] C.L. Haynes, A.D. Mcfarland, R.P. Van Duyne, Raman Spectroscopy, n.d.

[279] P. Rostron, S. Gaber, D. Gaber, Raman Spectroscopy, Review, 2016. www.erpublication.org .

[280] P.M. V Raja, A.R. Barron, Physical Methods in Chemistry and Nano Science, n.d. https://LibreTexts.org.

[281] ; Lothiax, Beer's Law and its Use in Analysis A Review, n.d.

[282] M. Dadi, M. Yasir, Spectroscopy and Spectrophotometry: Principles and Applications for Colorimetric and Related Other Analysis, in: A.K. Samanta (Ed.), Colorimetry, IntechOpen, Rijeka, 2022. https://doi.org/10.5772/intechopen.101106.

[283] S. Marhaba, Effect of Size, Shape and Environment on the Optical Response of Metallic Nanoparticles, in: Noble and Precious Metals - Properties, Nanoscale Effects and Applications, InTech, 2018. https://doi.org/10.5772/intechopen.71574.

[284] Uwe Kreibig, Michael Vollmer, Optical Properties of Metal Clusters, 1995.

[285] W.L. Barnes, Particle plasmons: Why shape matters, Am J Phys. 84 (2016) 593–601. https://doi.org/10.1119/1.4948402.

[286] S. Link, M.A. El-Sayed, Size and temperature dependence of the plasmon absorption of colloidal gold nanoparticles, Journal of Physical Chemistry B. 103 (1999) 4212–4217. https://doi.org/10.1021/jp984796o.

[287] H. Chen, X. Kou, Z. Yang, W. Ni, J. Wang, Shape- and size-dependent refractive index sensitivity of gold nanoparticles, Langmuir. 24 (2008) 5233–5237. https://doi.org/10.1021/la800305j.

[288] A. Attaran, S.D. Emami, M.R.K. Soltanian, R. Penny, F. behbahani, S.W. Harun, H. Ahmad, H.A. Abdul-Rashid, M. Moghavvemi, Circuit Model of Fano Resonance on Tetramers, Pentamers, and Broken Symmetry Pentamers, Plasmonics. 9 (2014) 1303–1313. https://doi.org/10.1007/s11468-014-9743-y.

[289] D. Mortazavi, A.Z. Kouzani, A. Kaynak, W. Duan, DEVELOPING LSPR DESIGN GUIDELINES, 2012.

[290] E.A. Chaffin, S. Bhana, R.T. O'Connor, X. Huang, Y. Wang, Impact of core dielectric properties on the localized surface plasmonic spectra of gold-coated magnetic core-shell nanoparticles, Journal of Physical Chemistry B. 118 (2014) 14076–14084. https://doi.org/10.1021/jp505202k.

[291] Wei. Hong, T.Jun. Cui, D.G. Fang, 2005 Asia-Pacific Microwave Conference : proceedings : December 4-7, 2005, Suzhou International Conference Center, Suzhou, China, IEEE, 2005.

[292] K.L. Kelly, E. Coronado, L.L. Zhao, G.C. Schatz, The optical properties of metal nanoparticles: The influence of size, shape, and dielectric environment, Journal of Physical Chemistry B. 107 (2003) 668–677. https://doi.org/10.1021/jp026731y.

[293] G. Zhou, L. Wang, X. Wang, Y. Yu, Deposition of nanostructured crystalline alumina thin film by twin targets reactive high power impulse magnetron sputtering, Appl Surf Sci. 455 (2018) 310–317. https://doi.org/10.1016/j.apsusc.2018.05.153.

[294] J. Wang, Y.H. Yu, S.C. Lee, Y.W. Chung, Tribological and optical properties of crystalline and amorphous alumina thin films grown by low-temperature reactive magnetron sputter-deposition, Surf Coat Technol. 146–147 (2001) 189–194. https://doi.org/10.1016/S0257-8972(01)01387-1.

[295] D. Bouchet, C. Colliex, Experimental study of ELNES at grain boundaries in alumina: Intergranular radiation damage effects on Al-L23 and O-K edges, Ultramicroscopy. 96 (2003) 139–152. https://doi.org/10.1016/S0304-3991(02)00437-0.

[296] V. Edlmayr, T.P. Harzer, R. Hoffmann, D. Kiener, C. Scheu, C. Mitterer, Effects of thermal annealing on the microstructure of sputtered Al2O3 coatings, Journal of Vacuum Science & Technology A: Vacuum, Surfaces, and Films. 29 (2011) 041506. https://doi.org/10.1116/1.3584803.

[297] N. Jiang, J.C.H. Spence, Interpretation of oxygen K pre-edge peak in complex oxides, Ultramicroscopy. 106 (2006) 215–219. https://doi.org/10.1016/j.ultramic.2005.07.004.

[298] H.O. Ayoola, C.-H. Li, S.D. House, C.S. Bonifacio, K. Kisslinger, J. Jinschek, W.A. Saidi, J.C. Yang, Origin and Suppression of Beam Damage-Induced Oxygen-K Edge Artifact from γ-Al2O3 using Cryo-EELS, Ultramicroscopy. 219 (2020) 113127. https://doi.org/10.1016/j.ultramic.2020.113127.

[299] H. Ayoola, C.-H. Li, S. House, J. Kas, J. Rehr, J. Jinschek, W. Saidi, J. Yang, C. Bonifacio, Probing the Cation Distribution in Gamma-alumina Enabled by O-K Edge Artifact Suppression Using Cryo-EELS, Microscopy and Microanalysis. 26 (2020) 2550–2552. https://doi.org/10.1017/s1431927620021996.

[300] S. Fritz, A. Seiler, L. Radtke, R. Schneider, M. Weides, G. Weiß, D. Gerthsen, Correlating the nanostructure of Al-oxide with deposition conditions and dielectric contributions of two-level systems in perspective of superconducting quantum circuits, Sci Rep. 8 (2018). https://doi.org/10.1038/s41598-018-26066-4.

[301] S. Nufer, T. Gemming, C.E. Elsa¨sser, S. Ko¨stlmeierko¨stlmeier, M.R. Ru¨hle, Core-hole effect in the ELNES of α-Al2O3 : experiment and theory, 2001.

[302] A. Anders, A structure zone diagram including plasma-based deposition and ion etching, Thin Solid Films. 518 (2010) 4087–4090. https://doi.org/10.1016/j.tsf.2009.10.145.

[303] Y. Dai, S. Li, Q. Sun, Q. Peng, C. Gui, Y. Zhou, S. Liu, Properties of AlN film grown on Si (111), J Cryst Growth. 435 (2016) 76–83. https://doi.org/10.1016/j.jcrysgro.2015.11.016.

[304] K. Yahiaoui, S. Abdelli-Messaci, S. Messaoud Aberkane, M. Siad, A. Kellou, Growth of γ-alumina thin films by pulsed laser deposition and plasma diagnostic, Appl Phys A Mater Sci Process. 123 (2017). https://doi.org/10.1007/s00339-017-1074-3.

[305] G. Balakrishnan, R. Thirumurugesan, E. Mohandas, D. Sastikumar, P. Kuppusami, J.I. Song, Phase transition and thermal expansion studies of alumina thin films prepared by reactive pulsed laser deposition, J Nanosci Nanotechnol. 14 (2014) 7728–7733. https://doi.org/10.1166/jnn.2014.9480.

[306] K. Sarakinos, L. Martinu, Synthesis of thin films and coatings by high power impulse magnetron sputtering, Elsevier Inc., 2019. https://doi.org/10.1016/B978-0-12-812454-3.00013-9.

[307] C.S. Gorham, J.T. Gaskins, G.N. Parsons, M.D. Losego, P.E. Hopkins, Density dependence of the room temperature thermal conductivity of atomic layer deposition-grown amorphous alumina (Al2O3), Appl Phys Lett. 104 (2014). https://doi.org/10.1063/1.4885415.

[308] J. Houska, J. Blazek, J. Rezek, S. Proksova, Overview of optical properties of Al2O3 films prepared by various techniques, Thin Solid Films. 520 (2012) 5405–5408. https://doi.org/10.1016/j.tsf.2012.03.113.

[309] X. Zhang, L. Hu, Estimating scattering of pure water from density fluctuation of the refractive index, 2009.

[310] V. Dimitrov, T. Komatsu, Electronic Ion Polarizability, Optical Basicity and Metal (or Nonmetal) Binding Energy of Simple Oxides, 1999.

[311] Stenzel, Thin Film Optical Spectra, 2013.

[312] J. Lermé, B. Palpant, B. Prével, E. Cottancin, M. Pellarin, M. Treilleux, J.L. Vialle, A. Perez, M. Broyer, Optical properties of gold metal clusters: A time-dependent local-density-approximation investigation, Springer-Verlag, 1998.

[313] S. Link, M.A. El-Sayed, Spectral Properties and Relaxation Dynamics of Surface Plasmon Electronic Oscillations in Gold and Silver Nanodots and Nanorods, Journal of Physical Chemistry B. 103 (1999) 8410–8426. https://doi.org/10.1021/jp9917648.

[314] S. Hajati, S. Tougaard, What nano-physical properties can be determined by analysis of elastic peak accompanied by its inelastic background tail in XPS and AES spectra?, Journal of Surface Analysis. 13 (2006) 148–155.

[315] A.P. Grosvenor, B.A. Kobe, N.S. McIntyre, S. Tougaard, W.N. Lennard, Use of QUASES^{TM}/XPS measurements to determine the oxide composition and thickness on an iron substrate, Surface and Interface Analysis. 36 (2004) 632–639. https://doi.org/10.1002/sia.1842.

[316] M.C. López-Santos, F. Yubero, J.P. Espinós, A.R. González-Elipe, Non-destructive depth compositional profiles by XPS peak-shape analysis, Anal Bioanal Chem. 396 (2010) 2757–2768. https://doi.org/10.1007/s00216-009-3312-9.

[317] S. Hajati, V. Zaporojtchenko, F. Faupel, S. Tougaard, Characterization of Au nano-cluster formation on and diffusion in polystyrene using XPS peak shape analysis, Surf Sci. 601 (2007) 3261–3267. https://doi.org/10.1016/j.susc.2007.06.001.

[318] C. Mansilla, F. Gracia, A.I. Martin-Concepción, J.P. Espinós, J.P. Holgado, F. Yubero, A.R. González-Elipe, Study of the first nucleation steps of thin films by XPS inelastic peak shape analysis, Surface and Interface Analysis. 39 (2007) 331–336. https://doi.org/10.1002/sia.2509.

[319] F.M. Mwema, E.T. Akinlabi, O.P. Oladijo, O.P. Oladijo, The Use of Power Spectrum Density for Surface Characterization of Thin Films, in: Photoenergy and Thin Film Materials, Wiley, 2019: pp. 379–411. https://doi.org/10.1002/9781119580546.ch9.

[320] J.H. Jeffries, J.K. Zuo, M.M. Craig, Instability of Kinetic Roughening in Sputter-Deposition Growth of Pt on Glass, Phys Rev Lett. 76 (1996) 4931–4934. https://doi.org/10.1103/PhysRevLett.76.4931.

[321] S. Christke, C. Katzer, V. Grosse, F. Schmidl, G. Schmidl, W. Fritzsche, J. Petschulat, T. Pertsch, M. Rettenmayr, Optical resonances of self-organized monocrystalline Au nanoparticles embedded in SrTiO_3 matrix, Opt Mater Express. 1 (2011) 890. https://doi.org/10.1364/ome.1.000890.

[322] N.M. Figueiredo, T. Kubart, J.A. Sanchez-García, R. Escobar Galindo, A. Climent-Font, A. Cavaleiro, Optical properties and refractive index sensitivity of reactive sputtered oxide coatings with embedded Au clusters, J Appl Phys. 115 (2014) 0–13. https://doi.org/10.1063/1.4861136.

[323] W.J. Lee, Y.H. Chang, Growth without postannealing of monoclinic VO2 thin film by atomic layer deposition using VCl4 as precursor, Coatings. 8 (2018). https://doi.org/10.3390/coatings8120431.

9. Scientific Outputs

Accepted publication:

1. Marta P. Ferreira*, D. Martínez-Martínez, J-B. Chemin, P. Choquet. ”Tuning the Characteristics of Al_2O_3 Thin Films Using Different Pulse Configurations: Mid-Frequency, High-Power Impulse Magnetron Sputtering, and their Combination.” (DOI: 10.1016/j.surfcoat.2023.129648).

Future publications:

2. Marta P. Ferreira*, D. Martínez-Martínez, J-B. Chemin, P. Choquet. “Deposition of Au on Al_2O_3 thin films of plasmonic applications I: an AFM study.”
3. Marta P. Ferreira*, D. Martínez-Martínez, Jérôme Guillot, J-B. Chemin, P. Choquet. “Deposition of Au on Al_2O_3 thin films for plasmonic applications II: influence of Au growth on the plasmonic effect.”
4. Marta P. Ferreira*, D. Martínez-Martínez, Nuno Figueiredo, J-B. Chemin, P. Choquet. “Au particles deposited on Al_2O_3 thin films: a semi-quantitative simulation of plasmonic behaviour based on growth parameters.”
5. Marta P. Ferreira*, D. Martínez-Martínez, J-B. Chemin, P. Choquet. “Influence of pulsing on the growth and plasmonic properties of Au/Al_2O_3 thin films.”
6. Marta P. Ferreira*, D. Martínez-Martínez, Simon Bulou, J-B. Chemin, P. Choquet. “Development of Au/Al_2O_3 SERS substrates by magnetron sputtering.”

Patent:

1. Marta P. Ferreira*, D. Martínez-Martínez, Simon Bulou, J-B. Chemin, P. Choquet. “Substrate with nanocomposite film, e.g., for SERS”, DPLIST0025LU filed on 16/08/2023.

Conference Presentations:

1. MSE 2020 - Materials Science and Engineering Conference: "Co-deposition process to elaborate a nanocomposite coating with Al_2O_3-NPs with plasmonic effect". (Online - Oral)
2. E-MRS Spring Meeting 2022 – "Tuning alumina matrix using MF and HiPIMS sputtering with gold nanoparticles for plasmonic coatings". (Online - Oral)
3. PSE 2022 – "Elaboration of plasma coating based on gold nanoparticles embedded in alumina matrix by sputtering techniques". (Poster)
4. PACEYSC 2022 – "Controlled growth of Au nanoparticles on Al_2O_3 coatings for enhanced localized surface plasmon resonance". (Oral)

Workshops:

1. 8th DocMASE Summer School 2019: surface structuring and functional coatings
2. 6th PLASMA Science and Entrepreneurship Workshop (2019)

Award:

1. Distinction Image on FNR Science Image Competition 2022